Waveguide Quantum Optics: A Wave-Function Based Approach

Zur Erlangung des akademischen Grades eines

DOKTORS DER NATURWISSENSCHAFTEN

von der Fakultät für Physik des
Karlsruher Instituts für Technologie (KIT)

genehmigte

DISSERTATION

von

Dipl.-Phys. Paolo Longo
aus Karlsruhe

Tag der mündlichen Prüfung: 20.07.2012
Referent: Prof. Dr. Kurt Busch
Korreferent: Prof. Dr. Martin Wegener

Fakultät für Physik
Institut für Theoretische Festkörperphysik

Waveguide Quantum Optics: A Wave-Function Based Approach

PhD Thesis

by

Dipl.-Phys. Paolo Longo

July 20, 2012

Instructor:	Prof. Dr. Kurt Busch
2nd Instructor:	Prof. Dr. Martin Wegener

Introduction

The interaction of light and matter is one of the oldest and—at the same time—one of the most active fields of research in fundamental and applied sciences. Its scope ranges from theoretical aspects of classical and quantum-mechanical electromagnetism over laser physics and optical technologies such as telecommunication and illumination to industrial and medical applications.

Prospective Key Technologies of the 21st Century...

The 21st century is said to be the century of the elementary excitation of the electromagnetic field—the photon. In analogy to electronics, scientists have coined the term "photonics". Concerning this matter, the German Federal Ministry of Education and Research loosely paraphrases the field of photonics as focusing on the generation, control, measurement, and "the use of light in virtually every area that is vital to society and the economy" [1]. Many subfields of photonic technologies already account for a considerable part of the European industry and a turnover of 30 billion euros is expected over the course of the next ten years in Germany [1].

In many respects, photonics already constitutes a mature and applied discipline that developed from the insights scientists gained into the fundamental concepts of light–matter interaction. In contrast to this, some subfields of quantum information may probably be just at the border of turning from a fundamental science into a technology in the not-too-far future. To this end, a "European strategy for research in the field of Quantum Information Sciences and Technologies" [2] has been initiated by the European Commission, which is just one example of the many international efforts in this realm. Probably the most revolutionary long-term goal of quantum information is the realization of large-scale quantum computation, which would solve problems that are intractable on a classical computer. In any case, the interaction of light and matter is at the heart of all building blocks which have been proposed in this context.

Current visions as well as mid- and long-term goals which are based on the understanding, control, and utilization of the physical mechanisms associated with light–matter interaction include, for instance, quantum computation and communication, quantum simulators, fast and all-optical signal processing, high-precision sensors, and concepts in metrology in general.

...and the Role of Physics

To scientifically evaluate the feasibility of such ambitious aims, a first step consists of a thorough analysis of light–matter interaction in prototypical, basic building blocks by means of simplified but not oversimplified model systems. Physicists mainly agree that light is a promising means of transmitting information. Indeed, fiber technology allows for the low-loss guidance of photons over long distances. Photons are also suitable in the context of on-chip structures in an integrated optical setting. Furthermore, physicists also agree that an ultimate key point in the context of light–matter interaction is the generation, manipulation, and detection of single photons [3–6].

In this regard, it is helpful to distinguish between the linear and nonlinear properties of light–matter interaction as follows. The linear properties are responsible for confining, guiding, and directing electromagnetic waves in a passive manner. Besides optical fibers, tailored materials which are structured on the length scale of the electromagnetic radiation's wavelength—so-called Photonic Crystals—have proven to be especially well-suited for these tasks [7]. Waveguiding structures in which the propagation of radiation is effectively reduced to one spatial dimension are particularly interesting. In these systems, the photon dynamics can easily be dominated by interference effects as a consequence of the reduced solid angle into which radiation can couple. Realizations of such one-dimensional systems include line defects in Photonic Crystal structures [8, 9], waveguides of coupled resonators [10–17], superconducting transmission lines in the microwave domain [18–21], Photonic Crystal fibers [22], and conventional optical fibers (cf. Fig. 1 for examples).

Usually, photons do not interact with each other. Controlling light with light therefore requires matter—or, more precisely, a nonlinearity—as a mediator of such interactions. Amongst the probably most common examples of realizing an effective photon–photon interaction are single (artificial) atoms which couple strongly to photons [23], Kerr nonlinearities [24], and the radiation-pressure induced interaction of mechanical motion and radiation [25].

Waveguide Quantum Optics

The combination of the aforementioned linear properties of light–matter interaction in the form of a one-dimensional waveguide and a single nonlinear subsystem allows for the study of interacting photons on a basic level. In a quantum-mechanical description, this setup represents a problem of "waveguide quantum optics", and is at the heart of the present thesis. Even though the above examples are predominantly motivated by photonics, it turns out that a number of analogous systems share many properties with typical "quantum photonic" realizations. To a certain degree, examples include the dynamics of magnons in spin chains [26, 27], cold atoms in optical lattices [28, 29], and waveguide arrays in the realm of classical optics [30, 31], just to name a few.

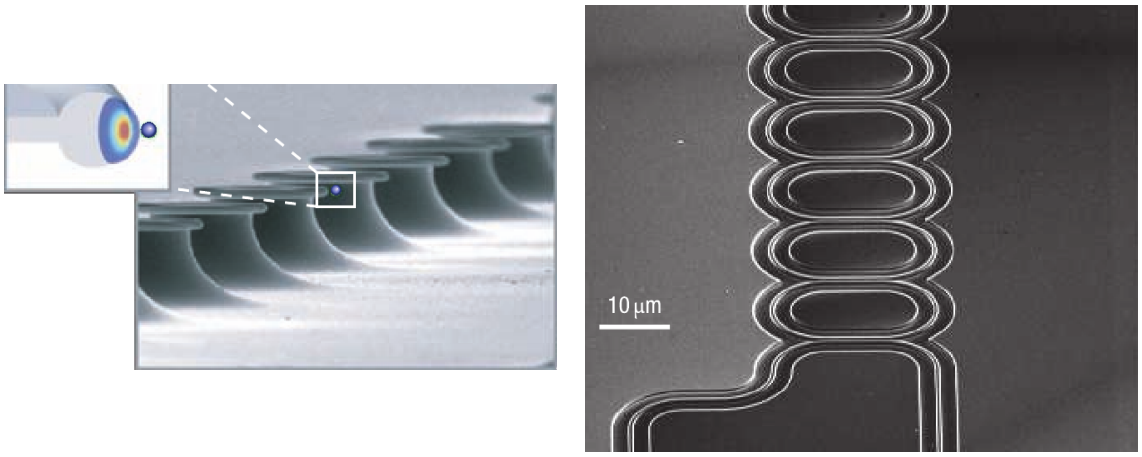

(a) (b)

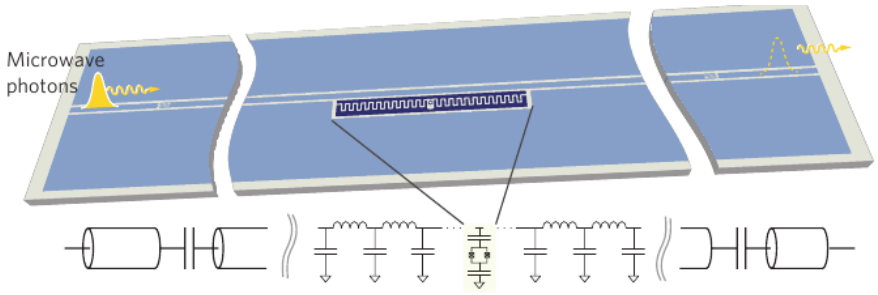

(c)

Figure 1: Realizations of one-dimensional waveguiding systems.
(a) A one-dimensional waveguide of coupled toroidal whispering-gallery mode resonators. The inset indicates the possibility of coupling an artificial atom to the waveguide (adapted from Ref. [14]). (b) Scanning electron micrograph of an optical delay line composed of photonic-wire ring resonators which are side-coupled to their neighbors over a gap distance of about 200 nm (adapted from Ref. [13]). In setups like (a) and (b), photons can "hop" along one spatial dimension if the resonators' spacing is such that the tails of the evanescent field modes of adjacent resonators overlap. (c) A transmission-line resonator can be coupled to a superconducting qubit to study the transport of microwave photons (adapted from Ref. [18]). Chapter 1 provides further examples of effectively one-dimensional waveguiding structures (cf. Fig. 1.1).

Outline of the Thesis

This thesis is organized as follows: Chapter 1 is dedicated to the theoretical foundations of electrodynamics in media and quantum optics as they are important for the following chapters. In Chap. 2, I introduce a discrete real-space formulation of the relevant Hamiltonians. Furthermore, the numerical framework central to this thesis—a wave-function based time-evolution scheme—is briefly presented.

Before I discuss the main results of this thesis, I give an introduction to the topic of waveguide quantum optics in Chap. 3. In particular, I provide a short review based on existing theoretical works on a one-dimensional waveguide coupled to a single emitter or a small number of emitters. Then, I discuss the properties of the relevant Hamiltonian of a one-dimensional tight-binding waveguide coupled to a single two-level atom, including its single-particle spectrum as well as the single- and two-photon transport. I clarify the role of the few-photon nonlinearity provided by the two-level atom and that of spatially localized atom–photon bound states. I describe the effect of interaction-induced radiation trapping, followed by a numerical study on the existence of photon–photon bound states. The introduction to waveguide quantum optics is completed by a short overview of related works in which I have been involved but which are beyond the scope of this thesis.

In Chap. 4, I investigate the Hong-Ou-Mandel effect in the context of two photons impinging from different ends of a waveguide towards a single scatterer. Specifically, I calculate the coincidence probability of finding one photon on each end of the waveguide after scattering. This results in a so-called Hong-Ou-Mandel dip which can in principle be used to identify effective photon–photon interactions as they are mediated by a two-level atom. The influence of atomic dissipation and dephasing is also taken into account.

The transport properties of coherent and single-photon-added coherent states in a waveguide with a side-coupled Kerr-nonlinear resonator are discussed in Chap. 5. Besides nonlinear effects such as self-induced transparency and bistability, I numerically demonstrate how the pulse propagation of a single-photon-added coherent state can be understood as a single-photon Fock state in an "alternative vacuum" provided by a coherent state. This leads to a time-dependent, tunable scattering potential on the single-photon level and can be exploited for the gating of single photons.

Chapter 6 is dedicated to the problem of spontaneous emission in a one-dimensional tight-binding waveguide. In particular, I identify the regimes of Markovian and non-Markovian radiation dynamics with the help of the time evolution of the atom's excited state, output spectra, atom–field and field–field correlation functions. Furthermore, several loss mechanisms such as atomic dissipation and dephasing, lossy field modes, and an open waveguide are taken into account.

In Chap. 7, I consider the dynamics of two magnons propagating in a Heisenberg spin chain under the influence of a non-uniform, external magnetic field. The external field is adjusted such that it forms a potential supporting exactly one single-particle bound state. For this situation, I demonstrate how an impinging spin wave can extract a magnon which

is stored in the ground state of the external potential to form a propagating two-magnon bound state. Such a mechanism of interaction-induced extraction of the stored magnon can be understood as a readout.

Chapter 8 summarizes and concludes the present thesis. It ends with an outlook on possible future studies in the field of waveguide quantum optics.

Contents

Introduction v

1 Fundamentals 1
- 1.1 Electrodynamics in Media . . . 1
  - 1.1.1 Classical Fields . . . 1
  - 1.1.2 Field Quantization . . . 5
- 1.2 Photonic Systems and Eigenmodes . . . 6
  - 1.2.1 **A**-, **E**-, and **H**-Fields of the Eigenmodes . . . 6
  - 1.2.2 Examples for Eigenmodes . . . 7
- 1.3 Concepts of Quantum Optics . . . 11
  - 1.3.1 Dynamics and States of the Electromagnetic Field . . . 12
  - 1.3.2 Light–Matter Interactions . . . 14
  - 1.3.3 Observables and Physical Quantities . . . 24
  - 1.3.4 Open System Dynamics and Quantum Jumps . . . 26

2 Lattice Models and Numerical Scheme 33
- 2.1 Discrete Systems . . . 33
- 2.2 Fourier Lattice Transform . . . 34
  - 2.2.1 Hamiltonians in Real Space . . . 34
- 2.3 Initial States . . . 35
  - 2.3.1 Wave Packets . . . 36
  - 2.3.2 Atomic Excitation . . . 38
- 2.4 Time Evolution and Numerics . . . 39

3 Waveguide Quantum Optics 41
- 3.1 Introduction to Waveguide Quantum Optics . . . 41
- 3.2 A Brief Review of the Field . . . 42
- 3.3 A Single Two-Level Atom in a One-Dimensional Waveguide . . . 46
  - 3.3.1 The Hamiltonian and its Single-Particle Eigenstates . . . 46
  - 3.3.2 Single-Photon Transport . . . 48
  - 3.3.3 Two-Photon Transport . . . 49
- 3.4 Related Works . . . 54
- 3.5 Conclusion and Outlook . . . 60

4 The Hong-Ou-Mandel Effect in the Context of Few-Photon Scattering 61
4.1 Introduction . . . 61
4.2 Fundamentals . . . 62
4.2.1 The Quantum-Mechanical Beam Splitter as a Four-Port Device and its Relation to Scattering Problems . . . 62
4.2.2 Hong-Ou-Mandel Interferometry as a Probe for Photon–Photon Interactions . . . 65
4.2.3 Types of Impurities and their Single-Particle Scattering Solution . . . 65
4.2.4 Influencing Variables for the Hong-Ou-Mandel Dip . . . 67
4.3 Initial States and Joint Probability . . . 68
4.4 Results and Discussion . . . 70
4.4.1 Local On-Site Potential in a Tight-Binding Waveguide . . . 70
4.4.2 Local Two-Level System in a Tight-Binding Waveguide . . . 71
4.5 Conclusion, Outlook, and Critical Discussion . . . 77

5 Dynamics of a Photon-Added Coherent State in a Waveguide Coupled to a Nonlinear Resonator 79
5.1 Introduction . . . 79
5.2 Theoretical Formulation . . . 80
5.2.1 The Hamiltonian . . . 80
5.2.2 Equations of Motion and Projection on States . . . 82
5.2.3 Occupation Numbers . . . 84
5.3 Transport Properties . . . 84
5.3.1 Coherent State . . . 84
5.3.2 Single-Photon-Added Coherent State . . . 87
5.3.3 Comment on a Possible Realization in an Optomechanical Setup . . . 92
5.4 Conclusion, Outlook, and Critical Discussion . . . 93

6 Spontaneous Emission of a Single-Photon Emitter in a Structured Continuum of Modes 97
6.1 Introduction . . . 97
6.2 Fundamentals . . . 99
6.2.1 Theoretical Formulation . . . 99
6.2.2 Formal Solution . . . 100
6.2.3 Physical Quantities . . . 101
6.2.4 Comments on a Semiclassical Treatment . . . 102
6.3 Emission Dynamic in a One-Dimensional System . . . 103
6.3.1 Formulation . . . 103
6.3.2 Density of States and Memory Kernel . . . 103
6.3.3 Emission Dynamics in the Lossless Case . . . 105
6.3.4 Influence of an Open Waveguide . . . 110

6.3.5 Influence of Atomic Dissipation, Dephasing, and Lossy Field Modes . 111
6.4 Conclusion, Outlook, and Critical Discussion 112

7 Magnon Collisions and Magnon Readout in One-Dimensional Spin Chains 115
7.1 Introduction 115
7.2 Fundamentals 116
7.2.1 The Hamiltonian 117
7.2.2 Holstein-Primakoff Transformation 117
7.3 Exact Two-Body Eigenstates in the Absence of an External Potential 119
7.4 Setup 120
7.4.1 Bound States of the Pöschl-Teller Potential 120
7.4.2 Initial States 121
7.4.3 Parameters for Maximized Overlap 122
7.5 Dynamics 123
7.5.1 Single-Particle Transmittance 124
7.5.2 Interaction-Induced Extraction of the Bound-State and Transfer to Propagating Magnon–Magnon Bound States 125
7.6 Conclusion, Outlook, and Critical Discussion 129

8 Summary, Conclusion, and Outlook 131
8.1 Summary 131
8.2 Conclusion and Outlook 132

A Dimensionless Units 137
A.1 Maxwell's Equations in Dimensionless Units 137
A.2 The Schrödinger Equation in Dimensionless Units 138

B Feynman Disentangling of Operators 139

C Numerical Details and Parameters of the Simulations 141
C.1 General Remarks 141
C.2 Time Evolution in the Context of Linear Schrödinger Equations 141
C.2.1 Action of the Hamiltonian on the Basis States 142
C.2.2 Krylov-Subspace Based Time Evolution 144
C.2.3 Stochastic Quantum Jumps 145
C.2.4 Software Packages and Parameters 146
C.2.5 Parameters Used in this Thesis 146
C.3 Time Evolution in the Context of Nonlinear Schrödinger Equations 146
C.3.1 Parameters Used in this Thesis 147

D Single-Particle Scattering Solutions and Beam-Splitter Constraint 149
D.1 General Form of the Scattering Equation 149

D.2 Local On-Site Potential 150
D.3 Local Two-Level System 151

E Density of States and Memory Kernel 153
E.1 Memory Kernel for the One-Dimensional Cosine Band and Constant Atom–Photon Coupling 153
E.2 Density of States for a One-Dimensional Liner Dispersion Relation Without Cutoff 154
E.3 Memory Kernel for a One-Dimensional Liner Dispersion Relation Without Cutoff and Constant Atom–Photon Coupling 154

F Two-Body Eigenstates in a One-Dimensional Heisenberg Spin Chain 155
F.1 Eigenproblem and Reduction to an Effective Single-Particle Problem 155
F.1.1 Scattering States 156
F.1.2 Magnon–Magnon Bound States 157

Bibliography 176

Publications and Miscellaneous 177

Acknowledgements 179

Chapter 1

1 Fundamentals

This chapter introduces the theoretical foundations and concepts of electrodynamics in media and quantum optics. The discussion is limited to topics relevant for later chapters. I start by adapting and rewriting Maxwell's macroscopic equations so that they take a form suitable for quantization. After the procedure of canonical quantization, I give a few examples for photonic systems and their eigenmodes with an emphasis on effectively one-dimensional waveguiding structures since they are of central interest in this thesis. I introduce basic notions of quantum optics such as the dynamics of the electromagnetic field, its most important states as well as different physical mechanisms of light–matter interaction. The chapter ends with the definition of observables and physical quantities followed by a short introduction to the dynamics of open systems with respect to the quantum jump approach.

1.1 Electrodynamics in Media

Throughout this thesis, I focus on single quantum mechanical subsystems and their interaction with electromagnetic radiation. Unless stated otherwise, I assume a linear, isotropic, non-dispersive, non-dissipative and source-free dielectric without magnetic response acting as a host medium. However, this medium can have structural features on the scale of the electromagnetic radiation's wavelength, which makes it possible to tailor the dispersion properties although the corresponding bulk material properties are non-dispersive.

In this section, I present the theoretical foundations for the description of the background medium. The incorporation of individual, quantum mechanical subsystems follows in Sec. 1.3.2.

1.1.1 Classical Fields

In the context of photonics, it is well-established to resort to Maxwell's macroscopic equations. Starting from the microscopic equations, a decomposition of the sources into free and

bound parts as well as an averaging over atomic scales leads to the equations of motion for the macroscopic fields which are defined on a coarser scale [32]. This is a safe approximation since atomic and optical scales differ by several orders of magnitude. For instance, imagine an atomic distance of the order of Ångstroms and an optical wavelength of several hundred nanometers as a rough estimate for the length scales involved. A similar argument holds for typical time scales.

In the following, I briefly recapitulate Maxwell's macroscopic equations and, by introducing potentials in a suitable gauge, rewrite them with the help of the Lagrange and Hamilton formalism such that they take a form which is convenient for quantization.

Maxwell's Equations

Given the aforementioned assumptions, electromagnetic fields in media are described by the macroscopic Maxwell equations. In the absence of free sources, they read (SI units) [32]

$$\boldsymbol{\nabla} \times \mathbf{E}(\mathbf{r},t) = -\frac{\partial}{\partial t}\mathbf{B}(\mathbf{r},t)\,, \tag{1.1a}$$

$$\boldsymbol{\nabla} \times \mathbf{H}(\mathbf{r},t) = \frac{\partial}{\partial t}\mathbf{D}(\mathbf{r},t)\,, \tag{1.1b}$$

$$\boldsymbol{\nabla} \cdot \mathbf{D}(\mathbf{r},t) = 0\,, \tag{1.1c}$$

$$\boldsymbol{\nabla} \cdot \mathbf{B}(\mathbf{r},t) = 0\,, \tag{1.1d}$$

where the electric field $\mathbf{E}(\mathbf{r},t)$, the magnetic induction $\mathbf{B}(\mathbf{r},t)$, the magnetic field $\mathbf{H}(\mathbf{r},t)$, and the dielectric displacement $\mathbf{D}(\mathbf{r},t)$ are real-valued fields as a function of position $\mathbf{r}$ and time t. The constitutive relations for the class of materials under consideration,

$$\mathbf{D}(\mathbf{r},t) = \epsilon_0\epsilon(\mathbf{r})\mathbf{E}(\mathbf{r},t)\,, \tag{1.2a}$$

$$\mathbf{B}(\mathbf{r},t) = \mu_0\mathbf{H}(\mathbf{r},t)\,, \tag{1.2b}$$

close the set of Eqs. (1.1). In Eq. (1.2a), ϵ_0 denotes the permittivity of vacuum and $\epsilon(\mathbf{r})$ is the position-dependent dielectric function of the medium. Examples for the dielectric function follow in Sec. 1.2. The permeability of vacuum is denoted by μ_0.

For the remainder of this thesis and if not stated otherwise, a unit system is chosen in which the vacuum speed of light becomes unity, i. e., $c = 1/\sqrt{\epsilon_0\mu_0} \equiv 1$. This corresponds to transforming Maxwell's equations to dimensionless units (see Appendix A for details). The introduction of a vector potential $\mathbf{A}(\mathbf{r},t)$ and a scalar potential $\phi(\mathbf{r},t)$ via

$$\mathbf{B}(\mathbf{r},t) = \boldsymbol{\nabla} \times \mathbf{A}(\mathbf{r},t)\,, \tag{1.3a}$$

$$\mathbf{E}(\mathbf{r},t) = -\boldsymbol{\nabla}\phi(\mathbf{r},t) - \frac{\partial}{\partial t}\mathbf{A}(\mathbf{r},t)\,, \tag{1.3b}$$

automatically satisfies Eqs. (1.1a) and (1.1d), and turns Eqs. (1.1b) and (1.1c) into a set of

coupled wave equations for the potentials, i. e.,

$$-\boldsymbol{\nabla}\times\boldsymbol{\nabla}\times\mathbf{A}(\mathbf{r},t)-\epsilon(\mathbf{r})\frac{\partial}{\partial t}\boldsymbol{\nabla}\phi(\mathbf{r},t)-\epsilon(\mathbf{r})\frac{\partial^2}{\partial t^2}\mathbf{A}(\mathbf{r},t) = 0\,, \tag{1.4a}$$

$$\big(\boldsymbol{\nabla}\epsilon(\mathbf{r})\big)\cdot\big(\boldsymbol{\nabla}\phi(\mathbf{r},t)\big)+\epsilon(\mathbf{r})\boldsymbol{\nabla}^2\phi(\mathbf{r},t)+\big(\boldsymbol{\nabla}\epsilon(\mathbf{r})\big)\cdot\left(\frac{\partial}{\partial t}\mathbf{A}(\mathbf{r},t)\right) +\epsilon(\mathbf{r})\frac{\partial}{\partial t}\boldsymbol{\nabla}\cdot\mathbf{A}(\mathbf{r},t) = 0\,. \tag{1.4b}$$

By utilizing the radiation gauge[1] in which $\phi(\mathbf{r},t)\equiv 0$, Eqs. (1.4a) and (1.4b) reduce to

$$\boldsymbol{\nabla}\times\boldsymbol{\nabla}\times\mathbf{A}(\mathbf{r},t)+\epsilon(\mathbf{r})\frac{\partial^2}{\partial t^2}\mathbf{A}(\mathbf{r},t)=0\,, \tag{1.5}$$

provided that

$$\boldsymbol{\nabla}\cdot\big(\epsilon(\mathbf{r})\mathbf{A}(\mathbf{r},t)\big)=0\,. \tag{1.6}$$

Equation (1.6) is a constraint to possible solutions of the wave equation (1.5) and simplifies to the Coulomb gauge, i. e., $\boldsymbol{\nabla}\cdot\mathbf{A}(\mathbf{r},t)=0$, in case the dielectric function represents a spatially homogeneous medium, i. e., $\boldsymbol{\nabla}\epsilon(\mathbf{r})=0$. Furthermore, Eq. (1.6) states that the vector potential is in general not transverse.

Mode Decomposition, Lagrangian, and Hamiltonian Density

A general solution of Eq. (1.5) is of the form[2]

$$\mathbf{A}(\mathbf{r},t)=\sum_\lambda\mathbf{A}_\lambda(\mathbf{r},t) = \sum_\lambda\left(\mathbf{A}_\lambda^{(+)}(\mathbf{r},t)+\mathbf{A}_\lambda^{(-)}(\mathbf{r},t)\right) = \sum_\lambda\left(\mathbf{A}_\lambda^{(+)}(\mathbf{r})a_\lambda(t)+\mathbf{A}_\lambda^{(-)}(\mathbf{r})a_\lambda^*(t)\right)\,, \tag{1.7}$$

where $a_\lambda(t)=a_\lambda(0)\mathrm{e}^{-\mathrm{i}\omega_\lambda t}$. The separation of variables turns Eq. (1.5) into the eigenvalue problem

$$\boldsymbol{\nabla}\times\boldsymbol{\nabla}\times\mathbf{A}_\lambda^{(\pm)}(\mathbf{r})=\epsilon(\mathbf{r})\omega_\lambda^2\mathbf{A}_\lambda^{(\pm)}(\mathbf{r})\,. \tag{1.8}$$

Note that the eigenmodes $\mathbf{A}_\lambda^{(\pm)}(\mathbf{r})$ are now complex-valued fields with

$$\mathbf{A}_\lambda^{(-)}(\mathbf{r})=\left(\mathbf{A}_\lambda^{(+)}(\mathbf{r})\right)^*\,, \tag{1.9}$$

which assures that the decomposition (1.7) is real-valued. The modes are labeled with a multi-index λ and the sum in Eq. (1.7) should, at this stage, be understood as allowing both

[1] This gauge is also called Dzyaloshinsky gauge.
[2] Different functions are distinguished by their variables.

a summation over discrete values of λ and an integration in case the spectrum is (partially) continuous.

Having identified the fundamental solutions of Eq. (1.5), the classical Lagrangian density $\mathcal{L}$ can be formulated in terms of the $\mathbf{A}_\lambda(\mathbf{r},t)$. Applying the Euler-Lagrange equations[3],

$$\frac{\partial}{\partial t}\frac{\partial \mathcal{L}}{\partial \dot{A}_i} + \sum_{j=x,y,z} \frac{\partial}{\partial x_j}\frac{\partial \mathcal{L}}{\partial(\frac{\partial A_i}{\partial x_j})} - \frac{\partial \mathcal{L}}{\partial A_i} = 0 \quad i = x,y,z\,, \tag{1.10}$$

to $\mathcal{L} = \sum_\lambda \mathcal{L}_\lambda$ with

$$\mathcal{L}_\lambda = \frac{1}{2}\epsilon(\mathbf{r})\dot{\mathbf{A}}_\lambda^2(\mathbf{r},t) - \frac{1}{2}\left(\boldsymbol{\nabla}\times\mathbf{A}_\lambda(\mathbf{r},t)\right)^2 \tag{1.11}$$

reproduces wave equation (1.5) for each $\mathbf{A}_\lambda(\mathbf{r},t)$ [33]. Thus, the $\mathbf{A}_\lambda(\mathbf{r},t)$ represent a valid choice for generalized coordinates and their associated canonical momenta are given by[4]

$$\boldsymbol{\pi}_\lambda = \frac{\partial \mathcal{L}}{\partial \dot{\mathbf{A}}_\lambda(\mathbf{r},t)} = \epsilon(\mathbf{r})\dot{\mathbf{A}}_\lambda(\mathbf{r},t)\,. \tag{1.12}$$

The classical Hamiltonian density $\bar{\mathcal{H}} = \sum_\lambda \bar{\mathcal{H}}_\lambda$ is obtained by performing a Legendre transformation, i. e., $\bar{\mathcal{H}} = \sum_\lambda \boldsymbol{\pi}_\lambda(\mathbf{r},t)\cdot\dot{\mathbf{A}}_\lambda(\mathbf{r},t) - \mathcal{L}$, arriving at

$$\bar{\mathcal{H}}_\lambda = \frac{\boldsymbol{\pi}_\lambda^2(\mathbf{r},t)}{2\epsilon(\mathbf{r})} + \frac{1}{2}\left(\boldsymbol{\nabla}\times\mathbf{A}_\lambda(\mathbf{r},t)\right)^2\,. \tag{1.13}$$

Equation (1.13) represents the energy density of the electromagnetic field for mode λ.

Next, it is convenient to define

$$\mathbf{A}_\lambda^{(+)}(\mathbf{r}) = \frac{1}{\sqrt{2\mathcal{V}_\lambda\omega_\lambda}}\mathbf{u}_\lambda(\mathbf{r})\,, \tag{1.14}$$

where $\mathcal{V}_\lambda$ is the mode volume in which the complex-valued and dimensionless eigenmode $\mathbf{u}_\lambda(\mathbf{r})$ is defined (cf. Eqs. (1.7)–(1.9)). The mode functions can be chosen such that they are orthogonal with respect to the scalar product

$$\int \mathrm{d}^3r\,\epsilon(\mathbf{r})\mathbf{u}_{\lambda'}^*(\mathbf{r})\cdot\mathbf{u}_\lambda(\mathbf{r}) = \mathcal{V}_\lambda\delta_{\lambda\lambda'}\,, \tag{1.15}$$

and satisfy

$$\int \mathrm{d}^3r\left(\boldsymbol{\nabla}\times\mathbf{u}_{\lambda'}^*(\mathbf{r})\right)\cdot\left(\boldsymbol{\nabla}\times\mathbf{u}_\lambda(\mathbf{r})\right) = \mathcal{V}_\lambda\omega_\lambda^2\delta_{\lambda\lambda'} \tag{1.16}$$

[3] Dots denote derivatives with respect to time.

[4] Applying constitutive relation (1.2a) and exploiting the radiation gauge, the canonical momenta are given by the dielectric displacement field, i. e., $\boldsymbol{\pi}_\lambda(\mathbf{r},t) = -\mathbf{D}_\lambda(\mathbf{r},t)$. Here, $\mathbf{D}_\lambda(\mathbf{r},t) = \epsilon(\mathbf{r})\mathbf{E}_\lambda(\mathbf{r},t)$ and $\mathbf{E}_\lambda(\mathbf{r},t)$ is defined in Eq. (1.26b). Note that Eq. (1.2a) has to be taken in dimensionless units (cf. Appendix A).

as well as

$$\mathbf{u}_\lambda^*(\mathbf{r}) = \mathbf{u}_{\lambda' \neq \lambda}(\mathbf{r})\,, \tag{1.17}$$

where $\delta_{\lambda\lambda'}$ is the Kronecker delta. Using these properties, inserting Eq. (1.7) together with Eqs. (1.14) and (1.12) into Eq. (1.13), integrating the Hamiltonian density (1.13) over all space, and suppressing the time arguments, the Hamilton function finally reads[5]

$$\mathcal{H} = \sum_\lambda \frac{\omega_\lambda}{2} \left(a_\lambda a_\lambda^* + a_\lambda^* a_\lambda \right) . \tag{1.18}$$

Hamiltonian (1.18) represents a sum over uncoupled harmonic oscillators of unit mass with the generalized coordinates $\{q_\lambda\}$ and canonical momenta $\{p_\lambda\}$ given by

$$q_\lambda = \frac{1}{\sqrt{2\omega_\lambda}} (a_\lambda + a_\lambda^*)\,, \tag{1.19a}$$

$$p_\lambda = \frac{1}{\mathrm{i}} \sqrt{\frac{\omega_\lambda}{2}} (a_\lambda - a_\lambda^*)\,. \tag{1.19b}$$

With regard to the canonical quantization in the next section, the Hamilton function (1.18) is written in a symmetric form.

1.1.2 Field Quantization

The correspondence principle[6] is utilized in order to arrive at a quantum mechanical description of the electromagnetic field. Canonical coordinates $\{q_\lambda\}$ and momenta $\{p_\lambda\}$ are replaced by operators $\{\hat{q}_\lambda\}$ and $\{\hat{p}_\lambda\}$, respectively, obeying the fundamental commutation relations

$$\left[\hat{q}_\lambda, \hat{p}_{\lambda'}\right] = \hat{q}_\lambda \hat{p}_{\lambda'} - \hat{p}_{\lambda'} \hat{q}_\lambda = \mathrm{i}\hbar \delta_{\lambda\lambda'}\,. \tag{1.20}$$

For the remainder of this thesis, units are chosen such that the reduced Planck constant $\hbar \equiv 1$ (see Appendix A for details). The amplitudes $\{a_\lambda\}$ and $\{a_\lambda^*\}$ as defined in Eqs. (1.19) are replaced by annihilation and creation operators $\{\hat{a}_\lambda\}$ and $\{\hat{a}_\lambda^\dagger\}$. According to Eqs. (1.19) and (1.20), they obey

$$\left[\hat{a}_\lambda, \hat{a}_{\lambda'}\right] = \left[\hat{a}_\lambda^\dagger, \hat{a}_{\lambda'}^\dagger\right] = 0\,, \tag{1.21a}$$

$$\left[\hat{a}_\lambda, \hat{a}_{\lambda'}^\dagger\right] = \delta_{\lambda\lambda'}\,. \tag{1.21b}$$

[5] Integrands proportional to $\mathbf{u}^2(\mathbf{r})$, $(\boldsymbol{\nabla} \times \mathbf{u}(\mathbf{r}))^2$, and the respective complex conjugate terms do not contribute because of property (1.17).

[6] Although Maxwell's microscopic equations are Lorentz invariant, the equations for the macroscopic fields are in general not. This stems from the fact that the transition from microscopic to macroscopic fields includes an arbitrary decomposition of the sources in free and bound parts as well as an averaging over atomic scales. The correspondence principle applied here and the equations of motion in this thesis are thus from the realm of non-relativistic quantum mechanics. This approach is widely used in the field of solid-state based quantum electrodynamics and has proven to be successful, although, at first sight, one might wonder why a non-relativistic theory is used to describe the propagation of photons.

Replacing the classical amplitudes by operators and utilizing Eq. (1.21b), the Hamilton operator reads

$$\hat{H} = \sum_{\lambda} \omega_{\lambda} \left(\hat{a}_{\lambda}^{\dagger} \hat{a}_{\lambda} + \frac{1}{2} \right) . \tag{1.22}$$

Equations (1.21) imply that the fundamental excitations of the free electromagnetic field described by a Hamiltonian of the form (1.22)—photons—are bosons[7]. Because of the correspondence principle, Hamiltonian (1.22) is in the Heisenberg picture but has the same form in the Schrödinger picture since $\hat{a}_{\lambda}(t) = \hat{a}_{\lambda}(0)\mathrm{e}^{-\mathrm{i}\omega_{\lambda}t}$.

Although the second term in Hamiltonian (1.22) (commonly referred to as zero point energy) can have interesting observable consequences, e. g., the Casimir effect [34, 35], it does not affect the dynamics of the systems studied in this thesis and will be ignored in the following. Furthermore, operators will not be indicated by hats anymore since it is clear from the context whether a function or an operator is meant.

1.2 Photonic Systems and Eigenmodes

The theoretical description of electromagnetic fields in Sec. 1.1 is—besides the assumptions on the general properties of the materials under investigation—not restricted to a specific realization of a photonic system. The quantization is especially valid for arbitrary profiles of the dielectric function $\epsilon(\mathbf{r})$ as long as the eigenmode solutions of Eq. (1.8) fulfill constraints (1.6) and (1.15)–(1.17). Here, I present the expansion of the field operators in terms of eigenmodes and I discuss examples for actual physical realizations of photonic systems in Sec. 1.2.2.

1.2.1 A-, E-, and H-Fields of the Eigenmodes

According to mode decomposition (1.7) and Eqs. (1.3) and (1.14), the operator of the vector potential

$$\mathbf{A}(\mathbf{r},t) = \sum_{\lambda} \left(\mathbf{A}_{\lambda}^{(+)}(\mathbf{r})\mathrm{e}^{-\mathrm{i}\omega_{\lambda}t} a_{\lambda}(0) + \mathbf{A}_{\lambda}^{(-)}(\mathbf{r})\mathrm{e}^{\mathrm{i}\omega_{\lambda}t} a_{\lambda}^{\dagger}(0) \right) \tag{1.23}$$

is related to its corresponding electric and magnetic field via

$$\mathbf{E}(\mathbf{r},t) = \sum_{\lambda} \left(\mathbf{E}_{\lambda}^{(+)}(\mathbf{r})\mathrm{e}^{-\mathrm{i}\omega_{\lambda}t} a_{\lambda}(0) + \mathbf{E}_{\lambda}^{(-)}(\mathbf{r})\mathrm{e}^{\mathrm{i}\omega_{\lambda}t} a_{\lambda}^{\dagger}(0) \right) \tag{1.24}$$

and

$$\mathbf{H}(\mathbf{r},t) = \sum_{\lambda} \left(\mathbf{H}_{\lambda}^{(+)}(\mathbf{r})\mathrm{e}^{-\mathrm{i}\omega_{\lambda}t} a_{\lambda}(0) + \mathbf{H}_{\lambda}^{(-)}(\mathbf{r})\mathrm{e}^{\mathrm{i}\omega_{\lambda}t} a_{\lambda}^{\dagger}(0) \right) , \tag{1.25}$$

[7] To be precise, the **D**-field already describes a combined excitation of light and matter. Photons in matter should therefore actually be referred to as polaritons. I disregard this subtlety in the following and continue to speak of photons.

where

$$\mathbf{A}_\lambda^{(+)}(\mathbf{r}) = \mathcal{A}_\lambda \mathbf{u}_\lambda(\mathbf{r}), \tag{1.26a}$$

$$\mathbf{E}_\lambda^{(+)}(\mathbf{r}) = \mathrm{i}\omega_\lambda \mathcal{A}_\lambda \mathbf{u}_\lambda(\mathbf{r}),$$

$$\mathbf{H}_\lambda^{(+)}(\mathbf{r}) = \mathcal{A}_\lambda \boldsymbol{\nabla} \times \mathbf{u}_\lambda(\mathbf{r}), \tag{1.26b}$$

$$\mathcal{A}_\lambda = \frac{1}{\sqrt{2\mathcal{V}_\lambda \omega_\lambda}}. \tag{1.26c}$$

The quantity $\mathcal{E}_\lambda = \omega_\lambda \mathcal{A}_\lambda$ is called vacuum field amplitude[8]. Note that all operators are in the Heisenberg picture and dimensionless units are chosen (cf. Appendix A). In order to actually calculate the eigenmodes, it is advantageous to reformulate the eigenvalue problem (1.8) in terms of the magnetic field [8, 36, 37], leading to[9]

$$\boldsymbol{\nabla} \times \frac{1}{\epsilon(\mathbf{r})} \boldsymbol{\nabla} \times \mathbf{H}_\lambda^{(+)}(\mathbf{r}) = \omega_\lambda^2 \mathbf{H}_\lambda^{(+)}(\mathbf{r}) \tag{1.27}$$

for each mode.

1.2.2 Examples for Eigenmodes

In this subsection, I present a few examples for photonic systems. The emphasis is on effectively one-dimensional waveguiding structures and the discussion is limited to a qualitative level.

Photonic Crystals

Periodic Nanostructures allow for tailored optical properties of dielectric media. In case the periodicity is of the order of the wavelength of light[10], these structures are termed "Photonic Crystals". Here, I briefly present the properties which are most relevant in the context of this thesis. For a more complete and thorough discussion, see Refs. [7, 8, 38, 39].

As already mentioned in Sec. 1.1, loss-less, dispersion-free, and isotropic materials are considered which can be described by a scalar dielectric function $\epsilon(\mathbf{r})$. In the case of Photonic Crystals, it is periodic, i. e.,

$$\epsilon(\mathbf{r}) = \epsilon(\mathbf{r} + \mathbf{R}), \tag{1.28}$$

where $\mathbf{R}$ is an arbitrary lattice vector from the underlying Bravais lattice. Depending on whether the dielectric function is periodic with respect to a one-, two- or three-dimensional

[8] The quantity $\mathcal{E}_\lambda$ is proportional to the vacuum fluctuations, i. e., $\sqrt{\langle 0|\mathbf{E}_\lambda^2(\mathbf{r},t)|0\rangle - \langle 0|\mathbf{E}_\lambda(\mathbf{r},t)|0\rangle^2} \propto \mathcal{E}_\lambda$. The vacuum state is denoted by $|0\rangle$ (cf. Sec. 1.3.1).

[9] For simplicity, I only write down the equations for the (+)-modes in the following since the corresponding (−)-modes can be obtained by complex conjugation (cf. Eqs. (1.9) and (1.23)–(1.25)).

[10] For the remainder, the term "light" is used to refer to any kind of electromagnetic radiation and is not restricted to the visible domain.

lattice one speaks of one-, two- or three-dimensional Photonic Crystals. The assumption of a periodic dielectric function simplifies eigenproblem (1.27) to an eigenproblem with periodic coefficients. Therefore, the eigenmodes fullfill Bloch's theorem, i. e., they are plane waves modulated by a lattice-periodic function:

$$\mathbf{H}(\mathbf{r}) = \mathbf{h}_{\mathbf{k}}(\mathbf{r})\mathrm{e}^{\mathrm{i}\mathbf{k}\mathbf{r}}\,, \tag{1.29a}$$

$$\mathbf{h}_{\mathbf{k}}(\mathbf{r}) = \mathbf{h}_{\mathbf{k}}(\mathbf{r}+\mathbf{R})\,. \tag{1.29b}$$

Similar to the case of an electronic band structure, the periodicity of the dielectric function leads to a band structure for electromagnetic fields, i. e., $\omega = \omega_{n\mathbf{k}}$. Eigenmodes and eigenfrequencies of a Photonic Crystal are thus labeled by a band index n and a wavevector $\mathbf{k}$, i. e.,

$$\mathbf{H}^{(+)}_{n\mathbf{k}}(\mathbf{r}) = \mathbf{h}_{n\mathbf{k}}(\mathbf{r})\mathrm{e}^{\mathrm{i}\mathbf{k}\mathbf{r}}\,. \tag{1.30}$$

The mode functions $\mathbf{h}_{n\mathbf{k}}(\mathbf{r})$ are defined in the Wigner-Seitz cell of the crystal so that the mode volume is the volume of the Wigner-Seitz cell, and wavevectors are restricted to the first Brillouin zone. For an infinite crystal, $\mathbf{k}$ is continuous and sums over wavevectors need to be replaced by integrals. These modes are consistent with the terminology and the properties introduced in Sec. 1.1. Most importantly, they fulfill[11]

$$\int \mathrm{d}^3 r \left(\mathbf{H}^{(+)}_{n'\mathbf{k}'}(\mathbf{r})\right)^* \mathbf{H}^{(+)}_{n\mathbf{k}}(\mathbf{r}) = \delta_{nn'}\delta(\mathbf{k}-\mathbf{k}')\,, \tag{1.31}$$

which means that there is no band mixing for the free electromagnetic field.

Probably the most remarkable property of Photonic Crystals is the possibility of a photonic band gap, i. e., a frequency range in which the density of electromagnetic states $\mathcal{N}(\omega)$, defined as

$$\mathcal{N}(\omega) = \sum_n \int_{\mathrm{BZ}} \mathrm{d}^q k\ \delta(\omega - \omega_{n\mathbf{k}}) \tag{1.32}$$

for a q-dimensional Photonic Crystal, is zero. The integral in Eq. (1.32) runs over the first Brillouin zone. Controlling spontaneous emission by modifying the density of electromagnetic states was one of the very first motivations in the field of Photonic Crystals, and I address this topic in Chap. 6 of this thesis.

Structures in which there is effectively only one dimension for the electromagnetic radiation to propagate exhibit very special features. For instance, spontaneous emission of an atom in a homogeneous background is most often regarded as a loss mechanism. The reduction to one spatial dimension, however, induces dominant interference effects as a consequence of the smaller solid angle radiation can couple into. In this thesis, the main emphasis is on such

[11] The integral in Eq. (1.31) runs over the Wigner-Seitz cell of the crystal and $\delta(\cdot)$ represents the Dirac delta function.

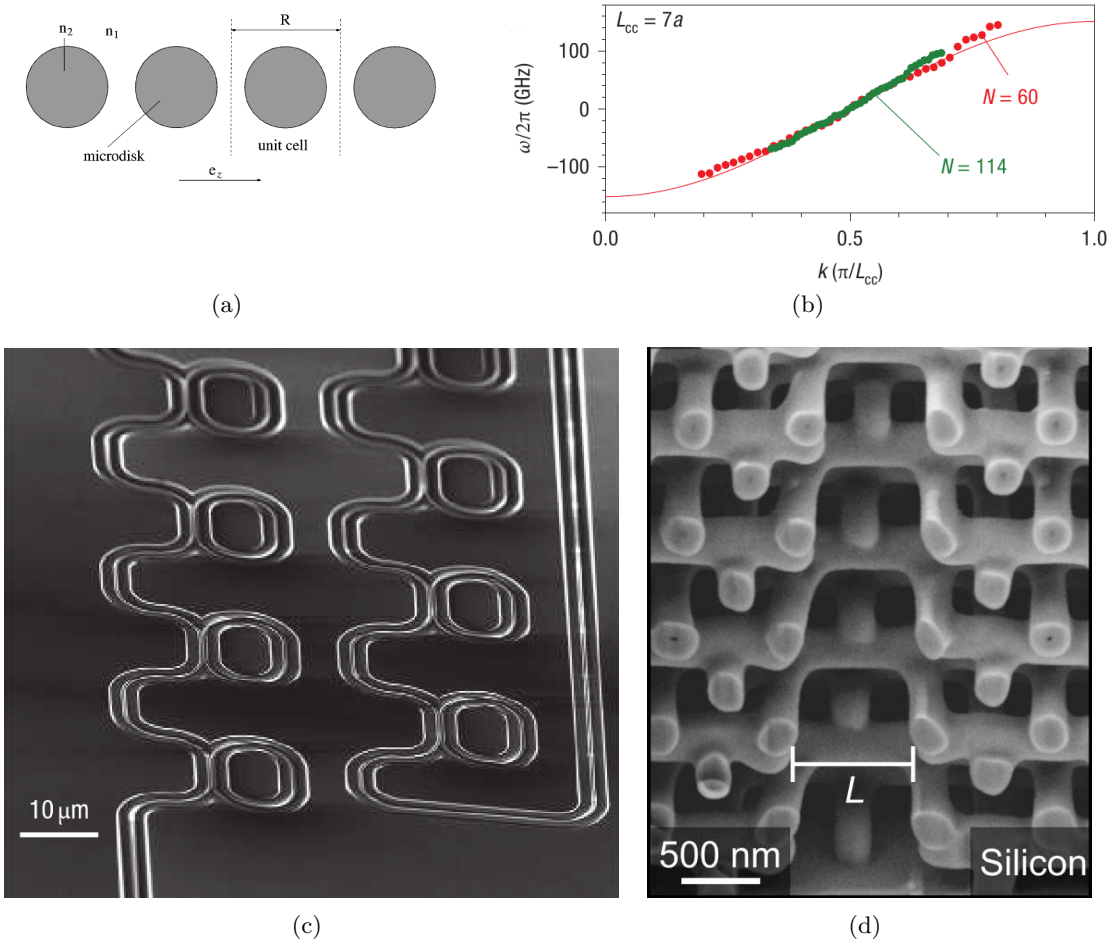

Figure 1.1: Examples of effectively one-dimensional waveguiding structures.
As a realization of a coupled-resonator optical waveguide, one of the early theoretical proposals [10] suggested, for instance, microdisk cavities (a). Here, the electromagnetic field modes of the cavities couple to their nearest neighbors via evanescent field tails, thus forming a one-dimensional waveguide. In (a), n_2 and $n_1 \neq n_2$ denote the different indices of refraction and R stands for the lattice constant (adapted from Ref. [10]). (b) Measured dispersion relation of coupled nanocavities (adapted from Ref. [11]). N denotes the number of cavities which form the waveguide and L_{cc} is the lattice constant (see Ref. [11] for details). Note the cosine shape of the dispersion relation. (c) Scanning electron micrograph of a delay line consisting of photonic-wire ring resonators which are coupled to a waveguide bus (adapted from Ref. [13]). (d) A line defect in a woodpile Photonic Crystal acting as a waveguide (adapted from Ref. [9]).

(effectively) one-dimensional systems. Figure 1.1 displays examples[12] for one-dimensional waveguiding structures.

In so-called coupled-resonator optical waveguides (CROWs), the electromagnetic field modes of neighboring cavities couple to each other via their evanescent field tails (Figs. 1.1(a), 1(a), and 1(b)). This effectively forms a one-dimensional waveguide for photons, which can be described by a tight-binding ansatz, leading to a dispersion relation of the form [10]

$$\omega_K = \Omega \left[1 - \frac{\Delta\alpha}{2} + \kappa_1 \cos(KR) \right] . \tag{1.33}$$

The wavenumber K is in the interval $\left[-2\pi/R, 2\pi/R\right]$ (see Fig. 1.1(b) for an example of a measured dispersion relation [10]). The nearest-neighbor coupling strength is given as the overlap of neighboring mode functions, i. e.,

$$\kappa_1 = \int \mathrm{d}^3 r \left[\epsilon_0(\mathbf{r} - R\mathbf{e}_z) - \epsilon(\mathbf{r} - R\mathbf{e}_z) \right] \mathbf{E}_\Omega(\mathbf{r}) \mathbf{E}_\Omega(\mathbf{r} - R\mathbf{e}_z) \, . \tag{1.34}$$

The eigenfrequency of a single, isolated cavity is denoted by Ω. The term $1 - \Delta\alpha/2$ merely shifts the zero of the dispersion relation and is therefore not considered in the following. Equation (1.34) contains the difference between the dielectric function of a single cavity, $\epsilon_0(\mathbf{r})$, and the total system of coupled resonators, $\epsilon(\mathbf{r})$, as well as the electric field mode functions $\mathbf{E}_\Omega(\mathbf{r})$ of a single cavity. $\mathbf{e}_z$ is a unit in vector in the direction of propagation (z direction). Equations (1.33) and (1.34) are taken from Ref. [10] without change of notation. The notation used in this thesis is slightly different and is introduced in Chap. 2.

A line defect in a Photonic Crystal represents another realization of a one-dimensional waveguide, providing a one-dimensional continuum[13] for photons. Realizations include, for instance, Photonic Crystal slab waveguides [8] or waveguides in three-dimensional woodpile structures [9] as shown in Fig. 1.1(d). Line defects can be engineered such that their dispersion relation lies in the band gap of the surrounding Photonic Crystal. Radiation can therefore not escape into the crystal. Even though the dispersion relations of such waveguides do not necessarily resemble the form of a cosine-dispersion relation, they could approximately be described by the latter for wavenumbers around a specific operating point.

The tight-binding description of one-dimensional waveguiding structures is extensively applied throughout this thesis. On the one hand, there exist experimental realizations for which a tight-binding formulation is an adequate description. On the other hand, if one just regards a one-dimensional tight-binding chain as a model system, it is important to point out that a cosine-dispersion relation, despite its simple form, qualitatively covers many physical aspects which would be absent in the case of unbound, linear dispersion relations. For

[12] Since these examples are adapted from different references, the notation, terminology, and unit system might slightly differ from those used in this thesis.

[13] For the remainder of the thesis, the term "continuum of modes" also refers to a quasi-continuum as it emerges in a finite system.

instance, attributes such as nonlinear group-velocity dispersion and the existence of a finite bandwidth, i. e., a cutoff in the density of states, are inherent properties of a cosine-dispersion relation. A more detailed description of the tight-binding approach is given in Chap. 2.

Optical Fibers

Optical fibers represent a well-established class of photonic systems and allow the low-loss guidance of light over large distances. Here, I only motivate qualitatively that optical fibers are another realization of a one-dimensional electromagnetic continuum which can also be considered in a quantum-optical framework.

The dielectric function of a conventional optical fiber is invariant with respect to rotations around the fiber axis and with respect to translations in fiber direction [40]. Thus, $\epsilon(\mathbf{r})$ only depends on the radial coordinate and represents the index profile[14] of the fiber, e. g., a step- or a gradient-index profile. Due to symmetry, the eigenproblem (1.27) reduces to a radial equation. Depending on the actual realization of the dielectric function's profile, different numbers of guided modes, i. e., field distributions which are localized in the high-index region of the fiber core and decay in the low-index region of the cladding, exist. The underlying guiding mechanism here is total internal reflection. These modes exhibit a one-dimensional dispersion relation. However, they do not exist for arbitrary frequencies and have an upper and lower cutoff.

Besides conventional optical fibers, so-called Photonic Crystal fibers [22] consist of the fiber core, which can be a low-index material or even air, surrounded by a two-dimensional Photonic Crystal structure. In case of a low-index core, the guiding mechanism is based on the existence of a photonic band gap of the surrounding Photonic Crystal. For these structures, eigenproblem (1.27) becomes more complicated when compared to a conventional fiber. Nonetheless, there are single-mode solutions which effectively constitute a one-dimensional electromagnetic continuum for propagation along the fiber axis. Furthermore, Photonic Crystal fibers provide properties which might also be appealing for quantum-optical experiments, e. g., for realizing a source of correlated photon pairs [41].

1.3 Concepts of Quantum Optics

In this section, I present basic notions and concepts of quantum optics. The discussion of the dynamics and the states of the electromagnetic field which are used in this thesis is followed by the introduction of different mechanisms of light–matter interaction. I then briefly define various observables and physical quantities which are important in later chapters, followed by the theoretical foundations for the dynamics of open systems with respect to the quantum jump approach. The emphasis is on the theoretical framework rather than on examples for

[14] To be precise, the refractive index here is $n(\mathbf{r}) = \sqrt{\epsilon(\mathbf{r})}$.

actual physical realizations. For the latter, I only make a few remarks and refer to the respective discussions in later chapters.

1.3.1 Dynamics and States of the Electromagnetic Field

In the Schrödinger picture, the time evolution of the electromagnetic field's state $|\Psi\rangle$ is described by the Schrödinger equation

$$\mathrm{i}\frac{\partial}{\partial t}|\Psi\rangle = H|\Psi\rangle\,, \tag{1.35}$$

where H is the Hamilton operator of the underlying system. In the following, I present three classes of states which represent possibles bases of the electromagnetic field.

Fock States

Since the Hamilton operator (1.22) represents a sum over individual harmonic oscillators, Fock states constitute a valid choice for a basis. The state of a multi-mode electromagnetic field with N modes is thus given as the direct product of the number states for each mode λ, i. e.,

$$|\{n_\lambda\}\rangle = |n_{\lambda_1}\rangle \otimes |n_{\lambda_2}\rangle \otimes \cdots \otimes |n_{\lambda_N}\rangle = \prod_{l=1}^{N} \frac{\left(a_{\lambda_l}^\dagger\right)^{n_{\lambda_l}}}{\sqrt{n_{\lambda_l}!}}\,|0\rangle\,, \tag{1.36}$$

where $|0\rangle$ denotes the vacuum state. The action of creation, annihilation, and number operators on a basis state are given by

$$a_{\lambda_p}^\dagger|n_{\lambda_1}, n_{\lambda_2}, \ldots, n_{\lambda_N}\rangle = \sqrt{n_{\lambda_p}+1}|n_{\lambda_1}, n_{\lambda_2}, \ldots, n_{\lambda_p}+1, \ldots, n_{\lambda_N}\rangle\,, \tag{1.37a}$$

$$a_{\lambda_p}|n_{\lambda_1}, n_{\lambda_2}, \ldots, n_{\lambda_N}\rangle = \sqrt{n_{\lambda_p}}|n_{\lambda_1}, n_{\lambda_2}, \ldots, n_{\lambda_p}-1, \ldots, n_{\lambda_N}\rangle\,, \tag{1.37b}$$

$$a_{\lambda_p}^\dagger a_{\lambda_p}|n_{\lambda_1}, n_{\lambda_2}, \ldots, n_{\lambda_N}\rangle = n_{\lambda_p}|n_{\lambda_1}, n_{\lambda_2}, \ldots, n_{\lambda_p}, \ldots, n_{\lambda_N}\rangle\,. \tag{1.37c}$$

The orthonormality relation reads

$$\langle n'_{\lambda_1}, n'_{\lambda_2}, \ldots, n'_{\lambda_N}|n_{\lambda_1}, n_{\lambda_2}, \ldots, n_{\lambda_N}\rangle = \prod_{l=1}^{N} \delta_{n'_{\lambda_l} n_{\lambda_l}}\,. \tag{1.38}$$

The expectation value of the electric field operator (1.24) vanishes for a Fock state, i. e.,

$$\langle n_{\lambda_1}, n_{\lambda_2}, \ldots, n_{\lambda_N}|\mathbf{E}(\mathbf{r}, t)|n_{\lambda_1}, n_{\lambda_2}, \ldots, n_{\lambda_N}\rangle = 0\,. \tag{1.39}$$

As long as there is no superposition of number states with different particle numbers, Fock states can therefore be regarded as being "very non-classical" in the sense that expectation values of field operators vanish and only quantum fluctuations exist. Fock states are eigenstates of the number operator (cf. Eq. (1.37c)) from which the light intensity can be obtained. Number operators do not commute with the field operators defined in Eqs. (1.23)–(1.25).

Coherent States

Coherent states as a description of the quantized electromagnetic field were first proposed by R. Glauber [42]. In fact, they can be regarded as being "as classical as possible" in the sense that they resemble a classical field very well. The state of a multi-mode electromagnetic field can be expressed as the direct product of coherent states for each mode, i. e.,

$$|\{\alpha_\lambda\}\rangle = |\alpha_{\lambda_1}\rangle \otimes |\alpha_{\lambda_2}\rangle \otimes \cdots \otimes |\alpha_{\lambda_N}\rangle \,. \tag{1.40}$$

Here, for the sake of simplicity, I only write down all expressions for a single coherent state.

A coherent state with a complex-valued amplitude α is defined as

$$|\alpha\rangle = \mathrm{e}^{-\frac{|\alpha|^2}{2}} \sum_{n=0}^{\infty} \frac{\alpha^n}{\sqrt{n!}} |n\rangle \,, \tag{1.41}$$

which represents an infinite sum over Fock states $|n\rangle$. Properties important in the context of this thesis include

$$\begin{aligned}
a\,|\alpha\rangle &= \alpha\,|\alpha\rangle \,, && (1.42a)\\
\langle\alpha|\alpha\rangle &= 1 \,, && (1.42b)\\
\langle\alpha|\beta\rangle &= \mathrm{e}^{-\frac{1}{2}|\alpha|^2 - \frac{1}{2}|\beta|^2 + \alpha^*\beta} \,, && (1.42c)\\
\frac{1}{\pi}\int \mathrm{d}^2\alpha |\alpha\rangle\langle\alpha| &= \mathbb{1} \,, && (1.42d)\\
\langle\alpha|a^\dagger a|\alpha\rangle &= |\alpha|^2 \,, && (1.42e)\\
\langle\alpha|\mathbf{E}(\mathbf{r},t)|\alpha\rangle &= \mathrm{i}\mathcal{E}\left(\alpha \mathrm{e}^{-\mathrm{i}\omega t}\mathbf{u}(\mathbf{r}) - \alpha^* \mathrm{e}^{\mathrm{i}\omega t}\mathbf{u}^*(\mathbf{r})\right) \,. && (1.42f)
\end{aligned}$$

Coherent states are an over-complete, non-orthogonal basis of the radiation field with a mean particle number of $|\alpha|^2$. According to Eq. (1.42f), they yield an expectation value of the electric field operator which takes the form of a classical field ($\mathcal{E}$ is the vacuum field amplitude).

Furthermore, by defining a unitary coherent state displacement operator,

$$D_a(\xi) = \mathrm{e}^{\xi a^\dagger - \xi^* a} \,, \tag{1.43}$$

a coherent state can be interpreted as a displaced vacuum state since

$$|\alpha\rangle = D_a(\alpha)|0\rangle \,. \tag{1.44}$$

Moreover, the displacement operator fulfills

$$\begin{aligned}
D_a^\dagger(\xi) = D_a^{-1}(\xi) &= D_a(-\xi) \,, && (1.45a)\\
D_a^\dagger(\xi) a D_a(\xi) &= a + \xi \,, && (1.45b)\\
D_a^\dagger(\xi) a^\dagger D_a(\xi) &= a^\dagger + \xi^* \,, && (1.45c)\\
D_a(\xi)\,|\mu\rangle &= |\xi + \mu\rangle \,. && (1.45d)
\end{aligned}$$

These properties are important for the analysis of photon-added coherent states which are discussed in the subsequent paragraph.

Photon-Added Coherent States

A so-called m-photon-added coherent state is obtained by successively applying the creation operator m times on a coherent state, i. e., $|\alpha, m\rangle \propto (a^\dagger)^m |\alpha\rangle$ [43]. In this thesis, only photon-added coherent states where a single photon is "added" are investigated. A single mode then takes the form

$$|\alpha, 1\rangle = \frac{1}{\sqrt{1+|\alpha|^2}} a^\dagger |\alpha\rangle \,. \tag{1.46}$$

Again, the direct product of all modes, i. e.,

$$|\{\alpha_\lambda, 1_\lambda\}\rangle = |\alpha_{\lambda_1}, 1_{\lambda_1}\rangle \otimes |\alpha_{\lambda_2}, 1_{\lambda_2}\rangle \otimes \cdots \otimes |\alpha_{\lambda_N}, 1_{\lambda_N}\rangle \tag{1.47}$$

is used to account for multi-mode fields. The following expressions are only for a single mode.

When compared to a single-photon Fock state, Eq. (1.46) can be interpreted as a single photon in an "alternative vacuum" given by the coherent state $|\alpha\rangle$. By applying the displacement operator (1.43) and exploiting properties (1.45a), (1.45c), and (1.45d), the single-photon-added coherent state transforms into a superposition of a single photon and the vacuum state,

$$\begin{aligned} D_a^\dagger(\alpha)|\alpha, 1\rangle &= \frac{1}{\sqrt{1+|\alpha|^2}} D_a^\dagger(\alpha) a^\dagger D_a(\alpha) D_a^\dagger(\alpha)|\alpha\rangle \\ &= \frac{1}{\sqrt{1+|\alpha|^2}} \left(a^\dagger + \alpha^*\right) D_a(-\alpha)|\alpha\rangle \\ &= \frac{1}{\sqrt{1+|\alpha|^2}} \left(a^\dagger|0\rangle + \alpha^*|0\rangle\right) . \end{aligned} \tag{1.48}$$

Displacing the basis of the "background" coherent state can therefore simplify the description of single-photon-added coherent states. Equation (1.48) is very important for Chap. 5. See Refs. [43, 44] for further details and properties of photon-added coherent states.

1.3.2 Light–Matter Interactions

Photons do not interact directly with each other[15], which makes them—at first sight—hard to manipulate and process. Different physical mechanisms can, however, lead to an effective photon–photon interaction at energy scales which are relevant in solid-state based (quantum) optical systems. In that case, a subsystem which mediates the effective interaction

[15] Direct photon–photon interactions only become relevant at very high intensities.

is required. Such systems include, for instance, artificial atoms acting as saturable absorbers, mechanical motion (phonons), and classical optical nonlinearities such as a Kerr-nonlinear response. In this section, I introduce the quantum mechanical description of these systems which is applied in later chapters.

Atom–Photon Interactions

In what follows, the term "atom" is used to refer to both natural and artificial atoms independent of their actual physical realization. Possible examples include quantum dots in Photonic Crystals or resonator arrays [4, 45, 46], fibers with side-coupled resonators [47], and qubits in superconducting circuitry [48–50].

Throughout this thesis, atom–photon interactions are restricted to the dipole approximation, i. e., the limit in which the spatial extent of the atom is much smaller than typical wavelengths of the radiation field. In this case, the appropriate interaction Hamiltonian[16]

$$H_{\mathrm{at-phot}} = -\mathbf{P}\cdot\mathbf{E}(\mathbf{R}_0) \tag{1.49}$$

describes the coupling of an electric dipole operator $\mathbf{P}$ to the electric field operator $\mathbf{E}(\mathbf{R}_0)$ at the position $\mathbf{R}_0$ of the atom. Moreover, only single-electron transitions are considered. Therefore, the atomic subsystem is taken into account as a single-particle problem. An expansion of the electric dipole moment operator in terms of single-particle eigenstates of the atomic subsystem, $\{|\Theta_n\rangle\}$, takes the form

$$\mathbf{P} = -e\mathbf{r} = -e\sum_{nm}|\Theta_n\rangle\langle\Theta_n|\mathbf{r}|\Theta_m\rangle\langle\Theta_m| = \sum_{nm}\mathbf{P}_{nm}|\Theta_n\rangle\langle\Theta_m|\,. \tag{1.50}$$

In Eq. (1.50),

$$\begin{aligned}\mathbf{P}_{nm} &= -e\langle\Theta_n|\mathbf{r}|\Theta_m\rangle\\ &= -e\int \mathrm{d}^3r\int \mathrm{d}^3r'\langle\Theta_n|\mathbf{r}\rangle\underbrace{\langle\mathbf{r}|\mathbf{r}|\mathbf{r}'\rangle}_{=\mathbf{r}\delta(\mathbf{r}-\mathbf{r}')}\langle\mathbf{r}'|\Theta_m\rangle\\ &= -e\int \mathrm{d}^3r\,\mathbf{r}\theta_n^*(\mathbf{r})\theta_m(\mathbf{r})\\ &= \mathbf{P}_{mn}^*\end{aligned} \tag{1.51}$$

denotes the dipole matrix elements, in which $-e$ is the electron's charge, $\mathbf{r}$ its position operator, and $\theta_n(\mathbf{r})$ signifies the electronic wave functions in real space. Note that $\mathbf{P}_{nn} = 0$ because the position operator has odd parity. Hence, the dipole operator induces transitions

[16] In the dipole approximation, Hamiltonian (1.49) is equivalent to the minimal coupling Hamiltonian of an electron in the electromagnetic field. As is extensively discussed in Ref. [51], the connection is given by a local gauge transformation.

between electronic levels. Using the general decomposition of the electric field operator, Eq. (1.24), the interaction Hamiltonian in the Schrödinger picture can be rewritten as

$$H_{\mathrm{at-phot}} = \sum_{\lambda nm} \left(V_{\lambda nm} |\Theta_n\rangle\langle\Theta_m| a_\lambda + V^*_{\lambda nm} |\Theta_m\rangle\langle\Theta_n| a^\dagger_\lambda \right) , \tag{1.52}$$

where

$$\begin{aligned} V_{\lambda nm} &= -\mathbf{P}_{nm} \cdot \mathbf{E}^{(+)}_\lambda(\mathbf{R}_0) \\ &= -\mathrm{i}\sqrt{\frac{\omega_\lambda}{2\mathcal{V}_\lambda}} \mathbf{P}_{nm} \cdot \mathbf{u}_\lambda(\mathbf{R}_0) \,. \end{aligned} \tag{1.53}$$

In general, the atom–photon coupling strength depends on the specific properties of the electromagnetic mode such as its vacuum field amplitude and the mode function $\mathbf{u}(\mathbf{R}_0)$ at the atom's position (cf. Sec. 1.2.1). The overlap of the dipole matrix elements $\mathbf{P}_{nm}$ with the mode functions contains all information about the relative spatial orientation. Note that $V_{\lambda nn} = 0$.

For the next argument, M non-degenerate electronic levels for the atomic subsystem with Hamiltonian

$$H_{\mathrm{at}} = \sum_{n=1}^{M} \Omega_n |\Theta_n\rangle\langle\Theta_n| \tag{1.54}$$

are assumed and the eigenenergies are labeled such that $\Omega_1 < \Omega_2 < \cdots < \Omega_M$. Furthermore, $\Omega_{nm} \equiv \Omega_n - \Omega_m = -\Omega_{mn}$ so that $\Omega_{nm} > 0$ holds for $n > m$. In the interaction picture, Hamiltonian (1.52) can be rewritten as

$$H_{\mathrm{at-phot}} = \sum_{\lambda\, n>m} V_{\lambda nm} \left(\mathrm{e}^{-\mathrm{i}(\Omega_{nm}-\omega_\lambda)t} |\Theta_n\rangle\langle\Theta_m| a_\lambda + \mathrm{e}^{+\mathrm{i}(\Omega_{nm}+\omega_\lambda)t} |\Theta_m\rangle\langle\Theta_n| a_\lambda \right) + \mathrm{h.c.} \,. \tag{1.55}$$

The so-called rotating-wave approximation is applied as follows. Hamiltonian (1.55) contains different time scales. Compared to the difference between the atomic transition energy and the photon energy, $\Omega_{nm} - \omega_\lambda$, the respective sum of these energies is regarded to result in a rapidly varying time exponential, which is, loosely speaking, "averaged out" and therefore neglected. To be precise, $|(\Omega_{nm} - \omega_\lambda)/\Omega_{nm}| \ll 1$ and $|V_{\lambda nm}/\omega_\lambda| \ll 1$ have to be fulfilled simultaneously for the rotating-wave approximation to be justified [52, 53]. Beyond this regime, especially in the case of ultra-strong coupling, the counter-rotating terms must not be neglected. However, throughout this thesis, I assume the rotating-wave approximation to be applicable. Hamiltonian (1.55) then simplifies to

$$H_{\mathrm{at-phot}} = \sum_{\lambda\, n>m} \left(V_{\lambda nm} |\Theta_n\rangle\langle\Theta_m| a_\lambda + V^*_{\lambda mn} |\Theta_m\rangle\langle\Theta_n| a^\dagger_\lambda \right) , \tag{1.56}$$

where all operators are in the Schrödinger picture.

In most situations, a large number of atomic levels in (1.54) is far detuned with respect to the frequency components of the electromagnetic fields involved. This motivates the restriction to only a few atomic levels. Although a very brief detour on three-level systems is given in Chap. 3, atom–photon interactions are, in this thesis, mainly investigated in the context of two-level systems. In that case, only $M = 2$ levels, $|\downarrow\rangle$ and $|\uparrow\rangle$, are considered. With the transition energy $\Omega \equiv \Omega_{\uparrow\downarrow} = \Omega_\uparrow - \Omega_\downarrow = -\Omega_{\downarrow\uparrow} > 0$ Hamiltonian (1.54) reads

$$H_{\mathrm{at}} = (\Omega + \Omega_\downarrow)|\uparrow\rangle\langle\uparrow| + \Omega_\downarrow|\downarrow\rangle\langle\downarrow| \,. \tag{1.57}$$

By choosing the ground state energy to be $\Omega_\downarrow = -\Omega/2$, the Hamiltonian simply reads

$$H_{\mathrm{at}} = \frac{\Omega}{2}\sigma_z \tag{1.58}$$

with the Pauli matrix

$$\begin{aligned} \sigma_z &= |\uparrow\rangle\langle\uparrow| - |\downarrow\rangle\langle\downarrow| \\ &= \sigma^+\sigma^- - \sigma^-\sigma^+ \,. \end{aligned} \tag{1.59}$$

The atomic raising and lowering operators are

$$\sigma^+ = |\uparrow\rangle\langle\downarrow| \,, \tag{1.60a}$$

$$\sigma^- = |\downarrow\rangle\langle\uparrow| \,, \tag{1.60b}$$

and satisfy the fundamental anti-commutation relation

$$\{\sigma^+, \sigma^-\} = \sigma^+\sigma^- + \sigma^-\sigma^+ = \mathbb{1} \,. \tag{1.61}$$

The dipole operator then reads

$$\mathbf{P} = \mathbf{P}_{\uparrow\downarrow}\sigma^+ + \mathbf{P}^*_{\uparrow\downarrow}\sigma^- \,, \tag{1.62}$$

leading, in the rotating-wave approximation, to an interaction Hamiltonian of the form

$$H_{\mathrm{at-phot}} = \sum_\lambda \left(V_\lambda \, a_\lambda \sigma^+ + V_\lambda^* a_\lambda^\dagger \sigma^- \right) \,. \tag{1.63}$$

The first term in Hamiltonian (1.63) describes the process of photon absorption combined with the excitation of the two-level system whereas the second term, vice versa, describes photon emission and atomic relaxation. A very important property, which is exploited in the numerical scheme presented in Chap. 2, is the conservation of the total excitation number, i. e.,

$$\mathcal{C} = \sum_\lambda a_\lambda^\dagger a_\lambda + \frac{1}{2}\left(\sigma_z + 1\right) \tag{1.64}$$

is a constant of motion of the Hamiltonian (1.63). This feature stems from the rotating-wave approximation and would be invalid if counter-rotating terms proportional to $a_\lambda^\dagger \sigma^+$ and $a_\lambda \sigma^-$ were taken into account[17].

Putting together Eqs. (1.22), (1.58), and (1.63), the total Hamiltonian

$$H = \sum_\lambda \omega_\lambda a_\lambda^\dagger a_\lambda + \frac{\Omega}{2}\sigma_z + \sum_\lambda \left(V_\lambda \, a_\lambda \sigma^+ + V_\lambda^* a_\lambda^\dagger \sigma^- \right) \tag{1.65}$$

describes the interaction of a multi-mode electromagnetic field with a single two-level system in the dipole- and rotating-wave approximation. Equation (1.64) is still a conserved quantity since the first two terms in the full Hamiltonian only act in their respective subspace, i. e., in the photonic or atomic subspace, without changing the excitation number. Hamiltonian (1.65) represents a multi-mode version of the Jaynes-Cummings model [56, 57]. In the context of few-photon transport, J. T. Shen and S. Fan coined the term[18] "Dicke Hamiltonian" for Eq. (1.65) [60]. A tight-binding formulation in real space is extensively applied in the following chapters.

One can arrive at an alternative and equivalent formulation of Hamiltonian (1.65) by regarding the two-level system as a bosonic degree of freedom with an infinite repulsion for multiple occupancy [61–63]. In that case, one applies the replacements

$$\sigma^+ \;\to\; b^\dagger \,, \tag{1.66a}$$

$$\sigma^- \;\to\; b \,, \tag{1.66b}$$

$$\frac{\Omega}{2}\sigma_z \;\to\; \Omega b^\dagger b - \frac{\Omega}{2}\mathbb{1} + U b^\dagger b (b^\dagger b - 1) \,, \tag{1.66c}$$

where $-\frac{\Omega}{2}\mathbb{1}$ merely represents a constant energy shift which can be ignored. The two-level description is recovered by taking the limit

$$U \to \infty \,. \tag{1.67}$$

The last term in Eq. (1.66c) only plays a role for two or more excitations. In the language of condensed matter theory, this system could be regarded as being "strongly correlated" and the atom clearly mediates an effective photon–photon interaction. The formulation (1.66) is used in Chaps. 3 and 4.

[17] Very often [35, 54, 55], terms proportional to $a_\lambda^\dagger \sigma^+$ and $a_\lambda \sigma^-$ are referred to as not conserving energy, which is misleading. In fact, as long as the Hamiltonian is time-independent, energy is *always* conserved. However, the total number of excitations defined in Eq. (1.64) is not conserved anymore once the counter-rotating terms are taken into account. This dramatically complicates both numerical as well as analytical approaches. For instance, an analytic solution to the Rabi model has been found just recently [53].

[18] Historically, the term "Dicke Hamiltonian" stands for a quantum system of many two-level systems coupled to a single electromagnetic mode [58, 59], which is not Hamiltonian (1.65). Unfortunately, this ambiguity can cause confusion.

Finally, another variation of Hamiltonian (1.65) where each electromagnetic mode is coupled to a single two level-system is worth mentioning. In a tight-binding formulation, this system is known as the Jaynes-Cummings-Hubbard system, which offers a variety of physical effects [64–68]. Aspects of this system are not investigated here since they are beyond the scope of this thesis. However, the Jaynes-Cummings-Hubbard model is directly amenable to the numerical scheme presented in Chap. 2.

Field Interactions via Kerr-type Nonlinearities

The formalism of field quantization for the macroscopic Maxwell equations in Sec. 1.1 was restricted to the case of linear, isotropic, dispersion- and loss-free dielectrics (cf. constitutive relations (1.2)). In the presence of non-resonant nonlinearities, the medium's response can be written as a power series in terms of the electric field, leading to a constitutive relation of the form[19] [69, 70]

$$D_i(\mathbf{r}) = E_i(\mathbf{r}) + \chi^{(1)}_{ij}(\mathbf{r})E_j(\mathbf{r}) + \chi^{(2)}_{ijk}(\mathbf{r})E_j(\mathbf{r})E_k(\mathbf{r}) + \chi^{(3)}_{ijkl}(\mathbf{r})E_j(\mathbf{r})E_k(\mathbf{r})E_l(\mathbf{r}) + \dots . \quad (1.68)$$

Here, the indices stand for Cartesian coordinates and the Einstein summation convention is assumed. For the remainder, I only consider isotropic media ($\chi^{(1)}_{ij}(\mathbf{r}) = \delta_{ij}\chi^{(1)}(\mathbf{r})$), for which $\epsilon(\mathbf{r}) = 1 + \chi^{(1)}(\mathbf{r})$, and assume the bulk material to be inversion-symmetric so that $\chi^{(2)}_{ijk} = 0$. Neglecting possible surface effects, the focus here is on the third-order nonlinear susceptibility—the Kerr nonlinearity.

Unlike the quantization procedure presented in Sec. 1.1, a rigorous, non-heuristic quantization for nonlinear media is highly sophisticated and complicated, which would go beyond the scope of this chapter. Instead, by referring to the corresponding references, I directly discuss the underlying Hamiltonian and its possible realizations.

J. E. Sipe *et al.* showed in a general context [71] as well as for the special situation of a Kerr nonlinearity in a Photonic Crystal [72] that the additional term in the Hamiltonian for a single mode of the electromagnetic field has the form

$$H_{\mathrm{NL}} \propto \left(\mathbf{w}a + \mathbf{w}^* a^\dagger\right)^4 , \quad (1.69)$$

where $\mathbf{w}$ and the missing prefactors will not be specified at this qualitative level. For a different approach, see the work of M. Hillery and L. D. Mlodinow [73] or Ref. [70]. Multiplying out all terms in Hamiltonian (1.69) and normal-ordering the operators reveals different processes occurring at separated time scales. For instance, in the Heisenberg picture, a term

[19] In nonlinear optics, Maxwell's equations cannot be scaled arbitrarily. The scale of the electric field (cf. Appendix A) becomes important and dimensionless units have to be used carefully. In the following, however, I do not address this issue since Kerr nonlinearites are taken into account in a phenomenological way instead of calculating coupling terms directly from, for instance, known values of $\chi^{(3)}$ in an *ab initio* fashion.

proportional to a^4 oscillates with a frequency that is four times the optical frequency of the mode, whereas a term proportional to $a^\dagger a^\dagger aa$ is static. In the spirit of the rotating-wave approximation, all rapidly varying terms are then neglected, leading to a simplified Hamiltonian,

$$H_{\mathrm{Kerr}} = \Delta a^\dagger a^\dagger aa\,, \tag{1.70}$$

in which Δ is the strength of the Kerr nonlinearity. In the case of an atomic ensemble, Hamiltonian (1.70) can be deduced by applying an adiabatic elimination [24]. Furthermore, despite all approximations applied, Hamiltonian (1.70) has proven to be a valid description in various physical realizations such as nonlinear cavities [24, 74, 75], exciton–exciton interactions in semiconductors [76], interacting polaritons in an array of coupled cavities [15–17], in the context of ultra-cold bosonic atoms [28], and in optomechanical systems [77], to name just a few. For the latter, an approach different to Ref. [77] is presented in the next section.

Phonon–Photon Interactions

Although a major part of quantum optics is concerned with atom–photon interactions, the coupling of the electromagnetic field to mechanical degrees of freedom has recently become a well-established subfield called optomechanics. The first speculations about the existence of radiation pressure can be dated back to Kepler [78] who tried to find an explanation for the fact that a comet's tail always points away from the sun. However, radiation pressure forces are not part of our everyday life's perception since they are very weak for macroscopic objects. Only with the advent of modern nanotechnological fabrication techniques, a systematic study of radiation pressure effects has become possible, allowing for significant coupling of mechanical motion and light in the regime of a few nanonewton. To date, a variety of different optomechanical systems exists. Vibrating waveguides in an integrated optics configuration [79–82], ground-state cooling of a single mechanical mode [83–85], optomechanical crystals [86, 87], and applications in quantum information [88] are just a few examples. See Refs. [89–92] for an overview.

Similar to the case of nonlinear dielectric media, the quantization of the electromagnetic field coupled to mechanical motion, which is usually taken into account in form of time-dependent boundary conditions, can be rather complicated. Reference [25] provides a detailed discussion of the classical and quantum mechanical problem. Here, I merely present a qualitative explanation.

Consider a single electromagnetic mode of frequency ω (operators a and $a^\dagger$) coupled to a mechanical oscillator (operators b and $b^\dagger$) via radiation pressure. The generic Hamiltonian has the form

$$H_{\mathrm{phon-phot}} = \omega a^\dagger a + \nu b^\dagger b + g a^\dagger a(b^\dagger + b)\,. \tag{1.71}$$

Here, ν is the mechanical resonator's eigenfrequency and g represents the optomechanical coupling strength. Qualitatively, Hamiltonian (1.71) can be understood as follows. For simplicity, assume a one-dimensional optical resonator (the argument also applies to more

general situations). Radiation pressure leads to a change in the mechanical oscillator's displacement, i. e., the length of the resonator, which, in turn, changes the displacement-dependent eigenfrequency of the electromagnetic field mode because the frequency of a resonator depends on its length. If these displacements are assumed to be small compared to the length scales of the quantization volume in equilibrium (equilibrium position x_0), the electromagnetic mode frequency $\omega(x)$ can be expanded to first order in the displacement x, i. e., $\omega(x) \approx \omega(x_0) + \partial\omega(x)/\partial x|_{x=x_0} \cdot (x - x_0)$. For the mechanical displacement, the proportionality $x - x_0 \propto b + b^\dagger$ holds, which, inserted into the Taylor expansion and into $\omega(x)a^\dagger a$, already yields the interaction term proportional to $a^\dagger a(b^\dagger + b)$. For the one-dimensional resonator, $\partial\omega(x)/\partial x|_{x=x_0} < 0$ so that $g < 0$, which also applies to more complicated systems. Note that the above explanations are heuristic and imprecise[20]. They merely serve as an intuitive and simple motivation of Hamiltonian (1.71). For a rigorous treatment, see Ref. [25].

Hamiltonian (1.71) can be generalized to

$$\begin{aligned} H = & \sum_\lambda \left(\omega_\lambda a_\lambda^\dagger a_\lambda + \nu_\lambda b_\lambda^\dagger b_\lambda + g_\lambda a_\lambda^\dagger a_\lambda (b_\lambda^\dagger + b_\lambda) \right) \\ & + \sum_{\lambda\lambda'} J_{\lambda\lambda'} a_\lambda^\dagger a_{\lambda'} \,. \end{aligned} \tag{1.72}$$

Here, each electromagnetic mode λ interacts with a single mechanical oscillator. In this Hamiltonian, ω_λ and ν_λ denote, respectively, the optical and mechanical eigenfrequencies with the corresponding photonic (a_λ and $a_\lambda^\dagger$) and phononic (b_λ and $b_\lambda^\dagger$) annihilation and creation operators. The optomechanical interaction strength due to radiation pressure is g_λ. All information about photonic inter-mode coupling is encoded in the hopping terms $J_{\lambda\lambda'} = J_{\lambda'\lambda}^*$. One specific realization of Hamiltonian (1.72) is addressed in Chap. 5. In this section, only general properties[21] are discussed.

Similar to the atom–photon interactions without the rotating-wave approximation (cf. Eq. (1.55)), Hamiltonian (1.72) does not conserve the total number of excitations. The quantity

$$\mathcal{C} = \sum_\lambda \left(a_\lambda^\dagger a_\lambda + b_\lambda^\dagger b_\lambda \right) \tag{1.73}$$

is therefore not a constant of motion. However, the on-site terms in the first line of Eq. (1.72) resemble the so-called independent boson model [93], which describes the interaction of an electronic level with a bosonic bath. Here, all operators are bosonic, which introduces a subtle and interesting difference when compared to the fermionic counterpart. To gain further

[20] Especially the replacement $x - x_0 \propto b + b^\dagger$ is very vague. In the Taylor expansion, $x - x_0$ is first assumed to be a real number, but later an operator is inserted. In a detailed analysis, as presented in Ref. [25], the photonic operators parametrically depend on the mechanical degrees of freedom.

[21] At this point, there is no need to interpret Hamiltonian (1.72) as an array of optomechanical resonators in real space. However, in Chap. 5, the $J_{\lambda\lambda'}$ actually represent such a realization.

insight into the properties of Hamiltonian (1.72), the method of canonical transformation [93] is utilized. Using

$$\begin{aligned}\bar{H} &= \mathrm{e}^{S} H(\{a_\lambda^\dagger\},\{a_\lambda\},\{b_\lambda^\dagger\},\{b_\lambda\})\mathrm{e}^{-S} \\ &= H(\{\bar{a}_\lambda^\dagger\},\{\bar{a}_\lambda\},\{\bar{b}_\lambda^\dagger\},\{\bar{b}_\lambda\}) \end{aligned} \tag{1.74}$$

with

$$S = \sum_\lambda \kappa_\lambda a_\lambda^\dagger a_\lambda (b_\lambda^\dagger - b_\lambda) \tag{1.75}$$

and the properties

$$\bar{a}_\lambda = \mathrm{e}^{S} a_\lambda \mathrm{e}^{-S} = a_\lambda X_\lambda(\kappa_\lambda)\,, \tag{1.76a}$$

$$\bar{b}_\lambda = \mathrm{e}^{S} b_\lambda \mathrm{e}^{-S} = b_\lambda - \kappa_\lambda a_\lambda^\dagger a_\lambda\,, \tag{1.76b}$$

results in

$$\begin{aligned}\bar{H} &= \sum_\lambda \left(\omega_\lambda a_\lambda^\dagger a_\lambda + \nu_\lambda b_\lambda^\dagger b_\lambda - \Delta_\lambda a_\lambda^\dagger a_\lambda a_\lambda^\dagger a_\lambda\right) \\ &+ \sum_{\lambda\lambda'} J_{\lambda\lambda'} a_\lambda^\dagger a_{\lambda'} X_{b_\lambda}^\dagger(\kappa_\lambda) X_{b_{\lambda'}}(\kappa_{\lambda'})\,. \end{aligned} \tag{1.77}$$

Here, $X_\lambda(\kappa_\lambda) = \mathrm{e}^{-\kappa_\lambda(b_\lambda^\dagger - b_\lambda)}$ denotes a displacement operator (cf. Eq. (1.43)), $\kappa_\lambda = g_\lambda/\nu_\lambda$, and $\Delta_\lambda = g_\lambda^2/\nu_\lambda = \kappa_\lambda g_\lambda$. Transformation (1.74) represents an intensity dependent displacement of the mechanical oscillators' amplitudes and is also known as "polaron transformation".

The photonic and phononic on-site terms in Hamiltonian (1.77) are now decoupled and the optomechanical nonlinearity results in an effective photon–photon interaction, resembling an attractive Bose-Hubbard model. In this formulation, photons and phonons do not interact directly, but photon hopping is accompanied by a change in the mechanical oscillators' amplitudes, which is expressed by the displacement operators. Photons in the same mode interact via an effective Kerr nonlinearity (cf. Eq. (1.70)). Also note that the interaction term can be rewritten according to

$$-\Delta_\lambda a_\lambda^\dagger a_\lambda a_\lambda^\dagger a_\lambda = -\Delta_\lambda a_\lambda^\dagger a_\lambda - \Delta_\lambda a_\lambda^\dagger a_\lambda^\dagger a_\lambda a_\lambda\,, \tag{1.78}$$

where the first term, $-\Delta a_\lambda^\dagger a_\lambda$, is usually referred to as the so-called "polaron shift". In the case of fermions, the interaction term $-\Delta a_\lambda^\dagger a_\lambda^\dagger a_\lambda a_\lambda$ would be absent because of Pauli's principle.

Up to this point, the transformation to Hamiltonian (1.77) is exact. However, because of the displacement operators, the hopping terms connect all particle numbers in the phononic Hilbert space. Similar to the case of atom–photon interactions, this renders both an analytical and a numerical treatment difficult.

In what follows, the aim is to derive an approximate Hamiltonian for the photons only. In order to eliminate the phononic degress of freedom, it is instructional to have a closer look at the combination of operators in the hopping terms and expand the displacement operators to first order in κ_λ, i. e.,

$$a_\lambda X_\lambda(\kappa_\lambda) \approx a_\lambda \left(1 - \kappa_\lambda(b_\lambda^\dagger - b_\lambda)\right) . \tag{1.79}$$

Hopping from mode λ to mode λ' thus reads

$$a_\lambda^\dagger X_\lambda^\dagger(\kappa_\lambda) a_{\lambda'} X_{\lambda'}(\kappa_{\lambda'}) \approx a_\lambda^\dagger a_{\lambda'} \left(1 + \kappa_\lambda(b_\lambda^\dagger - b_\lambda) - \kappa_{\lambda'}(b_{\lambda'}^\dagger - b_{\lambda'})\right) . \tag{1.80}$$

Hence, a photon which is scattered from mode λ' to mode λ additionally displaces both mechanical oscillators according to the amplitudes κ_λ and $\kappa_{\lambda'}$. Note that for real hopping amplitudes, i. e., $J_{\lambda\lambda'} = J_{\lambda'\lambda}$, and $\kappa_\lambda = \kappa_{\lambda'} = \kappa$, the first corrections are quadratic in κ because the Hermitian conjugate of Eq. (1.80) in the sum of Hamiltonian (1.77) cancels terms linear in κ.

The regime of $\kappa_\lambda \ll 1$ represents the situations in which the optomechanical nonlinearity is small compared to mechanical frequencies. In addition, optical frequencies exceed mechanical frequencies by orders of magnitude so that $\nu_\lambda \ll \omega_\lambda$. In analogy to cavity quantum electrodynamics, this is the regime of weak coupling. The assumption $\kappa_\lambda \ll 1$ should be valid for certain optomechanical systems (for instance, see Ref. [94]), allowing to subsume the net effect the phonons have on the photon's inter-mode scattering in effective, renormalized hopping terms. Furthermore, if the mechanical subsystem is not subject to a special state preparation, this can be achieved by replacing the phononic displacement operators by their thermodynamic expectation values with respect to the free phononic Hamiltonian $H_\mathrm{p} = \sum_\lambda \nu_\lambda b_\lambda^\dagger b_\lambda$, i. e.,

$$X_\lambda(\kappa_\lambda) \to \chi_\lambda(\kappa_\lambda) = \frac{\mathrm{tr}\left(X_\lambda(\kappa_\lambda)\mathrm{e}^{-\beta(H_\mathrm{p}-\mu N)}\right)}{\mathrm{tr}\left(\mathrm{e}^{-\beta(H_\mathrm{p}-\mu N)}\right)} . \tag{1.81}$$

The inverse thermal energy is denoted by β, $\mu = 0$ is the vanishing chemical potential for phonons, and N counts the total number of phonons. The method of Feynman disentangling of operators [93, 95, 96] (see Appendix B for details) finally yields

$$\chi_\lambda(\kappa_\lambda) = \mathrm{e}^{-\kappa_\lambda^2\left(B_{\nu_\lambda}(\beta)+\frac{1}{2}\right)} , \tag{1.82}$$

where $B_{\nu_\lambda}(\beta) = 1/(\mathrm{e}^{\beta\nu_\lambda} - 1)$ denotes the Bose-Einstein distribution. This replacement effectively decouples the photonic and phononic system such that the photonic Hamiltonian now reads

$$H = \sum_\lambda \left(\omega_\lambda - \Delta_\lambda\right) a_\lambda^\dagger a_\lambda - \sum_\lambda \Delta_\lambda a_\lambda^\dagger a_\lambda^\dagger a_\lambda a_\lambda + \sum_{\lambda\lambda'} J'_{\lambda\lambda'} a_\lambda^\dagger a_{\lambda'} , \tag{1.83}$$

where the renormalized hopping elements are

$$J'_{\lambda\lambda'} = \chi_\lambda(\kappa_\lambda)\chi_{\lambda'}(\kappa_{\lambda'})J_{\lambda\lambda'}\,. \tag{1.84}$$

Since Hamiltonian (1.83) is valid in the limit of weak coupling, the polaron shift is very small and $\omega_\lambda - \Delta_\lambda \approx \omega_\lambda$.

1.3.3 Observables and Physical Quantities

In this section, I give general definitions of observables and physical quantities. In later chapters, they are adapted and simplified according to the special type of problem under investigation. In the following, $\langle\cdot\rangle$ denotes the quantum-mechanical expectation value.

Occupation Numbers

The occupation number of a bosonic mode λ is defined as the expectation value of the corresponding number operator, i. e.,

$$\langle n_\lambda\rangle = \langle a_\lambda^\dagger a_\lambda\rangle\,. \tag{1.85}$$

In the context of transport calculations, quantities such as transmittance and reflectance can be constructed as a sum over selected modes. For a two-level system, the inversion $\langle\sigma_z\rangle \in [-1,1]$ is a typical measure for the atomic excitation. In this thesis, I prefer the occupation of the excited atomic state, i. e.,

$$\langle\sigma^+\sigma^-\rangle = \frac{1}{2}\left(\langle\sigma_z\rangle + 1\right)\,. \tag{1.86}$$

In the alternative formulation of a bosonic site with infinite on-site repulsion for two or more excitations, the atomic excitation reads $\langle b^\dagger b\rangle$ (cf. Sec. 1.3.2 and Eqs. (1.66)).

Field–Field Correlation Functions

Field–field auto and cross correlation functions, defined according to

$$C^{\mathrm{ff}}_{\lambda\lambda'}(t,t') = \langle a_\lambda^\dagger(t)a_{\lambda'}(t')\rangle\,, \tag{1.87}$$

help to identify memory effects between modes λ and λ'. Furthermore, the auto correlation function is proportional to the well-known amplitude correlation function $g^{(1)}$ [97, 98] and it determines the output spectrum (see below).

Output Spectrum

Imagine an ideal photo detector. It can be utilized to obtain emission spectra of atoms, e. g., of a single two-level system. The output or emission spectrum $S(\omega)$, which is sometimes also termed "fluctuation spectrum", is defined as the Fourier transform of the temporal cross correlation function of the field amplitudes [99]. The spectral contribution of mode λ reads

$$\begin{aligned} S_\lambda(\omega) &= \int_{-\infty}^{\infty} \mathrm{d}\tau \mathrm{e}^{\mathrm{i}\omega\tau} \langle a_\lambda^\dagger(t+\tau) a_\lambda(t) \rangle \\ &= \int_{-\infty}^{\infty} \mathrm{d}\tau \mathrm{e}^{\mathrm{i}\omega\tau} C_{\lambda\lambda}^{\mathrm{ff}}(t+\tau, t) \,. \end{aligned} \tag{1.88}$$

In this definition, it is assumed that the spectrum $S(\omega)$ does not depend on a time argument anymore, which requires the correlation function to be translationally invariant in time, i. e., it describes a stationary process. For a non-stationary processes such as when considering pulses, definition (1.88) still depends on one time argument. In that case, $S(\omega, t)$ is the spectrogram[22] of the process [100, 101].

In Chap. 6, Eq. (1.88) is adapted and simplified to the specific problem of a single-excitation wave function in order to study the spontaneous emission spectrum. Note that in Eq. (1.88) all contributions to the spectrum are given by degrees of freedom of the radiation field. If one is interested in the spectrum emitted by a two-level atom, one could also ask for the "spectrum" of the atomic degrees of freedom, i. e., the Fourier transform of $\langle \sigma^+(t+\tau)\sigma^-(t) \rangle$. Although, for instance, in the case of resonance fluorescence it is common to relate the output spectrum to the Fourier transform of the correlator $\langle \sigma^+(t+\tau)\sigma^-(t) \rangle$ [51], a detector only records the spectral information which is contained in electromagnetic field modes. Throughout this thesis, I therefore use Eq. (1.88) since the focus is on the spectral information which is accessible through the degrees of freedom of the radiation field.

Atom–Field Correlation Functions

In analogy to field–field correlators, atom–field correlation functions are defined via

$$C_\lambda^{\mathrm{af}}(t, t') = \langle \sigma^+(t) a_\lambda(t') \rangle \,. \tag{1.89}$$

These functions are, for instance, important for the investigation of memory effects between a field mode λ and a two-level system.

[22] Depending on the nomenclature of the different scientific communities, the spectrogram is also referred to as the "Wigner-Ville distribution". See Refs. [100, 101] for more details.

Joint Probabilities

The n-mode quantity

$$\mathcal{P}_{\lambda_1\lambda_2\ldots\lambda_n} = \langle a^\dagger_{\lambda_n} \ldots a^\dagger_{\lambda_2} a^\dagger_{\lambda_1} a_{\lambda_1} a_{\lambda_2} \ldots a_{\lambda_n} \rangle \tag{1.90}$$

is proportional to the probability of finding the radiation field in modes λ_1, λ_2, ..., and λ_n. In this thesis, I focus on the case of $n = 2$, i. e.,

$$\mathcal{P}_{\lambda_1\lambda_2} = \langle a^\dagger_{\lambda_2} a^\dagger_{\lambda_1} a_{\lambda_1} a_{\lambda_2} \rangle \,. \tag{1.91}$$

This quantity is adapted and properly normalized in order to suit the problem of photon transport in Chaps. 3 and 4. Note that Eq. (1.90) is reminiscent of the quantum-optical correlation functions $G^{(n)}$ introduced by R. Glauber [97, 98]. However, Eq. (1.90) only represents the special case in which the the operators have the same time argument.

Fidelity of Wave Functions

Consider two complex-valued, time-dependent quantities $\zeta_\lambda(t)$ and $\rho_\lambda(t)$ with norms $N_\zeta = \sqrt{\sum_\lambda |\zeta_\lambda|^2}$ and $N_\rho = \sqrt{\sum_\lambda |\rho_\lambda|^2}$. The fidelity,

$$\mathcal{F}_{\zeta\rho}(t) = \frac{\left|\sum_\lambda \zeta^*_\lambda(t)\rho_\lambda(t)\right|}{\sqrt{N_\zeta(t) N_\rho(t)}} \,, \tag{1.92}$$

serves as a measure for the overlap of these two quantities at equal times. Throughout this thesis, this simple definition of the fidelity is sufficient. For a formal treatment, temporal overlaps, and a generalization to mixed quantum states, see Ref. [102].

1.3.4 Open System Dynamics and Quantum Jumps

The time evolution of the total state vector of radiation field modes and further subsystems, e. g., two-level atoms, is given by the Schrödinger equation (1.35). It describes a coherent and deterministic evolution of a state $|\Psi(t)\rangle$ whose norm is conserved because the Hamiltonian is Hermitian. In this formulation, it is therefore very hard to describe open systems which are subject to irreversible loss mechanisms of different kinds. A common strategy to overcome this drawback lies in the reformulation of the problem in terms of a density matrix whose dynamics is given by a master equation, in which several super operators, e.g., Lindblad operators, describe the coupling to an environment [103, 104].

The introduction of a density matrix, however, drastically increases the number of degrees of freedom and therefore renders the problem computationally much more demanding. The numerical scheme used in this thesis is addressed in Chap. 2. Here, I focus on a brief description of the key elements of an approach which incorporates open system dynamics in a wave-function based formalism by means of stochastic quantum jumps. This quantum jump

approach, which is often also termed "Monte Carlo wave function method", has proven to be successful in a number of quantum-optical problems. For in-depth reviews, see Refs. [105, 106].

Master Equations in Lindblad Form, Jump Operators, and Stochastic Time Evolution

Consider the general form of a master equation,

$$\frac{\partial}{\partial t}\rho = \mathrm{i}[\rho, H] + \mathcal{L}(\rho)\,, \tag{1.93}$$

where $\rho = \sum_i w_i |\Psi_i\rangle\langle\Psi_i|$ is a density matrix, H the Hamilton operator for the coherent time evolution, and $\mathcal{L}(\rho)$ a super operator describing the incoherent open system dynamics. In this thesis, only super operators of Lindblad type, i. e.,

$$\mathcal{L}(\rho) = -\frac{1}{2}\sum_m \{C_m^\dagger C_m, \rho\} + \sum_m C_m \rho C_m^\dagger\,, \tag{1.94}$$

are considered. Curly brackets denote an anticommutator. $C_m^\dagger$ and C_m signify creation and annihilation operators, respectively, which are constructed out of the system's operators and chosen according to the special type of relaxation under consideration. They are termed "jump operators".

The central idea of emulating a master equation like Eq. (1.93) within a wave function formalism is to calculate many stochastic trajectories of the wave function $|\Psi^{(\mathrm{i})}(t)\rangle$, and to finally average observables $\hat{O}(t)$ over all M individual realizations, i. e.,

$$\langle\hat{O}(t)\rangle = \mathrm{tr}(\hat{O}(t)\rho) \approx \frac{1}{M}\sum_{i=1}^{M}\langle\Psi^{(\mathrm{i})}(t)|\hat{O}|\Psi^{(\mathrm{i})}(t)\rangle\,. \tag{1.95}$$

A single trajectory is obtained by using the following scheme, which can be interpreted as a series of successive *gedanken* measurements:

- For a time step Δt, propagate the wave function deterministically according to the Schrödinger equation with an effective, non-Hermitian Hamiltonian

$$H_{\mathrm{eff}} = H - \frac{\mathrm{i}}{2}\sum_m C_m^\dagger C_m\,. \tag{1.96}$$

- After time step Δt, calculate jump probabilities

$$p_m = \Delta t\langle\Psi(t)|C_m^\dagger C_m|\Psi(t)\rangle \tag{1.97}$$

  and obtain the total jump probability $p = \sum_m p_m$.

- Draw a uniformly distributed random number ς from the interval $[0, 1]$.
- If $\varsigma > p$, no jump occurs. Renormalize the wave function to unity and start with the next time step.
- If $\varsigma \leq p$, a quantum jump occurs. Pick a jump m' according to the probability $\frac{p_{m'}}{p}$, e. g., by drawing a random number and applying the method of linear search (cf. Ref. [103] and Appendix C).
  Collapse the wave function for the selected jump according to

$$|\Psi\rangle \to \frac{C_{m'}|\Psi\rangle}{\sqrt{\langle\Psi|C_{m'}^\dagger C_{m'}|\Psi\rangle}}\,. \tag{1.98}$$

  Start with the next time step.

Here, I only presented the realization of the quantum jump approach which is applied in this thesis. For further details and extended schemes, as well as a rigorous proof of the equivalence of this approach and a master equation of Lindblad type, see Refs. [105, 106].

Relaxation of T_1-type

In realistic situations, dissipation is a major concern. For instance, a two-level system eventually suffers from radiative and non-radiative damping. All microscopic mechanisms leading to damping are commonly subsumed in a single phenomenological time scale T_1.

The master equation for a damped two-level system [103, 104],

$$\frac{\partial}{\partial t}\rho = \mathrm{i}[\rho, H] - \frac{1}{2T_1}\{\sigma^+\sigma^-, \rho\} + \frac{1}{T_1}\sigma^-\rho\sigma^+\,, \tag{1.99}$$

is obtained by defining jump operators according to $C = \frac{1}{\sqrt{T_1}}\sigma^-$. This equation describes the coupling to a reservoir at zero temperature. For the case of a single two-level atom which is exclusively coupled to such a reservoir, i. e., $H = \frac{\Omega}{2}\sigma_z$, the initial condition $\rho(0) = |\uparrow\rangle\langle\uparrow|$ decays exponentially in time according to $\langle\uparrow|\rho(t)|\uparrow\rangle = \mathrm{e}^{-\frac{t}{T_1}}$. This approach can also be applied to a harmonic oscillator, e. g., a mode λ of the radiation field. In that case, one has to set $C_\lambda = \frac{1}{\sqrt{T_1}}a_\lambda$.

The coupling of a two-level atom to a reservoir of finite temperature can also be described within a Lindblad formalism with the help of two jump operators [104, 106]. A finite temperature results in a modification of the decay rate and induces a finite occupation of the excited atomic state in the long-time limit according to a Boltzmann factor $\mathrm{e}^{-\beta\Omega}$, where β is the inverse thermal energy. Similarly, in thermal equilibrium, the radiation field modes λ are occupied according to the Bose-Einstein distribution $B_{\omega_\lambda}(\beta)$ (cf. Sec. 1.3.2). Throughout this thesis, I restrict the investigations to a regime where both $\mathrm{e}^{-\beta\Omega} \ll 1$ and $B_{\omega_\lambda}(\beta) \approx 0$

holds. This allows one to model the coupling of T_1-type of two-level systems and bosonic modes to a reservoir of effectively zero temperature according to Eq. (1.99). For instance, this is justified for frequencies in the visible spectrum at room temperature.

Dephasing of T_2-type

Besides non-radiative decay, several processes can lead to dephasing, i. e., a randomization of the phase relations in the wave function. Phenomenologically, such processes can be related to a time scale T_2 [70, 107]. In the case of a two-level system, a jump operator $C = \frac{1}{\sqrt{2T_2}}\sigma_z$ results in the master equation

$$\frac{\partial}{\partial t}\rho = \mathrm{i}[\rho, H] - \frac{1}{2T_2}\rho + \frac{1}{2T_2}\sigma_z\rho\sigma_z\,. \tag{1.100}$$

Again, if the Hamiltonian is just $H = \frac{\Omega}{2}\sigma_z$, an initial condition $\rho(0) \propto |\uparrow\rangle\langle\downarrow|$ decays in time according to $\langle\uparrow|\rho(t)|\downarrow\rangle \propto \mathrm{e}^{-\frac{t}{T_2}}$. In situations where the state of the two-level system can be visualized on the Bloch sphere, dephasing of T_2-type damps the expectation values $\langle\sigma^+\rangle$ and $\langle\sigma^-\rangle$ on a time scale T_2. In this thesis, I do not describe the dynamics of a two-level system in terms of a reduced density matrix for the atom only and, therefore, not refer to the usual picture of the Bloch sphere but monitor the dephasing process with the help of atom–field correlators (cf. Chap. 6).

Finite Systems and the Problem of Absorbing Boundary Conditions

Since a computational domain is limited in practice, it is impossible to simulate an infinite system within the numerical framework which is presented in Chap. 2. Luckily, realistic nanophotonic structures have a finite size, e. g., a Photonic Crystal with a few unit cells. Radiation eventually leaks out at the boundaries of a finite system, which, again, poses the problem of an open quantum system. In classical computational electrodynamics, perfectly matched layers (PMLs) are used to absorb the outgoing energy. In many-body quantum mechanics, the problem of absorbing boundaries has—to the best of my knowledge—not yet been solved in general for arbitrary bosonic and fermionic systems. In this section, I motivate how the quantum jump approach can be used to absorb excitations leaving the system.

Consider a quantum system whose closed-system dynamics is governed by the Hamiltonian H_0. Let $\mathcal{B}$ define a subset of the full single-particle Hilbert space. The states $|\mu\rangle \in \mathcal{B}$ define the part of the system to which I refer as the boundaries, i. e., regions[23] which are "leaky", allowing incoming radiation to be absorbed with negligible back-reflection. This behavior can be achieved by introducing a Hamiltonian H_{abs} which only acts on states from

[23] So far, I did not introduce the notion of real space and momentum space. The arguments in this section apply in general. However, the concept of absorbing boundaries is most transparent and useful in real space.

the set $\mathcal{B}$ in addition to the normal dynamics given by H_0. H_{abs} is a Hamilton operator with non-Hermitian on-site terms,

$$H_{\mathrm{abs}} = -\mathrm{i}\sum_{\mu} \gamma_\mu a_\mu^\dagger a_\mu \,, \tag{1.101}$$

where the rates $\gamma_\mu \geq 0$. Thus, the total dynamics given by $H = H_0 + H_{\mathrm{abs}}$ leads to the time-evolution operator

$$U = \mathrm{e}^{-\mathrm{i}(H_0 + H_{\mathrm{abs}})t} \,. \tag{1.102}$$

Thus, the states $|\mu\rangle \in \mathcal{B}$ are damped exponentially in time according to the rates γ_μ. These rates have to be chosen such that reflections from the imaginary on-site potential are small (see Chap. 6 for an example). Using Eq. (1.102) in the quantum jump approach allows one to account for a finite and therefore lossy system. Its finite-size open system dynamics due to the absorbing boundaries can be interpreted as relaxations of T_1-type since the jump operators are given by

$$C_\mu = \sqrt{\gamma_\mu} a_\mu \,. \tag{1.103}$$

For simplicity, the approach presented here only includes bosonic degrees of freedom. However, it equally well applies to fermions or spins[24].

Comments on the Quantum Jump Approach with Respect to a Single-Particle Problem

Although the approach presented in the previous section is not limited to the single-excitation subspace of the Hilbert space, it greatly simplifies in that case. In this thesis, absorbing boundaries are only used for single-particle problems.

As explained before, the effect of T_1-relaxation on a single mode is to exponentially damp its occupation number. For the special case of a single-excitation problem, the same effect occurs in a single run using the non-Hermitian Hamiltonian (1.96) without collapsing the wave function. This stems from the fact that the collapse of a single-excitation state results in the vacuum state, which has no dynamics[25] since $H_{\mathrm{eff}}|0\rangle = 0$. As long as there is only a single excitation in the system, the effects of finite system size and T_1-relaxation can be accounted for via an effective Hamilton operator H_{eff} (cf. Eq. (1.96)) without collapsing the wave function.

This is not possible for dephasing of T_2-type or for the general case where there is more than one excitation in the system. For the latter case, a non-Hermitian Hamiltonian without appropriate quantum jumps would cause damping of excitations from regions outside the boundaries due to the entangled nature of the Fock basis. For instance, in the case of two

[24] No attempt is made to solve the problem of absorbing boundaries in the presence of a Fermi sea. The approach presented here is valid as long as losses eventually lead to a collapse of the wave function towards the vacuum state $|0\rangle$.

[25] To be precise, the property $H|0\rangle = 0$ only holds if H commutes with the total number of excitations. This is always the case for all numerical simulations throughout this thesis.

excitations, states like $|\mu_1\mu_2\rangle$ occur, for which only one of the quantum numbers μ_1 and μ_2 belongs to the boundaries. In this situation, if no quantum jumps are taken into account, the non-Hermitian Hamiltonian would damp the amplitude of the total state $|\mu_1\mu_2\rangle$, which is inappropriate.

Chapter 2

2 Lattice Models and Numerical Scheme

In this chapter, I present a discrete momentum and real-space formulation of the generic Hamiltonians introduced in Chap. 1. Specifically, by virtue of a Fourier lattice transform, relations for coupling constants and dispersion relations are obtained. After a discussion of the classes of initial states which are relevant for later chapters, the numerical framework is introduced—a wave-function based time-evolution scheme. Parts of this chapter have been published in Refs. [61, 63, 108], where further details can be found.

2.1 Discrete Systems

So far, the actual meaning of the sum over all modes, which appears throughout Sec. 1.3, was not specified. From now on, only discrete sums over a finite number of modes are considered. Although this discretization might be regarded as an approximation to a system with a continuous mode spectrum, e. g., the dispersion relation of an optical fiber or a one-dimensional line defect in a Photonic Crystal, there are photonic systems which are inherently discrete, e. g., finite arrays of cavities.

Furthermore, the mode index λ, which appeared in Chap. 1, remained unspecified so far. In the following, λ stands for a multi-index $\lambda = (n\mathbf{k})$ in which n is a discrete index depending on the specific system, e. g., the band index in a Photonic Crystal or a polarization index, and $\mathbf{k}$ denotes a wavevector[1] from the first Brillouin zone. The wavevector is discrete, either because a continuous system was discretized or the system itself is discrete. In any case, $\mathbf{k}$ is defined in reciprocal space and its components k_i can only take on values

$$k_i = -\frac{\pi}{\ell_i} + \frac{2\pi}{\ell_i} \cdot \frac{r}{N_i} \qquad r = 1, 2, \ldots, N_i \,, \tag{2.1}$$

[1] Since units are chosen in which $\hbar = 1$ (cf. Appendix A), the terms “wavevector” and “momentum” are used interchangeably.

where ℓ_i is the lattice constant in direction i and N_i denotes the number of supported modes along that direction. For the example of a resonator array, N_i simply counts the number of resonators along direction i.

2.2 Fourier Lattice Transform

In principle, all subsequent investigations could be directly carried out in the discrete $\mathbf{k}$-space formulation. I find it, however, useful to work with an equivalent real space formulation since the motion of wave packets can then easily be visualized. To this end, I apply a Fourier lattice transform to the bosonic operators in q-dimensional momentum space, i. e.,

$$a^\dagger_{n\mathbf{k}} = \frac{1}{\sqrt{N_1 \dots N_q}} \sum_{j_1=1}^{N_1} \cdots \sum_{j_q=1}^{N_q} \mathrm{e}^{\mathrm{i}\mathbf{k}\cdot\mathbf{r}} a^\dagger_{n\mathbf{r}} \,. \tag{2.2}$$

Here, $a^\dagger_{n\mathbf{r}}$ represents a creation operator from the q-dimensional real space lattice, i. e., it creates an excitation in mode n at lattice point $\mathbf{r} = (j_1\ell_1, \dots, j_q\ell_q)^{\mathrm{T}}$. The Fourier lattice transform does not alter the bosonic commutation relations, i. e.,

$$\left[a_{n\mathbf{r}}, a_{n'\mathbf{r}'}\right] = \left[a^\dagger_{n\mathbf{r}}, a^\dagger_{n'\mathbf{r}'}\right] = 0 \,, \tag{2.3a}$$

$$\left[a_{n\mathbf{r}}, a^\dagger_{n'\mathbf{r}'}\right] = \delta_{nn'}\delta_{\mathbf{r}\mathbf{r}'} \,. \tag{2.3b}$$

2.2.1 Hamiltonians in Real Space

The Fourier lattice transform is now applied to the Hamiltonians introduced in Secs. 1.1.2 and 1.3.2. Relations for coupling constants and dispersion relations are obtained.

Interaction of a Single Two-Level Atom with a Multi-Mode Field

In momentum space, Hamiltonian (1.65) reads

$$H = \sum_{n\mathbf{k}} \omega_{n\mathbf{k}} a^\dagger_{n\mathbf{k}} a_{n\mathbf{k}} + \frac{\Omega}{2}\sigma_z + \sum_{n\mathbf{k}} \left(V_{n\mathbf{k}} a_{n\mathbf{k}} \sigma^+ + V^*_{n\mathbf{k}} a^\dagger_{n\mathbf{k}} \sigma^- \right) , \tag{2.4}$$

where $\omega_{n\mathbf{k}}$ denotes the photonic dispersion relation or band structure and $V_{n\mathbf{k}}$ is the momentum-dependent atom–photon coupling strength. This Hamiltonian can be recast into

$$H = \sum_{n\mathbf{r}\mathbf{r}'} J_{n\mathbf{r}\mathbf{r}'} a^\dagger_{n\mathbf{r}}\, a_{n\mathbf{r}'} + \frac{\Omega}{2}\sigma_z + \sum_{n\mathbf{r}} \left(G_{n\mathbf{r}} a_{n\mathbf{r}} \sigma^+ + G^*_{n\mathbf{r}} a^\dagger_{n\mathbf{r}} \sigma^- \right) , \tag{2.5}$$

where the hopping elements read

$$J_{n\mathbf{r}\mathbf{r}'} \equiv J_{n\mathbf{r}-\mathbf{r}'} = \frac{1}{N_1 \dots N_q} \sum_{\mathbf{k}} \omega_{n\mathbf{k}} \mathrm{e}^{\mathrm{i}\mathbf{k}\cdot(\mathbf{r}-\mathbf{r}')} \,. \tag{2.6}$$

The atom–photon coupling takes the form

$$G_{n\mathbf{r}} = \frac{1}{\sqrt{N_1 \dots N_q}} \sum_{\mathbf{k}} V_{n\mathbf{k}} \mathrm{e}^{-\mathrm{i}\mathbf{k}\cdot\mathbf{r}} \,. \tag{2.7}$$

The corresponding inverse relations read

$$\omega_{n\mathbf{k}} = \sum_{\mathbf{r}-\mathbf{r}'} \mathrm{e}^{-\mathrm{i}\mathbf{k}\cdot(\mathbf{r}-\mathbf{r}')} J_{n\mathbf{r}-\mathbf{r}'} \,, \tag{2.8a}$$

$$V_{n\mathbf{k}} = \frac{1}{\sqrt{N_1 \dots N_q}} \sum_{\mathbf{r}} \mathrm{e}^{\mathrm{i}\mathbf{k}\cdot\mathbf{r}} G_{n\mathbf{r}} \,. \tag{2.8b}$$

Note that if the hopping elements in Eq. (2.8a) are only non-zero for nearest neighbors, a cosine-dispersion relation is obtained (cf. Chap. 3). Furthermore, if the atom–photon coupling strength is momentum-independent, it is local in real space.

Hamiltonian (2.5) conserves the total number of excitations, which can be written as (cf. Eq. (1.64))

$$\mathcal{C} = \sum_{n\mathbf{r}} a^\dagger_{n\mathbf{r}} a_{n\mathbf{r}} + \frac{1}{2}\left(\sigma_z + 1\right) \,. \tag{2.9}$$

A Multi-Mode Field with Kerr-type Nonlinearity

A real space Hamiltonian describing the interaction of a multi-mode field with a local Kerr nonlinearity of the form (1.70) can be formulated as

$$H = \sum_{n\mathbf{r}\mathbf{r}'} J_{n\mathbf{r}\mathbf{r}'} a^\dagger_{n\mathbf{r}} \, a_{n\mathbf{r}'} + \sum_{n\mathbf{r}} \Delta_{n\mathbf{r}} a^\dagger_{n\mathbf{r}} a^\dagger_{n\mathbf{r}} a_{n\mathbf{r}} a_{n\mathbf{r}} \,. \tag{2.10}$$

The strength of the Kerr nonlinearity for band n in unit cell $\mathbf{r}$ is denoted by $\Delta_{n\mathbf{r}}$. In this thesis, I focus on the case of a local nonlinearity, i. e., $\Delta_{n\mathbf{r}} \propto \delta_{\mathbf{r}\mathbf{r}_0}$ (see Chap. 5). Note that Hamiltonian (1.83), which was derived as an approximate Hamiltonian in the context of phonon–photon interactions, is of the same form as Eq. (2.10).

2.3 Initial States

In this thesis, quantum-optical problems are addressed in a time-dependent framework (see Sec. 2.4). Since the Schrödinger equation is first order in time, knowledge of the state vector at one point in time is sufficient to—at least in principle—calculate the state of the system at any other point in time. Here, I introduce different classes of initial states which are important for the preceding chapters.

2.3.1 Wave Packets

Although monochromatic plane waves are very often an excellent description for states of the electromagnetic field, they never occur in practice. From an experimental point of view, there are always wave packets of finite width, which exhibit a certain spectral distribution instead of being monochromatic. From a numerical point of view, real-space methods rely on a finite computational domain so that wave packets represent a "natural" choice anyway. In the following, a Gaussian wave packet is defined via

$$\varphi_{\mathbf{r}}^{(\mathbf{k}_0 \mathbf{r}_c s)} = C \mathrm{e}^{-\frac{(\mathbf{r}-\mathbf{r}_c)^2}{2s^2}} \mathrm{e}^{\mathrm{i}\mathbf{k}_0 \cdot \mathbf{r}}\,, \tag{2.11}$$

where $\mathbf{k}_0$ is the carrier wavevector, $\mathbf{r}_c$ and s denote center and width, respectively. C is a normalization constant[2]. For simplicity, the index n is suppressed in the following and all equations are written for the case of a single band.

Few-Photon Pulses

According to Eq. (1.36), the Fock basis for a multi-mode radiation field is given as the direct product of single-mode Fock states. In real space, the corresponding basis is given by the product of single-site states. Hence, a general bosonic m-excitation state can be constructed as

$$|\Psi\rangle = \sum_{\mathbf{r}_1} \cdots \sum_{\mathbf{r}_m} \Phi_{\mathbf{r}_1 \ldots \mathbf{r}_m} a_{\mathbf{r}_1}^\dagger \ldots a_{\mathbf{r}_m}^\dagger |0\rangle\,. \tag{2.12}$$

Due to the bosonic nature, $\Phi_{\mathbf{r}_1 \ldots \mathbf{r}_m}$ has to be totally symmetric with respect to permutations of the coordinates $\{\mathbf{r}_i\}$ and can thus be written as

$$\Phi_{\mathbf{r}_1 \ldots \mathbf{r}_m} = \hat{S}_{\mathbf{r}_1 \ldots \mathbf{r}_m} \varphi_{\mathbf{r}_1}^{(\mathbf{k}_0^{(1)} \mathbf{r}_c^{(1)} s^{(1)})} \ldots \varphi_{\mathbf{r}_m}^{(\mathbf{k}_0^{(m)} \mathbf{r}_c^{(m)} s^{(m)})}\,. \tag{2.13}$$

$\hat{S}_{\mathbf{r}_1 \ldots \mathbf{r}_m}$ denotes the symmetrization operator which performs a sum over all permutations of the coordinates and $\varphi_{\mathbf{r}}^{(\ldots)}$ is a single-particle Gaussian wave packet as defined in Eq. (2.11).

In this thesis, I focus on Fock states with one or two excitations only. For two excitations, Eq. (2.12) reads

$$|\Psi\rangle = \sum_{\mathbf{r}_1} \sum_{\mathbf{r}_2} \Phi_{\mathbf{r}_1 \mathbf{r}_2} a_{\mathbf{r}_1}^\dagger a_{\mathbf{r}_2}^\dagger |0\rangle\,, \tag{2.14}$$

where

$$\Phi_{\mathbf{r}_1 \mathbf{r}_2} = \frac{1}{\sqrt{2}} \left(\varphi_{\mathbf{r}_1}^{(\mathbf{k}_0^{(1)} \mathbf{r}_c^{(1)} s^{(1)})} \cdot \varphi_{\mathbf{r}_2}^{(\mathbf{k}_0^{(2)} \mathbf{r}_c^{(2)} s^{(2)})} + \varphi_{\mathbf{r}_2}^{(\mathbf{k}_0^{(1)} \mathbf{r}_c^{(1)} s^{(1)})} \cdot \varphi_{\mathbf{r}_1}^{(\mathbf{k}_0^{(2)} \mathbf{r}_c^{(2)} s^{(2)})} \right)\,. \tag{2.15}$$

[2] In the numerical simulations presented in the preceding chapters, all initial states are automatically normalized to unity before the time evolution. To be precise, in Eq. (2.11), s^2 is actually not the variance of the Gaussian $|\varphi_{\mathbf{r}}^{(\ldots)}|^2$ (the variance is $s^2/2$). However, for the remainder, I simply refer to s as the width of the wave function.

The single-excitation initial state takes the form

$$|\Psi\rangle = \sum_{\mathbf{r}} \varphi_{\mathbf{r}}^{(\mathbf{k}_0 \mathbf{r}_c s)} a_{\mathbf{r}}^{\dagger} |0\rangle \,. \tag{2.16}$$

For two excitations, a bosonic field defined on N lattice sites has

$$d^{(2)} = \sum_{i=1}^{N} \sum_{j=1}^{i} = \sum_{i=1}^{N} i = \frac{N}{2} \cdot (N+1) \sim N^2 \tag{2.17}$$

degrees of freedom, i. e., wave function coefficients in the Fock basis, whereas for a single particle

$$d^{(1)} = \sum_{i=1}^{N} = N \,. \tag{2.18}$$

In general, an m excitation state requires $d^{(m)} \sim N^m$ degrees of freedom.

Coherent State Pulses

In analogy to the previous section, a coherent state pulse which is defined on N lattice sites can be written as the tensor product of single-site coherent states, i. e.,

$$|\Psi\rangle = |\{\alpha_{\mathbf{r}}^{(\mathbf{k}_0 \mathbf{r}_c s)}\}\rangle = |\alpha_{\mathbf{r}_1}^{(\mathbf{k}_0 \mathbf{r}_c s)}\rangle \otimes \cdots \otimes |\alpha_{\mathbf{r}_N}^{(\mathbf{k}_0 \mathbf{r}_c s)}\rangle \,, \tag{2.19}$$

in which

$$\alpha_{\mathbf{r}}^{(\mathbf{k}_0 \mathbf{r}_c s)} = \alpha^{(0)} \cdot \varphi_{\mathbf{r}}^{(\mathbf{k}_0 \mathbf{r}_c s)} \,. \tag{2.20}$$

Since the wave function in Eq. (2.11) is normalized to unity,

$$\sum_{\mathbf{r}} \left| \alpha_{\mathbf{r}}^{(\mathbf{k}_0 \mathbf{r}_c s)} \right|^2 = \left| \alpha^{(0)} \right|^2 \tag{2.21}$$

holds. Similar to the case of a single-mode coherent state, which was introduced in Sec. 1.3.1, $|\alpha^{(0)}|^2$ denotes the mean particle number of the pulse.

Pulses of Photon-Added Coherent States

As mentioned in Sec. 1.3.1, I only focus on single-photon-added coherent states in this thesis. A pulse of such states can be regarded as a combination of pulses of a single-photon Fock state and a coherent state where the coherent state amplitudes take the role of the vacuum state, i. e.,

$$|\Psi\rangle = C \sum_{\mathbf{r}} \varphi_{\mathbf{r}}^{(\mathbf{k}_0 \mathbf{r}_c s)} a_{\mathbf{r}}^{\dagger} |\{\alpha_{\mathbf{r}}^{(\mathbf{k}_0' \mathbf{r}_c' s')}\}\rangle \,. \tag{2.22}$$

Note that the pulse parameters of the single-photon wave function and the coherent state need not be identical. C represents a normalization constant, which can be calculated as (superscripts suppressed)

$$\begin{aligned}\langle\Psi|\Psi\rangle &= C^2\sum_{\mathbf{r}_i\mathbf{r}_j}\varphi^*_{\mathbf{r}_j}\varphi_{\mathbf{r}_i}\langle\{\alpha_\mathbf{r}\}|\underbrace{a_{\mathbf{r}_j}a^\dagger_{\mathbf{r}_i}}_{\delta_{\mathbf{r}_i\mathbf{r}_j}+a^\dagger_{\mathbf{r}_i}a_{\mathbf{r}_j}}|\{\alpha_\mathbf{r}\}\rangle \\ &= C^2\left(\sum_i|\varphi_{\mathbf{r}_i}|^2+(\sum_i\varphi_{\mathbf{r}_i}\alpha^*_{\mathbf{r}_i})^2\right) \\ &= C^2(1+|\alpha^{(0)}|^2) \\ &\stackrel{!}{=} 1\end{aligned} \tag{2.23}$$

so that

$$C=\frac{1}{\sqrt{1+|\alpha^{(0)}|^2}}\,. \tag{2.24}$$

For the derivation of Eq. (2.23), I used Eqs. (1.42a), (2.11), and (2.21).

In Chap. 5, the action of a combined displacement operator (cf. Sec. 1.3.1)

$$D(\{\alpha_\mathbf{r}\})=\prod_{\mathbf{r}_i}D_{a_{\mathbf{r}_i}}(\alpha_{\mathbf{r}_i}) \tag{2.25}$$

on the single-photon-added coherent state (2.22) is exploited, i. e.,

$$\begin{aligned}D^\dagger(\{\alpha_\mathbf{r}\})|\Psi\rangle &= C\sum_\mathbf{r}\varphi_\mathbf{r}D^\dagger(\{\alpha_\mathbf{r}\})a^\dagger_\mathbf{r}D(\{\alpha_\mathbf{r}\})D^\dagger(\{\alpha_\mathbf{r}\})|\{\alpha_\mathbf{r}\}\rangle \\ &= C\sum_\mathbf{r}\left(\varphi_\mathbf{r}a^\dagger_\mathbf{r}|0\rangle+\varphi_\mathbf{r}\alpha^*_\mathbf{r}|0\rangle\right) \\ &= C\sum_\mathbf{r}\varphi_\mathbf{r}a^\dagger_\mathbf{r}|0\rangle+C\eta|0\rangle\,,\end{aligned} \tag{2.26}$$

where again all superscripts are suppressed and $\eta=\sum_\mathbf{r}\varphi_\mathbf{r}\alpha^*_\mathbf{r}$. In analogy to Eq. (1.48), Eq. (2.26) represents a superposition of the vacuum state and a single-photon wave function.

2.3.2 Atomic Excitation

So far, only initial states of the radiation field were introduced. In the context of spontaneous emission in Chap. 6, however, the radiation field is initially in its vacuum state and, in order to monitor the emission dynamics of a single two-level system, the initial condition

$$|\Psi\rangle=|\uparrow\rangle \tag{2.27}$$

is used (cf. Sec. 1.3.2).

2.4 Time Evolution and Numerics

All subsequent numerical studies rely on a numerical solution of the Schrödinger equation

$$\mathrm{i}\frac{\partial}{\partial t}|\Psi\rangle = H|\Psi\rangle \tag{2.28}$$

and, if the dynamics of open systems is taken into account, the incorporation of stochastic quantum jumps (cf. Sec. 1.3.4). For a time interval Δt during which no quantum jumps occur, the state vector of the system at time t is propagated to a later time $t + \Delta t$ with the help of the time-evolution operator according to

$$|\Psi(t + \Delta t)\rangle = \mathrm{e}^{-\mathrm{i}H\Delta t}|\Psi(t)\rangle\,. \tag{2.29}$$

Equation (2.29) is valid for all systems studied in this thesis since only time-independent Hamiltonians H are considered. The numerical time evolution is carried out using Krylov-subspace based operator-exponential techniques [109–111], which only rely on the implicit action of the Hamiltonian on a given state and never explicitly need the full Hamiltonian matrix, thus being well-suited for sparse problems. For details on the numerical scheme in the context of few-photon propagation, see Refs. [61, 108].

Although the Schrödinger equation (2.28) is a linear differential equation, it can lead to a nonlinear system as is, for instance, the case in Chap. 5 for coherent and photon-added coherent states. In such situations, the resulting effective equations of motion are integrated in time by means of a standard Runge-Kutta solver. In Chaps. 3–7, the discussion of numerical issues is in general omitted since—in my opinion—this would represent an interruption of the train of thoughts. See Appendix C for numerical details and parameters of all simulations presented in this thesis.

From a conceptual point of view, a wave-function based method in Fock space, such as the one used throughout this thesis, is only applicable if the Hilbert space is block diagonal with respect to different excitation numbers, i. e., for Hamiltonians which conserve the total number of excitations (cf. Eqs. (1.64), (1.73), and (2.9)). Only then, the problem can be subdivided into, for instance, the single- and the two-particle sector of the Hilbert space.

As far as the problem of finite system sizes is concerned, simulations have to be stopped before a noticeable amount of excitation reaches the system's boundaries in order to avoid artificial reflections. Admittedly, this statement is rather imprecise and it depends on the actual problem. Since all processes are monitored in real space, one can already gain an "intuitive feeling" for when the simulation needs to be stopped. It is important that no excitation reflected by the system's hard-wall boundaries interferes with the subsystem which is monitored. For instance, if the excitation of an atom is monitored, radiation may artificially be reflected by the boundaries but it must not return and interfere with the atom. If, furthermore, the pulse shape would be of interest, the simulation has to be stopped before the pulse's tail reaches the boundaries. For all results presented in this thesis, the distribution of

the time evolution of the occupation numbers in real space, $\langle a_{\mathbf{r}}^{\dagger} a_{\mathbf{r}} \rangle$, was monitored to assure there is no artificial corruption of the dynamics.

For the example of a pulse whose center propagates at group velocity v_{g} along a one-dimensional system of length L, the so-called transit time

$$\tau_{\mathrm{trans}} \sim \frac{L}{v_{\mathrm{g}}} \tag{2.30}$$

sets the scale of the maximal simulation time. This time, however, only serves as an estimate and depends on the actual problem. Furthermore, absorbing boundaries are taken into account in Chap. 6 (cf. Sec. 1.3.4) so that the simulation time can be enhanced.

Chapter 3
3 Waveguide Quantum Optics

This chapter provides an introduction to the field of waveguide quantum optics. After a short motivation of the term "waveguide quantum optics", I briefly review the field based on existing theoretical works. I introduce the prototypical model of a single two-level atom in a tight-binding waveguide and discuss its properties in the context of eigenstates as well as single- and two-photon transport. To complete the introduction, I mention related works in which I have been involved, followed by an outlook on the following chapters of this thesis.

3.1 Introduction to Waveguide Quantum Optics

There exists no rigorous definition for the term "waveguide quantum optics" or "waveguide quantum electrodynamics". Therefore, the following discussion of the scope of the research field "waveguide quantum optics" remains to be a personal opinion. Systems where a single or a few modes of the radiation field are coupled to a single emitter, a few, or an ensemble of emitters are investigated in the related field of "cavity quantum electrodynamics" (cavity QED). In this context, the Jaynes-Cummings [56, 57], the Rabi [53], and the Dicke model [58, 59] are commonly used to capture the essential physical mechanisms.

When compared to cavity QED, the crucial attribute of waveguide quantum optics is that the radiation field is described as a continuum (or in the case of finite and/or discrete systems as a quasi-continuum) of modes. Systems in which the propagation of photons is effectively reduced to one spatial dimension are of particular interest because the photon dynamics can be strongly dominated by interference effects. Such a one-dimensional continuum of electromagnetic modes is usually associated with a waveguide, hence, the term "waveguide quantum optics". For instance, physical realizations include artificial atoms in Photonic Crystal defect structures [4], silicon-based on-chip circuitry [3, 6, 112], and microwave photonics in the context of superconducting circuits [18, 49]. The detailed understanding of quantum-mechanical wave packet dynamics together with the characterization of the emission dynamics of single emitters in such systems are typical questions posed in the field of

waveguide quantum optics. Even though studying the transport in electronic systems seems to be similar at first sight, the behavior of photonic systems fundamentally differs from their "fermionic counterparts" due to the absence of a Fermi surface.

The specifics of the radiation field being described as a continuum of modes does not necessarily restrict physical realizations to systems which are effectively one-dimensional. Even though the prototypical models which are being studied in the field of waveguide quantum optics are predominantly motivated by photonic realizations, waveguide quantum optics can be—at least in my opinion—understood in a broader sense, including other areas of solid-state physics as well. To name just one example, by regarding the dynamics of bosons in general, the propagation of magnons in spin chains (cf. Chap. 7) also represents a problem of waveguide quantum optics.

This chapter is structured as follows. In Sec. 3.2, I start by providing a brief review of existing theoretical works in the context of the photon dynamics in a waveguide with a single atom and variations thereof. After that, I introduce and discuss the Hamiltonian of a tight-binding waveguide locally coupled to a single two-level atom in Sec. 3.3. This includes the identification of scattering states as well as atom–photon bound states in the single-particle spectrum and their influence on the single- and two-photon transport properties. In Sec. 3.4, I briefly mention related studies to complete the introduction to the field of waveguide quantum optics. I conclude the chapter in Sec. 3.5 where I also give an outlook on the following chapters of this thesis.

3.2 A Brief Review of the Field

In this section, I briefly review[1] the field of waveguide quantum optics. I restrict the discussion to theoretical works focusing on photon dynamics in a one-dimensional waveguide coupled to a single or a few emitters. The wave propagation in Jaynes-Cummings-Hubbard systems [65, 113] or Dicke-like setups [114, 115] is not addressed in the following. Even though I carefully selected the references, I do not claim this review to be exhaustive.

A discussion of the scientific terms used, e. g., "tight-binding waveguide" or "continuous waveguide", is given in Sec. 3.3. For now, it is sufficient to point out that the terms "tight-binding waveguide" and "discrete model" are used interchangeably as well as "continuous waveguide" and "continuum model".

The Years 2005–2007

In 2005, Fan and Shen investigated the transport of a single-photon in a one-dimensional waveguide coupled to a single two-level atom [60]. In their description, the waveguide mode

[1] I consider publications until April 2012. The order is chronological (up to the month) as they appeared in peer-reviewed journals. In case only a preprint exists, the date of publication of the preprint is taken into account. Furthermore, I also took diploma and master's theses I was aware of into account.

is assumed to exhibit a linear dispersion relation without cutoff, which makes the problem amenable to a field-theoretical description of the Hamiltonian in terms of left- and right-moving photons. Furthermore, the authors assume the atom–photon coupling to be local in real space. The main result of Ref. [60] states that the two-level atom behaves as an energy-dependent mirror. Consequently, a single frequency, i. e., a single plane-wave component, can be reflected completely if its corresponding energy is on resonance with the atomic transition. In addition, the authors propose the use of a single-photon transfer matrix in order to study setups of a chain of atoms or an atom surrounded by dielectric mirrors in a waveguide. As demonstrated in the following, the system investigated by Shen and Fan turned into an essential model—into one of the "hydrogen atoms"—of waveguide quantum optics. The results of Ref. [60] were adapted by the same authors to the case of a cooper pair box in a transmission line [116].

A considerable breakthrough with surprising results beyond the single-particle description was achieved by Shen and Fan in 2007. They analytically solved the problem of two-photon transport in the system described above [117, 118]. A consequence of the fact that the atom can absorb at most only one photon at a time is a strongly correlated two-photon transport, resulting in an effective, spatial attraction or repulsion of photons, the redistribution of the individual photon's energy under the constraint of global energy conservation, and the emergence of so-called photon–photon bound states. The latter is a two-particle state which decays exponentially as a function of the relative coordinate of the two photons (cf. Sec. 3.3.3).

The Year 2008

The work by Shen and Fan on the single-photon transport can be regarded as a precursor to a variety of different works on that particular kind of systems as well as on variations thereof. For instance, Fabry-Pérot-like effects were investigated by terminating a waveguide with a perfect mirror and a two-level system [119]. In addition to the field theoretical description of Shen and Fan, the single-particle scattering solutions of the discrete model were investigated by Zhou *et al.* [120]. The authors calculated reflection and transmission coefficients for a single-photon plane wave in a one-dimensional tight-binding waveguide coupled to a two-level system. Furthermore, it was shown that the results of Shen and Fan can be obtained by performing the continuum limit. The discrete model, which could be regarded as the other "hydrogen atom" of waveguide quantum optics, was then also investigated in various contexts. Gong *et al.* studied aspects of electromagnetically induced transparency for a Λ-type three-level atom [121] and Zhou discussed the properties of a potential "super cavity" formed by two atoms in a waveguide [122].

The Year 2009

In 2009, Shen and Fan presented studies on a single photon in a waveguide coupled to either a cavity containing an atom [123] or a whispering gallery mode resonator with an atom [124]. In the latter case, the resonator was modeled by means of clock- and anti-clockwise propagating photons. Shi *et al.* applied field-theoretical techniques [125] and complemented the work of Shen and Fan on the correlated two-photon transport. In the context of the discrete system, Jing *et al.* pointed out the existence of localized single-particle bound states [126]. The energy of such atom–photon bound states lies in the band gap of the waveguide's dispersion relation (cf. Sec. 3.3.1). These state are dressed eigenstates, i. e., of polaritonic nature, and occur, for instance, in the context of spontaneous emission (cf. Chap. 6). Furthermore, they played a central role in my diploma thesis [63], where I numerically investigated the transport of few-photon Fock states in a tight-binding waveguide coupled to a two-level system. Since atom–photon bound states are single-particle states, one can resort to the results obtained in the context of the single-particle properties of electronic systems [93].

More insights into the transport properties of a single photon were given by Lia *et al.*, who proposed to control the transmittance by tuning the frequency of one or two cavities that form the discrete waveguide [127]. Numerical techniques capable of describing the dynamics of few-photon wave packets were published in Ref. [108], which is also the groundwork for the numerical scheme utilized in this thesis (cf. Chap. 2). As a complement to Ref. [121], Tsoi and Law addressed the single-photon transport through a finite chain of Λ-type three-level atoms in a tight-binding waveguide [128].

The Year 2010

The year 2010 was characterized by a vast amount of publications in the field of waveguide quantum optics. For instance, it was pointed out that the few-photon nonlinearity realized by the two-level atom could be exploited to excite spatially localized atom–photon bound states, resulting in interaction-induced radiation trapping in a tight-binding waveguide [62] (cf. Sec. 3.3.3). Further studies on the single-photon transport in the continuous system were carried out by Yu and Fan, who introduced a harmonically driven cavity as another means to control photon transport [129], and by Zang and Yang, who further addressed Fabry-Pérot-like behavior in the context of different setups of two cavities side-coupled to a waveguide [130].

Based on the two-photon results of Shen and Fan [117, 118], Roy proposed a "few-photon optical diode" for a two-level atom asymmetrically coupled to the waveguide [131]. An in-depth discussion of the single-photon transport in a continuous waveguide coupled to a single driven or undriven V- or Λ-type three-level system was given by Witthaut *et al.* [132]. Focusing on the two-particle transport in the tight-binding waveguide, Becker analyzed the influence of a few two-level systems [133], whereas Stawiarski utilized path-integral techniques in order to describe the effect of radiation trapping in the language of condensed

matter theory [134]. Blancon employed the computational scheme outlined in Ref. [108] to the problem of microwave photon propagation in superconducting circuitry [50] (cf. Sec. 3.4). Shen and Fan continued to explore the propagation of a single photon in a waveguide coupled to a ring resonator containing an atom by deriving the parameters needed to achieve zero single-photon transmittance [135]. The interesting aspect of achieving full inversion of an atom by a single-photon pulse, which is related to the inverse problem of spontaneous emission, was addressed by Raphaeli *et al.* [136].

An important result is given by the fact that the two-photon transport in a waveguide with a local Kerr nonlinearity shares many properties with the transport through a two-level system. Specifically, Liao and Law proposed such a system as another candidate in which features such as the emergence of photon–photon bound states in analogy to Refs. [117, 118] can occur [74]. A significant step towards the general many-body solution of the original waveguide–atom system as introduced by Fan and Shen was given by Zheng *et al.* [137], who reported the existence of "multiphoton bound states" [137]. A technical aspect of photon scattering in a continuum of modes with a linear dispersion relation without cutoff was developed by Fan *et al.*, who adapted an input-output formalism to the scattering problem [138]. Hach *et al.* studied the single-photon solutions in the continuum model for the case of a Jaynes-Cummings cavity in a waveguide [139] similar to Refs. [123, 124].

The Year 2011

In 2011, Roy proposed a scheme to control photon–photon bound states by virtue of a driven Λ-type three-level system [140]. Details on the mechanism of interaction-induced radiation trapping occurring in the discrete system were published in Ref. [61], which is an extension to Ref. [62]. As a complement to Ref. [131], Yan *et al.* studied in detail the single-photon transport through a two-level atom asymmetrically coupled to a continuous waveguide [141]. An extensive study of the single-photon wave packet dynamics through driven and undriven three-level systems was carried out by Martens [142]. The idea of going beyond the two-level description led to a proposal of Zheng *et al.* to exploit N-type four level systems to generate and further control the propagation of photon–photon bound states [143]. Similarly, Raphaeli *et al.* studied the effect of a pair of non-identical atoms on the emergence of photon–photon bound states [144]. Shi *et al.* extended earlier works on the two-photon transport in the continuous waveguide to the case where the scatterer is a Jaynes-Cummings cavity [145].

The Year 2012 (until April)

In 2012, Yan *et al.* proposed a cavity containing a driven four-level system in a waveguide as an alternative scheme to control the photon correlations mediated by the scatterer [146]. The input-output theory as adapted by Fan *et al.* in Ref. [138] was applied to the problem of resonance fluorescence. Specifically, the authors calculated the spectrum of a coherent state scattered by a two-level atom in a continuous waveguide and found features such as the

Mollow triplet [147]. In Ref. [148], which is a direct application of the results from Ref. [60], Cheng and Song propose a pair of quantum dots as a means to control the transport of single surface plasmons. A complement to Ref. [134] is given by the work of Pletyukhov and Gritsev, who developed a general formalism for the calculation of the many-photon transport properties [149]. Their method is restricted to a one-dimensional continuum of waveguide modes exhibiting a linear and unbounded dispersion relation. Concerning the single-photon properties, Bradford *et al.* addressed mechanisms of single-photon frequency conversion in the context of a three-level atom embedded in the continuous waveguide [150, 151]. The problem of stimulated emission was investigated by Raphaeli and Fan in one of its most basic forms—a single photon incident on an excited atom in a waveguide [152]. An interesting proposal of converting coherent light into nonclassical radiation was given by Zheng *et al.* The authors showed that the many-body photon states, which can emerge in a waveguide coupled to a Λ-type three-level or an N-type four-level atom, can be exploited to generate a source of nonclassical light [153]. Moeferdt analyzed how the technique of full-counting statistics can be adapted to pulse propagation in the context of waveguide quantum optics [154].

3.3 A Single Two-Level Atom in a One-Dimensional Waveguide

In the following, I focus on a simplified but not oversimplified model system of a single two-level atom in a one-dimensional waveguide. The aforementioned model of a tight-binding waveguide captures physical features such as a nonlinear dispersion relation, the regime of slow light, and a band gap. These features cannot be accounted for in a model with a linearized dispersion relation without cutoff. A one-dimensional tight-binding model suggests experimental realizations such as coupled-resonator optical waveguides [11–13] or superconducting transmission line resonators [19–21]. However, if the underlying physical system is not discrete, a tight-binding formulation can serve as an approximation to the actual dispersion relation around a certain operating wavelength.

In this section, I introduce the Hamiltonian of a single two-level atom in a tight-binding waveguide. I discuss its single-particle eigenstates and summarize the single- and two-photon transport properties. For the latter, I especially explain the mechanism of interaction-induced radiation trapping, followed by a discussion about the existence of photon–photon bound states.

3.3.1 The Hamiltonian and its Single-Particle Eigenstates

Based on Eq. (2.5), the Hamiltonian of a two-level atom locally coupled to a single band tight-binding waveguide reads (cf. Fig. 3.1(a))

$$H = \sum_x \omega_0 a_x^\dagger a_x - J \sum_x \left(a_{x+1}^\dagger a_x + a_x^\dagger a_{x+1} \right) + \frac{\Omega}{2} \sigma_z + V \left(a_{x_0} \sigma^+ + a_{x_0}^\dagger \sigma^- \right) . \tag{3.1}$$

Here, ω_0 is the eigenenergy of a single resonator. The nearest-neighbor hopping amplitude J is determined by the overlap of the electromagnetic mode profiles of adjacent resonators (cf. Eq. (1.34)). The assumption of a local atom–photon coupling V implies its independence on the photon momentum (cf. Eq. (2.8b)). The site to which the single two-level atom is coupled is denoted by the index x_0. According to Eq. (2.6), the tight-binding description is equivalent to a waveguide dispersion $\epsilon_k = \omega_0 - 2J\cos(k)$. For convenience, I shift the middle of the waveguide band to zero so that

$$\epsilon_k = -2J\cos(k)\,, \tag{3.2}$$

which corresponds to setting $\omega_0 = 0$ in the Hamiltonian. Note that the eigenenergy of the free waveguide is bounded by $\pm 2J$, leading to a bandwidth of the dispersion relation of $4J$. Dimensionless units according to Appendix A are employed such that $\hbar \equiv 1$ and the lattice constant for the one-dimensional lattice is unity, i. e., $\ell = a \equiv 1$.

The Hamiltonian (3.1) is the prototypical model to which I referred in Sec. 3.2 as one of the "hydrogen atoms" of waveguide quantum optics. It is of central importance in this thesis. A field-theoretical continuum model can be obtained by assuming a linearized dispersion relation without cutoff and the introduction of field operators for right- and left-moving photons [60, 125].

To obtain the single-particle eigenstates of Hamiltonian (3.1), one has to solve the eigenproblem $(H - E)|\Psi\rangle = 0$ with $|\Psi\rangle = \sum_x \varphi_x a_x^\dagger |0,\downarrow\rangle + e|0,\uparrow\rangle$. As shown in Ref. [120] and in Appendix D, this leads to a set of coupled equations for the amplitudes φ_x and e, which can be combined to

$$0 = -E\varphi_x - J\left(\varphi_{x+1} + \varphi_{x-1}\right) + \frac{V^2}{E-\Omega}\varphi_{x_0}\delta_{xx_0}\,. \tag{3.3}$$

A complete basis of the single-particle Hilbert space consists of two classes of solutions. First, scattering eigenstates of the form

$$\varphi_x = \begin{cases} \mathrm{e}^{\mathrm{i}kx} + r_k \mathrm{e}^{-\mathrm{i}kx} & x < x_0 \\ \varphi_{x_0} & x = x_0 \\ t_k \mathrm{e}^{\mathrm{i}kx} & x > x_0 \end{cases} \tag{3.4}$$

with $E = -2J\cos(k)$ determine the single-photon transport properties through the reflection and transmission amplitudes r_k and t_k (cf. Sec. 3.3.2). Second, an ansatz of the form

$$\varphi_x \propto \mathrm{e}^{-\kappa|x-x_0|} \tag{3.5}$$

with $E = -2J\cosh(\kappa)$ yields the quartic equation

$$\eta^4 + \frac{\Omega}{J}\eta^3 + \left(\frac{V}{J}\right)^2 \eta^2 - \frac{\Omega}{J}\eta - 1 = 0 \tag{3.6}$$

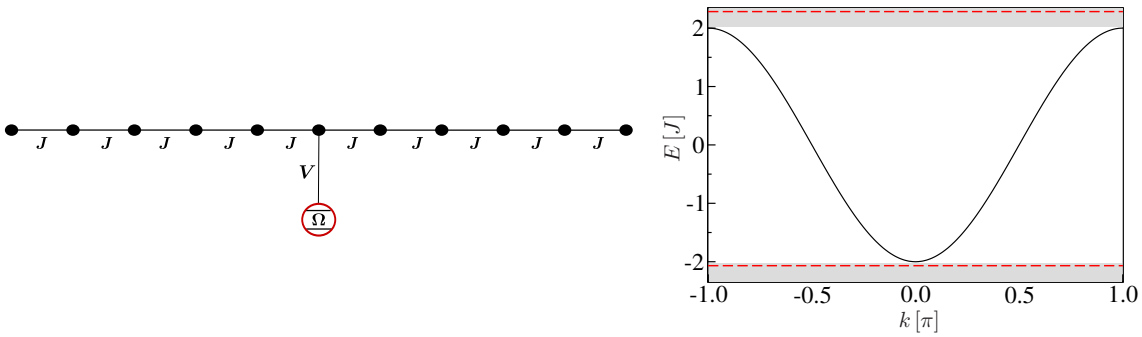

(a) (b)

Figure 3.1: Schematic sketch of a two-level atom in a tight-binding waveguide (a) and the corresponding single-particle eigenenergies (b).
The single-particle spectrum consists of two parts. The (quasi-)continuum of scattering states includes energies $E = \epsilon_k = -2J\cos(k)$, where the photon momentum is from the first Brillouin zone. In addition to that, there is one photon–atom bound state each above the upper and below the lower band edge. The gray shaded region indicates the band gap of the free waveguide. The red dashed lines denote the atom–photon bound states' energies obtained from Eq. (3.6) with $\Omega = \sqrt{2}J$ and $V = J$. Note that the x-axis (momentum) only applies to the continuum of scattering states.

for the variable $\eta \equiv \mathrm{e}^{-\kappa}$ (cf. Ref. [61]). This equation determines the eigenenergy of atom–photon bound states. Such states are spatially localized excitations of polaritonic nature—dressed states. In other words, a fraction of spatially localized radiation is accompanied by a finite occupation of the atom's excited level. Equation (3.6) supports exactly two physical solutions for which the ansatz (3.5) remains normalizable. For any finite values of Ω/J and V/J, there exists always one atom–photon bound state each below the lower and above the upper band edge. Figure 3.1(b) depicts the complete single-particle spectrum of the Hamiltonian (3.1).

3.3.2 Single-Photon Transport

The problem of single-photon transport was solved analytically by Zhou *et al.* in terms of monochromatic plane waves [120]. The ansatz (3.4) leads to a reflectance (cf. Ref. [120] and Appendix D)

$$|r_k|^2 = \frac{V^4}{V^4 + 4J^2\sin^2(k)\cdot(\epsilon_k - \Omega)^2}\,. \tag{3.7}$$

Hence, the two-level system can be regarded as being an energy-dependent mirror which can completely suppress the transmission of a single frequency component, provided that

the resonance condition $\epsilon_k = \Omega$ is fulfilled. For the propagation of a single-photon pulse, however, the atom can only be regarded as an "almost perfect mirror" since the resonance condition only holds for one of the pulse's Fourier components [108].

Here, the atom–photon bound states are irrelevant since they do not overlap with the initial condition of a photon in the waveguide and the atom being in its ground state. They are energetically separated from the continuum of waveguide modes. Nonetheless, in the context of spontaneous emission, which is also a single-particle problem, atom–photon bound states can play a crucial role (cf. Chap. 6).

3.3.3 Two-Photon Transport

In comparison to the single-photon problem, the two-photon transport turns out to be much more demanding, both numerically and analytically. To the best of my knowledge, an analytical solution of the two-particle eigenproblem for Hamiltonian (3.1) in terms of wave functions of the form

$$|\Psi\rangle = \sum_{x_1 x_2} \Phi_{x_1 x_2} a_{x_1}^\dagger a_{x_2}^\dagger |0,\downarrow\rangle + \sum_x e_x |0,\uparrow\rangle \tag{3.8}$$

has not been derived yet. The complexity of the problem arises due to several reasons. First, as demonstrated in Chap. 2, the dimension of the Hilbert space grows exponentially with the number of particles. Second, the two-level atom can at most absorb one photon at a time, representing a few-photon nonlinearity (cf. Eqs. (1.66)). This induces correlations between the photons so that the two-particle solution is not just given as the direct product of single-particle solutions. Third, the existence of atom–photon bound states adds another difficulty to the problem which does not occur in the case of a waveguide with an unbound dispersion relation. In the studies of Shen and Fan [117, 118], the linearized dispersion relation without cutoff effectively removes the atom–photon bound states from the accessible Hilbert space.

However, numerical studies explicitly demonstrated the importance of the atom–photon bound states for the two-photon dynamics in a system described by Hamiltonian (3.1). This issue is addressed below.

Interaction-Induced Radiation Trapping

With respect to global energy conservation, an initial state of two photons propagating in the waveguide can in principle excite a single-particle atom–photon bound state. However, this requires a nonlinear scattering mechanism such as it is provided by the two-level atom. According to Eqs. (1.66), the two-level atom can be regarded as an oscillator with infinite anharmonicity. The term $\Omega b^\dagger b + U b^\dagger b(b^\dagger b - 1)$ is equivalent to a two-level description in the limit $U \to \infty$, where double occupation of the atomic site becomes prohibited. This few-photon nonlinearity represents an effective photon–photon interaction mediated by the atom. It is absent in the case of a harmonic oscillator ($U = 0$).

Numerical simulations demonstrated that the few-photon nonlinearity provides a mechanism for in-band photons to excite the localized atom–photon bound states and, therefore, trap radiation [61–63]. This process of interaction-induced radiation trapping can be understood as follows. Once one of the two impinging photons excites the two-level atom, the second photon sees a modified and (partly) saturated atom. By virtue of the multi-particle scattering process provided by the nonlinear U-term, the second photon is scattered into the atom–photon bound states. After the scattering, the atom–photon bound states are again decoupled from the continuum of waveguide modes. Hence, the excited atom–photon bound states cannot decay. As shown in Sec. 3.3.1, they are eigenstates of the Hamiltonian (3.1). The polaritonic nature of the atom–photon bound states implies that a fraction of the radiation remains trapped in the spatial vicinity of the atom, which is accompanied by a partial occupation of the atom's excited level.

To trap a considerable amount of radiation, the system parameters and the properties of the initial photons need to be optimized [61–63]. For instance, since the atom–photon bound states' energies are in the band gap, the initial photon momenta should be close to one of the two band edges. However, a propagation of the wave packets without detrimental effects from the strong group-velocity dispersion near the band edge of the cosine-dispersion relation must still be possible. An initial carrier wavenumber of $k_0 = 3\pi/4$ has proven to be a reasonable compromise [61–63]. In that situation, only the atom–photon bound state from the upper band gap is considerably excited (cf. Fig. 3.1(b)). In addition to that, the detuning between each photon and the atom should be zero. In other words, efficient radiation trapping requires a resonant atom–photon interaction. Furthermore, in the tight-binding waveguide, the atom–photon coupling V should be of the same order as the nearest-neighbor hopping constant J, i. e., $V/J \sim 1$.

The studies in Refs. [61–63] also addressed the issue of controlling the amount of trapped radiation by changing the detuning of one of the two photons or by varying the initial spatial separation of the photon wave packets. Moreover, it was demonstrated that the effect of interaction-induced radiation trapping also occurs in waveguides which exhibit more complicated dispersion relations. Unlike in models of a waveguide with an unbound dispersion relation, the existence of a cutoff in the density of photonic states therefore introduces the interaction-induced effect of radiation trapping, which, consequently, does not exist in the studies by Shen and Fan [117, 118]. However, their studies reveal that the atom still induces correlations between two photons, leading to the emergence of photon–photon bound states. To date, an analytical solution of the two-photon eigenproblem of Hamiltonian (3.1) in terms of wave functions has not been derived yet. Therefore, the question whether photon–photon bound states also exist in the discrete model remains to be open. Below, I present a numerical study which addresses this issue.

On Photon–Photon Bound States

In the following, I numerically address the question of whether photon–photon bound states as found by Shen and Fan for the case of a waveguide with an unbound dispersion relation also exist in the tight-binding model. The concept of two-body bound states can actually be found in various contexts such as "dimer states" in the Bose-Hubbard model [155, 156], "polariton–polariton bound states" in the Jaynes-Cummings-Hubbard model [157], or bound pairs of magnons in the Heisenberg model (cf. Chap. 7). The crucial difference between these examples and Hamiltonian (3.1) is that the two-level atom represents a local nonlinearity in contrast to systems with spatially uniform nonlinearities.

As a first step, I identify the parameter regime in which the results for the waveguide with the unbound dispersion relation as obtained by Shen and Fan [117, 118] can be compared to the tight-binding model. This is achieved by matching the fundamental energy scales. In the model by Shen and Fan, there is no energy scale associated with the bandwidth of the dispersion relation since it is unbound. However, the authors set the group velocity to unity in Refs. [117, 118]. In the lattice model, the group velocity can be obtained from the derivative of the cosine-dispersion relation $\epsilon_k = -2J\cos(k)$ with respect to the momentum k, i. e., $v_g = 2J\sin(k)$. I therefore adjust the group velocity to the value used by Fan and Shen and I furthermore demand a vanishing group-velocity dispersion at a specific wavenumber k_0, which is the property of a linear dispersion. Consequently, $v_g = 1$ and $\partial^2\epsilon_k/\partial k^2|_{k=k_0} = 0$ yield $J = 0.5$ and $k_0 = \pm\pi/2$. Thus, initial states in the lattice model should only be from the linear regime of the dispersion relation (around $k_0 = \pm\pi/2$). Because of $J = 0.5$, the bandwidth of the free waveguide's dispersion relation is $4J = 2$.

Another important point when comparing the field-theoretical results of Shen and Fan [117, 118] to numerical findings in the tight-binding model is to understand the properties of wave packets of finite width. The transport properties of stationary plane waves can be approximately mimicked by assuring that the pulses are sufficiently broad in real space so that they only cover a narrow spectral window in momentum space. This requires sufficiently large computational domains.

The strategy to identify possible signatures of a photon–photon bound state in the discrete lattice model is as follows. First of all, the results of Shen and Fan from Refs. [117, 118] need a closer inspection. Two photons incident from the left end of the waveguide are scattered into a two-photon out-state which consists of three parts. They represent the situations in which both photons are reflected, one is reflected and one is transmitted, and both are transmitted. The wave function for the latter case reads [118]

$$t_2(x_r, x_c) = \frac{\sqrt{2}}{2\pi}\mathrm{e}^{\mathrm{i}Ex_c}\left(\bar{t}_k\bar{t}_p\cos(\Delta x_r) - \frac{\Gamma^2}{4\Delta^2 - (E - 2\Omega + \mathrm{i}\Gamma)^2}\mathrm{e}^{\mathrm{i}(E-2\Omega)\frac{|x_r|}{2} - \Gamma\frac{|x_r|}{2}}\right), \quad (3.9)$$

where x_r is the relative and x_c the center-of-mass coordinate of the two-particle wave function, respectively. The total energy of both photons is denoted by E and Δ is their energy difference. The single-particle transmission coefficients corresponding to momenta k and p

are $\bar{t}_k$ and $\bar{t}_p$, respectively. The atom–photon coupling strength is V and $\Gamma = 2V^2$. The transition energy of the two-level system is denoted by Ω.

The first term in Eq. (3.9) describes the situation of two photons passing the two-level atom as individual particles, whereas the second term is the photon–photon bound state induced by the correlations mediated by the atom. Note the exponential decay with respect to the relative coordinate. In general, the out-state for two photons being transmitted is thus a superposition of individual particles and the two-particle bound state. However, if the single-particle resonance condition is fulfilled, i. e., $k = \Omega$ in the model by Shen and Fan, the two-level atom acts as a perfect mirror for a single photon of momentum k. Furthermore, without loss of generality, I set the zero of the energy such that $\Omega = 0$ in the model by Shen and Fan.[2] This corresponds to the center of the waveguide band in the tight-binding model. In addition to that, I assume photons with equal momenta for the in-state. Altogether, this leads to $E = \Delta = \bar{t}_k = \bar{t}_p = 0$ and the wave function (3.9) simplifies to

$$t_2(x_r, x_c) = -\frac{\sqrt{2}}{2\pi} \mathrm{e}^{-V^2|x_r|} \,. \tag{3.10}$$

For this special case, the probability of finding two photons being transmitted is solely determined by the photon–photon bound state and can be controlled by the atom–photon coupling V.

Another problem when comparing to time-dependent transport calculations (besides the aforementioned non-monochromaticity) is that scattering states are not normalizable to unity. However, although Eq. (3.10) diverges when it is integrated over all space (i. e., over x_r and x_c), it has a precise physical meaning. First, the probability density is independent of the center-of-mass coordinate. The divergence only stems from the fact that Shen and Fan assumed an infinite system. Second, the integration with respect to the relative coordinate yields a finite result, i. e.,

$$\int_{-\infty}^{\infty} \mathrm{d}x_r |t_2(x_r, x_c)|^2 = \frac{1}{2\pi^2} \cdot \frac{1}{V^2} \propto \frac{1}{V^2} \,. \tag{3.11}$$

Hence, the probability of finding both photons after scattering on the right end of the waveguide is proportional to V^{-2}, which also sets the decay length of the wave function (3.10).

In order to test whether this dependence also holds for the two-photon transport in the tight-binding waveguide, I analyze the wave packet dynamics with the help of the numerical scheme outlined in Chap. 2. As mentioned above, the fixed system parameters for the lattice model are $J = 0.5$ and $\Omega = 0$. The computational domain of the tight-binding waveguide consists of 999 lattice sites and the atom is coupled to site 500. The initial state is the product of two single-particle Gaussian wave functions with equal parameters. As discussed

[2] Setting $\Omega = 0$ does not mean that the atom's levels are degenerate. The transition of the two-level atom couples to the dispersion relation of the waveguide at an energy $\Omega = 0$.

above, the initial carrier wavenumber is $k_0 = \pi/2$, the width of the wave packet is chosen to be $s = 70$, and for the initial center I choose $x_c = 250$ (cf. Sec. 2.3).

After scattering, I compute the quantity

$$P_{\mathrm{RR}} = \sum_{x_1 \in \mathcal{R}} \sum_{x_2 \in \mathcal{R}} \langle a_{x_2}^\dagger a_{x_1}^\dagger a_{x_1} a_{x_2} \rangle \,, \tag{3.12}$$

as a measure for the probability of finding two photons on the right-hand side of the atom (cf. Eq. (1.91), $\mathcal{R} = \{501, \ldots, 999\}$). The projection on two photons automatically excludes any possible contribution from an atom–photon bound state since such is a mixed atom–photon excitation (cf. Sec. 3.3.1).

In addition to that, I account for the non-monochromaticity of the wave packets as follows. Each simulation is re-run for the situation where the two-level system is replaced by a harmonic oscillator, i. e., a bosonic site. This represents the $U = 0$-case in the alternative description of the two-level atom (cf. Eqs. (1.66)). In that case, the many-body solution is given as the direct product of the single-particle solution so that photon–photon bound states cannot be excited. I then subtract the residual transmittance in the case of a harmonic oscillator from the case of a two-level atom, i. e.,

$$\delta P_{\mathrm{RR}} = P_{\mathrm{RR}}^{\mathrm{TLS}} - P_{\mathrm{RR}}^{\mathrm{HO}} \,. \tag{3.13}$$

Here, the individual terms are defined according to Eq. (3.12). As a result, δP_{RR} represents the "purified" probability of finding two photons being transmitted. The dependence of this quantity on the atom–photon coupling V can then finally be compared to Eq. (3.11).

Figure 3.2 displays δP_{RR} as defined in Eq. (3.13), $P_{\mathrm{RR}}^{\mathrm{TLS}}$, and $P_{\mathrm{RR}}^{\mathrm{HO}}$ as a function of V^{-2}. While δP_{RR} seems to be well-represented by a linear fit in the range of $V = 0.3$ ($V^{-2} = 11.11$) to $V = 0.7$ ($V^{-2} = 2.04$), deviations occur for both small and large V. For large V ($V^{-2} \to 0$), the curve flattens because the atom–photon coupling strength becomes comparable to the hopping amplitude J so that the finite bandwidth of the cosine dispersion relation becomes important. In this situation, the nonlinearity of the cosine-dispersion relation and the existence of band edges cannot be neglected. In the limit of small atom-photon coupling ($V^{-2} \to \infty$), the length scale of the photon–photon bound state according to the solution by Shen and Fan (cf. Eq. (3.10)) is not much smaller than the width of the wave packet used in the numerical simulation. In other words, the wave packet does not cover the spatial extent of the photon–photon bound state. This leads to a flattening of the predicted V^{-2}-behavior[3].

To summarize, I compared the results of Shen and Fan on the photon–photon bound state [117, 118] with results from a time-dependent transport simulation in the discrete model. For the specific situation where the transmission of a single (monochromatic) photon is suppressed, the results of Shen and Fan predict a transmittance which scales as V^{-2},

[3] Numerical experiments with wave packets of smaller widths confirm that deviations from the predicted behavior occur at even smaller V^{-2}.

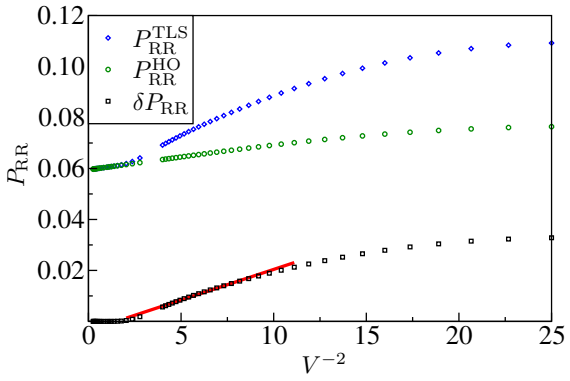

Figure 3.2: Probability of finding two photons after scattering in the right end of the waveguide.
The green circles represent the case of a harmonic oscillator ($P_{\mathrm{RR}}^{\mathrm{HO}}$), whereas the blue diamonds denote the results for a two-level atom ($P_{\mathrm{RR}}^{\mathrm{TLS}}$). The difference of these two quantities according to Eq. (3.13) is denoted by the black boxes. All quantities are plotted as a function of V^{-2}. While a linear fit (solid red line) seems to be reasonable for values $V = 0.3$ ($V^{-2} = 11.11$) to $V = 0.7$ ($V^{-2} = 2.04$), significant deviations occur outside this range (see text for explanation).

where V is the atom–photon coupling strength. According to Shen and Fan, this behavior can be attributed to a photon–photon bound state. Time-dependent transport calculations in the tight-binding model confirm such a dependence, albeit in a certain parameter range only. Deviations occur when either the atom–photon coupling strength becomes comparable to the bandwidth of the cosine-dispersion relation or the predicted spatial extent of the photon–photon bound state is not small compared to the width of the wave packets used in the numerical simulation. These findings suggest the existence of photon–photon bound states in the tight-binding model, provided that the comparison with the results of Shen and Fan is valid. However, unless an analytical solution for the tight-binding model in terms of two-photon wave functions is found, these findings must only be regarded as being a possible signature for the existence of photon–photon bound states rather than being a rigorous proof.

3.4 Related Works

Before the main results of this thesis are discussed in Chaps. 4–7, I briefly present a few excerpts of other related works from the field of waveguide quantum optics. The following studies have been carried out by master/diploma students at the Institut für Theoretische Festkörperphysik with whom I had the opportunity to work together. The presentation is restricted to a qualitative level and I provide the corresponding references for further details.

A Single Photon in Superconducting Circuitry—A Qubit Coupler Device

In his master's thesis, Jean-Christophe Blancon studied microwave photon transport processes through qubit-coupled superconducting metamaterials [50]. By employing the computational scheme of Chap. 2, it was demonstrated that the tunable dispersion relations resulting from superconducting transmission lines with embedded Josephson junctions can be exploited to realize a single-photon switch.

In essence, the switch is based on coupling two photonic bands via a two-level atom. The key ingredient is the tunability of the position of one of the two bands with respect to the other. Such a two-band model can be realized in superconducting transmission lines with embedded Josephson junctions [19, 20]. The studies of Blancon focused on the case where one of the transmission lines exhibits a so-called left-handed dispersion relation, i. e., group and phase velocity have opposite sign. Figures 3.3 and 3.4 summarize the functional principle of the qubit coupler (cf. Refs. [50, 158] for further details).

Single-Photon Transport Through Driven Three-Level Systems—Electromagnetically Induced Transparency

Christoph Martens studied the dynamics of single-photon wave packets in a tight-binding waveguide coupled to a three-level system [142, 159]. In the case of a driven Λ-type three-level system (cf. Fig. 3.5(a)), electromagnetically induced transparency of a single photon wave packet can be realized. Depending on the detunings between the impinging photon and the undriven transition as well as the classical field and the driven transition, the transmittance of the single-photon wave packet can be controlled. Specifically, if both detunings are identical ("two-photon resonance"), the photon is always transmitted even if it is resonant with a transition. Figure 3.5 displays a schematic sketch of the setup as well as an example for the transmittance as a function of both detunings.

A Coherent State Pulse Scattered at a Two-Level Atom—Nonlinear Spectral Features

Julia Werra investigated the dynamics of coherent state wave packets (cf. Sec. 2.3.1) in a tight-binding waveguide coupled to a single two-level atom [161]. In the spirit of a semiclassical description, the resulting equations are essentially the optical Bloch equations coupled to the degrees of freedom of a waveguide. The two-level atom induces a variety of nonlinear effects which determine the features of the scattered pulses' spectrum. Figure 3.6 displays the output spectrum (cf. Sec. 1.3.3) recorded at one lattice site next to the site to which the atom is coupled. The pulse impinges from the left hand side of the atom (carrier wavenumber $k_0 = \pi/2$) and its initial mean photon number $|\alpha^{(0)}|^2$ is varied.

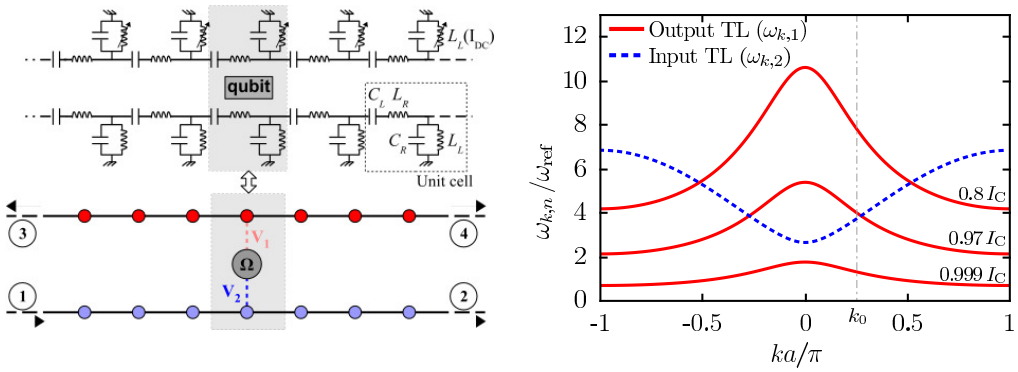

(a) (b)

Figure 3.3: Functional principle of the qubit coupler.
(a) The qubit coupler consists of two transmission lines which are coupled via a two-level atom. The parameters of the lower transmission line ("input line") are assumed to be fixed, whereas the properties of the upper transmission line ("output line") are tunable via a current that is applied on the Josephson junctions. Each transmission line exhibits a right- and a left-handed band [19, 20]. The input line is operated in its right- and the output line in its left-handed band. In the numerical simulation, the transmission lines are modeled as an array of coupled resonators (dots) with a specified dispersion relation. The two-level atom (transition energy Ω) is coupled to one of the resonators of each transmission line (atom–photon couplings V_1 and V_2). (b) The relative position of the output line's dispersion relation (red curves) to the input line (blue curve) can be tuned via a bias current on the Josephson junctions. Courtesy of Jean-Christophe Blancon [50].

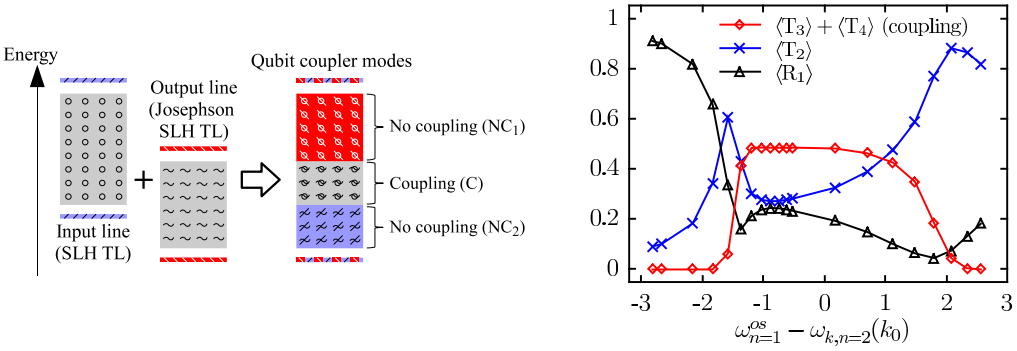

(a) (b)

Figure 3.4: Eigenenergies of the qubit coupler and numerical results.
(a) The single-particle eigenenergies of the combined system result from a hybridization of the two subsystems of transmission line and two-level atom (cf. Sec. 3.3.1). Depending on the relative detuning between the two bands of the transmission lines, the transfer of excitation from the input to the output line can be controlled. (b) As a function of the detuning between the two bands, the amount of excitation which is transferred to the output line (red curve) and remains in the input line (black and blue curves) demonstrates the characteristics of a switch. Courtesy of Jean-Christophe Blancon [50].

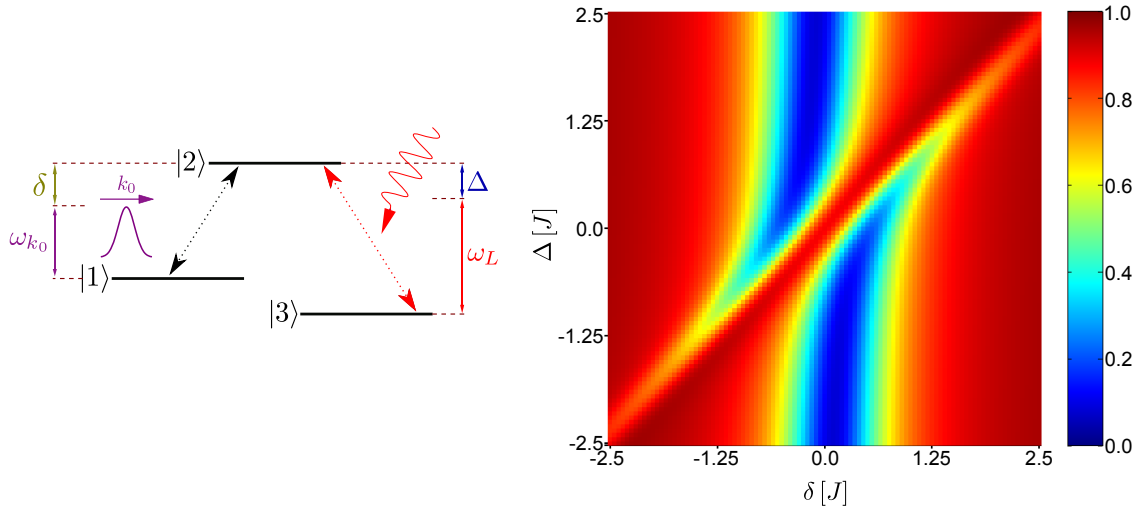

(a) (b)

Figure 3.5: Level scheme of a driven Λ-type three-level system and electromagnetically induced transparency.
(a) The impinging single photon (carrier wavenumber k_0) couples to the undriven transition (levels $|1\rangle$ and $|2\rangle$, detuning δ). In addition to that, a classical time-harmonic driving field (frequency ω_L) induces transitions between the levels $|3\rangle$ and $|2\rangle$. The corresponding detuning is denoted by Δ. (b) The transmittance of a single-photon wave packet ($k_0 = \pi/2$) depends on both detunings δ and Δ. For $\delta = \Delta$, the wave packet is always transmitted even if it is resonant with a transition. Courtesy of Christoph Martens [142].

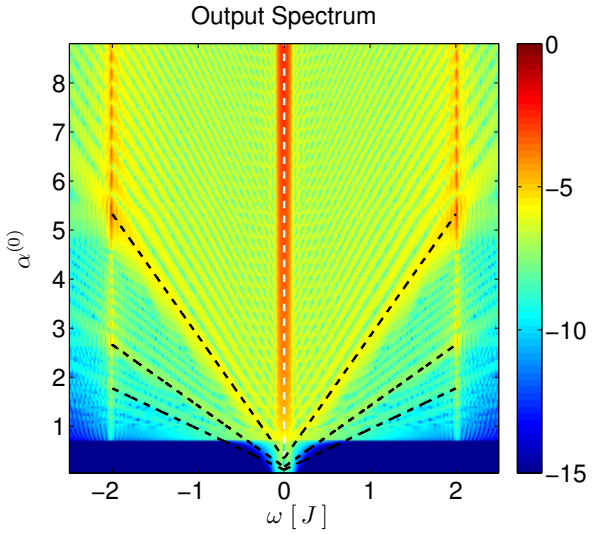

Figure 3.6: Output spectrum of a coherent state pulse scattered at a two-level atom. The nonlinear dynamics induced by the two-level atom results in various spectral features as a function of the initial pulse's amplitude (note that the scale of colorbar is logarithmic). Here, the carrier wavenumber is $k_0 = \pi/2$ and the atomic transition couples to the middle of the waveguide band, i. e., $\Omega = 0$ (cf. Sec. 3.3). The atom–photon coupling is $V = 0.7J$. The single-photon resonance condition is indicated by the vertical dashed line at $\omega = 0$. The transmission of the pulse is suppressed as long as the two-level atom is not significantly saturated ($\alpha^{(0)} \lesssim 0.7$). For higher pulse intensities, self-induced transparency occurs, i. e., spectral components around $\omega = 0$ are transmitted. As a consequence of cascaded nonlinear processes, side bands occur at multiples of the Rabi frequency (which corresponds to the pulse's maximum). The black dashed lines indicate the first three branches. The lowest side band can be understood as the Mollow triplet [160]. Depending on the number of inversion cycles the atom experiences during its interaction with the pulse, additional side bands occur at integer fractions of the Rabi frequency. Moreover, since the transmission spectrum is recorded in the vicinity of the atom, spectral components of the atom–photon bound states are visible slightly above the upper ($\omega > 2J$) and below the lower band edge ($\omega < -2J$). This spectral feature results from an intensity dependent, effective atom–photon coupling strength. See Ref. [161] for further details. Courtesy of Julia Werra.

3.5 Conclusion and Outlook

In this chapter, I gave an introduction to the field of waveguide quantum optics. I first motivated in Sec. 3.1 which classes of systems can be regarded as representing a problem of waveguide quantum optics. On the basis of a one-dimensional waveguide coupled to a single atom, I provided a brief review of existing theoretical works in Sec. 3.2. In Sec. 3.3, I presented the Hamiltonian of a tight-binding waveguide locally coupled to a single two-level atom. I introduced the single-particle eigenstates of the Hamiltonian, which can be separated into scattering states and atom–photon bound states. While the single-photon transport properties are solely determined by the scattering states (Sec. 3.3.2), atom–photon bound states can play an essential role in the transport of two photons (Sec. 3.3.3). Specifically, I discussed the effect of interaction-induced radiation trapping in this context. Moreover, I numerically addressed the question of the existence of photon–photon bound states which are induced by the atom. Finally, I briefly mentioned related studies in which I was partly involved but which are beyond the scope of this thesis (Sec. 3.4).

Undoubtedly, the field of waveguide quantum optics in general has not yet been analyzed in every detail. However, when it comes to the prototypical model of a single atom in a waveguide, many physical properties with respect to few-photon states have already been investigated (cf. Sec. 3.2). Therefore, it is the aim of this thesis to reveal the new physical mechanisms which can occur when the model of a single atom in a waveguide is analyzed from a new point of view and/or slightly modified. Specifically, if the two-level atom is regarded to act as a beam-splitting device, the Hong-Ou-Mandel effect can be exploited to identify effective photon–photon interactions mediated by the atom (Chap. 4). If the two-level atom is replaced by a Kerr nonlinearity, the transport properties of a coherent state can be utilized to control the transmission of the single-photon fluctuations in a single-photon-added coherent state (Chap. 5). Moreover, the single-particle problem of spontaneous emission in a waveguide geometry represents a paradigmatic system for studying non-Markovian dynamics (Chap. 6). Even though at first sight the dynamics of two magnons in a Heisenberg spin chain seems to be rather different from photons propagating in a fiber, interacting magnons actually represent another topic of waveguide quantum optics (Chap. 7). In Chap. 8, I provide a broader and more general outlook for future studies.

Chapter 4

4 The Hong-Ou-Mandel Effect in the Context of Few-Photon Scattering

The Hong-Ou-Mandel effect is studied in the context of two-photon transport in a one-dimensional waveguide with a single scatterer. Depending on the realization of the scatterer and its properties, I calculate the joint probability of finding both photons on either side of the waveguide after scattering. I specifically point out how Hong-Ou-Mandel interferometry techniques could be exploited to identify effective photon–photon interactions which are mediated by the scatterer. The Hong-Ou-Mandel dip is discussed in detail for the case of a single two-level atom embedded in the waveguide, and dissipation and dephasing are taken into account. Parts of this chapter have been published in Ref. [162].

4.1 Introduction

Two photons impinging on a balanced beam splitter from different ports leave the device together in either one of the two output ports. This rather counter-intuitive and inherently quantum mechanical phenomenon, which is known as the Houng-Ou-Mandel effect, was demonstrated experimentally in 1987 [163]. Since then, the topic of two-photon interference turned into a rich and multifaceted field of research. Besides the generalization of the Hong-Ou-Mandel effect to the multi-particle case [164] or the proposal of its fermionic analog [165], it is believed that Hong-Ou-Mandel interference can be successfully exploited in the context of linear-optical quantum computation [5]. Indeed, since photons themselves rarely interact with each other, they seem to be difficult to manipulate and process. The Hong-Ou-Mandel effect, however, solely relies on the statistics of the involved particles and is therefore at the very heart of quantum optics *per se*. To date, photon pairs can be routinely sent through optical fibers [166], and—due to the rapid progress in the fabrications of nanophotonic components—integrated optical waveguiding structures on silicon chips are very promising candidates towards more complicated networks of multimode interference

devices [6]. Furthermore, in the realm of optical metamaterials, the measurement of the Hong-Ou-Mandel dip for magnetic plasmon waves has been reported recently [167].

Of course, these examples only represent a very incomplete and biased selection from the vast amount of publications available on this topic and a well-balanced review of all relevant works is clearly beyond the scope of this chapter. However, the beam splitter in a Hong-Ou-Mandel setup is very often just regarded as an optical component with which one can study the quantum mechanical nature of light by means of coincidence experiments. In the following, I take a slightly different viewpoint and address the question of how the Hong-Ou-Mandel effect can be exploited—used as a probe—to learn something about the properties of the beam-splitting device itself. This question is of direct relevance to the problem of two photons propagating from different ends in a waveguide towards a scatterer, e. g., an artificial atom.

The outline of this chapter is as follows. In Sec. 4.2, I review the quantum mechanical description of a beam splitter, the Hong-Ou-Mandel effect, and its relation to scattering problems. After a qualitative motivation for why the Hong-Ou-Mandel effect can serve as a probe for effective photon–photon interactions, I introduce the types of scatterers which are investigated in this chapter, i. e., a local on-site potential and a two-level atom. I then formulate the corresponding Hamiltonians in analogy to Chap. 3, followed by the beam-splitter conditions which are deduced from the stationary single-particle scattering states. After that, the central quantity of this chapter—the joint probability of finding both photons on either side of the waveguide after scattering—is defined. In Sec. 4.4, I provide a detailed analysis of the Hong-Ou-Mandel dip for the case of a local on-site potential and a two-level atom. As mentioned in Chap. 3, the latter is a saturable absorber and effective photon–photon interactions are essential. In addition, I take the influence of dissipation of T_1-type and dephasing of T_2-type on the Hong-Ou-Mandel dip into account. I conclude the chapter in Sec. 4.5 and give a short outlook on possible future work.

4.2 Fundamentals

In this section, I begin with a review of the quantum mechanical description of a beam splitter and relate it to a scattering problem. I then introduce the Hong-Ou-Mandel effect as a probe for photon–photon interactions, the types of impurities which are investigated, and influencing variables for the Hong-Ou-Mandel dip.

4.2.1 The Quantum-Mechanical Beam Splitter as a Four-Port Device and its Relation to Scattering Problems

A consistent quantum-mechanical treatment of a beam splitter requires its interpretation as a four-port device [35, 163, 168]. Since the "conventional" type of beam splitter does not induce direct interactions between the involved particles—in the majority of cases photons—its single-particle solution can be readily applied to the multi-particle case. With the help of

the scattering matrix formalism, the operators for the input ports 0 and 1 (a_0 and a_1) can be related to the output ports 2 and 3 (operators a_2 and a_3, cf. Fig. 4.1). The transformation reads

$$\begin{pmatrix} a_2 \\ a_3 \end{pmatrix} = \hat{S} \begin{pmatrix} a_0 \\ a_1 \end{pmatrix} , \tag{4.1}$$

where

$$\hat{S} = \begin{pmatrix} t' & r \\ r' & t \end{pmatrix} \tag{4.2}$$

represents the scattering matrix with the corresponding reflection and transmission amplitudes (cf. Ref. [35]). Note that up to this point no statement about the commutation and anticommuation relations of the operators involved is required. This formalism is valid both for bosons and fermions. The reciprocity relations and the conservation of the total probability can be deduced by enforcing the same particle statistics for the operators describing the in- and output ports (cf. Eq. (4.1)).

The general form of the scattering matrix above allows for a description of unbalanced beam splitters which do not equally "split" a single photon into the two output ports. However, the effect which is of central importance in the following—the Hong-Ou-Mandel effect—can be best understood for the case where the beam splitter is balanced in the sense that a single particle scattering off the beam splitter is transferred to one of the output arms with equal probability of 50%.

For simplicity, only photons are considered in the following. The reflected beam undergoes a phase shift of $\pi/2$ and the transmission and reflection amplitudes are $t' = t = 1/\sqrt{2}$ and $r = r' = \mathrm{i}/\sqrt{2}$, respectively [163]. An input state with two photons in different input ports reads

$$|\mathrm{in}\rangle = a_0^\dagger a_1^\dagger |0\rangle , \tag{4.3}$$

where $|0\rangle$ represents the vacuum state. According to Eqs. (4.1) and (4.2), the corresponding output state is

$$\begin{aligned} |\mathrm{out}\rangle &= \frac{1}{2}\left(a_2^\dagger + \mathrm{i}a_3^\dagger\right)\left(\mathrm{i}a_2^\dagger + a_3^\dagger\right)|0\rangle \\ &= \frac{\mathrm{i}}{2}\left(a_2^\dagger a_2^\dagger + a_3^\dagger a_3^\dagger\right)|0\rangle . \end{aligned} \tag{4.4}$$

This remarkable result, which is known as the Hong-Ou-Mandel effect [163], states that two photons impinging on a beam splitter from different input ports leave the device "together" in either one of the output ports. For a balanced beam splitter, the probability of finding one photon in one output arm and the other photon in the other arm is zero. The Hong-Ou-Mandel effect is a true quantum mechanical effect in the sense that it cannot be obtained in the limit of a low-intensity coherent state (cf. Ref. [35]). The tendency of photons to "stick together" is a consequence of the bosonic particle statistics. Fermions behave the opposite way, i. e., the probability of finding two fermions in one output arm is zero.

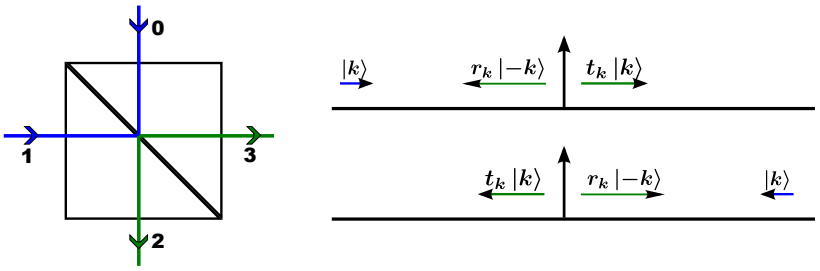

Figure 4.1: Schematic sketch of a beam splitter as a four-port device and its analogy to a scattering problem.

In experiments, one usually faces photonic wave packets of finite width. The initial difference in the distance of both wave packets to the beam splitter determines their overlap at the position of the beam splitter and thus influences the joint probability of both particles leaving the device in the same port. The joint probability of both photons leaving the device in different ports, which can be obtained from coincidence measurements, shows a dip as a function of the difference in the separation to the beam splitter. This dip is known as the "Hong-Ou-Mandel dip" and was first reported in 1987 [163].

Now, I establish a connection between the beam splitter as a four-port device and the scattering of photons at a local impurity. In scattering theory, one usually divides the system into left and right leads, e. g., a waveguide in the context of photons, and a local scattering potential which is placed in the middle. By means of the scattering matrix formalism, a single-particle input state $|\mathrm{in}\rangle = |k\rangle = a_k^\dagger|0\rangle$ of momentum k is transformed into a transmitted and a reflected momentum state according to $|\mathrm{out}\rangle = \hat{S}|\mathrm{in}\rangle$ with

$$a_k^\dagger \to \hat{S}a_k^\dagger = r_k a_{-k}^\dagger + t_k a_k^\dagger\,, \tag{4.5}$$

where r_k and t_k signify the reflection and transmission amplitudes, respectively. For an in-state in the left lead, the wavenumber needs to fulfill $k > 0$, for the right lead $k < 0$.[1] Thus, there are four "ports" in total, namely $k > 0$ and $k < 0$ for the left and the right lead, respectively (cf. Fig. 4.1). It is assumed that the magnitude of the momentum, $|k|$, is unchanged here. In other words, only elastic and time-reversal-symmetric single-particle scattering processes are considered, which is in accord with the Hamiltonians introduced in Sec. 4.2.3.

The analogy to the aforementioned balanced beam splitter is completed by demanding $|r_k|^2 = |t_k|^2 = \frac{1}{2}$ which—strictly speaking—can only be achieved for a single frequency since beam splitters are dispersive optical elements.

[1] This argument only holds for a so-called right-handed dispersion relation, for which group velocity and wavenumber have the same sign. As stated in Sec. 4.3, I assume $J > 0$ throughout the whole chapter.

4.2.2 Hong-Ou-Mandel Interferometry as a Probe for Photon–Photon Interactions

In many cases, the equations of motion for a single-photon state and a coherent state are identical or describe—at least approximately—the same dynamics in the low-intensity limit. Thus, although the equations for a single photon are deduced from the Schrödinger equation, they do not provide "more physics" than the corresponding equations for the coherent state. Of course, the evolution is always given by the Heisenberg equations of motion (or the Schrödinger equation), for either single-photon or coherent states. However, "true" quantum mechanical effects which go beyond interference effects in a wave mechanical sense mainly occur for two reasons.

First, the inherent statistics of the underlying fundamental excitations, e. g., fermions, bosons, spins, or polaritons as a mixture thereof, can cause such "true" quantum mechanical effects since the concept of the fundamental commutation and anticommutation relations does not exist for c-number fields. The Hong-Ou-Mandel effect is probably the most prominent example in this regard, even though it is often only referred to as an interference effect.

Second, interacting particles can lead to a strong modification of the many-body solution in contrast to the single particle case. The interactions might be either direct such as the Coulomb interaction of electrons or effectively mediated, e. g., an effective photon–photon interaction induced by a saturable absorber.

In Sec. 4.4, I demonstrate how the Hong-Ou-Mandel effect serves as a probe for identifying effective photon–photon interactions. Influencing variables are selectively taken into account to study their effects on the shape of the Hong-Ou-Mandel dip which is obtained from the solution of the time-dependent problem.

4.2.3 Types of Impurities and their Single-Particle Scattering Solution

In this section, I briefly introduce the types of scatterers which are investigated in the following, their stationary, single-particle scattering solution, and the corresponding beam-splitter constraint. See Appendix D for details on the calculation.

General Form of the Scattering Equation

For the remainder of this discussion, the leads of the system are modeled as a one-dimensional tight-binding waveguide (cf. Chap. 3) with Hamiltonian

$$H_{\text{leads}} = \sum_x \omega a_x^\dagger a_x - J \sum_x \left(a_{x+1}^\dagger a_x + a_x^\dagger a_{x+1} \right) \tag{4.6}$$

and the local impurity couples to site x_0. Similar to Ref. [120], the single-particle scattering solution is obtained by solving the eigenvalue problem in the single-excitation subspace using

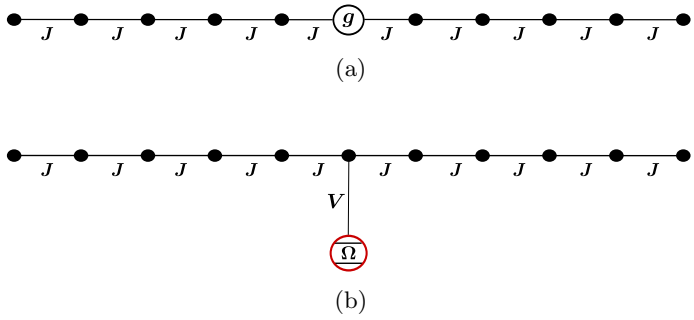

Figure 4.2: Schematic sketch of (a) a local on-site potential and (b) a two-level atom in a tight-binding waveguide.
The strength of the on-site potential is g, the atom–photon coupling strength and the atomic transition energy are V and Ω, respectively. The waveguide's hopping amplitude is denoted by J.

the ansatz

$$\varphi_x = \begin{cases} \mathrm{e}^{\mathrm{i}kx} + r_k \mathrm{e}^{-\mathrm{i}kx} & x < x_0 \\ t_k \mathrm{e}^{\mathrm{i}kx} & x \geq x_0 \end{cases} \tag{4.7}$$

for the wave function amplitudes in the waveguide (see Appendix D for details). The discrete scattering equation has the generic form

$$0 = (\omega - E)\varphi_x - J(\varphi_{x+1} + \varphi_{x-1}) + \delta_{xx_0} G(E)\varphi_{x_0} \tag{4.8}$$

where $E = \epsilon_k = \omega - 2J\cos(k)$ is the eigenenergy of the scattering state corresponding to wavenumber $k \in [-\pi, \pi]$ (cf. Chap. 3). The reflection amplitude is

$$r_k = -\mathrm{e}^{-2\mathrm{i}k} \frac{J^2 - (\omega - E + G(E) - J\mathrm{e}^{\mathrm{i}k})(\omega - E - J\mathrm{e}^{-\mathrm{i}k})}{J^2 - (\omega - E + G(E) - J\mathrm{e}^{\mathrm{i}k})(\omega - E - J\mathrm{e}^{\mathrm{i}k})} \,. \tag{4.9}$$

The function $G(E)$ depends on the actual realization of the impurity. Note that $1 + r_k = t_k$ and the conservation of probability, $|r_k|^2 + |t_k|^2 = 1$, hold. In the following, the free waveguide's dispersion relation is chosen such that it lies in the middle of the cosine band, i. e., $\omega = 0$.

Local On-Site Potential

A local on-site potential can be regarded as a deviation of the eigenfrequency of one of the cavities forming the tight-binding waveguide. In that case, the total Hamiltonian reads $H = H_{\mathrm{leads}} + H_{\mathrm{pot}}$, where

$$H_{\mathrm{pot}} = g a_0^\dagger a_0 \tag{4.10}$$

is the contribution due to the impurity which is part of the tight-binding chain itself and g is the strength of the local on-site potential (cf. Fig. 4.2).

The function $G(E)$ then simply becomes (cf. Eq. (4.8))

$$G(E) = g\,. \tag{4.11}$$

Consequently, the reflection amplitude takes the form

$$r_k = -\frac{g}{g - 2\mathrm{i}J\sin(k)}\,. \tag{4.12}$$

Thus, the balanced beam splitter with $|r_k|^2 = |t_k|^2 = \frac{1}{2}$ is realized for

$$g = \pm 2\left|J\right|\left|\sin(k)\right|\,. \tag{4.13}$$

Local Two-Level System

As shown in Chap. 3, the Hamiltonian of a single two-level atom in a waveguide can be written in the form of a single spin-$\frac{1}{2}$ locally side-coupled to a tight-binding waveguide (cf. Chap. 3), i. e.,

$$H = H_{\text{leads}} + \frac{\Omega}{2}\sigma_z + V\left(a_{x_0}^\dagger\sigma^- + a_{x_0}\sigma^+\right)\,. \tag{4.14}$$

The transition energy of the two-level atom is denoted by Ω and V is the atom–photon coupling strength (cf. Fig. 4.2 and Chaps. 2 and 3).

The single-particle solution to this problem yields

$$G(E) = \frac{V^2}{E - \Omega} \tag{4.15}$$

and thus [120]

$$r_k = \frac{V^2}{2\mathrm{i}J\sin(k)(-\Omega - 2J\cos(k)) - V^2}\,. \tag{4.16}$$

The condition $|r_k|^2 = |t_k|^2 = \frac{1}{2}$ results in the beam-splitter constraint (see Appendix D for details)

$$V = \pm\sqrt{\left|2J\sin(k)(-2J\cos(k) - \Omega)\right|}\,. \tag{4.17}$$

For instance, $k = 3\pi/4$ yields $V = \pm\sqrt{\sqrt{2}|J||\sqrt{2}J - \Omega|}$.

4.2.4 Influencing Variables for the Hong-Ou-Mandel Dip

In reality, various mechanisms lead to a fading of the Hong-Ou-Mandel dip. For instance, wave packets have a finite width. Thus, the temporal overlap of two excitations at the position of the scatterer does not only depend on the difference in the initial distance to

the latter but also on the widths of the wave packets. In realistic scenarios, single-particle excitations might experience a non-vanishing group-velocity dispersion, which also influences the temporal overlap at the position of the scatterer. Moreover, since the scattering solutions presented above are energy eigenstates, the condition for a balanced beam splitter can only be met for a single frequency out of the spectrum of the initial pulses.

From a theoretical point of view, it is interesting to monitor the qualitative change of the Hong-Ou-Mandel dip when the energy levels of the scatterer are smoothly changed from the harmonic to the strongly anharmonic case, i. e., when the transition from a harmonic oscillator to a two-level system is performed.

Additionally, in almost every realistic situation where atoms are coupled to light modes, dissipation and dephasing are important. In the quantum jump approach, dissipation of T_1-type is described by the relaxation operator $C_{T_1} = \sqrt{1/T_1}\sigma^-$. Similarly, dephasing of T_2-type requires $C_{T_2} = \sqrt{1/(2T_2)}\sigma_z$ (cf. Sec. 1.3.4 and Refs. [105, 106]).

4.3 Initial States and Joint Probability

Since the Hong-Ou-Mandel effect requires a minimum of two excitations to be investigated, I consider initial states according to Eq. (2.15) of the form (cf. Eq. (2.14))

$$\big|\Psi(0)\big\rangle = \sum_{x_1 x_2} \Phi_{x_1 x_2} a_{x_1}^\dagger a_{x_2}^\dagger \left|0\right\rangle \,, \tag{4.18}$$

where $\Phi_{x_1 x_2}$ is a boson-symmetric product of single-particle pulses launched from different ends of the waveguide (cf. Fig. 4.3). To be precise, the wave function is of the form

$$\Phi_{x_1 x_2} \propto \left(\varphi_{x_1}^{k_0^{(1)} x_c^{(1)} s^{(1)}} \cdot \varphi_{x_2}^{k_0^{(2)} x_c^{(2)} s^{(2)}} + \varphi_{x_2}^{k_0^{(1)} x_c^{(1)} s^{(1)}} \cdot \varphi_{x_1}^{k_0^{(2)} x_c^{(2)} s^{(2)}} \right), \tag{4.19}$$

where $\varphi_x^{k_0 x_c s}$ is a Gaussian wave function with carrier wavenumber k_0, center x_c, and width s (cf. Sec. 2.3.1). Unless stated otherwise, I choose $k_0^{(1)} = -k_0^{(2)} \equiv k_0 = 3\pi/4$, $s^{(1)} = s^{(2)} \equiv s = 7$, $x_c^{(1)} \equiv x_c = 50$, and $x_c^{(2)} = N + 1 - x_c + \Delta_x$ in the following. The relative displacement Δ_x is varied from -30 to $+30$ in order to record the Hong-Ou-Mandel dip. When $\Delta_x = 0$, both pulses initially have the same distance to the scatterer. The waveguide consists of $N = 199$ sites and the scatterer couples to site $x_0 = (N+1)/2 = 100$. For the remainder, the nearest-neighbor hopping strength J serves as the fundamental energy scale. I assume $J > 0$ so that the waveguide is "right-handed", i. e., group velocity and wavevector have the same sign. Time is measured in units[2] of J^{-1}. Furthermore, I choose $\Delta t = 0.1 J^{-1}$, which is smaller than any other time scale in the system, as the fundamental time step in the stochastic time evolution. See Refs. [61, 108], Chap. 2, and Appendix C for more details about the simulation.

[2] Note that dimensionless units according to Appendix A are employed.

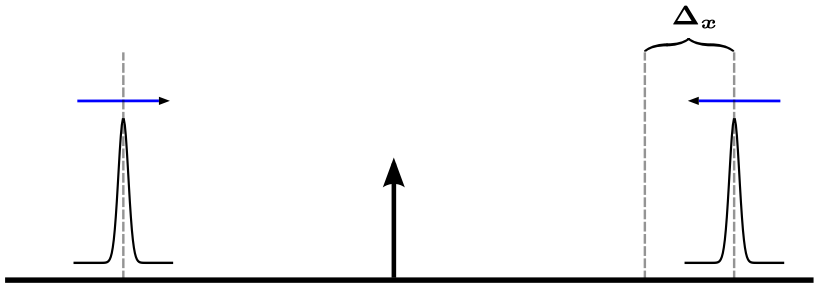

Figure 4.3: Schematic sketch of the two-excitation initial state.

The motion of the wave packets can be monitored in real space with the help the occupation numbers $\langle a_x^\dagger a_x\rangle(t)$. However, occupation numbers do not explicitly reveal correlations between the reflected and transmitted amounts of the two-excitation wave packet. Therefore, in order to obtain the Hong-Ou-Mandel dip, one has to consider the joint probability of finding one photon on the left and the other on the right-hand side of the impurity after scattering. Once a photon is detected, it is absorbed, i. e., the state after one photon was detected at site x and another photon at site y is proportional to $a_x a_y|\Psi\rangle$, where $|\Psi\rangle$ is the two-photon state after scattering. The probability is then proportional to

$$\sum_f \Big|\langle f|a_x a_y|\Psi\rangle\Big|^2 = \sum_f \langle\Psi|a_y^\dagger a_x^\dagger|f\rangle\langle f|a_x a_y|\Psi\rangle = \langle\Psi|a_y^\dagger a_x^\dagger a_x a_y|\Psi\rangle\,. \tag{4.20}$$

Since $|\Psi\rangle$ is a two-particle state, only the vacuum state contributes in the sum over all final states[3] $|f\rangle$. Equation (4.20) is the $n = 2$-mode joint probability as defined in Eq. (1.91). For the discussion of the Hong-Ou-Mandel dip, I use the normalized quantity

$$P_{\mathrm{LR}} = \frac{\sum_{\substack{x\in\mathcal{L}\\ y\in\mathcal{R}}}\langle a_y^\dagger a_x^\dagger a_x a_y\rangle}{\sum_{x,y\in\mathcal{L}\cup\mathcal{R}}\langle a_y^\dagger a_x^\dagger a_x a_y\rangle}\,, \tag{4.21}$$

which is the central quantity in this chapter. It is the joint probability of finding one photon on the left ($\mathcal{L} = \{1, 2, \ldots, x_0-1\}$) and the other on the right-hand side ($\mathcal{R} = \{x_0+1, \ldots, N\}$) of the scatterer. The projection of the state on two photons in the waveguide automatically excludes any possible contribution from an atom–photon bound state since such is a mixed atom–photon excitation (cf. Sec. 3.3.1). Expression (4.21) has to be evaluated for times after the wave packets have scattered at the impurity but before the reflected and transmitted pulses are influenced by the system's hard-wall boundaries (cf. Chap. 2 for details). Plotted as a function of Δ_x, i.e., as a function of the spatial separation of both incoming wave packets (cf. Fig. 4.3), Eq. (4.21) reproduces the famous Hong-Ou-Mandel dip.

[3]The final states form a complete basis, i. e., $\sum_f |f\rangle\langle f| = \mathbb{1}$.

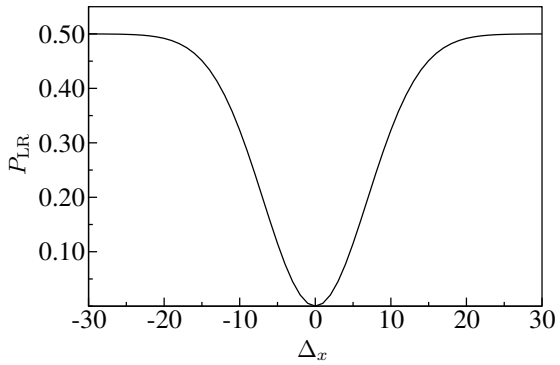

Figure 4.4: Hong-Ou-Mandel dip for a system where a local scattering potential is coupled to a photonic tight-binding waveguide.
The latter consists of $N = 199$ sites and the local scatterer in form of an on-site potential is coupled to site $x_0 = 100$. The strength of the potential is $g = 2|J||\sin(k_0 a)|$, which is the condition for a balanced beam splitter (cf. Eqs. (4.10) and (4.13)). The carrier wavenumber is $k_0 = \pi/2$.

4.4 Results and Discussion

In this section, I present results on the numerical study of Hong-Ou-Mandel interferometry according to the setup as described above. I start with a scatterer in form of a local on-site potential. This setup resembles the situation of a "usual" beam splitter and results in a Hong-Ou-Mandel dip as originally reported in [163]. After that, the emphasis is on a two-level atom, whose properties are gradually changed in order to study the resulting effects on the shape of the Hong-Ou-Mandel dip.

4.4.1 Local On-Site Potential in a Tight-Binding Waveguide

Figure 4.4 displays the Hong-Ou-Mandel dip for a system as described in Sec. 4.2.3 and Eq. (4.10). The strength of the on-site potential is set to $g = 2|J||\sin(k_0 a)|$ where the carrier wavenumber is $k_0 = \pi/2$. The coincidence probability of one photon being left and the other one being right practically vanishes for perfect overlap of the wave packets at the position of the scatterer, i. e., at $\Delta_x = 0$. For large separations, both wave packets pass the scatterer individually. Thus, one can read off the single-photon transmission probability at $\Delta_x \sim \pm 30$, which is (nearly) perfectly 50%. The reason why the local on-site potential works that well as a beam splitter for non-monochromatic excitations is because the reflectivity does not change for small deviations around the central carrier wavenumber of $k_0 = \pi/2$, i. e., $\partial_k |r_k|^2 \,|_{k=\pi/2} = 0$ (see Appendix D for details). This special property is due to a combination of the scatterer being part of the chain, i. e., it is not side-coupled, and the cosine dispersion

of the tight-binding waveguide. Furthermore, effects due to nonlinear dispersion are reduced since the group-velocity dispersion is zero at $k_0 = \pi/2$.

4.4.2 Local Two-Level System in a Tight-Binding Waveguide—the Hong-Ou-Mandel Effect as a Probe for Photon–Photon Interactions

Now, I turn to the question of how a two-level system, which—in contrast to an on-site potential—is a saturable scatterer, qualitatively influences the Hong-Ou-Mandel dip. In the single-excitation subspace, there is no difference whether the atomic degree of freedom is treated as such or merely replaced by a bosonic site. However, two excitations can dramatically change the transport properties as was already demonstrated in the context of radiation trapping in Refs. [61, 62]. For this trapping effect to be most efficient, the photon energy should be on resonance with the atomic transition energy. This resonance condition cannot be fulfilled in the Hong-Ou-Mandel setup because the condition for a balanced beam splitter is required to achieve single-particle reflection and transmission with equal probability (cf. Eq. (4.17)). In the following, I choose the carrier wavenumber to be $k_0 = 3\pi/4$ so that $V = \sqrt{\sqrt{2}|J||\sqrt{2}J - \Omega|}$ (cf. Sec. 4.2.3).

Influence of the Atomic Transition Energy on the Hong-Ou-Mandel Dip

I start by varying the atomic transition energy Ω whilst keeping the beam-splitter condition from Eq. (4.17). Increasing the atomic transition energy from $\Omega = 0$ to $\Omega = 1.2J$ has several consequences. First, the atom–photon detuning $\Omega - \epsilon_{k=3\pi/4} = \Omega - \sqrt{2}J$ is reduced. Second, the atom–photon coupling strength V is decreased. Figure 4.5(a) shows the tendency that the deviation from a perfect Hong-Ou-Mandel dip becomes more pronounced as the detuning is reduced. This is in line with Refs. [61, 62] because radiation trapping, which is one consequence of effective photon–photon interactions, is most efficient if $V \sim J$ and the resonance condition is fulfilled.

Mechanisms leading to such an effective photon–photon interaction can be identified in a faded Hong-Ou-Mandel dip. The fading is stronger than one would expect if only single-photon effects due to an unbalanced beam splitter were considered. This can be seen in Fig. 4.5(a) by noting that the limit of vanishing pulse overlap at the scatterer ($\Delta_x \to \pm\infty$) is nearly immune to changes in the atom–photon detuning. Since this limit represents individual particles passing the device, the fading of the Hong-Ou-Mandel dip must be due to effective photon–photon interactions whose effects can—at least in theory—be separated from signatures which are only induced by beam splitter imperfections.

The latter results in not all curves in Fig. 4.5(a) meeting exactly at $P_{\mathrm{LR}} = 0.5$. The two-level atom acts as a dispersive beam splitter and—in contrast to the on-site potential—the atomic degree of freedom is side-coupled. Additionally, the wavenumber $k_0 = 3\pi/4$ is from the nonlinear regime of the dispersion relation. Thus, the reflectivity does change to first

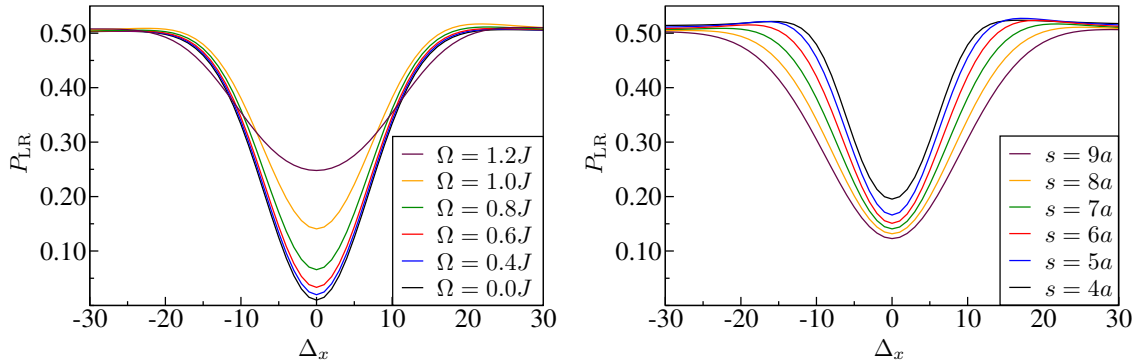

Figure 4.5: Hong-Ou-Mandel dip for a system where a two-level system is coupled to a photonic tight-binding waveguide.
For a central carrier wavenumber of $k_0 = 3\pi/4$, the beam-splitter condition reads $V = \sqrt{\sqrt{2}|J||\sqrt{2}J - \Omega|}$. (a) Note that by varying the atomic transition energy relative to the cosine band, the atom-photon coupling strength V changes as well due to the beam-splitter constraint. The combinations of transition energy and coupling strength used are $\Omega = 0$: $V = \sqrt{2}J$, $\Omega = 0.4J$: $V = 1.198J$, $\Omega = 0.6J$: $V = 1.073J$, $\Omega = 0.8J$: $V = 0.932J$, $\Omega = 1.0J$: $V = 0.765J$, $\Omega = 1.2J$: $V = 0.550J$. (b) The parameters are the same as in (a) except that $\Omega = J$ and the initial width of the wave packets is varied (cf. Sec. 2.3).

order in small deviations around $k_0 = 3\pi/4$, i.e., $\partial_k |r_k|^2 \mid_{k=3\pi/4} \neq 0$ (see Appendix D for details). As an example, I choose $\Omega = J$ in all subsequent considerations.

Influence of the Wave Packets' Width on the Hong-Ou-Mandel Dip

The influence of different initial widths of the wave packets on the Hong-Ou-Mandel dip is shown in Fig. 4.5(b). Hong-Ou-Mandel interferometry techniques can be exploited to actually determine the spatial overlap and thus the extent of the impinging wave packets. Both the single-photon limit and the depth of the Hong-Ou-Mandel dip change with the width of the wave packets. This can be understood as follows. As the extent of the wave packet gets smaller in real space, it covers a broader spectral range in momentum space. Since the beam-splitter condition only holds for a single frequency, more and more frequency components pass the beam splitter with a probability different than 50%. In addition, an increasing spectral range in momentum space leads to more frequency components which participate in the effective photon–photon interaction as discussed in Refs. [61, 62] and Chap. 3.

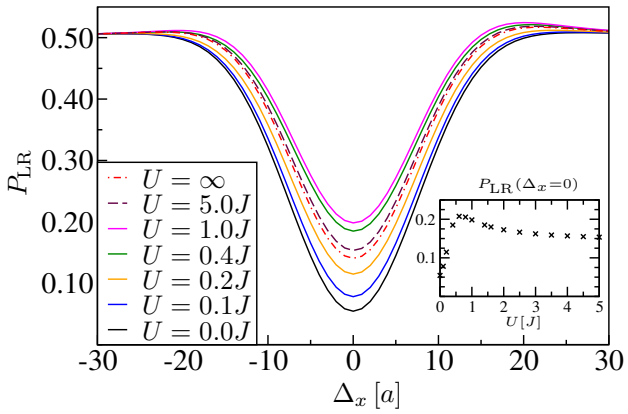

Figure 4.6: Hong-Ou-Mandel dip in analogy to Fig. 4.5(a) but for $\Omega = J$ and different strengths of the anharmonicity U (see text for details).
For $U = 0$, the fading of the Hong-Ou-Mandel dip is solely due to beam splitter imperfections at the single-photon level. The fading depends non-monotonically on the anharmonicity (see text for explanation). The single-photon limit ($\Delta \to \pm\infty$) is independent of the actual value of the anharmonicity. In the inset, I display the the depth of the Hong-Ou-Mandel dip as a function of the anharmonicity U.

From the Harmonic Oscillator to the Two-Level System

From a theoretical point of view, the transition from a harmonic oscillator to a two-level system, i. e., from the harmonic to the strongly anharmonic case is most elucidating. In line with Refs. [61, 62] and as described in Sec. 1.3.2, I therefore replace the Pauli operators of the two-level system in Eq. (4.14) by bosonic operators b and $b^\dagger$. Specifically, the formulation $\frac{\Omega}{2}\sigma_z \to \Omega b^\dagger b + U b^\dagger b(b^\dagger b - 1)$ describes a harmonic oscillator for $U = 0$ and a two-level system in the limit $U \to \infty$.

Figure 4.6 displays the Hong-Ou-Mandel dip for different strengths of the anharmonicity U. In the absence of interaction ($U = 0$), the Hong-Ou-Mandel dip becomes "perfect" besides the beam splitter imperfections due to the single-excitation transport characteristics. For $U > 0$, i. e., in the interacting system, the fading of the Hong-Ou-Mandel dip depends non-monotonically on the value of the anharmonicity until it saturates in the limit $U \to \infty$.

This behavior can be understood as follows. As demonstrated in Refs. [61, 62] and mentioned in Chap. 3, the interactions induced by a finite U-term become most pronounced if the atom–photon detuning is zero. However, in the Hong-Ou-Mandel setup, the resonance condition is not fulfilled since the scatterer acts as a beam splitter. To further understand this non-monotonicity, it is helpful to consider the detuning between two impinging photons and the energy they had in case they double-occupied the atomic site, i.e., $\delta = n\Omega + Un(n-1) - n\epsilon_{k_0}$, where $n = 2$ and ϵ_{k_0} is the single-photon energy. If the single-

particle resonance condition, i. e., $\Omega = \epsilon_{k_0}$, was fulfilled, δ would grow monotonically as U is increased. In the Hong-Ou-Mandel dip in Fig. 4.6, $\Omega - \epsilon_{k_0} = (1 - \sqrt{2})J < 0$ so that δ changes its sign as U grows. This eventually leads to the non-monotonic dependence of the depth of the Hong-Ou-Mandel dip.

Note again that the offset in Fig. 4.6 in the limit of $\Delta \to \pm\infty$ is independent of the actual value of the anharmonicity. In this limit, the excitations pass the device individually as single particles.

Influence of Dissipation and Dephasing

In reality, even if the waveguide is considered to be practically lossless, the two-level system still suffers from non-radiative losses and the coupling to non-guided modes (subsumed in time constant T_1) as well as from pure dephasing, i. e., the randomization of the phase relation between the atom's ground and excited state (subsumed in time constant T_2).

Figure 4.7(a) displays the effect of different T_1-times on the shape of the Hong-Ou-Mandel dip. Once a photon is lost, i. e., the T_1-relaxation operator was applied to the two-particle state (cf. Sec. 4.2.4), the wave function collapses to a single-particle state and two-particle coincidences become impossible, which leads to a less pronounced Hong-Ou-Mandel dip. However, since the definition of the joint probability P_{LR} in Eq. (4.21) is normalized to the total probability, the single-photon limit is independent of the value of T_1. Note that in the quantum jump approach as described in Sec. 1.3.4, all wave function trajectories enter the expectation values in Eq. (4.21), including those that represent zero coincidences.

The effect of pure dephasing on the Hong-Ou-mandel dip is displayed in Fig. 4.7(b). The two-level atom mediates the effective photon–photon interaction less efficiently once the phase coherence between the atom and the impinging photons is destroyed. This leads to a fading of the Hong-Ou-Mandel dip but for moderate T_2-times the single-photon limit seems to be practically unaffected. Only very short dephasing times lead to a significant change in the single-photon transport which results in the beam splitter being unbalanced and thus the single-photon limit changes.

This can be understood as follows. Pure dephasing can be regarded as the temporal fluctuation of the atom's level spacing. In the regime of strong dephasing, the detuning between the instantaneous atomic transition energy and the photon energy according to the central carrier wavenumber of the wave packet thus strongly fluctuates. This, in turn, implies that the condition for equal reflection and transmission of a monochromatic wave is only fulfilled for very short instances of time. In the present setup, this enhances the transmittance of the single-excitation wave packet (Fig. 4.8). Here, I use the definition $T = \frac{1}{2}\langle a_{x_0}^\dagger a_{x_0}\rangle + \sum_{x=x_0+1}^{N}\langle a_x^\dagger a_x\rangle$ for the transmittance. For the parameters chosen here, T_2-times comparable to the temporal overlap τ of the wave packet at the position of the atom lead to an enhanced transmission. As a crude estimate, $\tau \sim s/v_{\mathrm{g}}$, where $v_{\mathrm{g}} = 2J\sin(k_0)$ is the group velocity.

From the above investigations one might get the impression that a clear-cut separation of

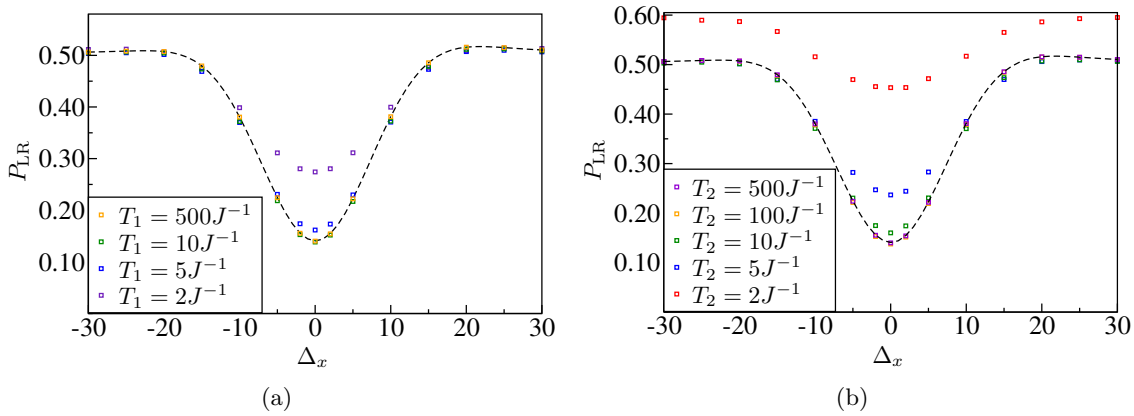

Figure 4.7: Influence of T_1-relaxation and T_2-depahsing on the Hong-Ou-Mandel dip. (a) Hong-Ou-Mandel dip for the same parameters as in Fig. 4.5(a) with $\Omega = J$ but the two-level system experiences losses of T_1-type. Even though losses of T_1-type lead to irreversible photon loss, the single-photon limit is independent of the value of T_1 because of the normalization of Eq. (4.21). The black dashed curve represents the lossless case in which $T_1 = \infty$. (b) Hong-Ou-Mandel dip as shown in Fig. 4.7(a) but now with pure dephasing of T_2-type instead of T_1-relaxation. Moderate dephasing times affect the depth of the Hong-Ou-Mandel dip but leave the single-photon limit practically unchanged. Very short dephasing times change the single-particle transport characteristics and, therefore, the single-photon limit in the Hong-Ou-Mandel dip. The black dashed curve represents the lossless case in which $T_2 = \infty$. In the simulation for the stochastic time evolution, 500 and 2000 samples were used for (a) and (b), respectively (cf. Appendix C).

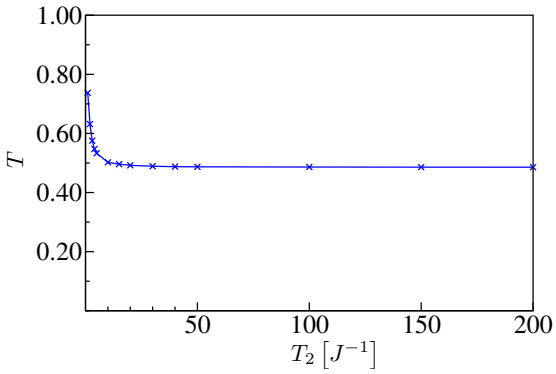

Figure 4.8: Single-particle transmittance T through a two-level system which is subject to pure dephasing of T_2-type.
For strong dephasing, i. e., T_2-times comparable to the temporal overlap of the wave packet at the position of the atom, the transmission is enhanced for the parameters chosen here. The parameters of the initial wave packet are $k_0 = 3\pi/4$, $s = 12$, and $x_c = 50$. 1000 samples were used in the simulation for the stochastic time evolution (cf. Appendix C). The solid line is just a guide to the eye.

the influences of the open system dynamics (T_1 and T_2) and the actual interaction between two excitations is impossible and one still would have to speculate to which degree an imperfect Hong-Ou-Mandel dip really is the signature for effective photon–photon interactions. I would like to emphasize that the previous studies were driven by the explicit knowledge of the stationary, i.e., the monochromatic, single-particle solution yielding a condition for the balanced beam splitter. This condition is, as was shown, not perfectly met for pulses of finite width. However, given a fixed width of the wave packets and fixed values of T_1 and T_2, the condition for the balanced beam splitter can be recovered in a trial-and-error fashion by tuning the two-level system's transition energy or coupling strength such that in a single-photon setup reflection and transmission occur with equal probability. In addition to that, carefully designed and/or tunable dispersion relations such as those available in Photonic Crystal waveguides [7] can reduce group-velocity dispersion over a broad range of carrier wavenumbers which makes the beam splitter less dispersive for the frequencies of interest.

Alternatively, the Hong-Ou-Mandel interferometry technique could also be exploited to probe the environment by comparison of the measured Hong-Ou-Mandel dip and the "clean" theoretical curve. A numerical fit in which the parameters of the environment are tuned such that the two curves match, finally allows to determine T_1 and/or T_2 times. In that case, however, one still would need sufficient knowledge about possible sources of either T_1-dissipation or T_2-dephasing, since these two quantities cannot be clearly separated from one another in the Hong-Ou-Mandel dip.

4.5 Conclusion, Outlook, and Critical Discussion

In conclusion, I presented a detailed analysis of the dynamics of two photons impinging from both ends of a tight-binding waveguide on a local scatterer. This scenario is intimately related to the fundamental Hong-Ou-Mandel effect. Specifically, the joint probability of finding one photon on either side of the impurity after scattering was calculated by means of the numerical framework as presented in Chap. 2. As a function of the initial difference in the wave packet separation to the impurity, this quantity is nothing but the famous Hong-Ou-Mandel dip.

In case the local scatterer is just given as an on-site potential, I demonstrated that the Hong-Ou-Mandel effect can become perfect in the sense that the joint probability is zero for maximal wave packet overlap at the scatterer. To this end, the parameters of the on-site potential were adjusted such that a (monochromatic) single photon is reflected and transmitted with equal probability.

I then applied the same strategy to the case of a single two-level system embedded in the waveguide. In this case, the Hong-Ou-Mandel effect can be less pronounced, resulting in a non-zero joint probability, even though beam splitter imperfections on the single-photon level due to non-zero group-velocity dispersion were taken into account. I therefore concluded that an "imperfect" Hong-Ou-Mandel dip can be interpreted as the signature for effective photon–photon interactions which are mediated by the two-level system. In addition, these findings were related to earlier works on interaction-induced radiation trapping (cf. Refs. [61, 62] and Chap. 3) in order to get a coherent and complete picture of the dynamics.

I then proceeded by investigating the influence of dissipation and dephasing on the shape of the Hong-Ou-Mandel dip. To this end, the stochastic quantum jump approach was employed (cf. Sec. 1.3.4) and I considered the two-level system to be subject to relaxation of T_1-type as well as pure dephasing of T_2-type. Due to the normalization of the joint probability to the total probability in the system, T_1-relaxation only affects the depth of the Hong-Ou-Mandel dip. T_2-dephasing can also change the offset since the single-photon transmittance is modified. Knowing these properties, Hong-Ou-Mandel interferometry techniques can—at least in principle—also be exploited to probe the environment.

A variety of extensions and modifications to the work presented in this chapter can be envisioned for future investigations. For instance, the Hong-Ou-Mandel effect could serve as a probe to identify signatures from more complicated structures such as Jaynes-Cummings cavities, Kerr-nonlinear media, or tunable few-level systems. Especially driven three-level systems might be interesting candidates towards a tunable Hong-Ou-Mandel effect. Besides this, the Hong-Ou-Mandel setup is also worth investigating in the context of polaritons such as those emerging in Jaynes-Cummings-Hubbard systems [15, 64, 65, 68, 157, 169]. Here, due to the mixed nature of the elementary excitations, coincidences can be investigated beyond the photon–photon sector.

The findings presented in this chapter could be criticized with regard to the following points. In order to clearly separate interaction-induced effects from effects which are due to

beam-splitter imperfections, a strategy needs to be developed with which a "clean" Hong-Ou-Mandel dip can be obtained, i. e., a Hong-Ou-Mandel dip free of beam-splitter imperfections. In addition to that, a functional dependency of the Hong-Ou-Mandel dip on T_1- and T_2-times (as well as on the U-term in case of an anharmonic oscillator) would clearly help to gain further insight even if such a function was only obtained empirically. I did not address such issues in this chapter. Furthermore, even though I considered dissipation and dephasing of the beam-splitting device, I neglected these effects in the waveguide.

Chapter 5

5 Dynamics of a Photon-Added Coherent State in a Waveguide Coupled to a Nonlinear Resonator

In this chapter, I study the dynamics of coherent states and photon-added coherent states in a tight-binding waveguide with a side-coupled Kerr-nonlinear resonator. The theoretical analysis is based on the Heisenberg equations of motion, which are solved in an appropriately displaced basis. For coherent states, I derive the stationary scattering states, and in the context of a single-photon-added coherent state, I investigate the problem of pulse propagation numerically. Specifically, I demonstrate how the fields provided by the coherent states facilitate a tunable scattering potential on the single-photon level, allowing for the gating of single photons. I address the issue of dissipation in terms of a "leaky" cavity, and I comment on a possible realization in the field of optomechanics. Parts of this chapter have been published in Ref. [170].

5.1 Introduction

Owing to the advances in nanotechnology, the realization of integrated quantum photonic circuitry has recently witnessed considerable progress towards the ultimate goal of creating, manipulating and detecting single photons [3–6]. Several systems such as arrays of coupled optical resonators [11, 15] and Photonic Crystals (cf. Sec. 1.2) are currently being explored. Interestingly, the approaches of introducing functionality in these waveguiding systems range from individual atoms over classical nonlinearities to the incorporation of mechanical degrees of freedom.

Despite the variety in actual physical realizations, a Kerr-nonlinear response very often represents a reasonable building block for a prototypical model system (cf. Sec. 1.3.2). With regard to the theoretical analysis in the realm of quantum optics, it is common to either

investigate the dynamics of the "most classical states"—coherent states—or, in contrast to that, Fock states. There is, however, a less-explored class of states—photon-added coherent states—, which are kind of "in between" coherent states and Fock states (cf. Sec. 1.3.1). The main emphasis in this chapter is on the dynamics of photon-added coherent states.

This chapter is structured as follows. In Sec. 5.2, I introduce the system of a tight-binding waveguide with a side-coupled Kerr-nonlinear resonator, the corresponding equations of motion, and the definition of the occupation numbers which represent the central quantity in this chapter. In Sec. 5.3, I derive the analytical scattering solution of the nonlinear problem in the context of coherent states and I comment on self-induced transparency and bistability. The dynamics of a single-photon-added coherent state is then investigated numerically. Specifically, I demonstrate how a coherent state can control the effective scattering potential which is "seen" by a single photon. This mechanism can be exploited for the gating of single photons. The issue of dissipation is addressed by taking radiation losses of the side-coupled resonator into account. After that, I comment on possible realizations in an optomechanical setup. I conclude the chapter in Sec. 5.4 and suggest possible topics for future studies.

5.2 Theoretical Formulation

In this section, I introduce the Hamiltonian of a tight-binding waveguide with a side-coupled Kerr-nonlinear cavity. Furthermore, I derive the Heisenberg equations of motion and project them on coherent states and photon-added coherent states, followed by the definition of occupation numbers used in this context.

5.2.1 The Hamiltonian

In the following, I consider a chain of identical and equally spaced optical resonators. They form a waveguide whose dispersion relation is centered around the resonators' resonance frequency ω_0. In addition, one of these resonators is side-coupled to a single resonator which exhibits a Kerr-nonlinear response (cf. Secs. 1.3.2 and 2.2.1). Such a system could, for instance, be realized by appropriately placed micro-disk resonators such as those mentioned in Sec. 1.2.2, where the side-coupled resonator is made from or coated with a different material. However, besides the realization in the field of cavity arrays [11, 15–17], the analysis is easily extended to similar waveguide–resonator systems such as optical fibers side-coupled to Kerr-nonlinear resonators [47], systems with ultracold bosonic atoms [28], and even optomechanical systems (see Ref. [77] and Sec. 1.3.2). A schematic sketch of the system is depicted in Fig. 5.1.

The Hamiltonian reads

$$H = \sum_x \omega_0 a_x^\dagger a_x - J\sum_x (a_{x+1}^\dagger a_x + a_x^\dagger a_{x+1}) - J'(a_{x_0}^\dagger c + a_{x_0} c^\dagger) + \Omega_0 c^\dagger c + \Delta c^\dagger c^\dagger c c - \frac{\mathrm{i}}{2}\Gamma c^\dagger c\,. \quad (5.1)$$

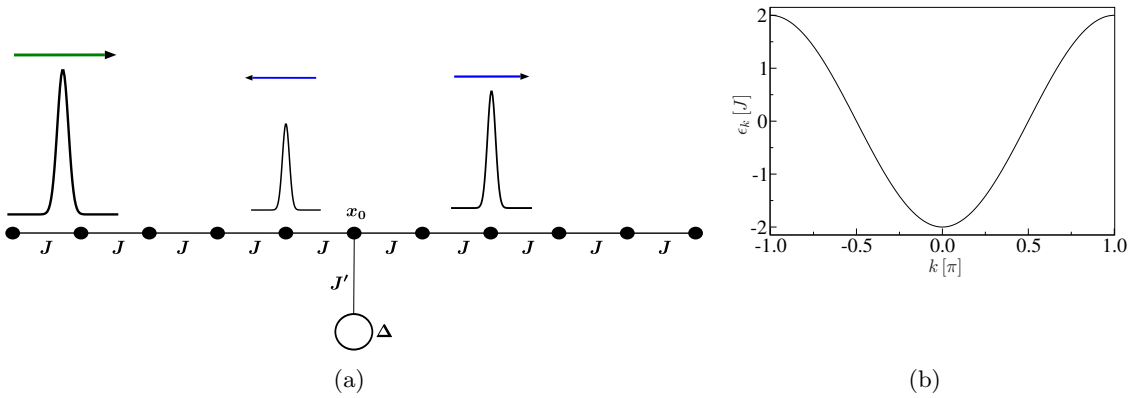

(a) (b)

Figure 5.1: Schematic sketch of a tight-binding waveguide with a side-coupled Kerr-nonlinear cavity.
The waveguide's nearest-neighbor hopping constant is J and the additional cavity with a Kerr-nonlinearity Δ is coupled to site x_0 with a side-coupling strength of J'. The waveguide's cosine-dispersion relation is depicted in (b), where the zero of the energy is shifted to the middle of the band.

Here, the coupled-resonator optical waveguide is described by a nearest-neighbor coupling constant J between the lattice sites x, leading to a cosine dispersion relation $\epsilon_k = \omega_0 - 2J\cos(k)$ of the waveguide[1] (cf. Sec. 1.2.2 and Chap. 3). As was pointed out in Chaps. 2 and 3, Hamiltonian (5.1) serves as an approximate model system if the underlying physical system is not inherently discrete, e. g., an optical fiber. In that case, the dispersion relation of the model system is matched to the one of the physical system around an operating wavelength. J' describes the coupling of the side-coupled resonator (operators $c^\dagger$ and c) to site x_0 which is in the middle of the waveguide. The eigenfrequency of the nonlinear cavity is Ω_0 and the strength of the Kerr nonlinearity is denoted by Δ (cf. Sec. 1.3.2). In principle, J' could be different from the waveguide's hopping strength J but, in order to keep the subsequent discussion simple, I assume $J' = J$. For the same reason, I assume that the side-coupled resonator's eigenfrequency coincides with those of the waveguide resonators, i. e., $\omega_0 = \Omega_0$. In the spirit of the quantum jump approach, which was introduced in Sec. 1.3.4, Γ describes the decay rate to modes other than the waveguide, e. g., photon loss to non-guided modes or due to scattering at fabrication imperfections.

As pointed out in Sec. 1.3.2, the Hamiltonians for a Kerr nonlinearity and the effective photon–photon interaction which is obtained in an optomechanical setup by eliminating the phononic degrees of freedom are, up to a few subtle differences, very similar. Although the results presented here refer to Hamiltonian (5.1), they can, in principle, also be obtained for

[1] Dimensionless units according to Appendix A are employed so that the lattice constant is unity.

an optomechanical realization. See Sec. 5.3.3 for a brief discussion of the latter.

5.2.2 Equations of Motion and Projection on States

For the subsequent considerations, it is useful to derive the Heisenberg equations of motion with respect to Hamiltonian (5.1) for the operators a_x and c, respectively. They read

$$\mathrm{i}\partial_t a_x = \omega_0 a_x - J(a_{x+1} + a_{x-1}) - J'\delta_{xx_0} c\,, \tag{5.2a}$$

$$\mathrm{i}\partial_t c = \Omega_0 c - J' a_{x_0} + 2\Delta c^\dagger c c - \mathrm{i}\frac{\Gamma}{2} c\,. \tag{5.2b}$$

I now project these equations of motion on the different classes of states which are discussed in the following, i. e., I multiply Eqs. (5.2) from the right with a ket $|\Psi\rangle$ and from the left with the corresponding bra $\langle\Psi|$.

Projection on Coherent States

Coherent states on the lattice as a product of single-site coherent states were introduced in Sec. 2.3. Applied to Eqs. (5.2a) and (5.2b), I get the equations of motion for the coherent states' amplitudes:

$$\mathrm{i}\partial_t \alpha_x = \omega_0 \alpha_x - J(\alpha_{x+1} + \alpha_{x-1}) - J'\delta_{xx_0}\gamma\,, \tag{5.3a}$$

$$\mathrm{i}\partial_t \gamma = \Omega_0 \gamma - J'\alpha_{x_0} + 2\Delta|\gamma|^2\gamma - \mathrm{i}\frac{\Gamma}{2}\gamma\,. \tag{5.3b}$$

Here, $\{\alpha_l\}$ and γ are the c-numbers associated with the single-site coherent states on the waveguide sites and the side-coupled resonator, respectively. These equations represent a variant of the nonlinear Schrödinger equation, in which the nonlinearity is local. The analytical solution to the nonlinear scattering problem is derived in Sec. 5.3.1.

Projection on Single-Photon-Added Coherent States

For the present problem, a single-photon-added coherent state as introduced in Eq. (2.22) takes the form

$$|\Psi\rangle = C\sum_x \left(\varphi_x a_x^\dagger + \psi c^\dagger\right)|\{\alpha_x\},\gamma\rangle\,. \tag{5.4}$$

As in the case of the "pure" coherent state, $\{\alpha_l\}$ and γ are the coherent states' complex-valued amplitudes, whereas φ_x and ψ denote the single-photon wave function amplitudes in the waveguide and the side-coupled resonator, respectively. In the following, it is helpful to perform the projection of Eqs. (5.2) on states like (5.4) in the displaced basis which was introduced in Eqs. (2.25) and (2.26). Here, the displaced single-photon-added coherent state reads

$$|\tilde{\Psi}\rangle = D^\dagger(\{\alpha_x\})|\Psi\rangle = C\sum_x \left(\varphi_x a_x^\dagger + \psi c^\dagger\right)|0\rangle + C\eta|0\rangle \tag{5.5}$$

with $\eta = \sum_x \varphi_x \alpha_x^* + \psi\gamma^*$. By multiplying Eqs. (5.2) from the right with $D(\{\alpha_l\})$ and from the left with $D^\dagger(\{\alpha_l\})$, the displacement operator's properties[2] (1.45b) and (1.45c) can be exploited. Separating c-numbers from operators (similar to Ref. [171]), I arrive at

$$\begin{aligned}
\mathrm{i}\partial_t \alpha_x &= \omega_0 \alpha_x - J(\alpha_{x+1} + \alpha_{x-1}) - J'\delta_{xx_0}\gamma\,, && (5.6a)\\
\mathrm{i}\partial_t a_x &= \omega_0 a_x - J(a_{x+1} + a_{x-1}) - J'\delta_{xx_0}c\,, && (5.6b)\\
\mathrm{i}\partial_t \gamma &= \Omega_0\gamma - J'\alpha_{x_0} + 2\Delta|\gamma|^2\gamma - \mathrm{i}\frac{\Gamma}{2}\gamma\,, && (5.6c)\\
\mathrm{i}\partial_t c &= \Omega_0 c - J' a_{x_0} - \mathrm{i}\frac{\Gamma}{2}c \\
&\quad +4\Delta|\gamma|^2 c \\
&\quad +4\Delta\gamma c^\dagger c + 2\Delta\gamma^2 c^\dagger \\
&\quad +2\Delta c^\dagger cc + 2\Delta\gamma^{*2} cc\,. && (5.6d)
\end{aligned}$$

The time evolution of the coherent states thus decouples from the single photon. Furthermore, the last two terms in Eq. (5.6d) do not contribute when projected on state (5.5). In the following, I refer to the coherent states as the mean field and regard the single photon part as fluctuations[3]. The latter can alternatively be described by the effective, time-dependent Hamiltonian

$$\begin{aligned}
H_{\mathrm{eff}} &= \sum_x \omega_0 a_x^\dagger a_x - J\sum_x (a_{x+1}^\dagger a_x + a_x^\dagger a_{x+1}) - J'(a_{x_0}^\dagger c + a_{x_0} c^\dagger) \\
&\quad +\Omega_0 c^\dagger c + 4\Delta|\gamma(t)|^2 c^\dagger c - \mathrm{i}\frac{\Gamma}{2}c^\dagger c \\
&\quad +\Delta\gamma^2(t) c^\dagger c^\dagger + 2\Delta\gamma(t) c^\dagger c^\dagger c\,. && (5.7)
\end{aligned}$$

The following arguments are needed for further simplifications. In the interaction picture, the annihilation operators oscillate according to $a_x \propto \mathrm{e}^{-\mathrm{i}\omega_0 t}$ and $c \propto \mathrm{e}^{-\mathrm{i}\Omega_0 t}$ in time. Moreover, for the solution of the scattering problem for coherent states, an incoming plane wave with wavenumber k results in $\gamma(t) \propto \mathrm{e}^{-\mathrm{i}\epsilon_k t}$, where $\epsilon_k = \omega_0 - 2J\cos(k)$ (shown in Sec. 5.3.1). Note that all phases except for those of the two last terms in Hamiltonian (5.7) are static[4]. In the spirit of the rotating-wave approximation, I neglect the term $\Delta\gamma^2(t)c^\dagger c^\dagger \propto \mathrm{e}^{4\mathrm{i}J\cos(k)\cdot t}$ and $2\Delta\gamma(t)c^\dagger c^\dagger c \propto \mathrm{e}^{2\mathrm{i}J\cos(k)\cdot t}$, which is justified as long as the energies corresponding to the dominant carrier wavenumbers of an incoming coherent state wave packet are detuned with respect to the eigenfrequency of the side-coupled cavity. For convenience, I furthermore set $\omega_0 = 0$, i. e., the zero of the waveguide's dispersion relation is shifted to the middle of

[2] In the Heisenberg picture, $D^\dagger(\{\alpha_l\})\partial_t a_x D(\{\alpha_l\}) = \partial_t\left(D^\dagger(\{\alpha_l\})a_x D(\{\alpha_l\})\right)$ holds because of $\partial_t D^\dagger(\{\alpha_l\}) = -\partial_t D(\{\alpha_l\})$.

[3] This does not mean that a mean-field approximation was applied.

[4] Remember that the eigenfrequencies of all cavities coincide, i. e., $\omega_0 = \Omega_0$.

the band. The simplified Hamiltonian then takes the form

$$H_{\text{eff}} = -J\sum_x (a_{x+1}^\dagger a_x + a_x^\dagger a_{x+1}) - J'(a_{x_0}^\dagger c + a_{x_0} c^\dagger) + 4\Delta|\gamma(t)|^2 c^\dagger c - \mathrm{i}\frac{\Gamma}{2} c^\dagger c\,. \tag{5.8}$$

This Hamiltonian describes the time evolution of the fluctuations which are controlled by the spatio-temporal profile of the coherent state's intensity in the side-coupled cavity. The term $4\Delta|\gamma(t)|^2 c^\dagger c$ thus represents a tunable, local scattering potential. The time evolution of the coherent state pulse as determined by Eqs. (5.6a) and (5.6c) serves as an input for Hamiltonian (5.8), which, in turn, acts on state (5.5). In this formulation, the total number of excitations $\mathcal{C} = \sum_x a_x^\dagger a_x + c^\dagger c$ is conserved.

5.2.3 Occupation Numbers

In this chapter, I restrict the discussion to the waveguide's occupation numbers, i. e., $\langle n_x\rangle = \langle a_x^\dagger a_x\rangle$ (cf. Sec. 1.3.3). For the "pure" coherent states, they simply read

$$\langle n_x\rangle = \langle a_x^\dagger a_x\rangle = |\alpha_x|^2\,, \tag{5.9}$$

whereas the single photon-added coherent state in the displaced basis yields

$$\begin{aligned}\langle n_x\rangle &= \langle D^\dagger(\{\alpha_x\}) a_x^\dagger a_x D(\{\alpha_x\})\rangle \\ &= \langle a_x^\dagger a_x\rangle + \alpha_x\langle a_x^\dagger\rangle + \alpha_x^*\langle a_x\rangle + |\alpha_x|^2 \\ &= |C\varphi_x|^2 + 2|C|^2\mathrm{Re}(\eta^*\alpha_x^*\varphi_x) + |\alpha_x|^2\,.\end{aligned} \tag{5.10}$$

In this chapter, I am only interested in the effects of the mean fields on the fluctuations. Hence, I monitor $|\alpha_x|^2$ and $|\varphi_x|^2$ separately instead of using the superposition (5.10). In order to compare the nonlinear dynamics of the mean field for different initial intensities $|\alpha^{(0)}|^2$ (cf. Sec. 2.3.1), all subsequent plots are normalized according to $|\alpha_x|^2/|\alpha^{(0)}|^2$.

5.3 Transport Properties

In this section, I discuss the transport properties of a coherent state and a single-photon-added coherent state. For the latter, I numerically investigate the problem of pulse propagation, whereas for the former the discussion is limited to the stationary scattering states of the nonlinear problem.

5.3.1 Coherent State

The exact analytical solution of the stationary scattering states for a coherent state in a system as described by Eqs. (5.3) is derived.[5] All formulae are written down for the lossless case ($\Gamma = 0$) and for the situation in which the resonator's eigenfrequencies coincide,

[5] After this chapter has been finished, I became aware of Ref. [172], in which a similar scattering problem is investigated.

i. e., $\omega_0 = \Omega_0$ (cf. Sec. 5.2.1). For convenience, the index of the site to which the nonlinear cavity couples is shifted to zero. For these equations, a time-harmonic ansatz[6] $\propto \mathrm{e}^{-\mathrm{i}\omega t}$ for the amplitudes yields the set of discrete scattering equations

$$\begin{aligned} \omega\alpha_i &= -J(\alpha_{i+1} + \alpha_{i-1}) - J'\delta_{i0}\gamma\,, && \text{(5.11a)} \\ \omega\gamma &= -J'\alpha_0 + 2\Delta|\gamma|^2\gamma\,, && \text{(5.11b)} \end{aligned}$$

for which I use the ansatz[7]

$$\alpha_x = \begin{cases} A\mathrm{e}^{\mathrm{i}kx} + r_k\mathrm{e}^{-\mathrm{i}kx} & x < 0 \\ \alpha_0 & x = 0 \\ t_k\mathrm{e}^{\mathrm{i}kx} & x > 0 \end{cases}, \qquad (5.12)$$

in which $k \geq 0$. The input power is denoted by $|A|^2$. Without loss of generality, $A \in \mathbb{R}$ is assumed. Evaluating Eq. (5.11a) for $x = -1$, $x = 0$, $x = 1$, and $x = 2$, respectively, yields

$$\begin{aligned} 0 &= r_k(-J\mathrm{e}^{\mathrm{i}k} - \omega)\mathrm{e}^{\mathrm{i}k} - J(\alpha_0 + A\mathrm{e}^{-2\mathrm{i}k}) - \omega A\mathrm{e}^{-\mathrm{i}k}\,, && \text{(5.13a)} \\ 0 &= r_k(-J\mathrm{e}^{\mathrm{i}k}) + t_k(-J\mathrm{e}^{\mathrm{i}k}) - JA\mathrm{e}^{-\mathrm{i}k} - \omega\alpha_0 - J'\gamma\,, && \text{(5.13b)} \\ 0 &= t_k(-J\mathrm{e}^{\mathrm{i}k} - \omega)\mathrm{e}^{\mathrm{i}k} - J\alpha_0\,, && \text{(5.13c)} \\ \omega &= -2J\cos(k)\,. && \text{(5.13d)} \end{aligned}$$

Combining Eq. (5.13d) with Eqs. (5.13a) and (5.13c) gives $\alpha_0 = t_k$ and $r_k = t_k - A$ which, after basic manipulations and using Eq. (5.13b), leads to

$$\gamma = -\frac{r_k}{J'}2\mathrm{i}J\sin(k)\,. \qquad (5.14)$$

Inserting this expression into Eq. (5.11b) finally gives, after some reordering, the central equation for the reflection amplitude

$$0 = |r_k|^2 r_k + a_k(\mathrm{i}b_k + c_k)r_k + \mathrm{i}a_k b_k A\,, \qquad (5.15)$$

which is nonlinear. In Eq. (5.15), I introduced the abbreviations

$$\begin{aligned} a_k &\equiv -\frac{J'^2}{2\Delta v_k^2}\,, && \text{(5.16a)} \\ b_k &\equiv \frac{J'^2}{v_k}\,, && \text{(5.16b)} \\ c_k &\equiv \epsilon_k\,, && \text{(5.16c)} \end{aligned}$$

[6] As before, no new symbol is introduced to denote the time-independent amplitudes so that, for instance, $\gamma(t) = \gamma\mathrm{e}^{-\mathrm{i}\omega t}$.

[7] I assume $J > 0$, i. e., a right-handed waveguide (see also Chap. 4).

in which $\epsilon_k = -2J\cos(k)$ is the dispersion relation of the waveguide and $v_k = 2J\sin(k)$ its corresponding group velocity. Note that $a_k, b_k, c_k, A \in \mathbb{R}$.

In order to solve Eq. (5.15), I start by rewriting the reflection coefficient as $r_k \equiv \sqrt{R_k}\mathrm{e}^{\mathrm{i}\phi_k}$ so that Eq. (5.15) takes the form

$$0 = R_k^{\frac{3}{2}} + a_k(\mathrm{i}b_k + c_k)R_k^{\frac{1}{2}} + \mathrm{i}a_k b_k F_k\,, \tag{5.17}$$

where $F_k \equiv A\mathrm{e}^{-\mathrm{i}\phi_k}$. The sum and the difference of Eq. (5.17) and its complex conjugate lead to

$$0 = R_k^{\frac{3}{2}} + a_k c_k R_k^{\frac{1}{2}} - a_k b_k \mathrm{Im}(F_k)\,, \tag{5.18a}$$

$$0 = R_k^{\frac{1}{2}} + \mathrm{Re}(F_k)\,. \tag{5.18b}$$

Using $\mathrm{Re}(F_k) = A\cos\phi_k$ and $\mathrm{Im}(F_k) = -A\sin\phi_k$, yields $R_k = A^2\cos^2\phi_k$ and

$$A^2\cos^3\phi_k + a_k c_k\cos\phi_k - a_k b_k\sin\phi_k = 0\,. \tag{5.19}$$

By exploiting $\cos^2\phi_k = 1/(1+\tan^2\phi_k)$, Eq. (5.19) can be further manipulated, yielding

$$w_k^3 - \eta_k w_k^2 + w_k - \eta_k - \mu_k = 0\,, \tag{5.20}$$

in which

$$w_k \equiv \tan\phi_k\,, \tag{5.21a}$$

$$\eta_k \equiv \frac{c_k}{b_k}\,, \tag{5.21b}$$

$$\mu_k \equiv \frac{A^2}{a_k b_k}\,, \tag{5.21c}$$

so that

$$R_k = \frac{A^2}{1+w_k^2}\,. \tag{5.22}$$

Eq. (5.20) is amenable to a computer algebra system[8]. The solutions read

$$w_k^{(1)} = \frac{1}{6}\left(2\eta_k + 2\cdot 2^{\frac{1}{3}}L_k + 2^{\frac{2}{3}}K_k\right)\,, \tag{5.23a}$$

$$w_k^{(2)} = \frac{1}{12}\left(4\eta_k - 4\cdot(-2)^{\frac{1}{3}}L_k + 2(-2)^{\frac{2}{3}}K_k\right)\,, \tag{5.23b}$$

$$w_k^{(3)} = \frac{1}{12}\left(4\eta_k + 4\cdot 2^{\frac{1}{3}}(-1)^{\frac{2}{3}}L_k - 2^{\frac{2}{3}}(1+\mathrm{i}\sqrt{3})K_k\right)\,, \tag{5.23c}$$

[8] `MATHEMATICA` was used to solve Eq. (5.20).

where

$$L_k \equiv \frac{1}{K_k}\left(-3+\eta_k^2\right), \tag{5.24a}$$

$$K_k \equiv \left(2\eta_k(9+\eta_k^2)+3(9\mu_k+S_k)\right)^{\frac{1}{3}}, \tag{5.24b}$$

$$S_k \equiv \sqrt{12(1+\eta_k^2)^2+12\eta_k(9+\eta_k^2)\mu_k+81\mu_k^2}. \tag{5.24c}$$

The criterion for selecting the appropriate solutions out of Eqs. (5.23) is

$$0 \leq \frac{R_k}{|A|^2} \leq 1 \tag{5.25}$$

since the the total power is conserved. The existence of multiple branches is thus in principle possible.

In Fig. 5.2(a), I display the transmittance for an incoming plane wave of power $|A|^2 = 1$ and momentum $k = \pi/2$ as a function of the side-coupling strength J' and the nonlinearity Δ. For these parameters, the solutions obtained from Eqs. (5.23)–(5.25) are unique. I explicitly accounted for the possibility of both positive and negative nonlinearities since there exist Kerr-nonlinear media of both types [173]. The features of Fig. 5.2(a) can be understood as follows. In the limit of vanishing nonlinearity, i. e., $\Delta \to 0$, a plane wave state with carrier momentum $k = \pi/2$ is always reflected completely, independent of the value of the side-coupling strength J'. The plane wave with energy $\epsilon_{k=\pi/2} = 0$ is on resonance with the side-coupled resonator's eigenfrequency $\Omega_0 = 0$. Conversely, if $J' \to 0$, any plane wave state is transmitted completely, since the side-coupled cavity is decoupled from the waveguide. Before discussing features such as self-induced transparency and bistability, Fig. 5.2(b) demonstrates that for the parameters investigated in Sec. 5.3.2, i. e., $J' = J$ and $\Delta = 0.05J$, the solutions (5.23) are unique. Similarly, Fig. 5.2(c) displays for a fixed side-coupling strength $J' = 0.6J$ and input power $|A|^2 = 1$ how an increasing nonlinearity Δ finally gives rise to a bistability in the transmission characteristics. Furthermore, Fig. 5.2(d) shows the tendency to enhance the transmittance when the input power is increased, resulting in self-induced transparency.

A complete analysis of the bistable transmission characteristics of coherent states in the underlying system would require a stability analysis of Eqs. (5.23). This, however, is beyond the scope of this chapter since, for the next section, I only need to know where a bistable situation could occur so that it can be avoided.

5.3.2 Single-Photon-Added Coherent State

In order to illustrate how the dynamics as described by Eqs. (5.6a), (5.6c), and Hamiltonian (5.8) may be exploited for manipulating photon transport on the few-photon level, I consider the situation of a propagating coherent state pulse which is "disturbed" by an accompanying single-photon wave packet.

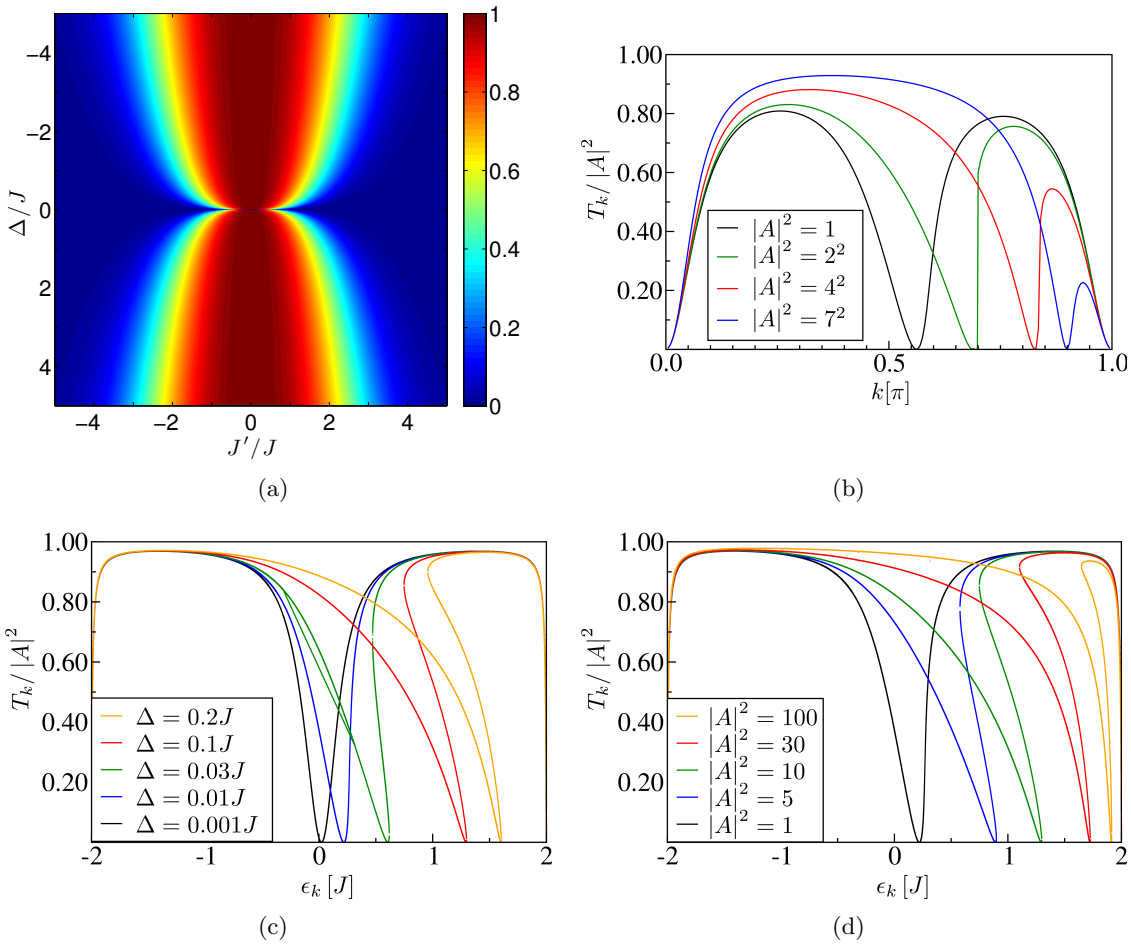

Figure 5.2: Transmission characteristics for a coherent state in a tight-binding waveguide with a side-coupled Kerr-nonlinear cavity.
(a) Normalized transmittance $T_k/|A|^2 = 1-R_k/|A|^2$ for an incoming plane wave of power $|A|^2 = 1$ and momentum $k = \pi/2$ as a function of the side-coupling strength J' and the nonlinearity Δ. For these parameters, the solutions according to Eqs. (5.23)–(5.25) are unique. (b) Normalized transmittance for $J' = J$ and $\Delta = 0.05J$ as a function of the wavenumber k. The resonance condition shifts with increasing input power $|A|^2$, which eventually leads to self-induced transparency. In the linear system, the resonance occurs at $k = \pi/2$ since $\epsilon_{\pi/2} = \Omega_0 = 0$. A slight shift can already be observed for $|A|^2 = 1$. The parameters for J' and Δ are those which are used in Sec. 5.3.2. Note that no bistability occurs. (c) Normalized transmittance as a function of the eigenenergy $\epsilon_k = -2J\cos(k)$ for a side-coupling strength of $J' = 0.6J$. The solutions according to Eqs. (5.23) become non-unique as the nonlinearity Δ is increased ($|A|^2 = 1$), leading to bistability. (d) An increase of the input power eventually leads to self-induced transparency ($\Delta = 0.01J$).

The initial center x_c and the width s (cf. Eq. (5.5) and Sec. 2.3.1) of both pulses are therefore chosen to be equal. The carrier wavenumbers, however, differ. I denote the latter by k_0^{MF} for the coherent state pulse, termed "mean field", and k_0^{FL} for the single-photon pulse, termed "fluctuations". As a specific example, I choose $k_0^{MF} = 0.6\pi$ and $k_0^{FL} = 0.5\pi$. This choice is guided by the fact that while the excitations are energetically well separated ($\epsilon(k_0^{MF}) = 0.618J$ and $\epsilon(k_0^{FL}) = 0$, cf. Fig. 5.1), their group velocities are quite similar ($v_{\mathrm{g}}(k_0^{MF}) = 1.902J$ and $v_{\mathrm{g}}(k_0^{FL}) = 2J$). The former property also ensures that the incoming coherent state pulse is sufficiently detuned with respect to the side-coupled resonator's eigenfrequency so that the approximations leading to the effective Hamiltonian (5.8) hold. The small difference in the group velocities results in a single-photon pulse which accompanies the coherent state pulse sufficiently long so that they still experience a strong spatial overlap when arriving at the position of the side-coupled resonator.[9] The fluctuations are on resonance with the latter, i. e., $\omega_0 = 0 = -2J\cos(k_0^{FL}a)$, while the mean-field part is detuned. Furthermore, for the subsequent computations, I choose $\Delta = 0.05J$ and denote the mean particle number in the initial coherent state pulse by $|\alpha^{(0)}|^2$. I would like to point out that the solution to the nonlinear scattering problem of the "pure" coherent states exhibits features such as self-induced transparency and bistability as was shown in Sec. 5.3.1. However, for the parameters I chose here, Eqs. (5.23) only yield one solution which satisfies constraint (5.25) (cf. Fig. 5.2(b)).

Figure 5.3(a) displays the corresponding time evolution for a weak mean-field part with $|\alpha^{(0)}|^2 = 1$ in the absence of losses ($\Gamma = 0$). In this case, the corresponding effective time-dependent scattering potential $4\Delta|\gamma(t)|^2$ is only weakly shifted from its bare (time-independent) value, which is zero (cf. Hamiltonian (5.8)). The single photon therefore essentially remains on resonance with the side-coupled resonator whereas the coherent state part is detuned. In essence, mean-field and fluctuations experience the side-coupled resonator as an energy-dependent mirror (cf. Ref. [108] and Chap. 3) resulting in the fluctuations being (almost completely) reflected while the mean-field part is partially reflected and partially transmitted. This situation can be drastically altered by increasing the mean-field intensity. In Fig. 5.3(b), the dynamics of the mean field and the fluctuations similar to Fig. 5.3(a) is shown but now with $|\alpha^{(0)}|^2 = 7^2$. For this intensity, the scattering potential is strongly modified such that the mean-field pulse is almost completely reflected. Conversely, the fluctuations are now partially transmitted and partially reflected. Upon interacting with the side-coupled resonator, the original pulse that consisted of a photon-added coherent state is split into a "purified" single-photon pulse in transmission and a reflected single-photon-added coherent state with a reduced intensity of the added photon. In other words, a single photon can be gated by a coherent state pulse.

[9] One could also envision a situation where the two pulses are launched from different positions such that they arrive simultaneously at the side-coupled cavity irrespective of their group-velocity mismatch. This scenario is not addressed in this chapter.

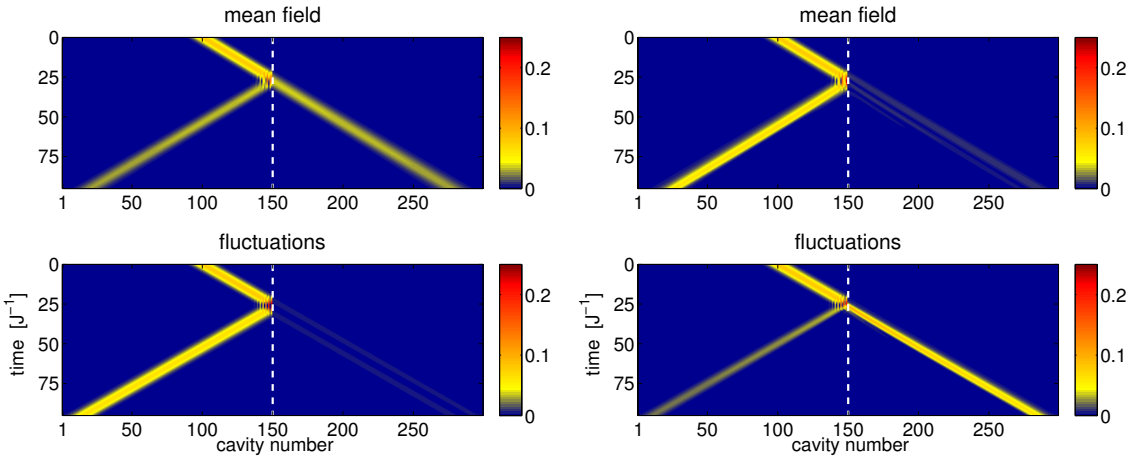

(a) $\alpha^{(0)} = 1$ (b) $\alpha^{(0)} = 7$

Figure 5.3: Time evolution of the normalized intensity for the coherent state's part ("mean field") and the "added" single-photon wave function ("fluctuations") in a single-photon-added coherent state.
The system parameters are $\Delta = 0.05J$, $J' = J$, and $\Gamma = 0$ (lossless case) for a coupled-resonator waveguide with 299 cavities. The side-coupled cavity couples to site $x_0 = 150$ (indicated by the white dashed line). The wavenumbers are $k_0^{MF} = 0.6\pi$ and $k_0^{FL} = 0.5\pi$ ($x_c = 100$ and $s = 7$). A change of the coherent state's initial field strength from (a) $\alpha^{(0)} = 1$ to (b) $\alpha^{(0)} = 7$ demonstrates how the tunable scattering potential for the fluctuations, which is controlled by the time evolution of the mean field, can be exploited to gate a single photon.

As can be seen from Fig. 5.3(b), the single photon is not transmitted completely. In order to realize full transmission while the coherent state part is completely reflected, a larger initial detuning between fluctuation and mean field would be required. However, for the underlying system, the cosine-dispersion relation of the tight-binding waveguide provides certain constraints on the detunings between both pulses and between the pulses and the side-coupled resonator. Due to the nonlinear nature of the cosine-dispersion relation a larger detuning would result in spatial walk-off effects between the two pulses as a consequence of group-velocity dispersion. Such limitations can in principle be overcome via tailored and/or tunable dispersion relations such as those in Photonic Crystal waveguides (cf. Sec. 1.2.2) or in dispersion-engineered superconducting circuitry in the microwave domain [19, 20].

The robustness of the gating mechanism is analyzed by repeating the above simulations for different values of the decay rate Γ of the side-coupled cavity (cf. Hamiltonian (5.8)). In order to quantify the effect of dissipation, I compute the normalized overlap for both the coherent state part and the single added photon in the lossless case ($\Gamma = 0$). According to

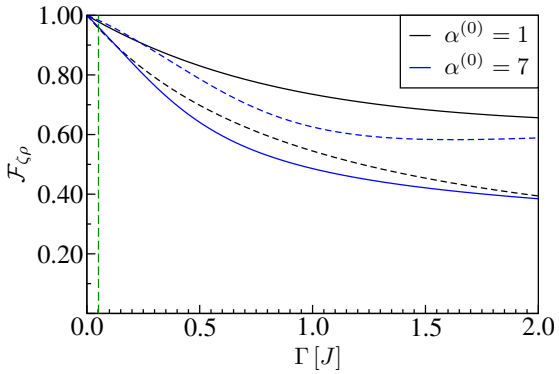

Figure 5.4: Fidelities as defined in Eq. (5.26) as a function of the decay rate Γ of the side-coupled cavity.
As a reference, the field distributions after scattering are used for the two lossless cases as shown in Fig. 5.3. Dashed lines correspond to fluctuations and solid lines represent mean fields. Black curves represent the case $\alpha^{(0)} = 1$ (cf. Fig. 5.3(a)) and blue curves denote the case $\alpha^{(0)} = 7$ (cf. Fig. 5.3(b)). The dashed green line indicates the value of the nonlinearity $\Delta = 0.05J$.

Eq. (1.92), the quantity

$$\mathcal{F}_{\zeta\rho}(t) = \frac{\left|\sum_x \zeta_x^*(t)\rho_x(t)\right|}{\sqrt{N_\zeta(t)N_\rho(t)}} \tag{5.26}$$

serves as a measure of the fidelity. In this definition, ζ_x and ρ_x signify, respectively, the wave function coefficients of the reference states, i. e., for $\Gamma = 0$, and for finite values of Γ. $\mathcal{N}_\zeta$ and $\mathcal{N}_\rho$ are the initial norms of both states. For the coherent state part, one has to set $\zeta, \rho = \alpha$, whereas for the added single photon $\zeta, \rho = \varphi$. Equation (5.26) is evaluated at time $t = 95J^{-1}$, which is when the scattering is completed but before the wave packets reach the system's boundaries.

In Fig. 5.4, I display the fidelities as defined in Eq. (5.26) for both the coherent state part and the single added photon as a function of the decay rate Γ of the side-coupled cavity. As expected, the performance of the demonstrated single-photon gate becomes worse as the decay rate is increased. However, this decay rate has to be compared to other scales in the system such as the nonlinearity $\Delta = 0.05J$. As can be seen from Fig. 5.4, the fidelities only slightly drop for decay rates comparable to the nonlinearity, i.e., $\Gamma \sim \Delta$. Only $\Gamma \gg \Delta$ seriously affects the fidelities. Thus, the investigated gating mechanism shows a certain degree of robustness against photon loss.

5.3.3 Comment on a Possible Realization in an Optomechanical Setup

Although the previous investigations and the underlying Hamiltonian (5.1) refer to "usual" Kerr-nonlinear systems, e. g., $\chi^{(3)}$-nonlinearities (cf. Sec. 1.3.2), one can also think of a realization in the context of optomechanics. As shown in Sec. 1.3.2, optomechanical systems in the limit of weak phonon–photon interactions and when the mechanical degrees of freedom are in contact with a thermal reservoir effectively behave like Kerr-nonlinear systems. Adapted to the geometry of a tight-binding waveguide of mechanically inactive resonators with a side-coupled optomechanical cavity, a Hamiltonian similar to Eq. (1.83) can be formulated, leading to

$$H = \sum_x \omega_0 a_x^\dagger a_x - J\sum_x (a_{x+1}^\dagger a_x + a_x^\dagger a_{x+1}) - \bar{J}'(a_{x_0}^\dagger c + a_{x_0} c^\dagger) + \big(\Omega_0 - \Delta\big)\, c^\dagger c - \Delta c^\dagger c^\dagger cc - \mathrm{i}\frac{\Gamma}{2} c^\dagger c\,. \tag{5.27}$$

Now, instead of a $\chi^{(3)}$-nonlinearity, the optomechanical nonlinearity g and the mechanical frequency of the side-coupled resonator ν constitute the nonlinearity $\Delta = g^2/\nu \geq 0$ (cf. Sec. 1.3.2). When compared to Eq. (5.1), the sign of the nonlinear term $-\Delta c^\dagger c^\dagger cc$ is always negative, leading to the effective photon–photon interaction being attractive. Furthermore, the side-coupled resonator's optical eigenfrequency experiences a polaron shift, which can be neglected in the case of a weak optomechanical nonlinearity. Then, the smallest energy scale in the original Hamiltonian (1.71) is set by g. Specifically, the elimination of the phononic degrees of freedom in Sec. 1.3.2 suggests $\kappa = g/\nu \ll 1$. In addition, the optical eigenfrequencies usually exceed the mechanical frequencies by orders of magnitude so that $\nu \ll \omega_0, \Omega_0$. The side coupling strength $\bar{J}'$ is "renormalized" according to Eq. (1.84), i. e.,

$$\bar{J}' = \chi(\kappa) J' \tag{5.28}$$

in which J' is the "bare" side-coupling strength and

$$\chi(\kappa) = \mathrm{e}^{-\kappa^2\left(B_\nu(\beta)+\frac{1}{2}\right)}\,, \tag{5.29a}$$

$$B_\nu(\beta) = \frac{1}{\mathrm{e}^{\beta\nu}-1}\,. \tag{5.29b}$$

Since only the side-coupled resonator is assumed to exhibit an optomechanical nonlinearity, only one factor of χ appears in Eq. (5.28) (cf. Eq. (1.84)). Note that in the case of a tight-binding waveguide consisting of optomechanically active resonators, the renormalization of the hopping terms can result in a reduction of the bandwidth[10] of the waveguide's dispersion relation. However, this issue is not discussed in this thesis.

In order to get a feeling of how the hopping terms are modified due to phonon–photon coupling, I give one example for the numerical value of $\chi(\kappa)$ by using (SI units, angular frequencies) $g = 1$ kHz, $\nu = 10$ MHz, and $T = 300$ K, which represent moderate values when

[10] The "bare" bandwidth of the tight-binding waveguide is $4J$.

compared to state-of-the art experiments (for instance, see Refs. [94, 174] and references therein). These parameters yield $\chi \simeq 0.96$. Even though the nonlinearity Δ can also be calculated from these numbers, its value needs to be compared to the waveguide's inter-cavity hopping term J, which determines the bandwidth of the dispersion relation and represents the "fundamental scale" in the system. Furthermore, for the gating of a single photon as demonstrated in Fig. 5.3, the actual value of Δ is not important since it can be compensated by higher mean-field intensities[11]. In other words, the effective scattering potential experienced by the fluctuations depends on the product of the coherent state's intensity in the side-coupled cavity and the nonlinearity (cf. Hamiltonian (5.8)).

Setting $\omega_0 = \Omega_0$, shifting the middle of the waveguide band to zero, and neglecting the polaron shift, the effective Hamiltonian experienced by a single photon in a photon-added coherent state reads (cf. Eq. (5.8))

$$H_{\text{eff}} = -J\sum_x (a^\dagger_{x+1}a_x + a^\dagger_x a_{x+1}) - \bar{J}'(a^\dagger_{x_0}c + a_{x_0}c^\dagger) - 4\Delta|\gamma(t)|^2 c^\dagger c - \mathrm{i}\frac{\Gamma}{2}c^\dagger c\,. \tag{5.30}$$

The only formal difference to Hamiltonian (5.8) is the minus sign in front of the scattering potential. Since in the optomechanical case, Δ is always positive, the shift which is induced by the mean-field intensity is always to lower energies in the cosine-dispersion relation. This corresponds to a negative nonlinearity in the analytical scattering solutions for coherent states (cf. Sec. 5.3.1). However, due to the symmetry of the cosine-dispersion relation, the results presented in Fig. 5.3 remain valid for the optomechanical case if the carrier wavenumber of the mean field is changed according to $k_0^{MF} = 0.6\pi \to 0.4\pi$. The wavenumber of the fluctuations need not be changed because $k_0^{FL} = 0.5\pi$ is in the middle of the waveguide band (cf. Fig. 5.1). Here, $\bar{J}' = \chi J' = J$ can either be approximately realized by assuming a weakly modified side-coupling strength and $J' = J$ or by different "bare" hopping terms which become equal after a modification due to phonon–photon coupling. However, in Sec. 5.3.2, I only assumed $J' = J$ for simplicity. This is not a crucial requirement of the gating mechanism. Altogether, the results presented in this chapter are applicable to a wide range of physical systems including optomechanical waveguide–cavity arrays in the certain limit discussed above and in Sec. 1.3.2.

5.4 Conclusion, Outlook, and Critical Discussion

In conclusion, I investigated the transport properties of coherent states and single-photon-added coherent states in a tight-binding waveguide with a side-coupled Kerr-nonlinear resonator. Interesting effects such as self-induced transparency and bistability occur on the level of coherent states. The analysis of single-photon-added coherent states revealed that

[11] However, if the intensities are too high, nonlinear effects up to ionization processes and material destruction become important.

the coherent state part effectively separates from the single-photon part, allowing for a tunable scattering potential. Given appropriately chosen initial states, this allows one to split off individual photons from composite pulses. Such a mechanism could be exploited for the gating of single photons, which is useful for solid-state based quantum optical functional elements. Due to the general and prototypical character of the model system I investigated, physical realizations can be envisioned in various fields. In addition to the realization in the context of a resonator with a classical $\chi^{(3)}$-nonlinearity, I specifically commented on a possible realization in the field of optomechanics.

Future work might include the investigation of the dynamics of Fock states. This is in very close analogy to the system of a two-level atom in a waveguide (cf. Chap. 3) and was already studied for a slightly different model system in Ref. [74]. Similar to the case of a two-level atom, unusual correlations such as photon–photon bound states [117, 118] and interaction-induced radiation trapping by virtue of atom–photon bound states (cf. Chap. 3 and Refs. [61, 62]) can become important. However, whereas a single two-level atom is a saturable absorber which cannot absorb two photons at once, Kerr nonlinearities are usually rather weak. The effect of a single Kerr-nonlinear resonator on the dynamics of, say, two photons should therefore be almost negligible. Nonetheless, considerable effects could be achieved by side-coupling a chain of nonlinear resonators to the waveguide. Such a system is in close analogy to Jaynes-Cummings-Hubbard systems [15, 64, 65, 68, 157, 169]. Similar to the emergence of polariton branches, the existence of an "impurity band" which is induced by the Kerr nonlinearity could be discussed.

A "natural" extension to the dynamics of a single-photon-added coherent state is the case of a two-photon-added coherent state. However, such an extension is non-trivial since some terms which vanish for the case of a single photon in Eq. (5.6d) contribute in the case of two photons. Furthermore, if it were possible to deduce an effective, time-dependent, two-photon Hamiltonian in analogy to Eq. (5.7), it would contain interaction terms. Even more problematic is the extension to the case of a two-level atom in a waveguide since the atomic degree of freedom is not bosonic and can therefore not be transformed to a displaced basis which enabled the discussion in Sec. 5.3.2.

The approach presented in this chapter could be criticized with regard to the following points. Even though the approximations leading to the effective, particle-number conserving Hamiltonian (5.8) were motivated on a qualitative level in the spirit of the rotating-wave approximation, I did not give a controlled approximation in the sense that I quantitatively defined the range of validity. The approximations performed were led by the idea of arriving at an effective Hamiltonian which conserves the total number of excitations so that a numerical approach becomes possible (cf. Chap. 2). Furthermore, as already mentioned above, an analysis by virtue of single-photon-added coherent states is not general or readily applicable to the multi-particle case.

With regard to the physical description, dissipation was only included in a simple manner, i. e., I only considered a "leaky" cavity. However, also the waveguide itself suffers from dissipation and, furthermore, the effect of dephasing was completely neglected in this chapter.

The discussion on a possible realization in the context of an optomechanical system (cf. Sec. 5.3.3) relies on the validity of the approximation performed in Sec. 1.3.2. Even though the idea of replacing all phononic operators by their free thermodynamic expectation values is reasonable if the mechanical degrees of freedom are not subject to a special state preparation, a rigorous quantitative statement on the validity of such an approximation was not given. Again, this approximation was driven by the goal of arriving at an effective Hamiltonian which conserves the total number of excitations.

Chapter 6

6 Spontaneous Emission of a Single-Photon Emitter in a Structured Continuum of Modes

In this chapter, I investigate spontaneous emission of a single two-level atom embedded in a structured continuum of electromagnetic modes. Quantities such as the population of the atom's excited state as a function of time, output spectra as well as atom–field and field–field correlation functions are determined. I explicitly consider dissipation and dephasing of the atom. In addition, lossy field modes and the effect of an open waveguide are taken into account. Specifically, I study a one-dimensional model of coupled resonators for which two regimes of radiation dynamics are identified, i. e., the "Purcell regime", in which the time evolution of the atomic degree of freedom does not strongly depend on its past, and the regime of non-Markovian dynamics, in which memory-induced back-action effects cause anomalous spontaneous emission.

6.1 Introduction

Spontaneous emission—the decay of an excited atom into the electromagnetic vacuum without external trigger—has many fascinating aspects and is both a long-standing fundamental problem in theoretical physics and of paramount importance in applied modern optical technologies. Historically, the first theoretical description of spontaneous emission can be dated back to Einstein's work on the quantum theory of radiation almost one century ago [175]. He coined the term "A coefficient", which became an essential component of modern laser theories [104]. Einstein's A coefficient is related to the atomic lifetime for which a theory was developed by Weisskopf and Wigner [176]. In these early descriptions, spontaneous emission is the exponential decay of the occupation of an excited atomic level and therefore characterized completely by the atomic lifetime.

Although this lifetime depends both on atomic and photonic properties, the features of the electromagnetic vacuum, i. e., its dispersion relation, enter the description just as external parameters. For a long time, there was no theoretical concept on how to qualitatively alter the exponential decay although a control of the decay rate could already be demonstrated by Purcell in the forties [177]. Moreover, there were several theoretical and experimental studies on the issue of spontaneous emission in the vicinity of metallic surfaces (for instance, see Refs. [178–180]). However, all these effects primarily cause a renormalization of the lifetime. Hence, the emission spectra exhibit a Lorentzian lineshape.

At first sight, one might call it pedantic to recheck the early theories of the exponential spontaneous decay since they are successfully applied in various situations. Nonetheless, the Wigner-Weisskopf theory relies on the approximation that the density of electromagnetic states is a slowly varying, featureless function of frequency in the vicinity of the atomic transition energy. This is especially true for vacuum or homogeneous bulk media where the dispersion relation is linear in the photon momentum and has no cutoff. With the advent of modern nanophotonics, new classes of optical materials, e. g., Photonic Crystals, were developed, which can be used to tailor the photonic dispersion relation almost arbitrarily at will (cf. Sec. 1.2.2). Given the rich band structure of these materials, especially the possibility of a photonic band gap, one has to carefully reexamine the applicability of the Wigner-Weisskopf theory and variations thereof.

E. Yablonovitch proposed structured dielectrics as a means to inhibit spontaneous emission in 1987 [181]. From the nineties on, S. John *et al.* demonstrated in a series of papers [182–189] that the problem of spontaneous emission in photonic band gap media can only be accounted for accurately if the description goes beyond the well-established Wigner-Weisskopf theory. In particular, rapid variations in the density of electromagnetic states can lead to non-Markovian dynamics, i. e., the time evolution of the atomic degree of freedom strongly depends on its past—the atom "develops a memory". Moreover, the existence of band gaps results in a special class of dressed eigenstates—atom–photon bound states. These polaritonic states result in a fractional decay in the long-time limit. In other words, the atom does not decay completely to its ground state and is surrounded by a spatially confined fraction of localized light.

From a theoretical point of view, topics such as non-Markovianity and atom–photon bound states are of great interest in their own right. Besides this, the ultimate control of spontaneous emission is a goal which would boost the progress in many fields of quantum optics. In the related problem of resonance fluorescence, bound atom–photon states might be an approach to realize an optical memory device [185] or to achieve all-optical switching [190, 191].

To date, non-Markovian radiation dynamics was investigated theoretically in a number of different contexts. The works of S. John *et al.* use analytical models for the photonic density of states. The authors of Ref. [192] provide an alternative, approximate numerical treatment, albeit with a simplified model of the dispersion relation. P. Kristensen *et al.* applied the method presented in Ref. [188] to the case of the three-dimensional inverse opal structure [193]. Non-Markovian dynamics was observed experimentally in the context of cav-

ity quantum electrodynamics [194]. However, signatures of non-Markovianity in nanoscopic systems where a single emitter is coupled to a continuum of modes (and not just to a single mode of a cavity) are still to be expected. To the best of my knowledge, the first experimental demonstration of non-Markovian dynamics in Photonic Crystals was given by U. Hoeppe *et al.* [195], who used a woodpile Photonic Crystal of macroscopic size in the microwave domain.

In this chapter, I apply the computational scheme I described in Chap. 2 to the problem of spontaneous emission in an effectively one-dimensional system. The outline is as follows. In Sec. 6.2, I review the theoretical foundations and the relevant physical quantities which are important for the investigation of spontaneous emission of a single two-level emitter in a structured continuum. Then, in Sec. 6.3, I present a study of the dynamics of spontaneous emission in a one-dimensional model of coupled resonators under the assumption of a momentum-independent atom–photon coupling. With the help of correlation functions and spatially resolved output spectra, I show how one can distinguish the "Purcell regime", in which the time evolution of the atomic degree of freedom does not strongly depend on its own past, from the regime of non-Markovian dynamics. In addition, the influence of non-radiative damping and dephasing of the emitter, an open waveguide, and lossy field modes are investigated. I conclude the chapter in Sec. 6.4.

6.2 Fundamentals

In this subsection, I present the theoretical description relevant to the problem of spontaneous emission of a single two-level atom in a structured continuum. This includes the formulation of the Hamiltonian, a suitable initial condition, and a formal solution of the problem. Furthermore, I adapt the quantities as defined in Sec. 1.3.3 for the purpose of this chapter.

6.2.1 Theoretical Formulation

Throughout this chapter, I study the radiation dynamics of a single two-level system which is coupled to a multi-mode radiation field via a dipole-allowed transition. In the dipole and rotating-wave approximation, the generic Hamiltonian for such a system is given by a Hamiltonian of the form (cf. Eq. (2.4) and Chaps. 1–2 for details)

$$H = \sum_{n\mathbf{k}} \omega_{n\mathbf{k}} a^\dagger_{n\mathbf{k}} a_{n\mathbf{k}} + \frac{\Omega}{2}\sigma_z + \sum_{n\mathbf{k}} \left(V_{n\mathbf{k}} a_{n\mathbf{k}} \sigma^+ + V^*_{n\mathbf{k}} a^\dagger_{n\mathbf{k}} \sigma^- \right) . \tag{6.1}$$

The corresponding real-space formulation according to Eq. (2.5) reads

$$H = \sum_{n\mathbf{r}\mathbf{r}'} J_{n\mathbf{r}\mathbf{r}'} a^\dagger_{n\mathbf{r}}\, a_{n\mathbf{r}'} + \frac{\Omega}{2}\sigma_z + \sum_{n\mathbf{r}} \left(G_{n\mathbf{r}} a_{n\mathbf{r}} \sigma^+ + G^*_{n\mathbf{r}} a^\dagger_{n\mathbf{r}} \sigma^- \right) . \tag{6.2}$$

As discussed in detail in Chaps. 1 and 2, these two Hamiltonians are equivalent and connected via a Fourier lattice transform (cf. Eqs. (2.6)–(2.8b)).

In the following, I use the initial condition of an excited atom and the radiation field being in its vacuum state (cf. Eq. (2.27)), i. e.,

$$|\Psi(0)\rangle = |0,\uparrow\rangle\,. \tag{6.3}$$

Since a single two-level system is a single-photon source and the Hamiltonians (6.1) and (6.2) conserve the total number of excitations, the problem of spontaneous emission is a single-particle problem. Hence, the total state vector of the combined system of atom and field modes can be written in the general form

$$|\Psi(t)\rangle = \sum_{n\mathbf{k}} g_{n\mathbf{k}}(t) a^\dagger_{n\mathbf{k}} |0,\downarrow\rangle + e(t)\,\big|0,\uparrow\big\rangle\,, \tag{6.4}$$

where $g_{n\mathbf{k}}(t)$ are the wave function amplitudes (in $\mathbf{k}$-space) of the radiation field and $e(t)$ is the probability amplitude of finding the atom in its excited state. Correspondingly,

$$|\Psi(t)\rangle = \sum_{n\mathbf{r}} \varphi_{n\mathbf{r}}(t) a^\dagger_{n\mathbf{r}} |0,\downarrow\rangle + e(t)\,\big|0,\uparrow\big\rangle \tag{6.5}$$

is the form of the state vector after a Fourier lattice transform was applied (cf. Chap. 2 for details).

6.2.2 Formal Solution

In the interaction picture, the solution of the time-dependent Schrödinger equation with Hamiltonian (6.1) and state (6.4) can be written as [184, 188]

$$\frac{\mathrm{d}}{\mathrm{d}t} e(t) = -\int_0^t \mathrm{d}t' K(t-t') e(t')\,. \tag{6.6}$$

In this integro-differential equation,

$$K(\tau) = \theta(\tau) \sum_{n\mathbf{k}} \big|V_{n\mathbf{k}}\big|^2\, \mathrm{e}^{-\mathrm{i}(\epsilon_{n\mathbf{k}}-\Omega)\tau} \tag{6.7}$$

is a time-delay Green's function (memory kernel) which accounts for all back-action effects on the atomic excitation due to the surrounding medium. The kernel can be calculated analytically for a few simplified situations (cf. Sec. 6.3.2).

However, already at this stage, one can see from Eq. (6.6) that true exponential decay occurs if and only if $K(\tau) = (\Gamma/2)\,\delta(\tau)$. If the memory kernel decays on a time scale which is faster than all other time scales in the problem, one expects the emission dynamics to be approximately exponential. Here, $\theta(\tau)$ and $\delta(\tau)$ are the Heaviside and the Dirac delta function, respectively. The spontaneous emission decay rate is Γ.

6.2.3 Physical Quantities

All relevant physical quantities which describe the radiation dynamics can be calculated from the state vector $|\Psi(t)\rangle$. Here, I briefly review and adapt these quantities as introduced in Chap. 1. Section 1.3.3 provides further details. In Sec. 6.3, the band indices are suppressed for the single-band model.

Occupation Numbers and Correlation Functions

The occupation of the excited atomic state as a function of time according to Eq. (1.86) is determined via

$$\langle\sigma^+\sigma^-\rangle(t) = \frac{1}{2}\left(\langle\sigma_z\rangle(t) + 1\right) , \tag{6.8}$$

for which $0 \leq \langle\sigma^+\sigma^-\rangle(t) \leq 1$ holds.

According to Eq. (1.87), field–field correlation functions are defined as

$$C^{\mathrm{ff}}_{n\mathbf{r}\ n'\mathbf{r}'}(t,t') = \langle a^\dagger_{n\mathbf{r}}(t) a_{n'\mathbf{r}'}(t')\rangle . \tag{6.9}$$

In this chapter, I only investigate temporal field–field correlation functions for $n = n'$ and $\mathbf{r} = \mathbf{r}' = \mathbf{R}_0$. Since the problem of spontaneous emission is a single-particle problem, higher order correlation functions such as $g^{(2)}$ are identical to zero. By the same token, atom–field correlation functions are obtained via (cf. Eq. (1.89))

$$C^{\mathrm{af}}_{n\mathbf{r}}(t,t') = \langle\sigma^+(t) a_{n\mathbf{r}}(t')\rangle . \tag{6.10}$$

In this chapter, I only consider atom–field correlations in the unit cell of the atom.

Output Spectrum

In line with Eq. (1.88), the contribution to the output spectrum of band n recorded in unit cell $\mathbf{r}$ reads

$$\begin{aligned} S_{n\mathbf{r}}(\omega) &= \int_{-\infty}^{\infty} \mathrm{d}\tau \mathrm{e}^{\mathrm{i}\omega\tau} \langle a^\dagger_{n\mathbf{r}}(t+\tau) a_{n\mathbf{r}}(t)\rangle \\ &= \int_{-\infty}^{\infty} \mathrm{d}\tau \mathrm{e}^{\mathrm{i}\omega\tau} C^{\mathrm{ff}}_{n\mathbf{r}n\mathbf{r}}(t+\tau, t) . \end{aligned} \tag{6.11}$$

Using the general form (6.5) for the state vector yields

$$C^{\mathrm{ff}}_{n\mathbf{r}\ n\mathbf{r}}(t+\tau, t) = \varphi^*_{n\mathbf{r}}(t+\tau) \cdot \varphi_{n\mathbf{r}}(t) \tag{6.12}$$

with which one arrives at

$$\begin{aligned} S_{n\mathbf{r}}(\omega) &= \int_{-\infty}^{\infty} \mathrm{d}\tau \mathrm{e}^{\mathrm{i}\omega\tau} \varphi_{n\mathbf{r}}^*(t+\tau)\varphi_{n\mathbf{r}}(t) \\ &= \left| \int_{-\infty}^{\infty} \mathrm{d}\tau \mathrm{e}^{\mathrm{i}\omega\tau} \varphi_{n\mathbf{r}}(\tau) \right|^2 \\ &= \left| \tilde{\varphi}_{n\mathbf{r}}(\omega) \right|^2 . \end{aligned} \tag{6.13}$$

Here, I applied the Wiener-Khintchine theorem in order to relate the Fourier transform of the temporal cross correlation function of a field to its power spectrum [99]. This procedure is only valid for a stationary process. However, as already mentioned in Sec. 1.3.3, $S_{n\mathbf{r}}(\omega)$ actually still depends on one time argument and is the spectrogram rather than the spectrum. Strictly speaking, spontaneous emission does not represent a stationary process. Nonetheless, in the single-particle case, Eq. (6.13) is just given by the Fourier transform of the photonic wave function, $S_{n\mathbf{r}}(\omega) = |\tilde{\varphi}_{n\mathbf{r}}(\omega)|^2$, which is a reasonable definition for a spectrum.

6.2.4 Comments on a Semiclassical Treatment

Radiation dynamics can in principle also be studied in a semiclassical approach according to the Maxwell-Bloch equations [107]. Here, I briefly comment on the peculiarities occurring in the context of spontaneous emission of a single-photon emitter as studied in this chapter.

In a semiclassical theory, an ensemble of two-level systems is effectively described as a single spin whose equations of motion are given by the optical Bloch equations [107]. In turn, they are driven by the classical electromagnetic field which propagates according to Maxwell's equations. The central approximation in the Maxwell-Bloch theory is a factorization of radiation field and atomic operators, i. e.,

$$\langle \sigma^+ a_{\mathbf{k}} \rangle \approx \langle \sigma^+ \rangle \langle a_{\mathbf{k}} \rangle . \tag{6.14}$$

In other words, atom–field correlations are neglected. The calculations presented in the preceding sections, however, confirm non-zero correlators (6.10) and, for a Fock state of the form (6.4), the expectation values do not factorize. In this chapter, I do not describe the dynamics of the two-level system in terms of a reduced density matrix for the atom. Hence, I do not refer to the usual picture of the Bloch sphere. Since I treat the electromagnetic field modes as part of the system rather than as passive reservoir degrees of freedom, the expectation values

$$\langle \sigma^+ \rangle = \langle \sigma^- \rangle = \langle a_{\mathbf{k}}^\dagger \rangle = \langle a_{\mathbf{k}} \rangle = 0 \tag{6.15}$$

vanish for a Fock state of the form (6.4).

6.3 Emission Dynamic in a One-Dimensional System

In this section, I investigate spontaneous emission in the context of a one-dimensional model continuum of modes. This model—a two-level atom in a tight-binding waveguide—exhibits atom–photon bound states (cf. Chap. 3) which can lead to non-Markovian behavior [184, 188].

6.3.1 Formulation

The Hamiltonian for a one-dimensional lattice with nearest-neighbor coupling J and a local atom–photon coupling V reads (cf. Chaps. 2–4 and Eq. (6.2))

$$H = -J \sum_x \left(a_{x+1}^\dagger a_x + a_x^\dagger a_{x+1} \right) + \frac{\Omega}{2} \sigma_z + V \left(\sigma^+ a_{x_0} + a_{x_0}^\dagger \sigma^- \right) , \tag{6.16}$$

where Ω is the transition energy of the two-level system. The photonic dispersion relation of the tight-binding lattice is $\epsilon_k = -2J\cos(k)$, where $k \in [-\pi, \pi]$ (cf. Fig. 6.1). Dimensionless units according to Appendix A are employed throughout this section.

6.3.2 Density of States and Memory Kernel

For the evaluation of the time-delay Green's function, I rewrite Eq. (6.7) according to

$$\begin{aligned} K(\tau) &= \theta(\tau) \sum_k \left| V_k \right|^2 \mathrm{e}^{-\mathrm{i}(\epsilon_k - \Omega)\tau} \\ &= \int_{-\infty}^{\infty} \mathrm{d}\omega \; \theta(\tau) \sum_k \frac{V^2}{N} \mathrm{e}^{-\mathrm{i}(\epsilon - \Omega)\tau} \delta(\omega - \epsilon_k) \\ &= \theta(\tau) V^2 \mathrm{e}^{\mathrm{i}\Omega\tau} \int_{-\infty}^{\infty} \mathrm{d}\omega \; \mathcal{N}(\omega) \mathrm{e}^{-\mathrm{i}\omega\tau} , \end{aligned} \tag{6.17}$$

where I used the definition $\mathcal{N}(\omega) = \frac{1}{N} \sum_k \delta(\omega - \epsilon_k)$ of the density of states[1]. Here, the atom–photon coupling in momentum space is $V_k = V/\sqrt{N}$, where N is the number of unit cells. The density of states as shown in Fig. 6.1 can be calculated analytically [93], yielding

$$\mathcal{N}(\omega) = \frac{1}{2\pi J} \frac{\theta(\omega + 2J)\theta(2J - \omega)}{\sqrt{1 - \left(\omega/2J\right)^2}} . \tag{6.18}$$

[1] This definition should be understood in the limit where k is quasi-continuous and the sum can be replaced by an integral (cf. Ref. [93]).

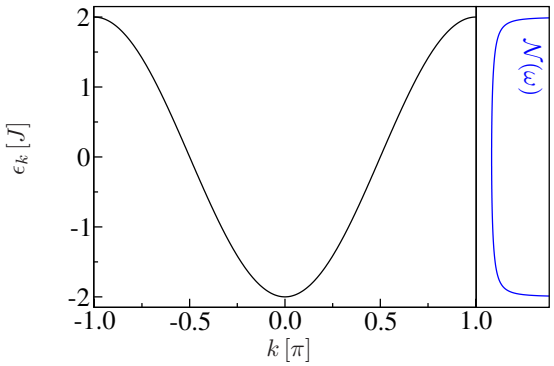

Figure 6.1: Cosine dispersion $\epsilon_k = -2J\cos(k)$ and corresponding density of states $\mathcal{N}(\omega)$.

Inserting Eq. (6.18) into Eq. (6.17) results in (cf. Appendix E)

$$K(\tau) = \theta(\tau)V^2 \mathrm{e}^{\mathrm{i}\Omega\tau} J_0(2J\tau)\,, \tag{6.19}$$

where J_0 signifies the zeroth order Bessel function of first kind. The asymptotic behavior of the Bessel function for $J\tau \gg 1$ is

$$K(\tau) \quad \approx \quad \theta(\tau)\frac{V^2}{\sqrt{\pi J\tau}}\mathrm{e}^{\mathrm{i}\Omega\tau}\cos(2J\tau - \frac{\pi}{4})\,. \tag{6.20}$$

Hence, the memory kernel can decay very slowly with respect to time, indicating long-time correlations between atom and field.

An important scale in the system described by Hamiltonian (6.16) is the bandwidth $4J$ of the dispersion relation. If J exceeds all other scales in the system (such as V and Ω), the band edges at energies $\pm 2J$ become unimportant. In that case, one expects the system to behave like a system with a one-dimensional linear dispersion relation without cutoff. The memory kernel corresponding to a dispersion relation $\epsilon_k = c|k|$ with photon velocity c takes the form (cf. Appendix E)

$$K(\tau) = \frac{V^2}{c}\delta(\tau)\,. \tag{6.21}$$

This kernel represents an exponential decay with a rate $\Gamma = 2V^2/c$. In order to relate this result to the scales of the tight-binding system, one has to identify the velocity scale c. To this end, I consider the magnitude of the group velocity v_g of the cosine dispersion[2] at $k = \pm\pi/2$, i. e., $|v_g| = |2J\sin(\pi/2)| = 2J$. The cosine-dispersion relation yields the best approximation to a linear dispersion relation at $k = \pm\pi/2$. Hence, I identify $c \to 2J$ so that

[2]For simplicity, I assume a so-called right-handed dispersion relation with $J > 0$. However, the argument could also be modified for $J < 0$.

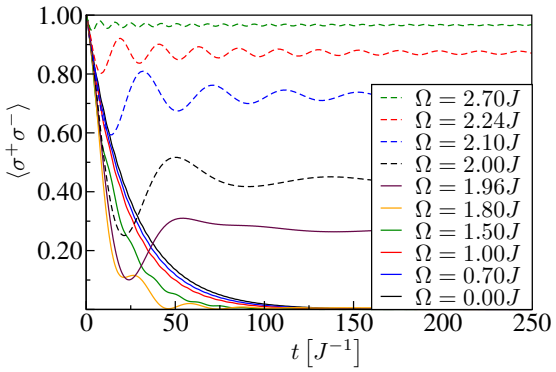

Figure 6.2: Time evolution of the occupation of the excited atomic level $\langle\sigma^+\sigma^-\rangle$ for an atom–photon coupling strength $V = 0.2J$ and different atomic transition energies Ω. For energies deep inside the band (solid black, blue and red line) the emission dynamics is exponential. When approaching the upper band edge, memory effects become more and more pronounced, resulting in self-induced Rabi oscillations and a fractional long-time excitation of the atom.

the decay rate becomes $\Gamma = V^2/J$. The proportionality $\Gamma \propto V^2$ is also consistent with a perturbative treatment according to Fermi's golden rule.

When the memory kernel is of the form (6.21) or it has the property that it decays on a time scale much smaller than all other time scales in the system, exponential or nearly exponential decay is observed. Such kind of Markovian dynamics gives rise to the Purcell effect [177], i. e., a modification of the spontaneous emission rate. In the following, I refer to the regime in which $K(\tau) \approx (\Gamma/2)\ \delta(\tau)$ holds as the "Purcell regime".

6.3.3 Emission Dynamics in the Lossless Case

Before I systematically investigate the influence of several loss mechanisms on the emission dynamics, I focus on the lossless case. In the following, I apply the numerical scheme outlined in Chap. 2 to a system of $N = 999$ lattice sites. The atom couples to site $x_0 = 500$, which is in the middle of the chain.

Influence of the Atomic Transition Energy and the Atom–Photon Coupling Strength

Figure 6.2 displays the time evolution of the excited atomic state for an atom–photon coupling strength $V = 0.2J$ and different atomic transition energies Ω below ($|\Omega| < 2J$) and above ($|\Omega| > 2J$) the band edges (cf. Fig. 6.1). For an atomic transition energy in the middle of the band ($\Omega = 0$) and weak coupling ($V \ll J$), the emission dynamics is characterized by an exponential decay with a rate $\Gamma = V^2/J$ (Fig. 6.3(a)). As the distance to a band edge is

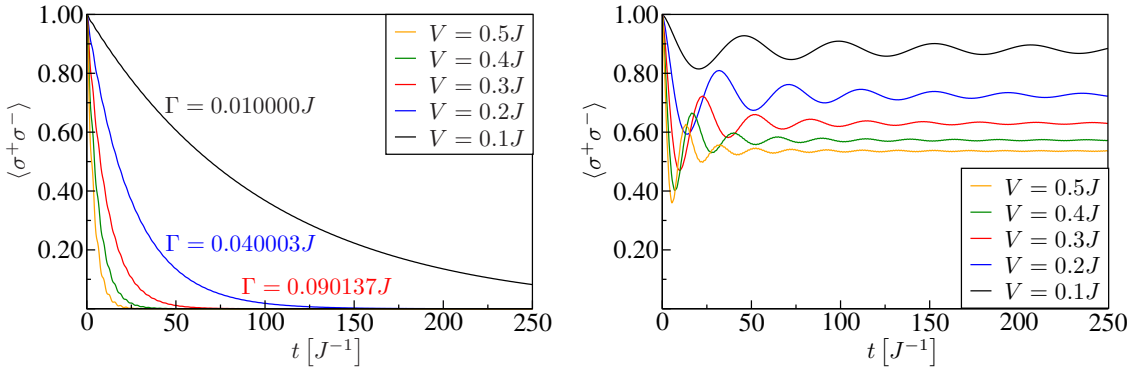

Figure 6.3: Time evolution of the occupation of the excited atomic level $\langle\sigma^+\sigma^-\rangle$ for different atom–photon coupling strengths V.
(a) The atomic transition energy $\Omega = 0$ is in the middle of the band. As long as the coupling strength V is small compared to the energy scale J, an exponential decay with a rate $\Gamma = V^2/J$ is a good description (black, blue and red curves). The values of Γ were obtained by an exponential fit. With larger V, the influence of the dispersion relation's band edges gives rise to a qualitative modification of the exponential decay (wobbles in green and orange curves). In that case, an exponential fit is not a valid description. (b) The atomic transition energy $\Omega = 2.1J$ lies above the upper band edge. Here, the short-time dynamics can still be understood as the onset of an exponential decay. However, the photon is reabsorbed due to strong Bragg scattering so that the atom develops a memory, resulting in self-induced Rabi oscillations whose frequencies depend on the coupling strength V.

slowly decreased, e. g., $\Omega = 0.7J$ and $\Omega = J$ in Fig. 6.2, the decay rate increases because the density of states increases (cf. Fig. 6.1). In this regime, the dynamics can be explained in terms of the Purcell effect, which is purely Markovian. However, if one further approaches the band edge ($\Omega = 1.5J$ and $\Omega = 1.8J$ in Fig. 6.2), the occupation of the excited atomic level becomes non-exponential until a finite atomic excitation remains in the long-time limit ($\Omega = 1.96J$ until $\Omega = 2.7J$ in Fig. 6.2). This non-Markovian behavior can be traced back to the excitation of a polaritonic atom–photon bound state (cf. Chap. 3). The deeper the atomic transition energy lies inside the band gap, the higher is the fractional excitation and the faster are the oscillations of the latter. In addition to this, the following intuitive pictorial description can be useful [39]. The excited atom emits a photon which is back-reflected to the atom due to Bragg scattering. It gets reabsorbed and the emission process starts again so that the atom "develops a memory" of its previous state.

As mentioned before, V determines the spontaneous emission rate in the "Purcell regime"

(Fig. 6.3(a)). The influence of the coupling strength in the non-Markovian regime is shown in Fig. 6.3(b). An increase of the atom–photon coupling V results in faster oscillations, which can be qualitatively understood in terms of self-induced vacuum Rabi oscillations whose frequencies depend on V. Since it takes a while for the photon to be reabsorbed, the short-time dynamics can still be understood as the onset of an exponential decay. Therefore, the occupation of the excited atomic level decays faster as V is increased, corresponding to an enhancement of the decay rate Γ.

Spectra

To complement the picture of the radiation dynamics in the lossless case, I investigate the output spectrum (cf. Eq. (6.13)). Figure 6.4(a) displays the spectrum recorded in the unit cell of the atom for a fixed coupling strength $V = 0.3J$ and different atomic transition energies Ω inside the photonic band. As long as Ω is sufficiently far detuned from the band edges, the spectrum has a Lorentzian lineshape with a width determined by the rate $\Gamma \propto V^2$. In this "Purcell regime", the natural atomic lineshape is simply renormalized with respect to vacuum. However, the shape of a spectrum and its features are always a combination of the emitter *and* the dispersion relation of the modes it is coupled to. For instance, this becomes clear for transition energies near a band edge, e. g., for $\Omega = 1.5J$ and $\Omega = 1.8J$ in Fig. 6.4(a). The line shape gradually becomes asymmetric and exhibits a tail in the direction of the band edge until it finally reaches the energy of the polaritonic atom–photon bound state outside the band. Since this bound state represents a single discrete level, the contribution to the spectrum is a delta function [93]. It can be resolved up to the spectral resolution given by $2\pi/T_{\mathrm{tot}}$, where T_{tot} is the total recording time. In order to obtain smooth spectra, I increased the system size to $N = 9999$ lattice sites and the total simulation time by a factor of 10.

At first sight, it seems to be astonishing that one is able to record spectral information from the band gap of the corresponding infinite system. However, the emission spectrum is position dependent. In Figs. 6.4(a) and 6.4(b), the spectrum is recorded in the unit cell of the atom, i. e., in the direct vicinity of the spatially confined atom–photon bound state. Hence, the spectral components of the photonic wave packet which undergoes self-induced Rabi oscillations can be resolved. When the distance between detector and emitter is increased, the spectral components originating from the band gap diminish (Fig. 6.5). Nonetheless, an asymmetry in the lineshape remains, which is the signature for the underlying non-Markovian emission dynamics.

Field–Field and Atom–Field Correlations

To conclude the dynamics in the lossless case, I study the relevant temporal field–field and atom–field correlation functions (6.9) and (6.10). Figure 6.6(a) displays the magnitude of the temporal correlation function between the atom and the atom's unit cell for parameters from the "Purcell regime". In that case, a decay on a scale determined by the lifetime

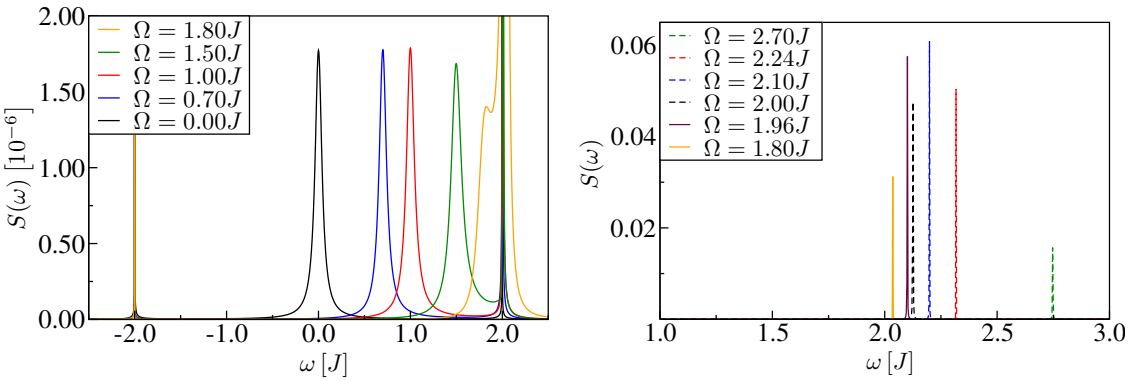

Figure 6.4: Output spectrum recorded in the unit cell of the atom for a coupling strength $V = 0.3J$ and different atomic transition energies Ω.
(a) The atomic transition energies Ω are all inside the photonic band. In the "Purcell regime", the lineshape is Lorentzian, whereas it becomes asymmetric in the non-Markovian regime close to the band edge. The spectral components of the atom–photon bound state give delta peaks near the upper and lower band edges ($\pm 2J$). In (b), the atomic transition energies are in- and outside the photonic band. Because of the different scale when compared to (a), in-band contributions are not visible in this plot.

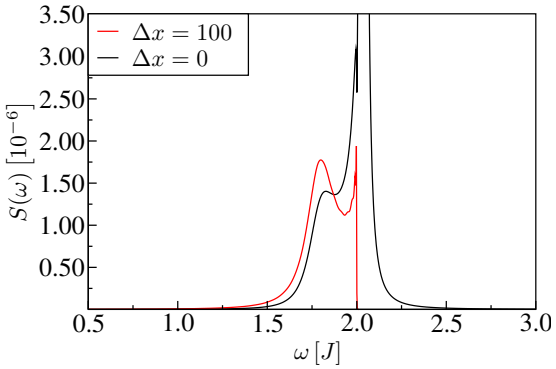

Figure 6.5: Output spectrum for $V = 0.3J$ and $\Omega = 1.8J$ recorded for different distances Δx between atom and detector.
While the spectral information of the atom–photon bound state strongly contributes to the emission spectrum in the emitter's unit cell (black curve), only the spectral information from within the band remains for a larger distance from the atom (red curve).

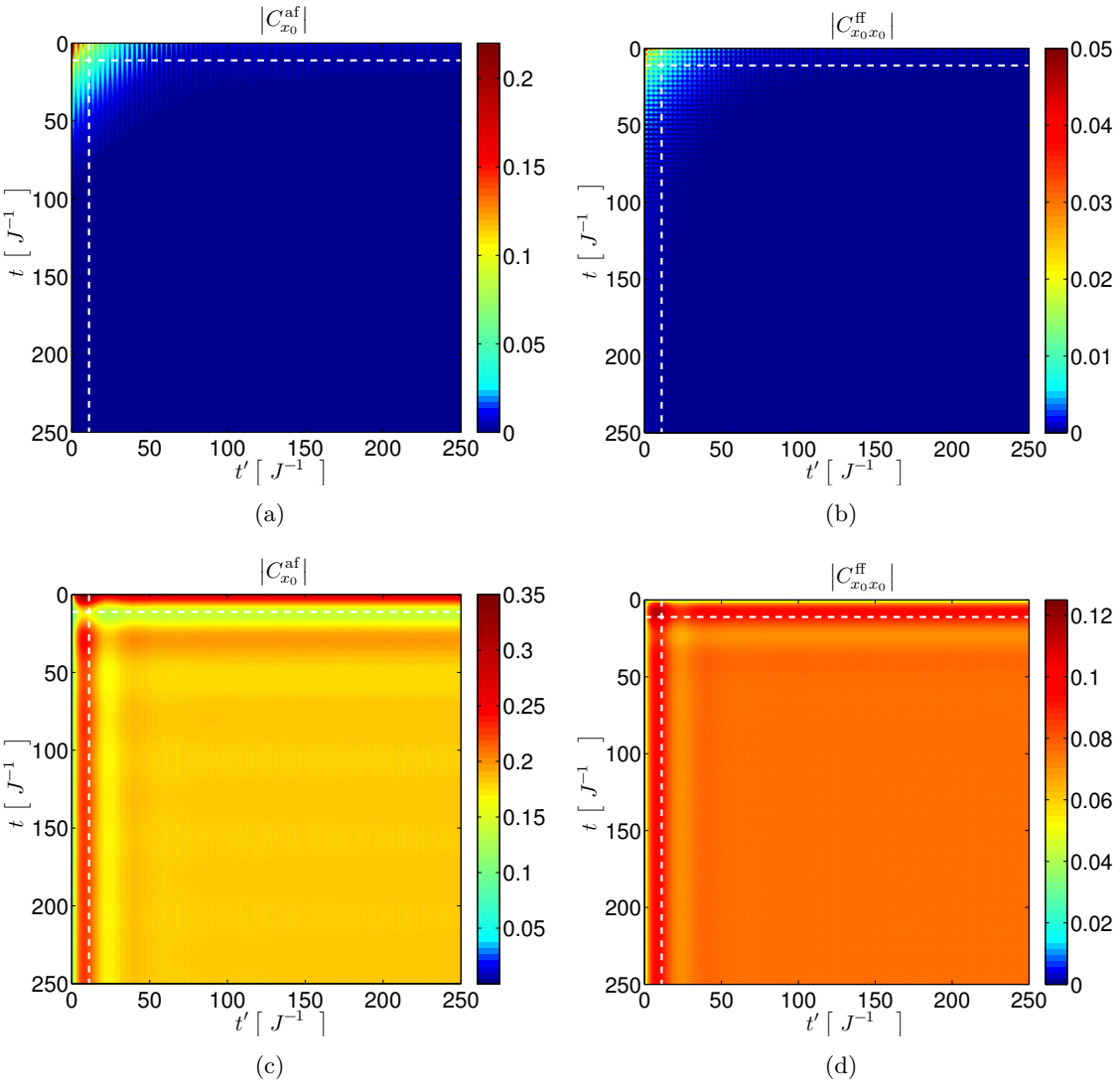

Figure 6.6: Magnitude of the temporal atom–field ($|C^{\mathrm{af}}_{x_0}(t,t')|$) and field–field ($|C^{\mathrm{ff}}_{x_0x_0}(t,t')|$) correlation functions according to Eqs. (6.10) and (6.9) in the unit cell x_0 of the atom.
In (a) and (b), $V = 0.3J$ and $\Omega = 0$ are parameters from the "Purcell regime". The correlation functions decay on a time scale set by $\Gamma^{-1} = J/V^2$ (dashed line). Hence, the emission dynamics is Markovian. Note the different color scale compared to (c) and (d). In (c) and (d), the parameters $V = 0.3J$ and $\Omega = 2.0J$ are from the non-Markovian regime. The emission dynamics is characterized by long-time correlations which last much longer than the scale set by Γ^{-1}. This renders an effective treatment of the field's degrees of freedom by means of a Born-Markov approximation invalid.

$\Gamma^{-1} = J/V^2$ is observed. This means that the emitted photonic wave packet can leave the atom's unit cell without being significantly back-reflected. Under such circumstances, the photonic dispersion relation can be regarded as a featureless reservoir of bosonic modes. Here, an approximative treatment in the spirit of a Born-Markov approximation would be valid since the temporal correlations of the photonic operators decay sufficiently fast [104] (Fig. 6.6(b)). In contrast to this, the situation differs dramatically for parameters from the non-Markovian regime. Both the atom–field (Fig. 6.6(c)) and the field–field correlators (Fig. 6.6(d)) are characterized by persistent temporal correlations.

6.3.4 Influence of an Open Waveguide

In realistic nanophotonic structures, photons may be irreversibly lost once they reach the system's boundaries. In the following, I choose a system with $N = 149$ lattice sites and the atomic unit cell to be at $x_0 = 75$. Absorbing boundaries according to Sec. 1.3.4 are employed and the profile of the imaginary on-site potential is symmetric with respect to the atom's unit cell x_0. I vary the distance Δx from the beginning of the absorbing regions to the emitter's unit cell. This approximately mimics the effect of different lengths of an open waveguide, i. e., a tight-binding chain without reflections from the boundaries. The imaginary on-site terms used for the absorbing boundaries (cf. Eq. (1.101)) are chosen such that the absorption rate γ_x grows linearly with a slope of $0.053J$ towards the ends of the waveguide. As confirmed by numerical experiments, this choice practically avoids artificial back reflections from the on-site potentials. Of course, there are spatial profiles for the

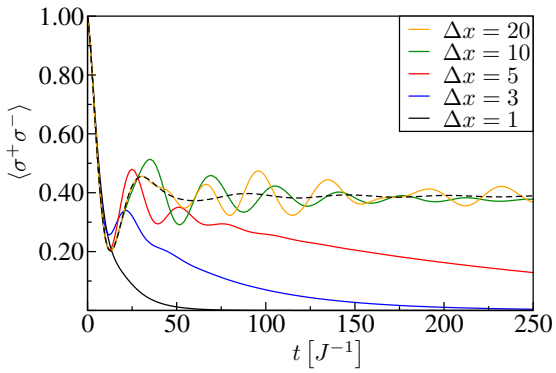

Figure 6.7: Time evolution of the occupation of the excited atomic level $\langle\sigma^+\sigma^-\rangle$ for different distances Δx of the emitter's lattice site to the beginning of the absorbing boundaries ($V = 0.3J$ and $\Omega = 1.98J$).
When compared to the dynamics of the ideal system (dashed curve), only a few unit cells are sufficient for the observation of non-Markovian dynamics. Note that Δx is measured in units of the lattice constant.

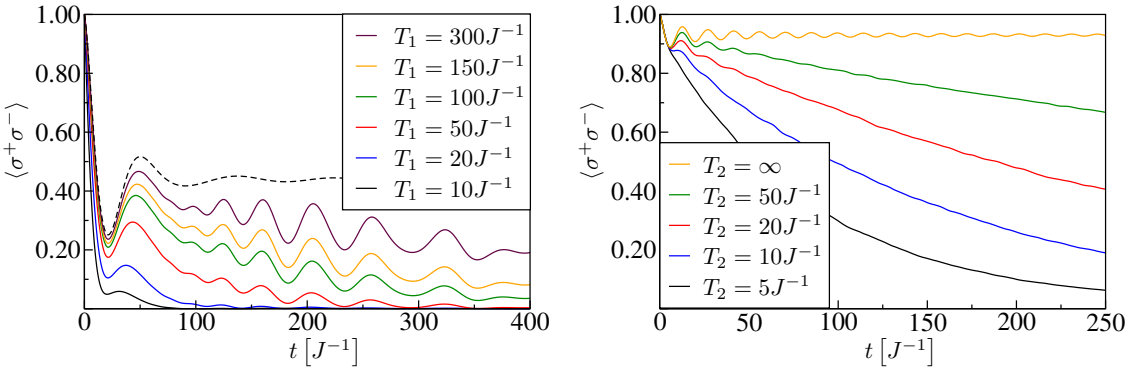

Figure 6.8: Time evolution of the occupation of the excited atomic level under the influence of atomic dissipation and dephasing.
(a) When compared to the ideal case (dashed curve), dissipation of T_1-type superimposes the non-Markovian dynamics with an exponential decay ($V = 0.2J$ and $\Omega = 2.0J$).
(b) Dephasing of T_2-type destroys the correlations between atom and field, leading to a suppression of non-Markovian dynamics ($V = 0.2J$ and $\Omega = 2.4J$). I used 1000 samples in the simulation for the stochastic time evolution.

absorbing potentials which are more efficient [37]. For the scope of this chapter, the simple linear profile is sufficient.

Figure 6.7 displays the time evolution of the occupation of the excited atomic level for different distances Δx of the emitter's unit cell to the beginning of the absorbing boundaries. For small distances, Bragg backscattering of the photonic wave packet emitted by the atom is reduced. Thus, $\langle\sigma^+\sigma^-\rangle$ eventually decays to zero. However, only a few unit cells are needed in order to observe non-Markovian dynamics.

6.3.5 Influence of Atomic Dissipation, Dephasing, and Lossy Field Modes

Radiative and non-radiative damping also results in irreversible photon loss, which reduces the probability of the photonic wave packet to contribute to the emitter's self-induced Rabi oscillations. Figure 6.8(a) displays the occupation of the atom's excited state with respect to different non-radiative losses of T_1-type. Non-radiative damping results in an exponential decay which is superimposed with the coherent time evolution. Although dephasing—the randomization of the phase between the atom's ground and excited state—does not cause photon loss, it can destroy atom–field correlations, leading to a suppression of non-Markovian dynamics (Fig. 6.8(b)).

Finally, the degrees of freedom of the radiation field themselves can be subject to irreversible losses such as Rayleigh scattering into a continuum of radiative modes. I therefore

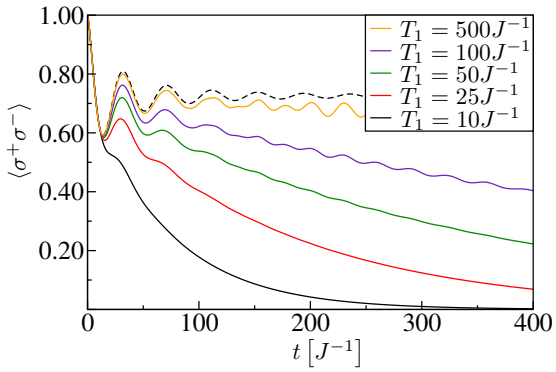

Figure 6.9: Time evolution of the occupation of the excited atomic level for different relaxation times T_1 of the waveguide's lattice sites ($V = 0.2J$ and $\Omega = 2.1J$) (the dashed line represents the lossless case).

investigate the influence of T_1-relaxation of all lattice sites, i. e., I consider a waveguide with losses. The time evolution of the atom's excited state population is displayed in Fig. 6.9.

6.4 Conclusion, Outlook, and Critical Discussion

In conclusion, I investigated spontaneous emission of a single-photon emitter embedded in a structured, one-dimensional continuum of modes. Specifically, I considered a single two-level atom in a one-dimensional tight-binding waveguide. Loss mechanisms such as atomic dissipation, dephasing, an open waveguide, and lossy field modes were taken into account phenomenologically by means of the quantum jump approach (cf. Sec. 1.3.4).

I demonstrated that the one-dimensional single-band model already exhibits all relevant physical features for the occurrence of non-Markovian dynamics. In Sec. 6.3, I identified the two distinct regimes of radiation dynamics. While the dynamics in the "Purcell regime" can be described by spontaneous emission rates, i. e., by an exponential decay of the excited atom, significantly different behavior occurs in the regime of non-Markovian dynamics. These findings were related to and explained by quantities such as (spatially dependent) spectra and correlation functions. Atomic dissipation of T_1-type, absorbing boundaries, and lossy field modes mainly result in a superimposed exponential decay. Dephasing of T_2-type affects atom–field correlations which are necessary in order to induce non-Markovianity. Hence, if subject to loss mechanisms, the atom eventually decays to its ground state.

Future investigations might include the study of three-dimensional structures such as a woodpile Photonic Crystal (cf. Refs. [7, 8, 195] and Sec. 1.2.2) or Photonic Crystal slab waveguides [196, 197]. Since the underlying equations of motion for the description of a single photon are linear, various frequency ranges could in principle be considered. However, the

influence of finite temperatures might not be disregarded in all cases so that a proper coupling to a bath of finite temperature can become important. Furthermore, from a theoretical point of view, it would be highly desirable to precompute parameters such as T_1 and T_2 by means of effective microscopic theories. In addition, a more sophisticated model of the emitter beyond the two-level description can become important for state-of-the art single-photon emitters.

Since spontaneous emission in photonic band gap media is an extensive field of research, several issues were not addressed in this chapter. First of all, I did not compare the parameters I chose in Sec. 6.3 to experimental values. Even though there exist various systems amenable to experimental investigations in the context of cavity quantum electrodynamics (for instance, see Ref. [198]), these parameters cannot be transferred directly to problems where an emitter is coupled to a continuum of modes rather than to a discrete level only. In such systems, an additional energy scale becomes important—the bandwidth of the waveguide's dispersion relation. Although, for instance, coupled-resonator optical waveguides are experimentally well-characterized [11–13], I am not aware of an overall characterization of such a system consisting of waveguide *and* emitter.

Besides this, the controlled excitation of a single emitter, followed by the emission and coherent propagation of a single-photon wave packet is challenging. Even though the development of single-photon sources is a field of research with rapid progress [199–201], experiments with conventional sources of electromagnetic radiation are easier to control. In the context of spontaneous emission, there is no difference between a two-level atom and a classical harmonic oscillator since the equations of motion employed in this chapter are linear and describe a single-particle problem[3]. This allows for the study of spontaneous emission in systems such as a macroscopic woodpile Photonic Crystal in the microwave domain [195].

Furthermore, I did not relate the findings of this chapter to the description employed in Ref. [195]. By the same token, I did not comment on the Lamb shift, nor did I explicitly calculate the time-delay Green's function in Sec. 6.3. These issues are beyond the scope of this chapter since the main emphasis here was to study radiation dynamics by means of a wave-function based method in the time domain as outlined in Chap. 2.

[3] If the rotating-wave approximation was not applied, the problem would not be restricted to the single-particle sector of the Hilbert space.

Chapter 7

7 Magnon Collisions and Magnon Readout in One-Dimensional Spin Chains

The dynamics of two magnons in a Heisenberg spin chain under the influence of a non-uniform, external magnetic field is investigated by means of a numerical wave-function based approach. The problem is formulated in terms of hard-core bosons with nearest-neighbor interaction by virtue of a Holstein-Primakoff transformation. The external magnetic field is localized in space such that it supports exactly one single-particle bound state. I demonstrate how a single spin wave can be utilized to probe the existence of a localized bound state. Specifically, I determine parameters for the efficient interaction-induced extraction of the bound magnon. This mechanism represents the readout of a single magnon[1].

7.1 Introduction

The Heisenberg model is one of the corner stones in the theoretical description of magnetism [203] and has become indispensable in the field of condensed matter physics in general. Besides the applicability in the context of ferromagnetism in conventional bulk materials, the success of the Heisenberg model can (at least partly) be attributed to the wide range of analogous physical realizations whose properties resemble those of a Heisenberg model even though "true" magnetic interactions are absent. For example, ultra-cold atoms trapped in optical lattices can be designed to emulate the dynamics of quantum spin systems [29], providing the advantage of single-site addressability and optical readout. Furthermore, mo-

[1]The work presented in this chapter was mainly carried out during my stay at the RMIT University Melbourne where I collaborated with Dr. Jared Cole. I thank Andrew Greentree and Melissa Makin for helpful discussions and I acknowledge financial support for my stay abroad by the Karlsruhe House of Young Scientists (KHYS). Parts of this chapter are in preparation for publication [202].

tivated by soliton solutions obtained in the continuum limit of the classical Heisenberg model [204, 205], spin waves actually share many properties with light pulses in optical waveguides [26]. Moreover, the field of quantum communication represents another subfield of solid-state based quantum technology where the Heisenberg model and variations thereof play a central role [27]. In addition, atom–cavity arrays are believed to be another route towards a large-scale realization of so-called quantum simulators [18] that mimic the dynamics of a spin chain in certain limits [65, 206].

As demonstrated in Ref. [26], a time-dependent external magnetic field allows one to deterministically transfer a single magnon in a one-dimensional Heisenberg spin chain by storing it in the ground state of the moving potential. In this chapter, I investigate a related aspect of such kind of systems. The analysis sheds light on the dynamics of interacting magnons in the discrete one-dimensional Heisenberg model under the influence of a static external potential. The results are obtained by means of the wave-function based numerical framework outlined in Chap. 2 and Appendix C.

This chapter is organized as follows. I begin by reviewing the theoretical foundations relevant to this chapter in Sec. 7.2. This includes the formulation of a Heisenberg Hamiltonian and its transformation to a form which is suitable for the subsequent considerations. In Sec. 7.3, I introduce the exact two-body eigenstates and energies of a one-dimensional $S = 1/2$-Heisenberg spin chain in the absence of an external magnetic field. I identify the two classes of states—two-body scattering states and propagating pairs of bound magnons. Then, in Sec. 7.4, I present the setup central to this chapter. An external potential, e. g., a static external magnetic field, is introduced and its single-particle bound states are discussed. I explain the initial state consisting of a spin wave impinging on a magnon which is stored in the ground state of the external potential. The spin wave's initial momentum is related to the bound state energy of the potential and adjusted in such a way that the transfer of the initial excitation to propagating magnon–magnon pairs is efficient. This extraction of excitation from the potential is then investigated numerically in Sec. 7.5, where I also determine the single-particle transport properties. The underlying physical mechanism allows for an interaction-induced readout of a bound magnon. Finally, I conclude the chapter in Sec. 7.6 and give a short outlook on possible future work.

7.2 Fundamentals

In this section, I formulate the Hamiltonian of a one-dimensional Heisenberg spin chain under the influence of an external magnetic field. I then transform the Hamiltonian to a system of interacting bosons by means of a Holstein-Primakoff transformation. The resulting Hamiltonian is exact in the single- and two-excitation subspace.

7.2.1 The Hamiltonian

The Heisenberg-Hamiltonian of a one-dimensional spin chain in the presence of an external magnetic field $\mathbf{B}(\mathbf{r})$ reads[2]

$$H = -\sum_{i \neq j} J_{ij} \mathbf{S}_i \cdot \mathbf{S}_j - \sum_i \mathbf{B}(\mathbf{r}_i) \cdot \mathbf{S}_i \,, \tag{7.1}$$

where $\mathbf{S}_i = (S_i^x, S_i^y, S_i^z)$ is a spin operators for a spin S on lattice site i and J_{ij} denotes the exchange coupling between sites i and j. Throughout this chapter, I assume that there exists a background field which imparts a uniform Zeeman shift across the chain in such a way that thermal effects can be neglected.[3] I introduce ladder operators according to $S_i^{\pm} = S_i^x \pm \mathrm{i} S_i^y$ and assume nearest-neighbor hopping, i. e., $J_{ij} = J(\delta_{i,j+1} + \delta_{i,j-1})$. Then, the Hamiltonian (in units of J) becomes

$$h = \frac{H}{J} = -\sum_i \left(S_i^+ S_{i+1}^- + S_i^- S_{i+1}^+ + 2 S_i^z S_{i+1}^z + V_i S_i^z \right) \,, \tag{7.2}$$

where V_i is the magnetic field (in units of J) at lattice site i. For the remainder, lengths are measured in units of the lattice constant $a \equiv 1$ (cf. Appendix A). Because the spin operators obey the algebra

$$\left[S_i^z, S_j^{\pm} \right] = \pm \delta_{ij} S_i^{\pm} \,, \tag{7.3a}$$

$$\left[S_i^+, S_j^- \right] = 2 \delta_{ij} S_i^z \,, \tag{7.3b}$$

they are neither bosonic nor fermionic. However, the Hamiltonian (7.2) can be transformed to a system of bosons or fermions by means of a Holstein-Primakoff [203, 207] or a Jordan-Wigner transformation [208, 209], respectively. The latter is only applicable for a system with $S = 1/2$, whereas the Holstein-Primakoff transformation is exact for arbitrary spin S.

7.2.2 Holstein-Primakoff Transformation

Following Ref. [203], I set

$$S_i^z = S - n_i \,, \tag{7.4a}$$

$$S_i^+ = \sqrt{2S} \phi(n_i) a_i \,, \tag{7.4b}$$

$$S_i^- = \sqrt{2S} a_i^\dagger \phi(n_i) \,, \tag{7.4c}$$

[2] To be precise, the magnetic moment (which is proportional to the spin operator) couples to the magnetic field. Here, units are chosen such that all prefactors (such as the Bohr magneton and the Landé factor) are absorbed into the coefficients of the Hamiltonian.

[3] A uniform background field in z-direction just adds additional on-site terms to the Hamiltonian which do not affect the dynamics. The strength of the background field is chosen such that the Boltzmann factor for a given temperature is much smaller than unity.

where $n_i = a_i^\dagger a_i$ is the usual number operator, $a_i^\dagger$ (a_i) are bosonic creation (annihilation) operators, and

$$\phi(n_i) = \sqrt{1 - \frac{n_i}{2S}} \tag{7.5}$$

is a nonlinear operator function. The original spin algebra thus results in a system of interacting bosons (magnons). The nonlinearity in Eq. (7.5) usually renders an analytical and a numerical solution to the general many-body problem intractable. A common strategy is to formally expand Eq. (7.5) in orders of the normal-ordered number operator [203], i. e.,

$$\phi(n_i) = 1 - \left(1 - \sqrt{1 - \frac{1}{2S}}\right) n_i + \mathcal{O}\left(:n_i^2:\right) , \tag{7.6}$$

where : . : denotes normal ordering. Usually, the so-called low-temperature approximation $\langle n_i \rangle / 2S \ll 1$ is applied and only a few lower order terms of Eq. (7.6) are taken into account.

In the following, I restrict the investigations to the dynamics of at most two magnons in the system. Hence, terminating the expansion in Eq. (7.6) after the first order results in an *exact* Hamiltonian for the single- and two-excitation subspace. Furthermore, I focus on a chain of $S = 1/2$-spins. By neglecting all constant energy terms and on-site terms I arrive at

$$\begin{aligned} h = -\sum_i \Big(\quad & a_i^\dagger a_{i+1} + a_i^\dagger a_{i-1} + V_i a_i^\dagger a_i + n_i n_{i+1} + n_i n_{i-1} \\ & - a_{i+1}^\dagger n_i a_i - a_{i-1}^\dagger n_i a_i - a_{i+1}^\dagger n_{i+1} a_i - a_{i-1}^\dagger n_{i-1} a_i \Big) , \end{aligned} \tag{7.7}$$

which can be recast into[4]

$$h = -\sum_i \left[\left(a_{i+1}^\dagger a_i + a_i^\dagger a_{i+1} \right) \left(2 - n_i - n_{i+1} \right) + 2 n_i n_{i+1} + V_i n_i \right] . \tag{7.8}$$

This Hamiltonian describes hard-core bosons with nearest-neighbor interaction in the presence of an external potential.

For $S = 1/2$, the Hamiltonian (7.2) can alternatively be mapped onto a system of fermions on a one-dimensional tight-binding chain with nearest-neighbor interactions. However, the underlying Jordan-Wigner transformation is nonlocal, which is inconvenient in the context of the time-evolution of two-magnon wave packets. In this chapter, I therefore focus on the Holstein-Primakoff approach.

[4] I perform an index shift and exploit the identities $a_{i+1}^\dagger n_i a_i = a_{i+1}^\dagger a_i n_i - a_{i+1}^\dagger a_i$ and $a_i^\dagger n_{i+1} a_{i+1} = a_i^\dagger a_{i+1} n_{i+1} - a_i^\dagger a_{i+1}$.

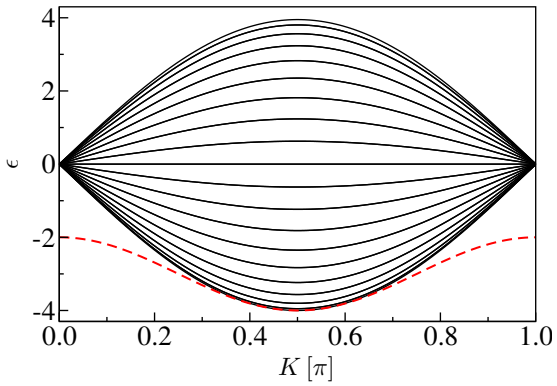

Figure 7.1: Eigenenergies of the two-particle scattering states (solid black lines) and the propagating magnon–magnon bound states (dashed red line).
The black lines correspond to selected, equidistant values of the relative momentum p (cf. Eq. (7.11)). The energies of the scattering states and the propagating magnon–magnon bound states never cross.

7.3 Exact Two-Body Eigenstates in the Absence of an External Potential

In the absence of an external potential ($V_i = 0$), the two-excitation eigenstates for the eigenproblem $(h - \epsilon)|\Psi\rangle = 0$ can be calculated analytically (cf. Refs. [210, 211] and Appendix F). The wave function for an eigenstate $|\Psi\rangle = \sum_{x_1 x_2} \Phi_{x_1 x_2} a^\dagger_{x_1} a^\dagger_{x_2} |0\rangle$ can be decomposed into a center-of-mass wave function (coordinate $c = (x_1 + x_2)/2$, momentum K) and a wave function in the relative coordinate ($r = x_1 - x_2$), i. e., $\Phi_{x_1 x_2} = \mathrm{e}^{\mathrm{i}Kc}\Psi_r$.

To form a complete basis of the two-excitation subspace, two classes of solutions need to be considered. For both classes, $\Psi_0 = 0$ holds because the Hamiltonian describes hard-core bosons. There exist scattering states described by

$$\Psi_r = \Psi_{-r} = \mathrm{e}^{\mathrm{i}p|r|} + \mathrm{e}^{\mathrm{i}\Delta_{Kp}}\mathrm{e}^{-\mathrm{i}p|r|} \quad \forall \quad r \neq 0\,, \tag{7.9}$$

where Δ_{Kp} is the scattering phase shift given by

$$\mathrm{e}^{\mathrm{i}\Delta_{Kp}} = -\frac{\epsilon_K + 2\mathrm{e}^{\mathrm{i}p}}{\epsilon_K + 2\mathrm{e}^{-\mathrm{i}p}} \tag{7.10}$$

and $\epsilon_K = -2\cos(K/2)$ is the dispersion relation of the center-of-mass. The relative momentum is denoted by p. The eigenenergy of this two-particle state reads (cf. Fig. 7.1)

$$\epsilon = \epsilon_{Kp} = \epsilon_K \cdot 2\cos(p)\,. \tag{7.11}$$

Magnon–magnon bound states exist with a relative wave function of the form

$$\Psi_r = \Psi_{-r} = \alpha^{|r|} \quad \forall \quad r \neq 0\,, \tag{7.12}$$

where $\alpha = -\epsilon_K/2$. Here, the eigenenergy is (cf. Fig. 7.1)

$$\epsilon = \epsilon_K^{\text{bound}} = -2 - \frac{1}{2}\epsilon_K^2\,. \tag{7.13}$$

In the single-excitation subspace, the eigenstates are plane waves with a momentum k and the eigenenergy is given by the dispersion relation[5] of the tight-binding lattice, i. e., $\epsilon = \omega_k = -2\cos(k)$.

Note that by ignoring the nearest-neighbor interaction terms in Hamiltonian (7.8), the magnon–magnon bound states disappear from the spectrum. Conversely, ignoring those hopping terms which depend on the occupation number (last line in Eq. (7.7)) results in modified wave functions for which $\Psi_0 \neq 0$ is allowed. Such a system does not describe hard-core bosons anymore. Still, modified magnon–magnon bound states exist in that hypothetical situation. Similar calculations can be found in Refs. [155, 156, 212].

7.4 Setup

In the absence of an external potential, the Hamiltonian (7.8) already exhibits an interesting interaction-induced effect—the existence of bound magnon–magnon pairs. However, there is no mechanism of transferring excitation from the scattering states to the bound states or vice versa. Therefore, I introduce localized single-particle bound states by virtue of an external potential, e. g., an external magnetic field. I exploit the discrete levels introduced by the potential to connect the hitherto separated classes of states. In the following, I shift the energy of the free dispersion relations such that the lowest energy (in the absence of a potential) is zero, i. e., I set $\omega_k \to \omega_k + 2$, $\epsilon_{Kp} \to \epsilon_{Kp} + 4$ and $\epsilon_K^{\text{bound}} \to \epsilon_K^{\text{bound}} + 4$ in the previous expressions.

7.4.1 Bound States of the Pöschl-Teller Potential

In principle, the effects I investigate in the following do not depend on the actual spatial profile of the external potential as long as the potential is such that it supports at least one bound state. I therefore choose a potential for which the analytical bound-state solution is available in the continuum limit[6]. One smooth potential of such kind is the Pöschl-Teller

[5] To avoid confusion with the two-body eigenenergies, the single-particle dispersion relation is denoted by ω_k (instead of ϵ_k as in previous chapters).

[6] The continuum limit corresponds to the limit in which the lattice constant goes to zero while the number of lattice points goes to infinity, whilst keeping the length of the system constant. In this limit, the tight-binding dispersion relation becomes (leading order in the lattice constant) $\omega_k = -2\cos(k) + 2 = -2(1 - \frac{1}{2}k^2 + \dots) + 2 \to k^2$. This is the dispersion relation of a massive particle with mass $m = 1/2$. Note that dimensionless units according to Appendix A are employed, masking the lattice constant.

potential [213–215] with

$$V(x) = -B_0 \mathrm{sech}^2\left(\frac{x-x'}{w}\right) , \tag{7.14}$$

where B_0 is the depth, w the width, and x' the center of the potential.

According to Ref. [215] and adapted to the notation and parameters of this chapter, the bound state energies read

$$E_n^{\mathrm{BS}} = -\frac{1}{4w^2}\left[-(1+2n) + \sqrt{1+4B_0w^2}\right]^2 . \tag{7.15}$$

The bound states are labeled by $n = 0, 1, 2, \ldots, n_{\max}$. Since $E_n^{\mathrm{BS}} < 0$ has to hold, there is only a finite number of supported bound states. To facilitate the discussion in the following, I restrict the discussion to the case where the potential supports exactly one bound state. The condition $E_{n_{\max}}^{\mathrm{BS}} = 0$ with $n_{\max} = 1$ yields $w = \sqrt{2/B_0}$. In the discrete system, the Pöschl-Teller potential is only defined at the lattice sites, i. e., $V_x = -B_0\mathrm{sech}^2(\sqrt{B_0/2}\ (x-x'))$. For the remainder of this chapter, I choose a finite system with N lattice sites where the potential is located at site $x' = N/2$ (N is even).

7.4.2 Initial States

In all discussions below, I choose the initial state of the system to be a two-particle state which is a symmetrized product of single-particle wave functions according to

$$\left|\Psi\right\rangle = \sum_{x_1x_2} \Phi_{x_1x_2} a_{x_1}^\dagger a_{x_2}^\dagger \left|0\right\rangle , \tag{7.16a}$$

$$\Phi_{x_1x_2} = \frac{1}{\sqrt{2}}\left(\varphi_{x_1}\chi_{x_2} + \varphi_{x_2}\chi_{x_1}\right) . \tag{7.16b}$$

Here,

$$\varphi_x \propto \mathrm{e}^{-\frac{(x-x_0)^2}{2s^2}} \mathrm{e}^{\mathrm{i}k_0x} \tag{7.17}$$

is a single-particle Gaussian wave function—a spin wave—with initial center x_0, width s, and carrier momentum k_0. The ground-state wave function of the Pöschl-Teller potential is denoted by χ_x and is obtained by means of an exact numerical diagonalization of the finite system in the single-excitation subspace. The incoming spin wave is launched from the left hand side of the potential with a carrier momentum $k_0 > 0$. A schematic sketch of the setup with two excitations is depicted in Fig. 7.2.

The goal in the following is to extract as much excitation as possible from the "stored" ground state wave function and to transfer it to propagating two-particle magnon–magnon bound states. To this end, the overlap of the initial state with the potential target states in the Hilbert space needs to be maximized. Alternatively, the situation where the stored excitation is transferred to the two-particle scattering states could also be investigated. However, this issue is not addressed in this chapter.

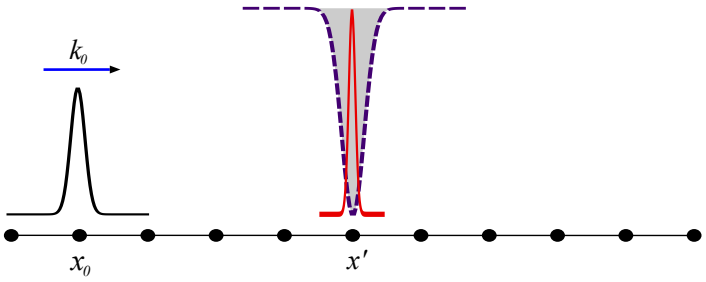

Figure 7.2: Schematic sketch of the setup.
The Pöschl-Teller potential (indicated by the dashed violet curve, centered around lattice site x') is initialized with the single-particle ground state wave function (red curve). A spin wave in the form of a Gaussian wave packet (black curve, carrier wavenumber k_0, centered around x_0) is launched towards the potential.

7.4.3 Parameters for Maximized Overlap

In a first step, I obtain a relation between the single-particle input momentum k_0 and the two-particle center-of-mass output momentum K as a function of the bound-state energy $b < 0$ of the potential. To this end, I consider global energy conservation. For the transfer of the initial excitation to magnon–magnon bound states (cf. Eq. (7.13)), energy conservation yields

$$\omega_{k_0} + b = \epsilon_K^{\text{bound}}\,, \tag{7.18a}$$

$$-2\cos(k_0) + 2 + b = -2 - \frac{1}{2}\left(-2\cos(\frac{K}{2})\right)^2 + 4\,, \tag{7.18b}$$

which results in

$$K = 2\arccos\left(\pm\sqrt{\cos(k_0) - \frac{b}{2}}\right)\,. \tag{7.19}$$

Note that condition (7.19) is only defined when $|\sqrt{\cos(k_0) - b/2}| \leq 1$, which is already a weak constraint for possible combinations of ground state energies and input momenta.

Similarly, the transfer of excitation to the scattering states (cf. Eq. (7.11)) requires

$$\omega_{k_0} + b = \epsilon_{Kp}\,, \tag{7.20a}$$

$$-2\cos(k_0) + 2 + b = -4\cos(\frac{K}{2})\cos(p) + 4\,, \tag{7.20b}$$

so that

$$K = 2\arccos\left[\frac{1}{2\cos(p)}\left(\cos(k_0) + 1 - \frac{b}{2}\right)\right]\,. \tag{7.21}$$

Note that Eq. (7.21) depends on the relative momentum p of the two-body scattering states to which the excitation is transferred.

In order to maximize the overlap of the initial state with the target states, I enforce the magnitudes of the center-of-mass momenta before and after scattering to be equal, i. e.,

$$\left|k_0 + 0\right| = \left|K\right| . \tag{7.22}$$

Then, I arrive at

$$k_0 = 2 \arcsin\left(\sqrt{-\frac{b}{2}}\right) \tag{7.23}$$

for the transfer of the initial excitation to magnon–magnon bound states (cf. Eq. (7.19)), whereas I need to choose

$$k_0 = 2 \arccos\left[\frac{1}{2}\left(\cos(p) \pm \sqrt{b + \cos^2(p)}\right)\right] \tag{7.24}$$

in the case of the scattering states (cf. Eq. (7.21)). In Eqs. (7.23) and (7.24), I only accounted for positive initial momenta k_0 so that the initial wave packet is a right-moving spin wave. These equations determine the initial momentum of the incoming spin wave as a function of the bound state energy of the potential. Note that $-2 \leq b < 0$ holds according to condition (7.23). As an estimate, the bound state energy can be approximated by $E_0^{\mathrm{BS}} = -B_0/2$, which is only exact in the continuum limit [215]. In the numerical simulations, I use the exact ground state energy b of the potential in the finite system (cf. Fig. 7.3).

As mentioned before, I focus on the transfer of the initial excitation to the magnon–magnon bound states. I therefore use Eq. (7.23) to initialize the momentum of the incoming spin wave. In order to be sure that the overlap with the scattering states does not seriously affect the transfer to bound magnon–magnon pairs, I equate Eqs. (7.23) and (7.24), yielding

$$\cos(p) = \frac{1}{2\sqrt{2}} \frac{4 + b}{\sqrt{2 + b}} . \tag{7.25}$$

Here, a real-valued solution for the relative momentum p exists only for $b = 0$, i. e., in the absence of a potential. Hence, the conditions (7.23) and (7.24) are incompatible. After scattering, all excitation is therefore either transferred to magnon–magnon bound states or remains in the form of a scattered spin wave and a localized excitation in the potential.

7.5 Dynamics

In the following, I study the wave packet dynamics with the help of the numerical framework developed in the context of few-photon transport (cf. Chap. 2, Appendix C, and Refs. [61, 62, 108]). All simulations are performed for a system with $N = 400$ lattice sites and the initial

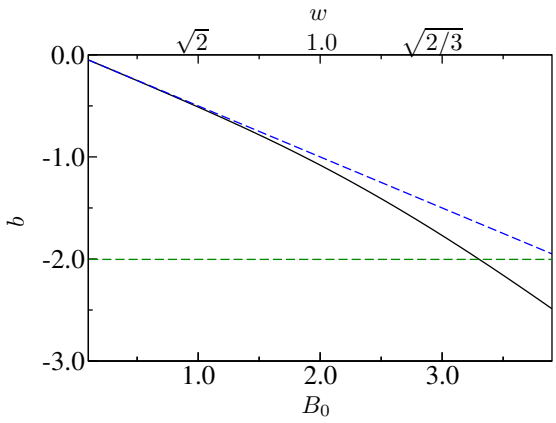

Figure 7.3: Ground state energy of the Pöschl-Teller potential as a function of the potential depth B_0 ($w = \sqrt{2/B_0}$).
The solid black line corresponds to values obtained by an exact numerical diagonalization of the discrete system with $N = 400$ lattice sites. The dashed blue line refers to the analytical result for the continuum case where $b = -B_0/2$. Deviations occur when the potential is narrow, i. e., its width is comparable to or smaller than the lattice spacing (which is unity here). The green dashed line shows the lower bound for allowed bound state energies as imposed by constraint (7.23).

condition (7.16) with parameters as described in Secs. 7.4.2 and 7.4.3. I choose $x_0 = 36$ as the initial center of the spin wave. A width of $s = 12$ ensures that the wave packet's width in momentum space only covers a small spectral window when compared to the full bandwidth of the single-particle cosine-dispersion relation (which is 4 in units of J).

7.5.1 Single-Particle Transmittance

So far, I only discussed the effect of the external potential in terms of the existence of an additional discrete level—the bound state. However, the potential also affects the two-particle eigenstates discussed in Sec. 7.3. In general, incoming plane waves are partly reflected and partly transmitted. In order to better understand the two-particle dynamics, I first obtain the transmission characteristics for a single spin wave impinging on the empty Pöschl-Teller potential. Interestingly, the Pöschl-Teller potential belongs to a class of reflectionless potentials [216]. However, the property of unity transmittance only exists in the continuous system for waves with special constraints. Since the present system is discrete and I do not impose any special restriction on the incoming spin wave (besides being a Gaussian wave packet with a certain carrier momentum), the potential causes non-zero reflection.

Figure 7.4 displays the transmittance $T_{k_0}(B_0)$ through the potential. The quantity $T_{k_0}(B_0)$

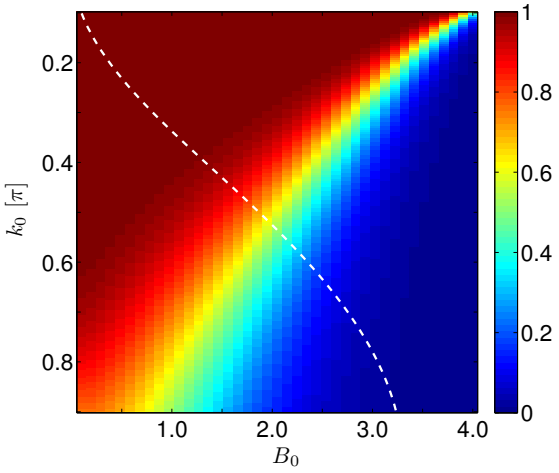

Figure 7.4: Single-particle transmittance through the Pöschl-Teller potential obtained from a time-dependent transport simulation for an initial Gaussian spin wave.
The pulse parameters are $s = 12$ and $x_0 = 36$ and the carrier momentum k_0 and the potential depth B_0 are varied. The dashed line corresponds to pairs of B_0 and k_0 for which constraint (7.23) holds.

is defined as the sum of all occupation numbers on the right hand side of the system at a time after the wave packet passed the potential, i. e., $T_{k_0}(B_0) = \sum_{i=N/2+1}^{N} \langle n_i \rangle$. Here, the potential depth B_0 and the input momentum k_0 are varied independently. Note that the parameter for the potential's width is $w = \sqrt{2/B_0}$. The dashed line in the color plot signifies pairs of B_0 and k_0 for which constraint (7.23) holds. All following two-particle simulations correspond to such pairs of B_0 and k_0. Hence, B_0 is the only free parameter left (according to Eq. (7.23), k_0 depends on the ground state energy b which is a function of B_0).

7.5.2 Interaction-Induced Extraction of the Bound-State and Transfer to Propagating Magnon–Magnon Bound States

Now, I discuss the physical mechanism central to this chapter—the interaction-induced extraction of excitation from the potential and its transfer to propagating magnon–magnon bound states. To quantify the efficiency of extraction, it is advantageous to transform to the number basis of the single-particle energy eigenstates (which are obtained by means of exact numerical diagonalization). Let $u_x^{(\lambda)}$ be the (real space) wave function of the single-particle energy eigenstate with eigenenergy λ in the presence of the external potential, i. e., $h \left|\lambda\right\rangle = \lambda \left|\lambda\right\rangle$ and $\left\langle 0\right| a_x \left|\lambda\right\rangle = u_x^{(\lambda)}$. Then, by employing the change of basis $a_\lambda^\dagger = \sum_x u_x^{(\lambda)} a_x^\dagger$,

the quantity

$$\langle n_\lambda \rangle = \langle a_\lambda^\dagger a_\lambda \rangle = \sum_{xx'} u_{x'}^{(\lambda)^*} u_x^{(\lambda)} \langle a_x^\dagger a_{x'} \rangle \tag{7.26}$$

is the occupation of the single-particle state $\big|\lambda\big\rangle$. Consequently, the amount of extracted excitation is given by

$$\begin{aligned} \eta &= \langle n_{\lambda_0} \rangle (t=0) - \langle n_{\lambda_0} \rangle (t = t_{\mathrm{end}}) \\ &= 1 - \langle n_{\lambda_0} \rangle (t = t_{\mathrm{end}})\,. \end{aligned} \tag{7.27}$$

At the beginning of the simulation, the potential is initialized in its bound state $\big|\lambda_0 = b\big\rangle$ so that $\langle n_{\lambda_0} \rangle (t=0) = 1$. The time at the end of the simulation is denoted by t_{end}, which is long enough after the incoming spin wave scattered at the potential, but before the boundaries of the computational domain corrupt the results (cf. Chap. 2).

Figure 7.5 displays the amount of extracted excitation from the potential as a function of the potential depth B_0. The actual shape of the curve is a result of the interplay of the incoming spin wave's reflected and transmitted parts (cf. Fig. 7.4) and the non-zero group-velocity dispersion which affects the shape of the wave packet. Those regions in parameter space where the potential induces either unity transmittance or reflectance belong to the nonlinear regime of the cosine dispersion. In other words, the group-velocity dispersion causes the wave packet to spread out rapidly so that its maximum is significantly decreased when arriving at the potential. This causes an inefficient extraction of the bound state (cf. $B_0 < 0.82$ and $B_0 > 3.14$ in Figs. 7.4 and 7.5). Conversely, under the constraints imposed, those regions in parameters space where the influence of the cosine dispersion's nonlinearity is minimal (around $k_0 = \pi/2$) are subject to both significant reflection and transmission, resulting only in a moderate extraction efficiency. In between these two regimes, the maxima of the extraction efficiency can be found at $B_0 = 0.82$ and $B_0 = 3.14$. At these points, a single spin wave is either almost completely transmitted or reflected (cf. Fig. 7.4) whilst the influence of the nonlinear dispersion relation is moderate. In all cases, the extraction efficiency is smaller than unity, which is a consequence of the fact that the wave packets experience a finite dwell time, i. e., a finite interaction time with the "stored" bound state in the potential.

Figure 7.6 displays space-time plots of the wave packet dynamics in real space for $B_0 = 0.82$. In order to demonstrate the importance of the interaction terms of Hamiltonian (7.8), the dynamics of an interaction-free tight-binding chain is also plotted for comparison. In the latter case, the two excitations pass each other without any effect besides wave interference. In the absence of the interaction, the spin wave passes through the potential as if it was empty. The delay induced by the interaction terms, i. e., the presence of a magnon in the potential, can be interpreted as a signature for an occupied potential, effectively enabling a readout. The slopes of the "rays" leaving the potential region after scattering clearly indicate that the excitation is transferred to states with different group velocities. In addition, I display a series of "snapshots" of the transport process in Fig. 7.7.

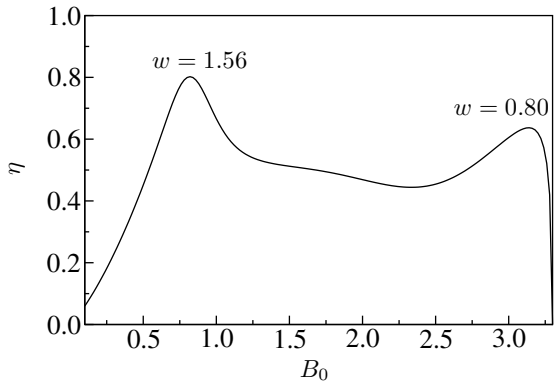

Figure 7.5: Amount of extracted excitation according to Eq. (7.27).
Under the constraints imposed, $B_0 \simeq 0.82$ represents an optimal set of parameters.

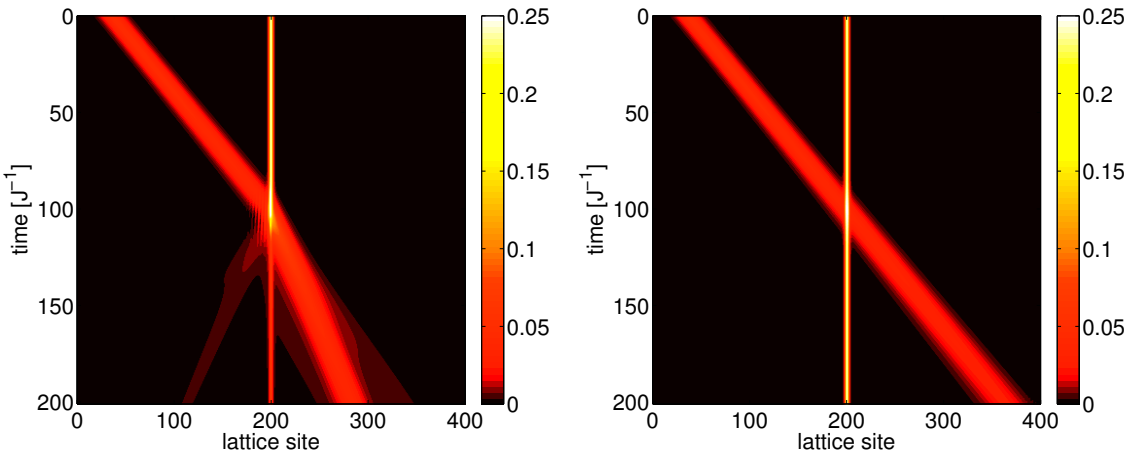

Figure 7.6: Space-time plot of the occupation numbers in real space ($B_0 = 0.82$).
In the left panel, the dynamics according to Hamiltonian (7.8) is shown, whereas the right panel corresponds to the system of an interaction-free tight-binding chain. Note the different slopes of the "rays" after scattering, corresponding to different group velocities. The magnon–magnon interaction induces a delay for the transmitted spin wave when compared to the interaction-free case. In the latter, the dynamics of the spin wave is not affected by the existence of a bound state. Thus, the delay can be interpreted as an interaction-induced signature of the single-magnon readout.

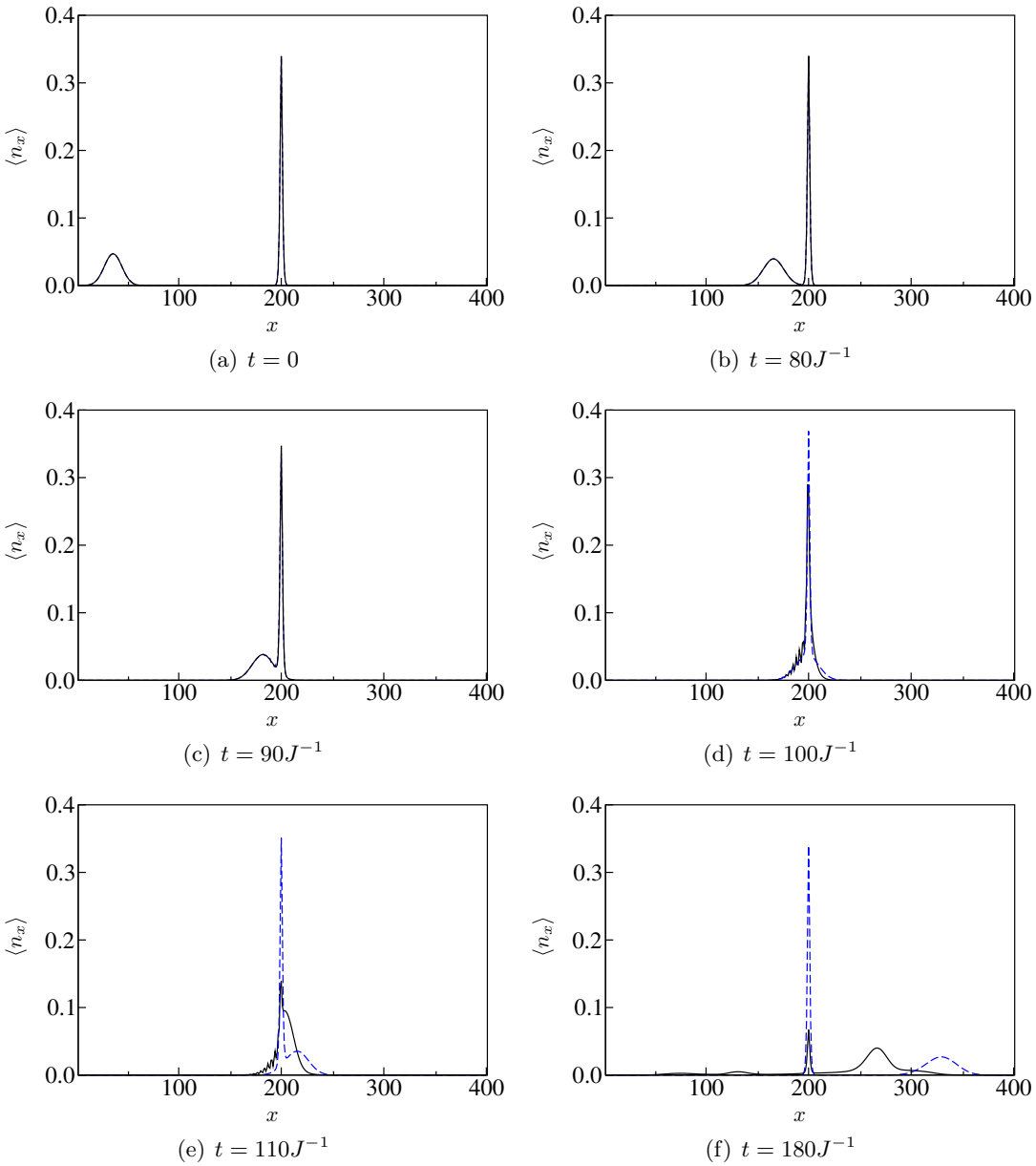

(a) $t = 0$ (b) $t = 80J^{-1}$

(c) $t = 90J^{-1}$ (d) $t = 100J^{-1}$

(e) $t = 110J^{-1}$ (f) $t = 180J^{-1}$

Figure 7.7: Expectation values of the occupation numbers in real space at different instances of time ($B_0 = 0.82$).
The solid black line denotes the wave packet dynamics for the full Hamiltonian (7.8), whereas the dashed blue line refers to an interaction-free system of a tight-binding chain (curves partially on top of each other). The delay induced by the interaction terms, i. e., the presence of excitation in the potential, can be utilized to decide whether or not a magnon was stored in the potential, which represents the readout of a single magnon.

7.6 Conclusion, Outlook, and Critical Discussion

In conclusion, I numerically analyzed the interaction-induced readout of a single magnon stored in a potential. In essence, the localized bound state was probed with an impinging spin wave whose parameters were adjusted in such a way that the initial excitation can be transferred efficiently to propagating pairs of bound magnons. Specifically, I related the spin wave's initial momentum to the bound state energy. The width of the potential was chosen such that it supports exactly one bound state. I furthermore determined and discussed the extraction efficiency as a function of the potential depth. In addition, I illustrated the wave packet dynamics in real space by monitoring the time evolution of the occupation numbers.

A variety of extensions and modifications to the work presented in this chapter can be envisioned for future investigations. In particular, as the efficiency of the readout with a single spin wave is less than unity, one can imagine a sequence of probe pulses to overcome this limitation. In analogy to optics, by controlling the actual shape of the readout pulse, it should be possible to gain further control over the extraction efficiency. In the spirit of Ref. [26], time-dependent external fields add a novel twist to the dynamics of interacting magnons and could open up a variety of interesting physical mechanisms. Furthermore, engineered hopping amplitudes would allow for a perfect state transfer [27] and minimize the effect of group-velocity dispersion. In general, more complicated scenarios involve more than two excitations for which higher-order terms in the expansion of the operator function (7.5) need to be taken into account. Moreover, a more realistic description of spin chain systems needs to address the issue of decoherence, i. e., relaxation and dephasing of individual spins.

Admittedly, the realization of an integrated quantum-optical circuitry with magnons still has to be regarded as a visionary long-term goal and a lot of issues remain to be investigated. The study presented in this chapter did not consider a specific realization of a spin chain and was, therefore, generic in nature. However, it remains an open question whether the parameter regime studied here (for instance, B_0 in units of J and w in units of the lattice constant) is feasible in the context of magnon extraction. Since the potential was localized at the length scale comparable to the lattice constant, control of the external field on a spatial scale below the lattice constant is required. In addition, I implicitly assumed the hopping parameters to be independent of the applied external field, which is actually only valid as long as the orbitals entering the overlap integral which determines J do not strongly depend on the magnetic field. Besides this, I did not comment on the actual preparation of the initial state. The preparation of the single-excitation ground state in the Pöschl-Teller potential as well as the controlled excitation of a single spin wave with definite carrier momentum was not discussed. Furthermore, I did not investigate the extraction effect in the case of multiple bound states in the potential. Moreover, the transfer of excitation to the scattering states rather than to the magnon–magnon bound states was not addressed in this chapter.

Chapter 8
8 Summary, Conclusion, and Outlook

Having presented the results of my studies in the preceding chapters, I would like to briefly summarize my findings, conclude the thesis, and give an outlook on possible future studies in the field of waveguide quantum optics.

8.1 Summary

The aim of the present thesis was to investigate problems of waveguide quantum optics within a wave-function based framework.

To this end, I first introduced the theoretical foundations of electrodynamics in media and quantum optics in Chap. 1. This included Maxwell's macroscopic equations, their canonical quantization in a suitable gauge, and examples for effectively one-dimensional photonic continua. Moreover, I discussed states of the electromagnetic field, their dynamics as well as mechanisms of light–matter interaction and the physical observables relevant in the context of this thesis. In addition to that, I introduced the quantum jump approach to account for open systems.

In Chap. 2, I presented a discrete real-space formulation of the Hamiltonians as well as the numerical framework central to this thesis—a wave-function based time-evolution scheme.

Before I turned to the main results of this thesis, I gave an introduction to the topic of waveguide quantum optics in Chap. 3. Specifically, I reviewed the field on the basis of existing theoretical works on a one-dimensional waveguide coupled to a single or a few emitters. I then introduced the Hamiltonian of a tight-binding waveguide coupled to a single two-level atom and I discussed its properties in terms of single-particle eigenstates, as well as single- and two-photon transport. For the latter, I explicitly pointed out that the interplay of the few-photon nonlinearity provided by the two-level atom and spatially localized atom–photon bound states can lead to the effect of interaction-induced radiation trapping. Furthermore, I presented a numerical study on the existence of photon–photon bound states. To complete the introduction, I provided a brief overview of related works in which I have been involved

but which are beyond the scope of this thesis.

In Chap. 4, I studied the Hong-Ou-Mandel effect in the context of two photons impinging from different ends of a waveguide towards a single scatterer. From the coincidence probability of finding one photon on each end of the waveguide after scattering—i. e., from the Hong-Ou-Mandel dip—one can identify effective photon–photon interactions as they are mediated by a two-level atom. In addition to that, I studied the influence of atomic dissipation and dephasing on the Hong-Ou-Mandel dip, which can be regarded as a possible approach for using the Hong-Ou-Mandel to probe the influences of the environment.

In Chap. 5, I investigated the transport properties of coherent and single-photon-added coherent states in a waveguide with a side-coupled Kerr-nonlinear resonator. On the level of coherent states, nonlinear effects such as self-induced transparency and bistability can occur. I discussed how the pulse propagation of a single-photon-added coherent state can be understood as a single-photon Fock state in an "alternative vacuum" provided by a coherent state. In essence, this led to a time-dependent scattering potential on the single-photon level. I explicitly demonstrated that this scattering potential is controlled by the coherent state part of the composite pulse and allows for the gating of single photons.

After that, I turned to the problem of an initially excited atom in an empty one-dimensional, structured continuum (Chap. 6). I investigated the dynamics of spontaneous emission of a single two-level atom in a tight-binding waveguide. I identified the regimes of Markovian and non-Markovian dynamics with the help of the time evolution of the atom's excited state, output spectra as well as atom–field and field–field correlation functions. In addition to that, I accounted for several loss mechanisms such as atomic dissipation and dephasing, lossy field modes, and an open waveguide.

In Chap. 7, I reformulated the problem of two magnons propagating in a Heisenberg spin chain under the influence of a non-uniform, external magnetic field such that it became amenable to the numerical wave-function based approach employed in this thesis. In essence, a Holstein-Primakoff transformation led to a system of hard-core bosons with nearest-neighbor interaction. I furthermore adjusted the external magnetic field such that it forms a potential which supports exactly one single-particle bound state. I then demonstrated how an impinging spin wave can extract a magnon which was stored in the ground state of the external potential to form a propagating two-magnon bound state. This interaction-induced extraction of the stored magnon can, loosely speaking, be interpreted as a readout.

8.2 Conclusion and Outlook

In conclusion, I investigated the dynamics of bosonic excitations in a one-dimensional continuum of modes—a waveguide. In particular, such a waveguide was coupled to a smaller subsystem, e. g., a two-level atom or a nonlinear cavity, or exposed to an external potential (cf. Chap. 7). In these systems, the dynamics of few-boson states or composite pulses (cf. Chap. 5) qualitatively differs from the single-particle case. For these problems, which

can be analyzed in a Hilbert space of only a few particles (or, as in Chap. 5, in the basis of coherent states and single photons), a time-dependent wave-function based approach was proven to be well-suited.

A number of open questions leading to possible future studies can be envisioned. The Hamiltonians studied in this thesis can be regarded as simplified but not oversimplified model systems. A more sophisticated and detailed description could be realized with respect to the following points.

Towards a More Detailed Physical Description

In this thesis, the waveguide was modeled as a spin-independent, single-band tight-binding chain, leading to a cosine-dispersion relation. By including more than just nearest-neighbor hopping terms (or, alternatively, discretizing a given dispersion relation directly in momentum space) more complicated multi-band dispersion relations can be realized (cf. the studies by J.-C. Blancon [50, 158] in Sec. 3.4). However, this refinement most likely leads to quantitative but not qualitative differences when compared to a tight-binding chain.

Alternatively, the level of detail in the description of the subsystems coupled to the waveguide could be increased. For instance, in the case of atoms, one could think of going beyond the two- or three-level description towards multi-level atoms. Since quantum interference effects can already dramatically influence the single-particle dynamics in the case of three-level systems (cf. the studies by C. Martens in Sec. 3.4), the inclusion of more levels may provide even more possibilities of gaining control over the transport. Moreover, going beyond the description of atoms in terms of single-electron systems would not only allow for the investigation of effective interactions (or correlations) between photons, but, vice versa, also include the question of how photons may be exploited to generate an entangled or correlated state of matter.

Besides the refinement of what one usually refers to as being "the system", the influence of the environment ("the reservoir") plays a crucial role in nearly all solid-state based quantum-optical systems. In this thesis, a first approach towards that direction was given by the quantum jump approach by means of which I was able to account for (purely Markovian) T_1- and T_2-relaxations at zero temperature. The overall spirit here was to regard the influence of any external source of dissipation and dephasing as being detrimental to the coherent dynamics of the system. While being true for the problems studied in this thesis, this only represents a limited point of view. In fact, the coupling to an environment can generate so-called "decoherence-free subspaces" [217], i. e., mixed steady states of system and environment which are immune to dissipation and dephasing. Moreover, the influence of an environment may even be exploited as a source for the generation of entanglement [218].

Irrespective of extensions to the coherent (and incoherent) system dynamics, different initial states could be analyzed. Throughout this thesis, all wave packets exhibited a Gaussian envelope. However, one could imagine specially shaped and/or chirped pulses to gain coherent control over the dynamics of the subsystem coupled to the waveguide. In the microwave

domain, pulses of single-photon Fock states can be generated and coupled into networks of waveguiding structures in a controlled way [219]. In contrast to this, many quantum-optical experiments in an integrated setup in the optical domain still rely on (low-intensity) coherent states. Therefore, the nonlinear dynamics of coherent states is very important (cf. the studies by J. Werra [161] in Sec. 3.4).

Apart from that, the capability of accounting for Hamiltonians which are explicitly time-dependent would allow for the investigation of systems under the influence of an external driving field. To account for such non-equilibrium situations, the existing Krylov time integrator would have to be modified and/or replaced by a variation which does not rely on time-independent Hamiltonians. Possible applications include, for instance, the coherent control of atoms by the spatio-temporal profile of an external pulse or the (adiabatic) guiding of excitations in a moving potential as an extension to the investigations of Chap. 7 in the spirit of Ref. [26].

Extensions and Modifications of the Wave-Function Based Scheme

The above ideas are intertwined with and rely on the further development of the wave-function based scheme as introduced in Chap. 2 and Appendix C.

Certainly, one of the strengths of the numerical method is that the state vector's coefficients from the Hilbert space of waveguide and subsystem are fully accessible, which—at least in principle—allows for the calculation of arbitrary observables as a function of time. This strong point is at the same time a severe limitation since the dimension of the Hilbert space grows exponentially with the number of excitations (cf. Chap. 2). The employed method is numerically exact in the sense that the Hilbert space is not truncated. The exponential increase of the degrees of freedom with the excitation number, however, can only be reduced by working in a truncated but optimized basis. Loosely speaking, one could truncate the Hilbert space based on the level of entanglement between single-particle states by virtue of a Schmidt decomposition [220]. This might be especially suited for the problem of an interaction-free waveguide with only a single scatterer. Away from the scatterer, the dynamics of few-particle wave packets is just determined by the dynamics of independent product states of single-particle states. Only the local scatterer induces a non-separability on states that were initially separable.

So far, the "wave function" in the numerical scheme was given by the state vector, which evolved in time according to the Schrödinger equation. In a broader sense, one could also envision the state vector to be replaced by a density matrix since a master equation of Lindblad type can be recast into Schrödinger form by rearranging the entries of the density matrix into a vector [221, 222]. Of course, when compared to a pure state of dimension N, a density matrix has already N^2 degrees of freedom[1]. Still, in the subspace of only a few excitations, the calculations should be feasible. The advantage of such an approach would be

[1] At this qualitative level, I disregard the fact that not all of the N^2 entries of the density matrix are independent of each other.

the possibility to directly account for the dynamics of open systems in a single run without the need of a stochastic quantum jump formalism.

Closing Remarks

Clearly, a lot of important and interesting issues in the field of waveguide quantum optics have already been addressed and answered over the course of the last few years (cf. Sec. 3.2). Nonetheless, even more tasks still need to be accomplished in order to reach a maturity which is nearly comparable to, say, classical (computational) nanophotonics. Most importantly, an extensive and continuous dialogue with experimental groups needs to be established. Otherwise, waveguide quantum optics will remain to be a predominantly theoretical field of research.

Appendix A

A Dimensionless Units

Maxwell's Equations and the Schrödinger equation are transformed to dimensionless units.

A.1 Maxwell's Equations in Dimensionless Units

Maxwell's macroscopic equations (1.1) have the property that they do not contain a fundamental length scale. Furthermore, for the linear constitutive relations (1.2), the field strengths can be changed arbitrarily. These features can be exploited to rescale Maxwell's equations to dimensionless units. By introducing a length scale ℓ_0 and a field strength E_0, a rescaling according to

$$\tilde{\mathbf{H}} = \frac{1}{\sqrt{\frac{\epsilon_0}{\mu_0}}E_0}\mathbf{H}\,, \tag{A.1a}$$

$$\tilde{\mathbf{E}} = \frac{\mathbf{E}}{E_0}\,, \tag{A.1b}$$

$$\tilde{\mathbf{r}} = \frac{\mathbf{r}}{\ell_0}\,, \tag{A.1c}$$

$$\tilde{t} = \frac{c}{\ell_0}t\,, \tag{A.1d}$$

yields Maxwell's equations in dimensionless units, i. e.,

$$\boldsymbol{\nabla}\times\tilde{\mathbf{E}} = -\frac{\partial}{\partial t}\tilde{\mathbf{B}}\,, \tag{A.2a}$$

$$\boldsymbol{\nabla}\times\tilde{\mathbf{H}} = \frac{\partial}{\partial t}\tilde{\mathbf{D}}\,, \tag{A.2b}$$

$$\boldsymbol{\nabla}\cdot\tilde{\mathbf{D}} = 0\,, \tag{A.2c}$$

$$\boldsymbol{\nabla}\cdot\tilde{\mathbf{B}} = 0\,, \tag{A.2d}$$

in which $\tilde{\mathbf{D}} = \mathbf{D}/D_0$ and $\tilde{\mathbf{B}} = \mathbf{B}/B_0$ with $D_0 = \epsilon_0 E_0$ and $B_0 = \sqrt{\mu_0 \epsilon_0} E_0$. The constitutive relations in dimensionless units read

$$\tilde{\mathbf{D}} = \epsilon \tilde{\mathbf{E}}\,, \tag{A.3a}$$

$$\tilde{\mathbf{B}} = \tilde{\mathbf{H}}\,. \tag{A.3b}$$

In these units, the speed of light is unity. In the main chapters, the tilde is dropped after the introduction of dimensionless units.

A.2 The Schrödinger Equation in Dimensionless Units

The Schrödinger equation

$$\mathrm{i}\hbar \frac{\partial}{\partial t} |\Psi\rangle = H|\Psi\rangle \tag{A.4}$$

is a linear differential equation. Introducing an energy scale J and applying the rescaling

$$\tilde{t} = \frac{J}{\hbar} t\,, \tag{A.5a}$$

$$\tilde{H} = \frac{H}{J}\,, \tag{A.5b}$$

yields the dimensionless Schrödinger equation

$$\mathrm{i}\frac{\partial}{\partial \tilde{t}} |\Psi\rangle = \tilde{H}|\Psi\rangle\,. \tag{A.6}$$

These units are equivalent to setting $\hbar \equiv 1$. In the main chapters, the tilde is dropped and time is measured in units of J^{-1}. In the case of a tight-binding waveguide, J corresponds to the hopping amplitude. The information about length scales is contained in the Hamiltonian and depends on the actual system. For the case of a one-dimensional lattice, the lattice constant a serves as a fundamental length scale, which is equivalent to setting $a = 1$. Thus, wavenumbers have the unit $1/a = 1$. Since $\hbar \equiv 1$, the terms "momentum" and "wavenumber" as well as "energy" and "frequency" are used interchangeably.

B Appendix B

Feynman Disentangling of Operators

Following Ref. [93], the derivation leading from Eq. (1.81) to Eq. (1.82) is presented. The procedure is known as "Feynman Disentangling of Operators".

The concept of what is called Feynman disentangling of operators in the literature can be found in Ref. [93] and was, for instance, applied in Ref. [95]. The goal is to calculate the thermodynamic expectation value of the phononic displacement operator $X_{\lambda'} = \mathrm{e}^{-\kappa_{\lambda'}(b^\dagger_{\lambda'} - b_{\lambda'})}$ with respect to the free phononic Hamiltonian (cf. Eq. (1.81)). Specifically, the expression

$$\mathrm{tr}\left(\mathrm{e}^{-\beta H_\mathrm{P}} X_{\lambda'}(\kappa_{\lambda'})\right) = \sum_{n_1=0}^{\infty} \cdots \sum_{n_N=0}^{\infty} \langle n_1 \ldots n_N | \mathrm{e}^{-\beta \sum_{\lambda=1}^{N} (\nu-\mu)\, b^\dagger_\lambda\, b_\lambda}\, \mathrm{e}^{-\kappa_{\lambda'}(b^\dagger_{\lambda'} - b_{\lambda'})} | n_1 \ldots n_N \rangle \tag{B.1}$$

has to be calculated. For simplicity, all N phonon frequencies are assumed to be equal, i. e., $\nu_i = \nu$. Equation (B.1) factorizes into the free partition function $Z_0 = 1/(1 - \mathrm{e}^{-\beta(\nu-\mu)})$, except for mode λ', yielding

$$\mathrm{tr}\left(\mathrm{e}^{-\beta H_\mathrm{P}} X_{\lambda'}(\kappa_{\lambda'})\right) = Z_0^{N-1} \sum_{n=0}^{\infty} \left[\mathrm{e}^{-\beta(\nu-\mu)}\right]^n \langle n | \mathrm{e}^{-\kappa(b^\dagger - b)} | n \rangle \,, \tag{B.2}$$

where the indices are suppressed. A crucial step is the evaluation of the matrix element

$$\langle n | \mathrm{e}^{-\kappa(b^\dagger - b)} | n \rangle = \mathrm{e}^{-\frac{\kappa^2}{2}} \langle n | \mathrm{e}^{-\kappa b^\dagger} \mathrm{e}^{\kappa b} | n \rangle \,, \tag{B.3}$$

in which the Baker-Hausdorff formula was applied. The action of the exponential on a number state can be written as

$$\mathrm{e}^{\alpha b} | n \rangle = \sum_{l=0}^{\infty} \frac{\alpha^l}{l!} b^l | n \rangle = \sum_{l=0}^{n} \frac{\alpha^l}{l!} \sqrt{\frac{n!}{(n-l)!}} \, | n - l \rangle \,, \tag{B.4}$$

which allows one to calculate the overlap needed in Eq. (B.3), yielding

$$\begin{aligned}
\langle n|\mathrm{e}^{-\kappa(b^\dagger - b)}|n\rangle &= \mathrm{e}^{-\frac{\kappa^2}{2}} \sum_{l=0}^{n}\sum_{l'=0}^{n} \frac{\kappa^l}{l!}\frac{(-\kappa)^{l'}}{l'!}\frac{n!}{\sqrt{(n-l)!(n-l')!}}\langle n-l'|n-l\rangle \\
&= \mathrm{e}^{-\frac{\kappa^2}{2}} \sum_{l=0}^{n} \frac{(-1)^l\kappa^{2l}}{(l!)^2}\frac{n!}{(n-l)!} \\
&= \mathrm{e}^{-\frac{\kappa^2}{2}} \sum_{l=0}^{n} \frac{(-\kappa^2)^l}{(l!)^2}\binom{n}{l} \\
&= \mathrm{e}^{-\frac{\kappa^2}{2}} L_n(\kappa^2)\,. \qquad \text{(B.5)}
\end{aligned}$$

The L_n denote Laguerre polynomials. Coming back to Eq. (B.2), an expression of the form

$$\sum_{n=0}^{\infty} z^n L_n(x) = \frac{\mathrm{e}^{-xz/(1-z)}}{1-z}\,, \qquad \text{(B.6)}$$

where the generating function of the Laguerre polynomials was used, has to be calculated. Finally, Eq. (B.2) takes the form

$$\mathrm{tr}\left(\mathrm{e}^{-\beta H_\mathrm{p}} X(\kappa)\right) = Z_0^{N-1}\mathrm{e}^{-\kappa^2(g_{\nu-\mu}(\beta)+\frac{1}{2})}\mathrm{e}^{\beta(\nu-\mu)}B_{\nu-\mu}(\beta)$$

with which the thermodynamic expectation value becomes

$$\begin{aligned}
\chi(\kappa) &= \frac{\mathrm{tr}\left(X(\kappa)\mathrm{e}^{-\beta(H_\mathrm{p}-\mu N)}\right)}{\mathrm{tr}\left(\mathrm{e}^{-\beta(H_\mathrm{p}-\mu N)}\right)} \\
&= \mathrm{e}^{-\kappa^2(B_{\nu-\mu}(\beta)+\frac{1}{2}}\,. \qquad \text{(B.7)}
\end{aligned}$$

$B_{\nu-\mu}(\beta) = 1/(\mathrm{e}^{\beta(\nu-\mu)}-1)$ is the Bose-Einstein distribution function.

Appendix C

C Numerical Details and Parameters of the Simulations

I provide numerical details on the computational methods employed in the main chapters. Specifically, I describe the time evolution in the context of linear and nonlinear Schrödinger equations.

C.1 General Remarks

This appendix is organized as follows. In Sec. C.2, I summarize and explain the key elements of the numerical time evolution of Fock States in the context of linear Schrödinger equations. The corresponding in-house code is written in `C++` and used for all simulations presented in Chaps. 3–4 and 6–7. In Sec. C.3, I briefly give the details of the numerical time evolution employed in Chap. 5.

Note that neither mathematical proofs of convergence nor the improvement of numerical algorithms on the level of numerical mathematics are the focus of this thesis. I therefore merely combined existing and well-tested "low-level" routines. The corresponding references are provided at the end of each subsection.

C.2 Time Evolution in the Context of Linear Schrödinger Equations

In this subsection, I describe the action of a Hamilton operator on basis states, I briefly review the Krylov-subspace based time evolution, and I comment on the realization of stochastic quantum jumps. Parts of this subsection are also discussed in Ref. [63].

C.2.1 Action of the Hamiltonian on the Basis States

The current version of the in-house code is capable of simulating three excitations at maximum. In Chaps. 3–4 and 6–7, however, only two excitations at most are investigated. I therefore restrict the discussion to one- and two-particle states only.

Basis States

The wave function coefficients in the Fock basis are stored in a linear array. For a single-particle state, I use the basis vectors

$$|e_i^{(1)}\rangle = a_i^\dagger |0\rangle \,. \tag{C.1}$$

The expansion coefficients $c_i^{(1)}$ of a single-particle state with N sites,

$$|\Psi^{(1)}\rangle = \sum_{i=1}^{N} c_i^{(1)} |e_i^{(1)}\rangle \,, \tag{C.2}$$

can be addressed in a one-dimensional array via the mapping

$$i \to S = i \,. \tag{C.3}$$

In the case of two excitations, I use

$$|e_{ij}^{(2)}\rangle = a_i^\dagger a_j^\dagger \, |0\rangle \quad i \geq j \tag{C.4}$$

as basis vectors. These basis vectors are not normalized to unity, which has to be taken into account when the action of the Hamiltonian is calculated. The restriction $i \geq j$ is a consequence of the particles being identical. The expansion coefficients $c_{ij}^{(2)}$ of a two-particle state,

$$|\Psi^{(2)}\rangle = \sum_{i \geq j}^{N} \sum_{j=1}^{N} c_{ij}^{(2)} |e_{ij}^{(2)}\rangle \,, \tag{C.5}$$

can be addressed in a one-dimensional array via

$$(i,j) \to S = j + \big(i-1\big) \cdot \frac{i}{2} \,. \tag{C.6}$$

The size of the array is $\frac{N}{2} \cdot \big(N+1\big)$ (cf. Sec. 2.3.1).

Action of Operators on the Basis States

In order to implement the action of a Hamilton operator as described in Chap. 2, the action of the different terms which can occur needs to be considered. The action of a hopping term $a_i^\dagger a_j$ on a state can be determined as follows.

- Determine how many excitations N_i and N_j exist at site i and j, respectively.
- Stop if $N_j = 0$ since such states do not contribute. Decrease the number of excitations of site j by 1 and increase it for site i by 1. (In case of a two-level atom, one needs to additionally account for the fact that double occupation is prohibited.)
- Multiply the new state with $\sqrt{(N_i + 1) \cdot N_j}$.

On-site terms are just a special type of hopping terms. In the single-particle case, a hopping term just swaps two entries in the array of the expansion coefficients. For two particles, each tuple (x_1, x_2) describes the situation of one particle being at site x_1 *and* another particle being at site $x_2 \leq x_1$. Hence, for each component (x_1, x_2), one first needs to determine the set of target states $\{(x_1', x_2')\}$ which in principle contribute to the hopping. They fulfill

$$\begin{array}{llllll} x_1 = j \geq x_2 & \wedge & x_1' & = & i \geq x_2' & \wedge \quad x_2' = x_2\,, \\ x_1 = j \geq x_2 & \wedge & x_1' & = & x_2 & \wedge \quad x_2' = i < x_2\,, \\ x_2 = j \geq x_2 & \wedge & x_1' & = & i \geq x_2' & \wedge \quad x_2' = x_1 \leq x_1'\,, \\ x_2 = j \geq x_2 & \wedge & x_1' & = & x_1 & \wedge \quad x_2' = i < x_1'\,. \end{array} \tag{C.7}$$

Another type of terms which occurs in the Hamiltonians presented in Chap. 2 is a two-body interaction term $a_i^\dagger a_j^\dagger a_k a_l$. Since it has two annihilation operators, it yields zero when applied to a single-particle state. The action on a two-particle state can be determined as follows.

- Determine how many excitations N_i, N_j, N_k, and N_l exist at site i, j, k, and l.
- Stop if $N_k = 0$ or $N_l = 0$ since these states do not contribute. Decrease the number of excitations of sites k and l by 1. Increase it for site i and j by 1.
- Multiply the new state with $\sqrt{(N_i + 1) \cdot (N_j + 1) \cdot N_k \cdot N_l}$.

Again, staring from a tuple (x_1, x_2), one needs to determine the set of target states $\{(x_1', x_2')\}$ which contribute to the interaction. The target states obey

$$\begin{array}{lll} x_1 = k,\ x_2 = l,\ x_1' = i,\ x_2' = j & : & k \geq l,\ i \geq j\,, \\ x_1 = l,\ x_2 = k,\ x_1' = i,\ x_2' = j & : & l > k,\ i \geq j\,, \\ x_1 = k,\ x_2 = l,\ x_1' = j,\ x_2' = i & : & k \geq l,\ j > i\,, \\ x_1 = l,\ x_2 = k,\ x_1' = j,\ x_2' = i & : & l > k,\ j > i\,. \end{array} \tag{C.8}$$

C.2.2 Krylov-Subspace Based Time Evolution

The core of the numerical scheme is the time evolution of states, i. e.,

$$|\Psi(t)\rangle = \mathrm{e}^{-\mathrm{i}H\cdot(t-t_0)}|\Psi(t_0)\rangle\,. \tag{C.9}$$

The state vector is propagated from its initial state at t_0 to time t, using n sufficiently small, equidistant time steps Δt, i. e.,

$$t - t_0 \to n\cdot\Delta t\,. \tag{C.10}$$

A proper choice of the time step Δt is discussed later (cf. Eq. (C.15)).

Here, I only give a brief description of how the action of the operator exponential $\mathrm{e}^{-\mathrm{i}H\cdot(t-t_0)}$ on a state $|\Psi\rangle$ can be calculated. See Refs. [109–111] for further details. For many practical purposes, the explicit calculation of the operator exponential in the eigenbasis of the Hamiltonian is either very inconvenient or even impossible. The calculation of the matrix

$$\mathrm{e}^{-\mathrm{i}H\cdot(t-t_0)} = U\mathrm{e}^{-\mathrm{i}H_{\mathrm{diag}}\cdot(t-t_0)}U^\dagger \tag{C.11}$$

relies on the diagonalization of the Hamiltonian H, i. e., $H_{\mathrm{diag}} = U^\dagger H U$. Diagonalizing the full Hamiltonian can become very inefficient or even impossible once the degrees of freedom exceed the memory available.

Luckily, the Krylov-subspace method only relies on the action of a Hamiltonian on given basis states and does not explicitly require the Hamiltonian matrix. In other words, at no point does one need to store the full Hamiltonian matrix and its action on basis states can be implemented implicitly. The main idea is to project the "big" $d\times d$ matrix $\tilde{H} = -\mathrm{i}H$ onto the smaller $d\times l$-dimensional Krylov subspace. The latter can be constructed by successive application of the matrix $\tilde{H}$ on the state to be propagated Ψ_0, i. e.,

$$\mathcal{K}_l = \mathrm{span}\left\{\Psi_0, \tilde{H}\cdot\Psi_0, \tilde{H}^2\cdot\Psi_0, \ldots, \tilde{H}^{l-1}\cdot\Psi_0\right\}\,. \tag{C.12}$$

Here, only the action of $\tilde{H}$ on Ψ_0 is required. The Krylov subspace $\mathcal{K}_l$ can be transformed to an orthonormal basis $\{V_l\}$ (for instance, by using the Arnoldi algorithm [109]). The system matrix $\tilde{H}$ can be projected onto the Krylov subspace with the help of the matrix V, which contains the V_l as column vectors. Specifically,

$$H_l = V^\dagger\tilde{H}V \tag{C.13}$$

results in an upper $(l+1)\times l$-dimensional Hessenberg matrix H_l. The entries of the matrix H_l are obtained during the Arnoldi algorithm.

Finally, the time evolution of the state Ψ_0 can be approximated by [109]

$$\mathrm{e}^{\Delta t\tilde{H}}\Psi_0 \approx \|\Psi\|_2 V_l \mathrm{e}^{\Delta t H_l}\mathbf{e}_1\,. \tag{C.14}$$

Here, Δt is the time step, $\|\Psi\|_2$ denotes the 2-norm of vector Ψ_0, and $\mathbf{e}_1$ signifies the first unit vector of V_l which allows one the projection back to the "big" Hilbert space. The explicit

calculation of the matrix exponential $\mathrm{e}^{\Delta t H_l}$ is less problematic since H_l is a dense but small matrix when compared to $\tilde{H}$ and a Padé approximation [223] is usually applied.

Rigorous error bounds for approximation (C.14) are deduced in Ref. [109]. The maximal error accumulated for a time step Δt and a Krylov subspace of dimension l is

$$\left\| \mathrm{e}^{\Delta t \tilde{H}} \Psi - \left\| \Psi \right\|_2 V_l \mathrm{e}^{\Delta t H_l} \mathbf{e}_1 \right\|_2 \leq 2 \left\| \Psi \right\|_2 \frac{\mathrm{e}^{\Delta t \| \tilde{H} \|_2}}{l!} \left(\| \tilde{H} \|_2 \Delta t \right)^l . \tag{C.15}$$

Here, $\| \tilde{H} \|_2$ denotes the 2-norm of the matrix $\tilde{H}$. Equation (C.15) states that the numerical error can be controlled by both the dimension of the Krylov subspace l and the time step Δt. Hence, one can trade off memory consumption (determined by the Krylov subspace dimension) against CPU time (determined by the time step). See Sec. C.2.5 for the choices of l and Δt used in this thesis.

C.2.3 Stochastic Quantum Jumps

The deterministic part of the time evolution is carried out according to the scheme described in Sec. C.2.2. In case the dynamics of open systems is taken into account, the decision whether or not a quantum jump occurs is made after each time step Δt. The general procedure is discussed in Sec. 1.3.4 and Refs. [105, 106].

In order to draw random numbers, an open source library which generates uniformly distributed random numbers is used (see Sec. C.2.4). If there are k competing jumps with jump probabilities $p_1, p_2, \ldots, p_k$, the method of linear search [103] is utilized to select one jump. This method works as follows.

- Subdivide the interval $[0, 1]$ into k sub-intervals $I_1, I_2, \ldots, I_k$ of lengths $p_1, p_2, \ldots, p_k$.
- Draw a uniformly distributed random number.
- Search for the interval which contains the random number.
- Select the jump corresponding to this interval.

According to Eq. (1.97), the jump probability is proportional to the ratio of the time step and the time scale which determines the flow of probability out of the system, e. g., the T_1-time in case of a lossy two-level atom (cf. Sec. 1.3.4). The time step needs to be adjusted such that the jump probability is much smaller than unity [106]. Loosely speaking, the time step then needs to be smaller than any decay time to the environment. On the other hand, the resulting jump probability still needs to be larger than the resolution of the random number generator. A thorough discussion of the statistical error of the quantum jump approach can be found in Ref. [106]. See Sec. C.2.5 for the choices of the time step and the number of samples used in this thesis.

C.2.4 Software Packages and Parameters

I use the open-source software package `Expokit` [224] for the Krylov-subspace based time evolution. Specifically, the `FORTRAN` routines are linked to the `C++`-code. `Expokit` takes

- the Krylov subspace dimension l,
- the time step Δt,
- the degree of the symmetric Padé approximation m,
- and the maximal error per time step according to Eq. (C.15)

as input parameters which control the numerical error. In case the desired tolerance cannot be realized, `Expokit` automatically decreases the time step.

I use `boost/random.hpp` as a random number generator from the open-source `C++` library `boost` [225] (version 1.42). Various low-level linear algebra operations are performed with the help of the free libraries `BLAS` [226] and `LAPACK` [227]. In order to import configuration files, I utilize the software package `TinyXML` [228], which is an XML parser. The results of each simulation are stored using the `HDF5` format [229] (version 1.8.4). `MATLAB` is used for the post-processing. For instance, Fourier transforms (cf. Chap. 6) are carried out using the `MATLAB` [230] routine `fft`, which is based on the library `FFTW` [231].

C.2.5 Parameters Used in this Thesis

For all simulations in Chaps. 3–4 and 6–7, I set the Krylov subspace dimension to $l = 33$, the degree of the symmetric Padé approximation to $m = 6$, and the maximal error per time step to 10^{-14}. This choice of parameters is based on numerical experiments, i. e., empirical convergence studies.

The actual number of samples used in the stochastic time evolution is also based on numerical experiments and is specified in the main chapters where needed. The time step in the quantum jump approach coincides with the time step which is given as an input to the `Expokit` routine. Table C.1 lists the time steps[1] for the simulations presented in Chaps. 3–4 and 6–7. I provide all other parameters, e. g., system sizes, directly in the main chapters.

C.3 Time Evolution in the Context of Nonlinear Schrödinger Equations

When compared to linear Schrödinger equations, I performed much less simulations in the context of nonlinear Schrödinger equations in this thesis. Only the problem investigated in Chap. 5 requires the numerical solution of a Schrödinger equation with a local nonlinearity.

[1] The time step is given in dimensionless units as stated in the corresponding main chapters and Appendix A.

Simulation as shown in	time step Δt	Simulation as shown in	time step Δt
Fig. 3.2	0.2	Fig. 4.4	0.2
Fig. 4.5	0.2	Fig. 4.6	0.2
Fig. 4.7	0.1	Fig. 4.8	0.1
Fig. 6.2	0.1	Fig. 6.3	0.1
Fig. 6.4	0.1	Fig. 6.5	0.1
Fig. 6.6	0.1	Fig. 6.7	0.1
Fig. 6.8	0.1	Fig. 6.9	0.1
Fig. 7.4	0.1	Fig. 7.5	0.1
Fig. 7.6	0.1	Fig. 7.7	0.1

Table C.1: Time Steps Δt used in the simulations of Chaps. 3–4 and 6–7.

For these simulations, I employed the solver `ode45` of `MATLAB` (version 7.11.1 [230]), which is a Runge-Kutta solver. See the `MATLAB` manual for further details.

The routine takes

- `RelTol`, the relative error tolerance which applies to all components of the solution vector, and
- `AbsTol`, the absolute error tolerances which apply to the individual components of the solution vector,

as input parameters which control the numerical accuracy.

C.3.1 Parameters Used in this Thesis

For all simulations in Chap. 5, i. e., for all results as presented in Figs. 5.3 and 5.4, I set `RelTol` = `AbsTol` = 10^{-12}. The wave function coefficients are saved after each time step of $\Delta t = 0.1$. This time step does not influence the numerical accuracy since it may be adjusted internally to meet the desired constraints as imposed by `RelTol` and `AbsTol`.

D Appendix D

Single-Particle Scattering Solutions and Beam-Splitter Constraint

I present the single-particle scattering solutions for a local on-site potential and a two-level atom in a tight-binding waveguide, respectively. Specifically, reflection and transmission amplitudes are used to deduce the beam-splitter constraints employed in Chap. 4 and the first-order Taylor expansion of the reflectance is discussed.

D.1 General Form of the Scattering Equation

In this section, I motivate the general form of the single-particle scattering equation for a system of a tight-binding waveguide and a local scatterer. The waveguide is described by the Hamiltonian (cf. Eq. (4.6))

$$H_{\text{leads}} = \sum_x \omega_0 a_x^\dagger a_x - J \sum_x \left(a_{x+1}^\dagger a_x + a_x^\dagger a_{x+1} \right) . \tag{D.1}$$

The scatterer whose free dynamics is governed by the Hamiltonian H_{imp} couples locally at site x_0 to the waveguide. The coupling Hamiltonian is of the form

$$H_{\text{coup}} = V \left(a_{x_0}^\dagger b + a_{x_0} b^\dagger \right) , \tag{D.2}$$

where V is the coupling strength and b and $b^\dagger$ describe annihilation and creation operators of the scatterer. Independent of the actual realization of the scatterer, these operators can be assumed to be bosonic since only the single-particle sector is considered here[1]. The Hamiltonian of the free scatterer, H_{imp}, only depends on the operators b and $b^\dagger$.

[1] In the single-excitation subspace, there is no difference between bosonic, fermionic, or spin excitations.

A general single-particle eigenstate is of the form

$$|\Psi\rangle = \sum_x a_x^\dagger \varphi_x |0\rangle + \psi b^\dagger |0\rangle \,. \tag{D.3}$$

In order to derive the scattering states, I use the ansatz[2]

$$\varphi_x = \begin{cases} \mathrm{e}^{\mathrm{i}kx} + r_k \mathrm{e}^{-\mathrm{i}kx} & x < x_0 \\ \varphi_{x_0} & x = x_0 \\ t_k \mathrm{e}^{\mathrm{i}kx} & x > x_0 \end{cases} . \tag{D.4}$$

For the scatterers investigated in Chap. 4, i. e., a local on-site potential and a local two-level system, the eigenproblem

$$\Big(H_\mathrm{leads} + H_\mathrm{imp} + H_\mathrm{coup} - E\Big)\,|\Psi\rangle = 0 \tag{D.5}$$

leads to a discrete scattering equation of the form

$$0 = \big(\omega_0 - E\big)\,\varphi_x - J\left(\varphi_{x+1} + \varphi_{x-1}\right) + \delta_{xx_0} G(E) \varphi_{x_0} \,. \tag{D.6}$$

Evaluating Eq. (D.6) at $x = x_0 - 1, x_0, x_0 + 1, x_0 + 2$ yields $1 + r_k = t_k$, $\varphi_{x_0} = t_k$, and the eigenenergy is $E = \omega_0 - 2J\cos(k)$. The reflection amplitude takes the form

$$r_k = -\mathrm{e}^{-2\mathrm{i}k} \frac{J^2 - \Big(\omega_0 - E + G(E) - J\mathrm{e}^{\mathrm{i}k}\Big)\Big(\omega_0 - E - J\mathrm{e}^{-\mathrm{i}k}\Big)}{J^2 - \Big(\omega_0 - E + G(E) - J\mathrm{e}^{\mathrm{i}k}\Big)\Big(\omega_0 - E - J\mathrm{e}^{\mathrm{i}k}\Big)} \,. \tag{D.7}$$

The function $G(E)$ depends on the actual realization of the scatterer.

D.2 Local On-Site Potential

For a local on-site potential, the Hamiltonian of the scatterer reads $H_\mathrm{imp} = g a_{x_0}^\dagger a_{x_0}$, where g is the strength of the potential. Furthermore, $H_\mathrm{coup} = 0$ since the scatterer is part of the tight-binding chain. For convenience, I set the zero of the free waveguide's energy in the middle of the band, i. e., $\omega_0 = 0$. Then, the discrete scattering equation (D.6) becomes

$$0 = -E\varphi_x - J\left(\varphi_{x+1} + \varphi_{x-1}\right) + g\varphi_{x_0}\delta_{xx_0} \,. \tag{D.8}$$

Here, $G(E) = g$ so that the reflection amplitude is

$$r_k = -\frac{g}{g - 2\mathrm{i}J\sin(k)} \,. \tag{D.9}$$

[2] This ansatz would be inappropriate in the context of bound states.

The corresponding transmission amplitude reads

$$t_k = -\frac{2J}{2J + \mathrm{i}g/\sin(k)} \,. \tag{D.10}$$

The reflectance $|r_k|^2$ and transmittance $|t_k|^2$,

$$|r_k|^2 = \frac{g^2}{g^2 + 4J^2\sin^2(k)} \,, \tag{D.11a}$$

$$|t_k|^2 = \frac{4J^2\sin^2(k)}{g^2 + 4J^2\sin^2(k)} \,, \tag{D.11b}$$

can be combined to deduce the beam-splitter condition $|r_k|^2 = |t_k|^2$ which is extensively used in Chap. 4. Here, the beam-splitter constraint reads

$$g = \pm 2\left|J\right|\left|\sin(k)\right| \,. \tag{D.12}$$

In Chap. 4, the example of $J > 0$ and $k = \pi/2$ is investigated, which results in $g = \pm 2J$.

The derivative of the reflectance with respect to the wavenumber is

$$\frac{\partial|r_k|^2}{\partial k} = \frac{1}{g^2}|r_k|^4\left(-8J^2\sin(k)\cos(k)\right) \,. \tag{D.13}$$

Hence, the reflectance does not change to first order around $k = \pi/2$.

D.3 Local Two-Level System

For a two-level atom embedded in the waveguide, the Hamiltonian of the free scatterer is $H_{\mathrm{scatt}} = (\Omega/2)\,\sigma_z$ and the coupling Hamiltonian is $H_{\mathrm{coup}} = V(a_{x_0}^\dagger\sigma^- + a_{x_0}\sigma^+)$ (cf. Secs. 1.3.2 and 2.2.1). The derivation of the scattering states can be found in Ref. [120]. Adapted to the notation used in this thesis, the discrete scattering equation reads

$$0 = -E\varphi_x - J\left(\varphi_{x+1} + \varphi_{x-1}\right) + \frac{V^2}{E-\Omega}\varphi_{x_0}\delta_{xx_0} \,, \tag{D.14}$$

where I set $\omega = 0$ for convenience. Here, $G(E) = \frac{V^2}{E-\Omega}$ so that the reflection and transmission amplitudes are

$$r_k = \frac{V^2}{2\mathrm{i}J\sin(k)(-\Omega - 2J\cos(k)) - V^2} \,, \tag{D.15a}$$

$$t_k = \frac{2J\sin(k)(-\Omega - 2J\cos(k))}{2J\sin(k)(-\Omega - 2J\cos(k)) + \mathrm{i}V^2} \,. \tag{D.15b}$$

The corresponding reflectance and transmittance are

$$|r_k|^2 = \frac{V^4}{V^4 + 4J^2 \sin^2(k)(-2J\cos(k) - \Omega)^2}\,, \tag{D.16a}$$

$$|t_k|^2 = \frac{4J^2 \sin^2(k)(-2J\cos(k) - \Omega)^2}{V^4 + 4J^2 \sin^2(k)(-2J\cos(k) - \Omega)^2}\,. \tag{D.16b}$$

The beam-splitter condition $|r_k|^2 = |t_k|^2$ yields

$$V = \pm\sqrt{\left|2J\sin(ka)(-2J\cos(k) - \Omega)\right|}\,. \tag{D.17}$$

In Chap. 4, the example of $J > 0$ and $k = 3\pi/4$ is investigated, which results in $V = \pm\sqrt{\sqrt{2}J|\sqrt{2}J - \Omega|}$.

Here, the derivative of the reflectance with respect to the wavenumber reads

$$\frac{\partial |r_k|^2}{\partial k} = \frac{1}{V^8}|r_k|^4 \cdot 8J^3 \sin(k)\cos(2k)\,. \tag{D.18}$$

This expression is non-zero for $k = 3\pi/4$, i. e., the reflectance does change to first order for wavenumbers around around $k = 3\pi/4$.

Appendix E

Density of States and Memory Kernel

In this appendix, I derive Eqs. (6.19) and (6.21) of Chap. 6. I calculate the memory kernel for a two-level atom coupled to a one-dimensional cosine band in the case of constant atom–photon coupling. Furthermore, I present the density of states for a one-dimensional linear dispersion relation without cutoff and the corresponding memory kernel.

E.1 Memory Kernel for the One-Dimensional Cosine Band and Constant Atom–Photon Coupling

Equation (6.19) is obtained by inserting the density of states for the one-dimensional cosine band (cf. Eq. (6.18)),

$$\mathcal{N}(\omega) = \frac{1}{2\pi J} \frac{\theta(\omega + 2J)\theta(2J - \omega)}{\sqrt{1 - \left(\omega/2J\right)^2}}\,, \tag{E.1}$$

into Eq. (6.17), yielding

$$\begin{aligned} K(\tau) &= \theta(\tau)\frac{V^2}{2\pi J}\mathrm{e}^{\mathrm{i}\Omega\tau}\int\limits_{-2J}^{2J}\mathrm{d}\omega\frac{\mathrm{e}^{-\mathrm{i}\omega\tau}}{\sqrt{1-\left(\frac{\omega}{2J}\right)^2}} \\ &= \theta(\tau)\frac{V^2}{\pi}\mathrm{e}^{\mathrm{i}\Omega\tau}\int\limits_{-1}^{1}\mathrm{d}\xi\frac{\mathrm{e}^{-\mathrm{i}2J\tau\xi}}{\sqrt{1-\xi^2}} \\ &= \theta(\tau)V^2\mathrm{e}^{\mathrm{i}\Omega\tau}J_0(2J\tau)\,, \end{aligned} \tag{E.2}$$

where J_0 is the zeroth order Bessel function of first kind.

E.2 Density of States for a One-Dimensional Liner Dispersion Relation Without Cutoff

Consider a one-dimensional dispersion relation without cutoff of the form

$$\epsilon_k = c|k|\,, \tag{E.3}$$

where c is the photon's velocity. The corresponding density of states reads

$$\begin{aligned}
\mathcal{N}(\omega) &= \int_{-\infty}^{\infty} \mathrm{d}k\,\delta(\omega - c|k|) \\
&= \int_{-\infty}^{0} \frac{\mathrm{d}k}{c}\delta(\frac{\omega}{c} + k) + \int_{0}^{\infty} \frac{\mathrm{d}k}{c}\delta(\frac{\omega}{c} - k) \\
&= \frac{1}{c}\left(\theta(-\frac{\omega}{c}) + \theta(\frac{\omega}{c})\right) \\
&= \frac{1}{c}\,.
\end{aligned} \tag{E.4}$$

E.3 Memory Kernel for a One-Dimensional Liner Dispersion Relation Without Cutoff and Constant Atom–Photon Coupling

Inserting expression (E.4) into Eq. (6.17) yields the memory kernel (6.21), i. e.,

$$\begin{aligned}
K(\tau) &= \theta(\tau)V^2\mathrm{e}^{\mathrm{i}\Omega\tau} \int_{-\infty}^{\infty} \mathrm{d}\omega \frac{1}{c}\mathrm{e}^{-\mathrm{i}\omega\tau} \\
&= \theta(\tau)V^2\mathrm{e}^{\mathrm{i}\Omega\tau}\frac{1}{c}\delta(\tau) \\
&= \frac{V^2}{c}\delta(\tau)\,.
\end{aligned} \tag{E.5}$$

This memory kernel describes an exponential decay with a rate $\Gamma = 2V^2/c$ (cf. Sec. 6.3.2).

Appendix F

Two-Body Eigenstates in a One-Dimensional Heisenberg Spin Chain

In this Appendix, I derive the exact two-body eigenstates of Hamiltonian (7.7) in the absence of an external potential.

F.1 Eigenproblem and Reduction to an Effective Single-Particle Problem

In order to solve the eigenproblem $(h-\epsilon)\left|\Psi\right\rangle = 0$ with $\left|\Psi\right\rangle = \sum_{x_1 x_2} \Phi_{x_1 x_2} a^\dagger_{x_1} a^\dagger_{x_2} \left|0\right\rangle$, the action of the different terms in the Hamiltonian (7.7) on the basis states needs to be calculated, i. e.,

$$a^\dagger_x a_y a^\dagger_{x_1} a^\dagger_{x_2} \left|0\right\rangle = \left(\delta_{x_2 y} a^\dagger_x a^\dagger_{x_1} + \delta_{x_1 y} a^\dagger_x a^\dagger_{x_2}\right) \left|0\right\rangle \ , \tag{F.1a}$$

$$a^\dagger_{i+1} a^\dagger_i a_i a_i a^\dagger_{x_1} a^\dagger_{x_2} \left|0\right\rangle = 2\delta_{x_1 i}\delta_{x_2 i} a^\dagger_{i+1} a^\dagger_i \left|0\right\rangle \ , \tag{F.1b}$$

$$a^\dagger_{i-1} a^\dagger_i a_i a_i a^\dagger_{x_1} a^\dagger_{x_2} \left|0\right\rangle = 2\delta_{x_1 i}\delta_{x_2 i} a^\dagger_{i-1} a^\dagger_i \left|0\right\rangle \ , \tag{F.1c}$$

$$a^\dagger_{i+1} a^\dagger_{i+1} a_{i+1} a_i a^\dagger_{x_1} a^\dagger_{x_2} \left|0\right\rangle = \left(\delta_{x_1 i}\delta_{x_2 i+1} + \delta_{x_2 i}\delta_{x_1 i+1}\right) a^\dagger_{i+1} a^\dagger_{i+1} \left|0\right\rangle \ , \tag{F.1d}$$

$$a^\dagger_{i-1} a^\dagger_{i-1} a_{i-1} a_i a^\dagger_{x_1} a^\dagger_{x_2} \left|0\right\rangle = \left(\delta_{x_1 i}\delta_{x_2 i-1} + \delta_{x_2 i}\delta_{x_1 i-1}\right) a^\dagger_{i-1} a^\dagger_{i-1} \left|0\right\rangle \ , \tag{F.1e}$$

$$a^\dagger_x a_x a^\dagger_y a_y a^\dagger_{x_1} a^\dagger_{x_2} \left|0\right\rangle = \left(\delta_{x_1 i}\delta_{x_2 i+1} + \delta_{x_1 i+1}\delta_{x_2 i}\right) a^\dagger_x a^\dagger_y \left|0\right\rangle \ . \tag{F.1f}$$

Using Eqs. (F.1), the eigenproblem yields

$$\begin{aligned} 0 = & - \left(\Phi_{x_1+1x_2} + \Phi_{x_1-1x_2} + \Phi_{x_1x_2+1} + \Phi_{x_1x_2-1}\right) \\ & - \epsilon\Phi_{x_1x_2} \\ & - 2\left(\delta_{x_1x_2-1} + \delta_{x_1-1x_2}\right)\Phi_{x_1x_2} \\ & + 2\left(\delta_{x1_1x_2}\Phi_{x_1-1x_2} + \delta_{x_1+1x_2}\Phi_{x_1+1x_2}\right) \\ & + \delta_{x_1x_2}\left(\Phi_{x_1-1x_2} + \Phi_{x_1x_2-1} + \Phi_{x_1x_2+1} + \Phi_{x_1+1x_2}\right) \end{aligned} \tag{F.2}$$

for the wave function coefficients. The introduction of a center-of-mass coordinate $c \equiv (x_1 + x_2)/2$ and a relative coordinate $r \equiv x_1 - x_2$ transforms Eq. (F.2) to

$$\begin{aligned} 0 = & - \left(\tilde{\Phi}_{c+\frac{1}{2}r+1} + \tilde{\Phi}_{c-\frac{1}{2}r-1} + \tilde{\Phi}_{c+\frac{1}{2}r-1} + \tilde{\Phi}_{c-\frac{1}{2}r+1}\right) \\ & - \epsilon\tilde{\Phi}_{cr} \\ & - 2\left(\delta_{r1} + \delta_{r-1}\right)\tilde{\Phi}_{cr} \\ & + 2\left(\delta_{r1}\tilde{\Phi}_{c-\frac{1}{2}0} + \delta_{r-1}\tilde{\Phi}_{c+\frac{1}{2}0}\right) \\ & + \delta_{r0}\left(\tilde{\Phi}_{c-\frac{1}{2}-1} + \tilde{\Phi}_{c-\frac{1}{2}1} + \tilde{\Phi}_{c+\frac{1}{2}-1} + \tilde{\Phi}_{c+\frac{1}{2}1}\right), \end{aligned} \tag{F.3}$$

where $\tilde{\Phi}_{cr}$ denote the wave function coefficients in the new coordinates. Next, I separate the center-of-mass motion in order to arrive at an effective single-particle problem. The ansatz

$$\tilde{\Phi}_{cr} = \mathrm{e}^{\mathrm{i}Kc} \cdot \Psi_r \qquad \Psi_r = \Psi_{-r} \tag{F.4}$$

yields the single-particle problem

$$\begin{aligned} 0 = & - \epsilon_K\left(\Psi_{r+1} + \Psi_{r-1}\right) \\ & + \epsilon\Psi_r \\ & + 2\Psi_1\left(\delta_{r1} + \delta_{r-1}\right) \\ & - 2\Psi_0\left(\delta_{r1}\mathrm{e}^{-\mathrm{i}\frac{K}{2}} + \delta_{r-1}\mathrm{e}^{\mathrm{i}\frac{K}{2}}\right) \\ & + 2\Psi_1\epsilon_K\delta_{r0}, \end{aligned} \tag{F.5}$$

where $\epsilon_K = -2\cos(K/2)$.

F.1.1 Scattering States

For the scattering states, I utilize the ansatz

$$\Psi_r = \mathrm{e}^{\mathrm{i}p|r|} + \mathrm{e}^{\mathrm{i}\Delta_{Kp}}\mathrm{e}^{-\mathrm{i}p|r|} = \Psi_{-r} \qquad \forall \quad r \geq 1, \tag{F.6}$$

where δ_{Kp} denotes the scattering phase shift. Evaluating Eq. (F.5) for $r = 2, 1, 0$ results in

$$\epsilon = \epsilon_K \cdot 2\cos(p)\,, \tag{F.7a}$$
$$\Psi_0 = 0\,, \tag{F.7b}$$
$$\mathrm{e}^{\mathrm{i}\Delta_{Kp}} = -\frac{\epsilon_K + 2\mathrm{e}^{\mathrm{i}p}}{\epsilon_K + 2\mathrm{e}^{-\mathrm{i}p}}\,. \tag{F.7c}$$

F.1.2 Magnon–Magnon Bound States

By the same token,

$$\Psi_r = \alpha^{|r|} = \Psi_{-r} \qquad \forall \quad r \geq 1 \tag{F.8}$$

serves as an ansatz for the bound-state solution. From Eq. (F.5), I find

$$\epsilon = \epsilon_K \cdot \frac{\alpha^2 + 1}{\alpha} = -2 - \frac{1}{2}\epsilon_K^2\,, \tag{F.9a}$$
$$\alpha = -\frac{1}{2}\epsilon_K\,, \tag{F.9b}$$
$$\Psi_0 = 0\,. \tag{F.9c}$$

List of Figures

1 One-Dimensional Waveguiding Structures I vii

1.1 One-Dimensional Waveguiding Structures II 9

3.1 Schematic Sketch of a Two-Level Atom in a Tight-Binding Waveguide and Single-Particle Eigenenergies 48
3.2 Evidence for Photon–Photon Bound States in the Tight-Binding Waveguide . 54
3.3 Functional Principle of the Qubit Coupler I 56
3.4 Functional Principle of the Qubit Coupler II 57
3.5 Level Scheme of a Driven Λ-Type Three-Level System and Electromagnetically Induced Transparency 58
3.6 Output Spectrum of a Coherent State Pulse Scattered at a Two-Level Atom . 59

4.1 A Beam Splitter as a Four-Port Device and its Analogy to a Scattering Problem 64
4.2 Schematic Sketch of a Local On-Site Potential and a Two-Level Atom in a Tight-Binding Waveguide 66
4.3 Schematic Sketch of the Two-Excitation Initial State in the Hong-Ou-Mandel Setup 69
4.4 Hong-Ou-Mandel Dip for an On-Site Potential 70
4.5 Hong-Ou-Mandel Dips as a Function of the Atomic Transition Energy and the Wave Packets' Width 72
4.6 Hong-Ou-Mandel Dip for an Anharmonic Oscillator 73
4.7 Influence of T_1-Relaxation and T_2-Depahsing on the Hong-Ou-Mandel Dip . . 75
4.8 Single-Particle Transmittance Through a Two-Level Atom Subject to Pure Dephasing of T_2-Type 76

5.1 Schematic Sketch of a Tight-Binding Waveguide with a Side-Coupled Kerr-Nonlinear Cavity 81
5.2 Transmission Characteristics for a Coherent State in a Tight-Binding Waveguide with a Side-Coupled Kerr-Nonlinear Cavity 88
5.3 Gating of a Single Photon in a Photon-Added Coherent State 90
5.4 Influence of Losses on the Fidelities for the Gating of a Single Photon in a Photon-Added Coherent State 91

6.1 Cosine-Dispersion Relation and Corresponding Density of States 104
6.2 Time Evolution of the Excited State's Population as a Function of the Atomic Transition Energy 105
6.3 Time Evolution of the Excited State's Population for Different Atom–Photon Coupling Strengths 106
6.4 Output Spectrum as a Function of the Atomic Transition Energy 108
6.5 Output Spectrum as a Function of the Detector Position 108
6.6 Atom–Field and Field–Field Correlation Functions 109
6.7 Time Evolution of the Excited State's Population for Different Distances of the Emitter's Lattice Site to the Beginning of the Absorbing Boundaries . . . 110
6.8 Influence of Dissipation (T_1) and Dephasing (T_2) on Non-Markovian Dynamics 111
6.9 Time Evolution of the Excited State's Population in the Presence of a Lossy Waveguide 112

7.1 Eigenenergies of Two-Magnon Scattering States and Magnon–Magnon Bound States 119
7.2 Schematic Sketch of a Spin Wave Impinging on a Potential Storing a Single Magnon 122
7.3 Ground State Energy of the Pöschl-Teller Potential as a Function of the Potential Depth 124
7.4 Single-Particle Transmittance Through the Pöschl-Teller Potential 125
7.5 Single-Magnon Extraction Efficiency 127
7.6 Space-Time Plot of the Magnon Propagation 127
7.7 Snapshots of the Magnon Propagation 128

Bibliography

[1] http://www.bmbf.de/en/3591.php.

[2] "QIPC, Quantum Information Processing and Communication—Strategic report on current status, visions and goals for research in Europe (http://qist.ect.it/Reports/reports.htm)", (2008).

[3] J. O'Brien and J. Akira Furusawa, "Photonic quantum technologies", Nature Photonics **3**, 687 (2009).

[4] O. Benson, "Assembly of hybrid photonic architectures from nanophotonic constituents", Nature **480**, 193 (2011).

[5] I. Walmsley and M. Raymer, "Toward quantum-information processing with photons", Science **307**, 1733 (2005).

[6] A. Peruzzo, A. Laing, A. Politi, T. Rudolph, and J. O'Brien, "Multimode quantum interference of photons in multiport integrated devices", Nature communications **2**, 224 (2011).

[7] K. Busch, G. von Freymann, S. Linden, S. F. Mingaleev, L. Tkeshelashvili, and M. Wegener, "Periodic nanostructures for photonics", Physics Reports **444**, 101 (2007).

[8] J. D. Joannopoulos, S. G. Johnson, J. N. Winn, and R. D. Meade, *Photonic Crystals: Molding the Flow of Light (Second Edition)* (Princeton University Press, 2008).

[9] I. Staude, G. von Freymann, S. Essig, K. Busch, and M. Wegener, "Waveguides in three-dimensional photonic-bandgap materials by direct laser writing and silicon double inversion", Optics Letters **36**, 67 (2011).

[10] A. Yariv, Y. Xu, R. K. Lee, and A. Scherer, "Coupled-resonator optical waveguide: a proposal and analysis", Optics Letters **24**, 711 (1999).

[11] M. Notomi, E. Kuramochi, and T. Tanabe, "Large-scale arrays of ultrahigh-Q coupled nanocavities", Nature Photonics **2**, 741 (2008).

[12] F. Xia, L. Sekaric, M. O'Boyle, and Y. Vlasov, "Coupled resonator optical waveguides based on silicon-on-insulator photonic wires", Applied Physics Letters **89**, 041122 (2006).

[13] F. Xia, L. Sekaric, and Y. Vlasov, "Ultracompact optical buffers on a silicon chip", Nature Photonics **1**, 65 (2007).

[14] H. J. Kimble, "The quantum internet", Nature **453**, 1023 (2008).

[15] M. J. Hartmann, F. G. S. L. Brandao, and M. B. Plenio, "Strongly interacting polaritons in coupled arrays of cavities", Nature Physics **2**, 849 (2006).

[16] G. Lepert, M. Trupke, M. Hartmann, M. Plenio, and E. Hinds, "Arrays of waveguide-coupled optical cavities that interact strongly with atoms", New Journal of Physics **13**, 113002 (2011).

[17] J. Poon, J. Scheuer, Y. Xu, and A. Yariv, "Designing coupled-resonator optical waveguide delay lines", Journal of the Optical Society of America B **21**, 1665 (2004).

[18] A. Houck, H. Türeci, and J. Koch, "On-chip quantum simulation with superconducting circuits", Nature Physics **8**, 292 (2012).

[19] H. Salehi, A. Majedi, and R. Mansour, "Analysis and design of superconducting left-handed transmission lines", IEEE Transactions on Applied Superconductivity **15**, 996 (2005).

[20] H. Salehi, R. Mansour, and A. Majedi, "Nonlinear Josephson left-handed transmission lines", Microwaves, Antennas & Propagation, IET **1**, 69 (2007).

[21] M. Leib, F. Deppe, A. Marx, R. Gross, and M. Hartmann, "Networks of nonlinear superconducting transmission line resonators", ArXiv e-prints 1202.3240 (2012).

[22] P. Russell, "Photonic Crystal Fibers", Science **299**, 358 (2003).

[23] H. Kimble, "Strong interactions of single atoms and photons in cavity QED", Physica Scripta **76**, 127 (1998).

[24] A. Imamoğlu, H. Schmidt, G. Woods, and M. Deutsch, "Strongly Interacting Photons in a Nonlinear Cavity", Physical Review Letters **79**, 1467 (1997).

[25] C. K. Law, "Interaction between a moving mirror and radiation pressure: A Hamiltonian formulation", Physical Review A **51**, 2537 (1995).

[26] M. I. Makin, J. H. Cole, C. D. Hill, and A. D. Greentree, "Spin Guides and Spin Splitters: Waveguide Analogies in One-Dimensional Spin Chains", Physical Review Letters **108**, 017207 (2012).

[27] S. Bose, "Quantum communication through spin chain dynamics: an introductory overview", Contemporary Physics **48**, 13 (2007).

[28] D. Jaksch and P. Zoller, "The cold atom Hubbard toolbox", Annals of physics **315**, 52 (2005).

[29] L.-M. Duan, E. Demler, and M. D. Lukin, "Controlling Spin Exchange Interactions of Ultracold Atoms in Optical Lattices", Physical Review Letters **91**, 090402 (2003).

[30] S. Longhi, "Optical realization of the two-site Bose–Hubbard model in waveguide lattices", Journal of Physics B: Atomic, Molecular and Optical Physics **44**, 051001 (2011).

[31] Y. Lahini, M. Verbin, S. D. Huber, Y. Bromberg, R. Pugatch, and Y. Silberberg, "Quantum Walk of Two Interacting Bosons", ArXiv e-prints 1105.2273 (2011).

[32] J. D. Jackson, *Classical Electrodynamics* (John Wiley & Sons Inc., 1999).

[33] G. Kweon and N. Lawandy, "Quantum electrodynamics in photonic crystals", Optics Communications **118**, 388 (1995).

[34] M. Sparnaay, "Attractive forces between flat plates", Nature **180**, 334 (1957).

[35] C. C. Gerry and P. L. Knight, *Introductory quantum optics* (Cambridge University Press, Cambridge, 2005).

[36] S. Johnson and J. Joannopoulos, "Block-iterative frequency-domain methods for Maxwell's equations in a planewave basis", Optics Express **8**, 173 (2001).

[37] C. Wolff, "Band Structure Based Analysis of Certain Photonic Crystal Structures", Ph.D. Thesis, Institut für Theoretische Festkörperphysik, Karlsruher Institut für Technologie (KIT) (2011).

[38] K. Busch, S. Lölkes, R. B. Wehrspohn, and H. Föll, *Photonic Crystals: Advances in Design, Fabrication, and Characterization* (Wiley-VCH, 2004).

[39] A. Birner, K. Busch, and F. Müller, "Photonische Kristalle", Physikalische Blätter **55**, 27 (1999).

[40] B. E. A. Saleh and M. C. Teich, *Fundamentals of Photonics (Wiley Series in Pure and Applied Optics)* (John Wiley & Sons, 1991).

[41] J. Rarity, J. Fulconis, J. Duligall, W. Wadsworth, and P. Russell, "Photonic crystal fiber source of correlated photon pairs", Optics Express **13**, 534 (2005).

[42] R. J. Glauber, "Coherent and Incoherent States of the Radiation Field", Physical Review **131**, 2766 (1963).

[43] G. S. Agarwal and K. Tara, "Nonclassical properties of states generated by the excitations on a coherent state", Physical Review A **43**, 492 (1991).

[44] A. Zavatta, S. Viciani, and M. Bellini, "Quantum-to-Classical Transition with Single-Photon-Added Coherent States of Light", Science **306**, 660 (2004).

[45] M. Barth, S. Schietinger, T. Schröder, T. Aichele, and O. Benson, "Controlled coupling of NV defect centers to plasmonic and photonic nanostructures", Journal of Luminescence **130**, 1628 (2010).

[46] D. Englund, A. Majumdar, A. Faraon, M. Toishi, N. Stoltz, P. Petroff, and J. Vučković, "Resonant Excitation of a Quantum Dot Strongly Coupled to a Photonic Crystal Nanocavity", Physical Review Letters **104**, 073904 (2010).

[47] J. Ward and O. Benson, "WGM microresonators: sensing, lasing and fundamental optics with microspheres", Laser & Photonics Reviews **5**, 553 (2011).

[48] J. Clarke and F. Wilhelm, "Superconducting quantum bits", Nature **453**, 1031 (2008).

[49] D. Zueco, J. José Mazo, E. Solano, and J. José García-Ripoll, "Microwave photonics with Josephson junction arrays", ArXiv e-prints 1110.1184 (2011).

[50] J.-C. Blancon, "Few-Photon-Quantum Transport in Low-Dimensional Systems: Functional Elements and Circuitry", Master's Thesis, Institut für Theoretische Festkörperphysik, Karlsruher Institut für Technologie (KIT) (2010).

[51] M. O. Scully and S. M. Zubairy, *Quantum Optics* (Cambridge University Press, 1997).

[52] P. W. Milonni and J. H. Eberly, *Laser physics* (Wiley, 2010).

[53] D. Braak, "Integrability of the Rabi Model", Physical Review Letters **107**, 100401 (2011).

[54] M. Orszag, *Quantum Optics: Including Noise Reduction, Trapped Ions, Quantum Trajectories, and Decoherence; 2nd ed.* (Springer, Berlin, 2000).

[55] R. Loudon, *The Quantum Theory of Light* (OUP Oxford, 2000).

[56] E. T. Jaynes and F. W. Cummings, "Comparison of quantum and semiclassical radiation theories with application to the beam maser", Proceedings of the IEEE **51**, 89 (1963).

[57] M. Bina, "The coherent interaction between matter and radiation - A tutorial on the Jaynes-Cummings model", ArXiv e-prints 1111.1143 (2011).

[58] R. H. Dicke, "Coherence in Spontaneous Radiation Processes", Physical Review **93**, 99 (1954).

[59] B. Garraway, "The Dicke model in quantum optics: Dicke model revisited", Philosophical Transactions of the Royal Society A: Mathematical, Physical and Engineering Sciences **369**, 1137 (2011).

[60] J.-T. Shen and S. Fan, "Coherent photon transport from spontaneous emission in one-dimensional waveguides", Optics Letters **30**, 2001 (2005).

[61] P. Longo, P. Schmitteckert, and K. Busch, "Few-photon transport in low-dimensional systems", Physical Review A **83**, 063828 (2011).

[62] P. Longo, P. Schmitteckert, and K. Busch, "Few-Photon Transport in Low-Dimensional Systems: Interaction-Induced Radiation Trapping", Physical Review Letters **104**, 023602 (2010).

[63] P. Longo, "Einfluss einer Zwei-Niveau-Störstelle auf den Transport von Photonen in effektiv eindimensionalen Wellenleiter-Systemen", Diploma Thesis, Institut für Theoretische Festkörperphysik, Universität Karlsruhe (TH) (2009).

[64] A. Greentree, C. Tahan, J. Cole, and L. Hollenberg, "Quantum phase transitions of light", Nature Physics **2**, 856 (2006).

[65] M. I. Makin, J. H. Cole, C. D. Hill, A. D. Greentree, and L. C. L. Hollenberg, "Time evolution of the one-dimensional Jaynes-Cummings-Hubbard Hamiltonian", Physical Review A **80**, 043842 (2009).

[66] M. I. Makin, J. H. Cole, C. Tahan, L. C. L. Hollenberg, and A. D. Greentree, "Quantum phase transitions in photonic cavities with two-level systems", Physical Review A **77**, 053819 (2008).

[67] M. I. Makin, "The Jaynes-Cummings-Hubbard model", Ph.D. Thesis, School of Physics, University of Melbourne (2011).

[68] J. Q. Quach, C.-H. Su, A. M. Martin, A. D. Greentree, and L. C. L. Hollenberg, "Reconfigurable quantum metamaterials", Optics Express **19**, 11018 (2011).

[69] R. W. Boyd, *Nonlinear optics* (Elsevier/Academic Press, Amsterdam, 2008).

[70] L. Mandel and E. Wolf, *Optical coherence and quantum optics* (Cambridge University Press, Cambridge, 1995).

[71] J. E. Sipe, "Photons in dispersive dielectrics", Journal of Optics A: Pure and Applied Optics **11**, 114006 (2009).

[72] J. E. Sipe, N. A. R. Bhat, P. Chak, and S. Pereira, "Effective field theory for the nonlinear optical properties of photonic crystals", Physical Review E **69**, 016604 (2004).

[73] M. Hillery and L. D. Mlodinow, "Quantization of electrodynamics in nonlinear dielectric media", Physical Review A **30**, 1860 (1984).

[74] J.-Q. Liao and C. K. Law, "Correlated two-photon transport in a one-dimensional waveguide side-coupled to a nonlinear cavity", Physical Review A **82**, 053836 (2010).

[75] S. Ferretti, L. C. Andreani, H. E. Türeci, and D. Gerace, "Photon correlations in a two-site nonlinear cavity system under coherent drive and dissipation", Physical Review A **82**, 013841 (2010).

[76] Y. Yamamoto and A. Imamoglu, *Mesoscopic Quantum Optics* (Wiley-Interscience, 1999).

[77] Z. R. Gong, H. Ian, Y.-x. Liu, C. P. Sun, and F. Nori, "Effective Hamiltonian approach to the Kerr nonlinearity in an optomechanical system", Physical Review A **80**, 065801 (2009).

[78] F. Hammer, ed., *Johannes Kepler Gesammelte Werke Band 8: Mysterium Cosmographicum. Editio altera cum notis. De Cometis. Hyperaspistes* (C. H. Beck, 1963).

[79] W. Pernice, M. Li, K. Fong, and H. Tang, "Modeling of the optical force between propagating lightwaves in parallel 3D waveguides", Optics Express **17**, 16032 (2009).

[80] W. Pernice, M. Li, and H. Tang, "Optomechanical coupling in photonic crystal supported nanomechanical waveguides", Optics Express **17**, 12424 (2009).

[81] W. Pernice, M. Li, and H. Tang, "Theoretical investigation of the transverse optical force between a silicon nanowire waveguide and a substrate", Optics Express **17**, 1806 (2009).

[82] G. S. Wiederhecker, L. Chen, A. Gondarenko, and M. Lipson, "Controlling photonic structures using optical forces", Nature **462**, 633 (2009).

[83] F. Marquardt, J. P. Chen, A. A. Clerk, and S. M. Girvin, "Quantum Theory of Cavity-Assisted Sideband Cooling of Mechanical Motion", Physical Review Letters **99**, 093902 (2007).

[84] F. M. Max Ludwig, "Der Klang der Quantentrommel", Physik Journal **9**, 20 (2010).

[85] C. Metzger and K. Karrai, "Cavity cooling of a microlever", Nature **432**, 1002 (2004).

[86] M. Eichenfield, J. Chan, R. M. Camacho, K. J. Vahala, and O. Painter, "Optomechanical crystals", Nature **462**, 78 (2009).

[87] D. Chang, A. Safavi-Naeini, M. Hafezi, and O. Painter, "Slowing and stopping light using an optomechanical crystal array", New Journal of Physics **13**, 023003 (2011).

[88] K. Stannigel, P. Rabl, A. S. Sørensen, P. Zoller, and M. D. Lukin, "Optomechanical Transducers for Long-Distance Quantum Communication", Physical Review Letters **105**, 220501 (2010).

[89] M. Aspelmeyer, S. Groeblacher, K. Hammerer, and N. Kiesel, "Quantum optomechanics—throwing a glance [Invited]", Journal of the Optical Society of America B **27**, A189 (2010).

[90] A. Jayich, J. Sankey, B. Zwickl, C. Yang, J. Thompson, S. Girvin, A. Clerk, F. Marquardt, and J. Harris, "Dispersive optomechanics: a membrane inside a cavity", New Journal of Physics **10**, 095008 (2008).

[91] T. J. Kippenberg and K. J. Vahala, "Cavity Optomechanics: Back-Action at the Mesoscale", Science **321**, 1172 (2008).

[92] F. Marquardt, "Licht macht Druck", Physik Journal **8**, 67 (2009).

[93] G. D. Mahan, *Many particle physics* (Plenum Press, New York, 1980).

[94] S. Groblacher, K. Hammerer, M. R. Vanner, and M. Aspelmeyer, "Observation of strong coupling between a micromechanical resonator and an optical cavity field", Nature **460**, 724 (2009).

[95] C. Roy and S. John, "Microscopic theory of multiple-phonon-mediated dephasing and relaxation of quantum dots near a photonic band gap", Physical Review A **81**, 023817 (2010).

[96] E. Anda and J. Ernesto Ure, "A model for hydrogen chemisorption including image charge effects", Surface Science **83**, 572 (1979).

[97] R. J. Glauber, "The Quantum Theory of Optical Coherence", Physical Review **130**, 2529 (1963).

[98] R. J. Glauber, "Photon Correlations", Physical Review Letters **10**, 84 (1963).

[99] W. H. Louisell, *Quantum Statistical Properties of Radiation (Pure & Applied Optics)* (John Wiley & Sons Inc, 1973).

[100] W. Kozek, F. Hlawatsch, H. Kirchauer, and U. Trautwein, "Correlative time-frequency analysis and classification of nonstationary random processes", pp. 417–420 (1994).

[101] F. Hlawatsch and G. Matz, "Time-frequency signal processing: a statistical perspective", pp. 207–219 (1998).

[102] R. Jozsa, "Fidelity for mixed quantum states", Journal of Modern Optics **41**, 2315 (1994).

[103] H.-P. Breuer and F. Petruccione, *The theory of open quantum systems* (Clarendon Press, Oxford, 2010).

[104] H. Carmichael, *Statistical methods in quantum optics*, vol. 1: Master equations and Fokker-Planck equations of *Texts and monographs in physics* (Springer, Berlin, 1999).

[105] M. B. Plenio and P. L. Knight, "The quantum-jump approach to dissipative dynamics in quantum optics", Reviews of Modern Physics **70**, 101 (1998).

[106] K. Mølmer, Y. Castin, and J. Dalibard, "Monte Carlo wave-function method in quantum optics", Journal of the Optical Society of America B **10**, 524 (1993).

[107] L. Allen and J. H. Eberly, *Optical resonance and two-level atoms* (Dover Publ., New York, 1987).

[108] P. Longo, P. Schmitteckert, and K. Busch, "Dynamics of photon transport through quantum impurities in dispersion-engineered one-dimensional systems", Journal of Optics A: Pure and Applied Optics **11**, 114009 (2009).

[109] Y. Saad, "Analysis of Some Krylov Subspace Approximations to the Matrix Exponential Operator", SIAM Journal on Numerical Analysis **29**, 209 (1992).

[110] J. Niegemann, L. Tkeshelashvili, and K. Busch, "Higher-Order Time-Domain Simulations of Maxwell's Equations Using Krylov-Subspace Methods", Journal of Computational and Theoretical Nanoscience **4**, 627 (2007).

[111] K. Busch, J. Niegemann, M. Pototschnig, and L. Tkeshelashvili, "A Krylov-subspace based solver for the linear and nonlinear Maxwell equations", physica status solidi (b) **244**, 3479 (2007).

[112] A. Politi, M. J. Cryan, J. G. Rarity, S. Yu, and J. L. O'Brien, "Silica-on-Silicon Waveguide Quantum Circuits", Science **320**, 646 (2008).

[113] L. Zhou, Y. B. Gao, Z. Song, and C. P. Sun, "Coherent output of photons from coupled superconducting transmission line resonators controlled by charge qubits", Physical Review A **77**, 013831 (2008).

[114] Y. Chang, Z. R. Gong, and C. P. Sun, "Multiatomic mirror for perfect reflection of single photons in a wide band of frequency", Physical Review A **83**, 013825 (2011).

[115] L. Zhou, J. Lu, and C. P. Sun, "Coherent control of photon transmission: Slowing light in a coupled resonator waveguide doped with Λ atoms", Physical Review A **76**, 012313 (2007).

[116] J.-T. Shen and S. Fan, "Coherent Single Photon Transport in a One-Dimensional Waveguide Coupled with Superconducting Quantum Bits", Physical Review Letters **95**, 213001 (2005).

[117] J.-T. Shen and S. Fan, "Strongly Correlated Two-Photon Transport in a One-Dimensional Waveguide Coupled to a Two-Level System", Physical Review Letters **98**, 153003 (2007).

[118] J.-T. Shen and S. Fan, "Strongly correlated multiparticle transport in one dimension through a quantum impurity", Physical Review A **76**, 062709 (2007).

[119] H. Dong, Z. Gong, H. Ian, L. Zhou, and C. Sun, "Intrinsic Cavity QED and Emergent Quasi-Normal Modes for Single Photon", ArXiv e-prints 0805.3085 (2008).

[120] L. Zhou, Z. R. Gong, Y.-X. Liu, C. P. Sun, and F. Nori, "Controllable Scattering of a Single Photon inside a One-Dimensional Resonator Waveguide", Physical Review Letters **101**, 100501 (2008).

[121] Z. R. Gong, H. Ian, L. Zhou, and C. P. Sun, "Controlling quasibound states in a one-dimensional continuum through an electromagnetically-induced-transparency mechanism", Physical Review A **78**, 053806 (2008).

[122] L. Zhou, H. Dong, Y. Liu, C. Sun, and F. Nori, "Quantum supercavity with atomic mirrors", Physical Review A **78**, 63827 (2008).

[123] J.-T. Shen and S. Fan, "Theory of single-photon transport in a single-mode waveguide. I. Coupling to a cavity containing a two-level atom", Physical Review A **79**, 023837 (2009).

[124] J.-T. Shen and S. Fan, "Theory of single-photon transport in a single-mode waveguide. II. Coupling to a whispering-gallery resonator containing a two-level atom", Physical Review A **79**, 023838 (2009).

[125] T. Shi and C. P. Sun, "Lehmann-Symanzik-Zimmermann reduction approach to multiphoton scattering in coupled-resonator arrays", Physical Review B **79**, 205111 (2009).

[126] L. Jing, D. Hui, and K. Le-Man, "Transferring and Bounding Single Photon in Waveguide Controlled by Quantum Node Based on Atomic Ensemble", Communications in Theoretical Physics **52**, 500 (2009).

[127] J. Liao, Z. Gong, L. Zhou, Y. Liu, C. Sun, and F. Nori, "Controlling the transport of single photons by tuning the frequency of either one or two cavities in an array of coupled cavities", Physical Review A **81**, 042304 (2010).

[128] T. S. Tsoi and C. K. Law, "Single-photon scattering on Λ-type three-level atoms in a one-dimensional waveguide", Physical Review A **80**, 033823 (2009).

[129] Z. Yu and S. Fan, "Optical resonances created by photonic transitions", Applied Physics Letters **96**, 011108 (2010).

[130] X. Zang and C. Jiang, "Single-photon transport properties in a waveguide–cavity system", Journal of Physics B: Atomic, Molecular and Optical Physics **43**, 065505 (2010).

[131] D. Roy, "Few-photon optical diode", Physical Review B **81**, 155117 (2010).

[132] D. Witthaut and A. S. Sørensen, "Photon scattering by a three-level emitter in a one-dimensional waveguide", New Journal of Physics **12**, 043052 (2010).

[133] P. Becker, "Stark korrelierter Photonentransport in dotierten Wellenleitersystemen", Diploma Thesis, Insitut für Theoretische Festkörperphysik, Karlsruher Institut für Technologie (KIT) (2010).

[134] C. Stawiarski, "Funktionale Integration zur Berechnung von Photonenstreuung an Störstellen in Wellenleiterstrukturen", Diploma Thesis, Insitut für Theorie der Kondensierten Materie, Karlsruher Institut für Technologie (KIT) (2010).

[135] J.-T. Shen and S. Fan, "Quantum critical coupling conditions for zero single-photon transmission through a coupled atom-resonator-waveguide system", Physical Review A **82**, 021802 (2010).

[136] E. Rephaeli, J.-T. Shen, and S. Fan, "Full inversion of a two-level atom with a single-photon pulse in one-dimensional geometries", Physical Review A **82**, 033804 (2010).

[137] H. Zheng, D. J. Gauthier, and H. U. Baranger, "Waveguide QED: Many-body bound-state effects in coherent and Fock-state scattering from a two-level system", Physical Review A **82**, 063816 (2010).

[138] S. Fan, S. E. Kocabaş, and J.-T. Shen, "Input-output formalism for few-photon transport in one-dimensional nanophotonic waveguides coupled to a qubit", Physical Review A **82**, 063821 (2010).

[139] E. E. Hach, A. W. Elshaari, and S. F. Preble, "Fully quantum-mechanical dynamic analysis of single-photon transport in a single-mode waveguide coupled to a traveling-wave resonator", Physical Review A **82**, 063839 (2010).

[140] D. Roy, "Two-Photon Scattering by a Driven Three-Level Emitter in a One-Dimensional Waveguide and Electromagnetically Induced Transparency", Physical Review Letters **106**, 053601 (2011).

[141] C.-H. Yan, L.-F. Wei, W.-Z. Jia, and J.-T. Shen, "Controlling resonant photonic transport along optical waveguides by two-level atoms", Physical Review A **84**, 045801 (2011).

[142] C. Martens, "Photonentransport in eindimensionalen Wellenleitern mit seitengekoppelten Drei-Niveau-Systemen", Diploma Thesis, Institut für Theoretische Festkörperphysik, Karlsruher Institut für Technologie (KIT) (2011).

[143] H. Zheng, D. J. Gauthier, and H. U. Baranger, "Cavity-Free Photon Blockade Induced by Many-Body Bound States", Physical Review Letters **107**, 223601 (2011).

[144] E. Rephaeli, S. E. Kocabaş, and S. Fan, "Few-photon transport in a waveguide coupled to a pair of colocated two-level atoms", Physical Review A **84**, 063832 (2011).

[145] T. Shi, S. Fan, and C. P. Sun, "Two-photon transport in a waveguide coupled to a cavity in a two-level system", Physical Review A **84**, 063803 (2011).

[146] W.-B. Yan, Q.-B. Fan, and L. Zhou, "Control of correlated two-photon transport in a one-dimensional waveguide", Physical Review A **85**, 015803 (2012).

[147] S. E. Kocabaş, E. Rephaeli, and S. Fan, "Resonance fluorescence in a waveguide geometry", Physical Review A **85**, 023817 (2012).

[148] M. Cheng and Y. Song, "Fano resonance analysis in a pair of semiconductor quantum dots coupling to a metal nanowire", Optics Letters **37**, 978 (2012).

[149] M. Pletyukhov and V. Gritsev, "Scattering of massless particles in one-dimensional chiral channel", ArXiv e-prints 1203.0451 (2012).

[150] M. Bradford, K. C. Obi, and J.-T. Shen, "Efficient Single-Photon Frequency Conversion Using a Sagnac Interferometer", Physical Review Letters **108**, 103902 (2012).

[151] M. Bradford and J.-T. Shen, "Single-photon frequency conversion by exploiting quantum interference", Physical Review A **85**, 043814 (2012).

[152] E. Rephaeli and S. Fan, "Stimulated Emission from a Single Excited Atom in a Waveguide", Physical Review Letters **108**, 143602 (2012).

[153] H. Zheng, D. J. Gauthier, and H. U. Baranger, "Strongly correlated photons generated by coupling a three- or four-level system to a waveguide", Physical Review A **85**, 043832 (2012).

[154] M. Moeferdt, "Vollständige Zählstatistik in eindimensionalen wellenleitenden Systemen", Diploma Thesis, Insitut für Theoretische Festkörperphysik, Karlsruher Institut für Technologie (KIT) (2012).

[155] M. Valiente and D. Petrosyan, "Scattering resonances and two-particle bound states of the extended Hubbard model", Journal of Physics B: Atomic, Molecular and Optical Physics **42**, 121001 (2009).

[156] D. Petrosyan and M. Valiente, in *Modern Optics and Photonics Atoms and Structured Media* (2010), pp. 222–236.

[157] M. T. C. Wong and C. K. Law, "Two-polariton bound states in the Jaynes-Cummings-Hubbard model", Physical Review A **83**, 055802 (2011).

[158] J.-C. Blancon, P. Longo, and K. Busch, in preparation.

[159] C. Martens, P. Longo, and K. Busch, in preparation.

[160] B. Mollow, "Power spectrum of light scattered by two-level systems", Physical Review **188**, 1969 (1969).

[161] J. Werra, "Propagation of coherent light pulses coupled to a two-level system (working title)", Diploma Thesis, Institut für Theoretische Festkörperphysik, Karlsruher Institut für Technologie (KIT), to be submitted in August (2012).

[162] P. Longo, J. H. Cole, and K. Busch, "The Hong-Ou-Mandel effect in the context of few-photon scattering", Optics Express **20**, 12326 (2012).

[163] C. K. Hong, Z. Y. Ou, and L. Mandel, "Measurement of subpicosecond time intervals between two photons by interference", Physical Review Letters **59**, 2044 (1987).

[164] Y. L. Lim and A. Beige, "Generalized Hong–Ou–Mandel experiments with bosons and fermions", New Journal of Physics **7**, 155 (2005).

[165] V. Giovannetti, D. Frustaglia, F. Taddei, and R. Fazio, "Electronic Hong-Ou-Mandel interferometer for multimode entanglement detection", Physical Review B **74**, 115315 (2006).

[166] H. Takesue, "1.5 μm band Hong-Ou-Mandel experiment using photon pairs generated in two independent dispersion shifted fibers", Applied Physics Letters **90**, 204101 (2007).

[167] S. Wang, S. Mu, C. Zhu, Y. Gong, P. Xu, H. Liu, T. Li, S. Zhu, and X. Zhang, "Hong-Ou-Mandel interference mediated by the magnetic plasmon waves in a three-dimensional optical metamaterial", Optics Express **20**, 5213 (2012).

[168] Z. Ou, C. Hong, and L. Mandel, "Relation between input and output states for a beam splitter", Optics Communications **63**, 118 (1987).

[169] D. Angelakis, M. Santos, and S. Bose, "Photon-blockade-induced Mott transitions and XY spin models in coupled cavity arrays", Physical Review A **76**, 31805 (2007).

[170] P. Longo and K. Busch, "Pulse propagation of photon-added coherent states in waveguides with side-coupled nonlinear cavities", Optics Letters **37**, 1793 (2012).

[171] M. W. Jack and M. Yamashita, "Bose-Hubbard model with attractive interactions", Physical Review A **71**, 023610 (2005).

[172] A. E. Miroshnichenko, S. F. Mingaleev, S. Flach, and Y. S. Kivshar, "Nonlinear Fano resonance and bistable wave transmission", Physical Review E **71**, 036626 (2005).

[173] M. Sheik-Bahae, D. J. Hagan, and E. W. Van Stryland, "Dispersion and band-gap scaling of the electronic Kerr effect in solids associated with two-photon absorption", Physical Review Letters **65**, 96 (1990).

[174] T. J. Kippenberg and K. J. Vahala, "Cavity opto-mechanics", Optics Express **15**, 17172 (2007).

[175] A. Einstein, "On the quantum theory of radiation", Zeitschrift für Physik **18**, 121 (1917).

[176] V. Weisskopf and E. Wigner, "Calculation of the natural lineshape based on Dirac's quantum theory of light", Zeitschrift für Physik **63**, 54 (1930).

[177] E. M. Purcell, "Spontaneous emission probabilities at radio frequencies", Physical Review **69**, 681 (1946).

[178] J. M. Wylie and J. E. Sipe, "Quantum electrodynamics near an interface", Physical Review A **30**, 1185 (1984).

[179] J. M. Wylie and J. E. Sipe, "Quantum electrodynamics near an interface. II", Physical Review A **32**, 2030 (1985).

[180] R. M. Amos and W. L. Barnes, "Modification of the spontaneous emission rate of Eu^{3+} ions close to a thin metal mirror", Physical Review B **55**, 7249 (1997).

[181] E. Yablonovitch, "Inhibited Spontaneous Emission in Solid-State Physics and Electronics", Physical Review Letters **58**, 2059 (1987).

[182] S. John and J. Wang, "Quantum electrodynamics near a photonic band gap: Photon bound states and dressed atoms", Physical Review Letters **64**, 2418 (1990).

[183] S. John and J. Wang, "Quantum optics of localized light in a photonic band gap", Physical Review B **43**, 12772 (1991).

[184] S. John and T. Quang, "Spontaneous emission near the edge of a photonic band gap", Physical Review A **50**, 1764 (1994).

[185] T. Quang, M. Woldeyohannes, S. John, and G. S. Agarwal, "Coherent Control of Spontaneous Emission near a Photonic Band Edge: A Single-Atom Optical Memory Device", Physical Review Letters **79**, 5238 (1997).

[186] T. Quang and S. John, "Resonance fluorescence near a photonic band edge: Dressed-state Monte Carlo wave-function approach", Physical Review A **56**, 4273 (1997).

[187] K. Busch, N. Vats, S. John, and B. C. Sanders, "Radiating dipoles in photonic crystals", Physical Review E **62**, 4251 (2000).

[188] N. Vats, S. John, and K. Busch, "Theory of fluorescence in photonic crystals", Physical Review A **65**, 043808 (2002).

[189] M. Woldeyohannes and S. John, "Coherent control of spontaneous emission near a photonic band edge", Journal of Optics B Quantum and Semiclassical Optics **5**, 43 (2003).

[190] M. Florescu and S. John, "Single-atom switching in photonic crystals", Physical Review A **64**, 033801 (2001).

[191] M. Florescu and S. John, "Resonance fluorescence in photonic band gap waveguide architectures: Engineering the vacuum for all-optical switching", Physical Review A **69**, 53810 (2004).

[192] M. W. Jack and J. J. Hope, "Resonance fluorescence in a band-gap material: Direct numerical simulation of non-Markovian evolution", Physical Review A **63**, 043803 (2001).

[193] P. Kristensen, A. Koenderink, P. Lodahl, B. Tromborg, and J. Mørk, "Fractional decay of quantum dots in real photonic crystals", Optics Letters **33**, 1557 (2008).

[194] K. H. Madsen, S. Ates, T. Lund-Hansen, A. Löffler, S. Reitzenstein, A. Forchel, and P. Lodahl, "Observation of Non-Markovian Dynamics of a Single Quantum Dot in a Micropillar Cavity", Physical Review Letters **106**, 233601 (2011).

[195] U. Hoeppe, C. Wolff, J. Küchenmeister, J. Niegemann, M. Drescher, H. Benner, and K. Busch, "Direct Observation of Non-Markovian Radiation Dynamics in 3D Bulk Photonic Crystals", Physical Review Letters **108**, 043603 (2012).

[196] L. C. Andreani and D. Gerace, "Photonic-crystal slabs with a triangular lattice of triangular holes investigated using a guided-mode expansion method", Physical Review B **73**, 235114 (2006).

[197] C. Creatore and L. C. Andreani, "Quantum theory of spontaneous emission in multilayer dielectric structures", Physical Review A **78**, 063825 (2008).

[198] G. Khitrova, H. M. Gibbs, M. Kira, S. W. Koch, and A. Scherer, "Vacuum Rabi splitting in semiconductors", Nature Physics **2**, 81 (2006).

[199] J. Kim, O. Benson, H. Kan, and Y. Yamamoto, "A single-photon turnstile device", Nature **397**, 500 (1999).

[200] P. Michler, A. Kiraz, C. Becher, W. V. Schoenfeld, P. M. Petroff, L. Zhang, E. Hu, and A. Imamoglu, "A Quantum Dot Single-Photon Turnstile Device", Science **290**, 2282 (2000).

[201] C. Santori, D. Fattal, J. Vuckovic, G. S. Solomon, and Y. Yamamoto, "Indistinguishable photons from a single-photon device", Nature **419**, 594 (2002).

[202] P. Longo, A. Greentree, K. Busch, and J. H. Cole, in preparation.

[203] W. Nolting and A. Ramakanth, *Quantum theory of magnetism* (Springer Verlag, 2009).

[204] M. Cieplak and L. Turski, "Solitons in quantum Heisenberg chain", Journal of Physics C: Solid State Physics **13**, 5741 (1980).

[205] H. Fogedby, "Solitons and magnons in the classical Heisenberg chain", Journal of Physics A: Mathematical and General **13**, 1467 (1980).

[206] A. Kay and D. G. Angelakis, "Reproducing spin lattice models in strongly coupled atom-cavity systems", Europhysics Letters **84**, 20001 (2008).

[207] T. Holstein and H. Primakoff, "Field dependence of the intrinsic domain magnetization of a ferromagnet", Physical Review **58**, 1098 (1940).

[208] P. Jordan and E. Wigner, "Über das Paulische Äquivalenzverbot", Zeitschrift für Physik A **47**, 631 (1928).

[209] S. Feng, "Jordan-Wigner approach to the spin excitation spectrum in the Heisenberg antiferromagnet", Physical Review B **53**, 11671 (1996).

[210] T. Schneider, "Solitons and magnon bound states in ferromagnetic Heisenberg chains", Physical Review B **24**, 5327 (1981).

[211] M. Wortis, "Bound states of two spin waves in the Heisenberg ferromagnet", Physical Review **132**, 85 (1963).

[212] J. Javanainen, O. Odong, and J. C. Sanders, "Dimer of two bosons in a one-dimensional optical lattice", Physical Review A **81**, 043609 (2010).

[213] G. Pöschl and E. Teller, "Bemerkungen zur Quantenmechanik des anharmonischen Oszillators", Zeitschrift für Physik A **83**, 143 (1933).

[214] N. Rosen and P. Morse, "On the vibrations of polyatomic molecules", Physical Review **42**, 210 (1932).

[215] M. Nieto, "Exact wave-function normalization constants for the $B_0 \tanh z - U_0 \cosh^{-2} z$ and Pöschl-Teller potentials", Physical Review A **17**, 1273 (1978).

[216] J. Lekner, "Reflectionless eigenstates of the sech^2 potential", American Journal of Physics **75**, 1151 (2007).

[217] J. Jeske, J. H. Cole, C. Müller, M. Marthaler, and G. Schön, "Dual-probe decoherence microscopy: probing pockets of coherence in a decohering environment", New Journal of Physics **14**, 023013 (2012).

[218] F. Benatti, R. Floreanini, and M. Piani, "Environment Induced Entanglement in Markovian Dissipative Dynamics", Physical Review Letters **91**, 070402 (2003).

[219] D. Bozyigit, C. Lang, L. Steffen, J. M. Fink, C. Eichler, M. Baur, R. Bianchetti, P. J. Leek, S. Filipp, M. P. da Silva, et al., "Antibunching of microwave-frequency photons observed in correlation measurements using linear detectors", Nature Physics **7**, 154 (2011).

[220] G. Vidal, "Efficient Simulation of One-Dimensional Quantum Many-Body Systems", Physical Review Letters **93**, 040502 (2004).

[221] M. Knap, E. Arrigoni, W. von der Linden, and J. H. Cole, "Emission characteristics of laser-driven dissipative coupled-cavity systems", Physical Review A **83**, 023821 (2011).

[222] J. H. Cole and J. Jeske, private communication (2011).

[223] C. Moler and C. V. Loan, "Nineteen Dubious Ways to Compute the Exponential of a Matrix, Twenty-Five Years Later", SIAM Review **45**, 3 (2003).

[224] R. B. Sidje, "EXPOKIT: Software Package for Computing Matrix Exponentials", ACM Transactions on Mathematical Software **24**, 130 (1998).

[225] http://www.boost.org/.

[226] http://www.netlib.org/blas/.

[227] http://www.netlib.org/lapack/.

[228] http://www.grinninglizard.com/tinyxml/.

[229] http://www.hdfgroup.org/HDF5/.

[230] http://www.mathworks.de/products/matlab/.

[231] http://www.fftw.org/.

Publications and Miscellaneous

Publications in Peer-Reviewed Journals

- Paolo Longo, Peter Schmitteckert, and Kurt Busch, *Dynamics of Photon Transport Through Quantum Impurities in Dispersion-Engineered One-Dimensional Systems*, Journal of Optics A: Pure and Applied Optics **11**, 114009 (2009).

- Paolo Longo, Peter Schmitteckert, and Kurt Busch, *Few-Photon Transport in Low-Dimensional Systems: Interaction-Induced Radiation Trapping*, Physical Review Letters **104**, 023602 (2010).

- Paolo Longo, Peter Schmitteckert, and Kurt Busch, *Few-Photon Transport in Low-Dimensional Systems*, Physical Review A **83**, 063828 (2011).

- Paolo Longo and Kurt Busch, *Pulse Propagation of Photon-Added Coherent States in Waveguides with Side-Coupled Nonlinear Cavities*, Optics Letters **37**, 1793 (2012).

- Paolo Longo, Jared H. Cole, and Kurt Busch, *The Hong-Ou-Mandel Effect in the Context of Few-Photon Scattering*, Optics Express **20**, 12326 (2012).

Publications in Preparation

- Paolo Longo, Andrew D. Greentree, Kurt Busch, and Jared H. Cole, *Quantum Bocce: Magnon-Magnon Collisions between Propagating and Bound States in 1D Spin Chains*, submitted (2012).

- Jean-Christophe Blancon, Paolo Longo, and Kurt Busch, *A Quantum Switch Based on Superconducting Metamaterials*, in preparation for submission to Physical Review A.

- Christoph Martens, Paolo Longo, and Kurt Busch, *Photon Transport in One-Dimensional Systems Coupled to Three-Level Quantum Impurities*, in preparation for submission to New Journal of Physics.

- Julia F. M. Werra, Paolo Longo, and Kurt Busch, *Propagation of Coherent Light Pulses Coupled to a Two-Level System*, in preparation for submission to Optics Letters.

Supervised Theses

- Jean-Christophe Blancon, *Few-Photon-Quantum Transport in Low-Dimensional Systems: Functional Elements and Circuitry*, Master Thesis (as part of the Master program of the Karlsruhe School of Optics and Photonics (KSOP)), Institut für Theoretische Festkörperphysik, Karlsruher Institut für Technologie (KIT), August 2010.
- Christoph Martens, *Photonentransport in eindimensionalen Wellenleitern mit seitengekoppelten Drei-Niveau-Systemen*, Diploma Thesis, Institut für Theoretische Festkörperphysik, Karlsruher Institut für Technologie (KIT), October 2011.
- Julia F. M. Werra, *Propagation of Coherent Light Pulses Coupled to a Two-Level System* (working title), Diploma Thesis, Institut für Theoretische Festkörperphysik, Karlsruher Institut für Technologie (KIT), in collaboration with the Institut für Physik at the Humboldt-Universität zu Berlin (AG Theoretische Optik & Photonik), ongoing (hand-in date August 2012).

Stay Abroad

- September 2011–December 2011, RMIT University Melbourne, Chemical and Quantum Physics, School of Applied Sciences, Dr. J. Cole

Acknowledgements

My thesis in its current form would not have been possible without a number of people.

First of all, I would like to thank Prof. Kurt Busch who accepted me as a Ph.D. student and employee. He gave me the freedom to independently explore my own ideas which he greatly supported with his expertise. Without his friendly and liberal spirit, the results of this thesis would have been impossible.

I am very grateful to Prof. Martin Wegener for agreeing to co-referee my thesis.

I would like to express my gratitude to Jean-Christophe Blancon, Christoph Martens and Julia Werra. It was a pleasure for me to assist you during your time as a master/diploma student in the Photonics Group. I am thankful for everything we learned together, for the friendly atmosphere, your patience and your trust.

Proof-reading of a Ph.D. thesis can be quite time-consuming and annoying. I am deeply indebted to Jean-Christophe Blancon, Jan Jeske, Jens Küchenmeister, Christoph Martens, Matthias Moeferdt, Julia Werra, and Christian Wolff, who thoroughly went through the details of my drafts and provided me with indispensable corrections, suggestions and comments. You did a great job!

I would like to thank Jared Cole who encouraged me to spend a few months of my time in Melbourne. I am very grateful for his support and advice. I acknowledge the fruitful discussions I had with Jared Cole, Jan Jeske and Melissa Makin during my stay in Melbourne. I would like to furthermore thank Andrew Greentree for his interest in my work. The friendliness of the whole Chemical and Quantum Physics Group at RMIT turned my stay in Melbourne into an unforgettable memory. I acknowledge financial support for my stay abroad by the Karlsruhe House of Young Scientists (KHYS).

I enjoyed my time as a member of the Photonics Group in Karlsruhe. All the barbecues, pizzas, cakes and ice creams provided more than just a nice and friendly atmosphere to work in. I thank everybody who contributed to the team spirit of the Photonics Group. I am especially grateful for the trustful atmosphere during the last months.

Last bot not least, many thanks go to my family. I thank my parents, my sister and Fabienne for all the support, encouragement and understanding.

Yame!